EUROPEAN ORGANIZATION FOR NUCLEAR RESEARCH

CERN/SPSLC 96-14
SPSC/P 297
March 1, 1996

PROPOSAL

Common Muon and Proton Apparatus for Structure and Spectroscopy

The COMPASS Collaboration

Abstract

We propose to study hadron structure and hadron spectroscopy with high-rate hadron and muon beams and a new spectrometer to be built at the CERN SPS. The experiment can start up in 1999 and a program of physics measurements for an initial period of 5 more years is planned.

The COMPASS Collaboration

Universität Bielefeld, Bielefeld, Germany
G. Baum, J. Kyynäräinen, A. Tripet
Universität Bochum, Bochum, Germany
R. Gehring, S. Goertz, W. Meyer, G. Reicherz
Institut für Strahlen- und Kernphysik, Universität Bonn, Bonn, Germany
B.M. Barnett, J. Bisplinghoff, F. Hinterberger, H. Kalinowsky, E. Klempt, R. Maschuw, Chr. Straßburger
Physikalisches Institut, Universität Bonn, Bonn, Germany
F. Klein
H.H. Wills Laboratory, University of Bristol, Bristol, United Kingdom
S.L. McKennan, V.J. Smith
Université de Bruxelles, Bruxelles, Belgium
F. Binon, J.M. Frère, J.P. Stroot
Chiba University, Chiba, Japan
H. Kawai
JINR, Dubna, Russia
V. Artemov, M. Finger, M. Finger Jr, O.E. Gortchakov, A. Janata, Yu.F. Kisselev, V. Kurbatov, D.V. Peshekhonov, D. Pose, A.M. Rozhdestvensky, M.G. Sapozhnikov, I.A. Savin, M. Slunecka, G.I. Smirnov, L.G. Tkatchev, S.B. Vorozhtsov
Universität Erlangen, Erlangen, Germany
G. Anton, W. Eyrich, F. Stinzing, S. Wirth
Universität Freiburg, Freiburg, Germany
H. Fischer, J. Franz, H.J. Kessler, K. Königsmann, U. Landgraf, H. Schmitt, A. Simon, A. Witzmann
CERN, Genève, Switzerland
U. Wiedner
Max-Planck-Institut für Kernphysik, Heidelberg, Germany
W. Brückner, U. Dersch, F. Dropmann, I. Konorov, S. Masciocchi, S. Paul, J. Pochodzalla, B. Povh, L. Schmitt, J. Zimmer
Physikalisches Institut der Universität Heidelberg, Heidelberg, Germany
*E. Chudakov*1)*, H.W. Siebert*
Helsinki University of Technology, Helsinki, Finland
P. Berglund
Kernforschungsanlage Jülich, Jülich, Germany
D. Gronzka, K. Kilian, W. Oelert, K. Röhrich, T. Sefzick
Universität Mainz, Mainz, Germany
*A. Bravar, D. von Harrach, E.M. Kabuß, A. Kotzinian, G.K. Mallot, U. Müller*2)*, J. Pretz, G. Rosner, A. Steinmetz, B. Volkemer, T. Walcher*
Miyazaki University, Miyazaki, Japan
K. Takamatsu

---

[1] on leave of absence from Moscow State Univ., Moscow, Russia
[2] presently at CERN, Div. PPE, Geneva

Université de Mons-Hainaut, Mons, Belgium
R. Windmolders

Inst. for Nuclear Research, Moscow, Russia
V. Bolotov, E. Guschin, V. Lebedev, A. Proskuryakov, V. Shmatkov

Lebedev Physical Institute, Moscow, Russia
Yu. Alexandrov, S. Gerassimov, P. Netchaeva, M. Zavertiaev

Universität München, München, Germany
M. Fässler, A. Staude

Nagoya University, Nagoya, Japan
T. Hasegawa, N. Hayashi, N. Horikawa, S. Ishimoto, T. Iwata, A. Kishi, T. Matsuda, K. Mori

University of Osaka, Osaka, Japan
T. Kinashi, M. Nomachi

IHEP, Protvino, Russia
Yu.I. Arestov, A.A. Derevschikov, S.V. Donskov, V. Dorofeev, R. Dzhelyadin, A.V. Inyakin, V.A.Kachanov, G.V. Khaustov, V.Yu. Khodyrev, Yu. Khokhlov, V.A. Medvedev, A. Ostankov, Yu. D.Prokoshkin, P.A. Semenov, P.M. Shagin, A.V. Singovsky, A. Sobol, V.L. Solovianov, V.P. Sugonyaev, M.N. Ukhanov

Rutgers University, New Jersey, USA
R. Ransome

Tohoku University, Sendai, Japan
T. Nakagawa

Tel Aviv University, Tel Aviv, Israel
J. Lichtenstadt, M.A. Moinester

INFN, Sezione di Torino, e Università di Torino, Torino, Italy
R. Bertini, S. Costa(3), *P. Damiani, L. Ferrero, R. Garfagnini, L. Isnardi, A. Maggiora, D. Panzieri, L. Valaccal*

INFN, Sezione di Trieste, e Università di Trieste, Trieste, Italy
R. Birsa, F. Bradamante(3),*A. Bressan, S. Dalla Torre, M. Giorgi, M. Lamanna, A. Martin, A. Penzo, P. Schiavon, F. Tessarotto, A.M. Zanetti*

Soltan Institute for Nuclear Studies and Warsaw University, Warsaw, Poland
K. Kurek, J. Nassalski, E. Rondio, A. Sandacz, W. Wislicki

KEK, Tsukuba, Japan
S. Inaba, T. Tsuru, Y. Yasu

Yamagata University, Yamagata, Japan
H. Shimizu, H. Yoshida

Universität Zürich, Zürich, Switzerland
C. Amsler

Spokespersons: *F. Bradamante*
S. Paul

---

(3) presently at CERN, Div. PPE, Geneva

Contents

1 INTRODUCTION 6

2 OVERVIEW 7

2.1 Physics Objectives 7

2.2 Apparatus Overview 9

3 PHYSICS WITH MUON BEAM 15

3.1 GLUON POLARISATION $\Delta G/G$ 15

3.1.1 Open charm leptoproduction 16

3.1.2 Monte Carlo studies 19

3.1.3 Reconstruction of open charm events 20

3.1.4 The measurement of the asymmetry $A_{\gamma\mathrm{N}}^{\mathrm{c\bar{c}}}$ 21

3.1.5 D^{*+} tagging 22

3.1.6 Reconstruction of the D meson from other decay channels 24

3.1.7 Measurement of g_1 and estimate of $\Delta G/G$ from its Q^2 evolution . . 24

3.1.8 Comparison with other experiments on ΔG 25

3.2 LONGITUDINAL SPIN DISTRIBUTION FUNCTIONS 26

3.2.1 Rate estimates 28

3.2.2 Flavour decomposition of the distribution functions 29

3.3 MEASUREMENT OF Λ AND $\overline{\Lambda}$ POLARISATION 30

3.3.1 The target fragmentation region 31

3.3.2 The current fragmentation region 32

3.3.3 Simulation of the detector efficiencies for Λ production 34

3.4 TRANSVERSE SPIN DISTRIBUTION FUNCTIONS 36

3.4.1 Measurement of $\Delta_T q(x)$ 36

3.4.2 Collins effect for leading pions 37

3.4.3 Statistical accuracy 39

3.4.4 Systematics uncertainties 41

3.4.5 Measurement of $g_2(x)$ 42

4 PHYSICS WITH HADRON BEAM 44

4.1 STUDIES OF CHARMED HADRONS 44

4.1.1 Status of charmed baryons and previous experiments 44

4.1.2 Charmed Baryon Decays 44

4.1.3 Studies of Charm Hadroproduction 48

4.1.4 Double-Charmed Baryons 50

4.1.5 Studies with D-mesons 53

4.1.6 The technical challenge 54

4.1.7 Yields 54

4.2 STUDY OF GLUONIC SYSTEMS 64

4.2.1 The existence and signatures of glueballs 64
4.2.2 Status of the search for glueballs 65
4.2.3 Study of glueballs within the scope of this proposal 66
4.2.4 Production of mesons through diffractive processes 68
4.3 HADRONIC STRUCTURE WITH VIRTUAL PHOTONS 69
4.3.1 Diffractive Cross Sections 76
4.4 CHARM EXOTICS 77
4.4.1 Singly Charmed Pentaquark 77
4.4.2 Doubly Charmed Tetraquark 78
4.5 OUTLOOK 80

5 THE EXPERIMENTAL APPARATUS 81
5.1 COMMON EQUIPMENT 81
5.1.1 Beam Considerations 81
5.1.2 General layout 81
5.1.3 The Honey-Comb Trackers 83
5.1.4 Multi-Wire Proportional Chambers 85
5.1.5 The RICH Detectors 85
5.1.6 The Electromagnetic Calorimeters 98
5.1.7 The Hadron Calorimeters 99
5.1.8 The Muon Filters 99
5.2 MUON PROGRAMME 102
5.2.1 Design criteria of the LAS 102
5.2.2 The muon beam and beam detectors 104
5.2.3 The polarised target 107
5.2.4 The Large Angle Spectrometer Magnet 111
5.2.5 The D° invariant mass resolution 111
5.2.6 The muon trigger hodoscopes 115
5.3 HADRON PROGRAMME 116
5.3.1 Beam Requirements 116
5.3.2 Beam identification 118
5.3.3 Target region 119
5.3.4 The SM1h magnetic spectrometer 121
5.3.5 Microstrip Gas Chambers 124
5.3.6 Electron Identification 124
5.3.7 Trigger 125

6 READ-OUT ELECTRONICS AND DATA ACQUISITION 128
6.1 Frontends 129
6.2 DAQ computer 135

7 COST ESTIMATE 140
7.1 Estimate for the Cost of the Equipments 140
7.2 Total Cost of COMPASS 148
7.3 Responsibilities 149

8 TIME SCALE AND RUNNING STRATEGIES 151

9 REQUEST TO CERN 153

A Longitudinal spin asymmetries in hadron production **156**

B Transverse spin asymmetries in hadron production **158**

C Doubly Charmed Baryons **160**

References **171**

1 INTRODUCTION

The main goal of the proposed experiment is the investigation of hadron structure and hadron spectroscopy, which are both manifestations of non-perturbative QCD. Comparison with lattice calculations and with model predictions based on chiral symmetry or on effective degrees of freedom will help improve our understanding of hadrons. To reach this objective requires large integrated luminosities for different projectiles, ranging from muons to hadrons with energies varying from 100 GeV to a few hundred GeV.

A key feature of the experiment will be the detection of high statistics samples of charmed particles. From a measurement of the cross-section asymmetry for open charm production in deep inelastic scattering of polarised muons on polarised nucleons we will determine the *gluon polarisation* ΔG. Predictions of QCD-inspired models or lattice calculations start being available for this quantity. Using hadron beams we will study *semi-leptonic decays* of charmed-baryons as well *doubly charmed baryons*. Both measurements will allow to address fundamental issues of hadron structure and to test Heavy Quark Effective Theory (HQET) calculations.

Either in parallel to the charm program, or, to a lesser extent, in dedicated runs, we will carry out a wide programme of physics measurements with unprecedented sensitivity. For example, we will address the long standing question of *exotic states*, which are foreseen by QCD but have not yet been firmly established. We will also investigate *transverse spin distribution functions* and *fracture functions*, whose theoretical relevance has only recently been recognised.

To perform these measurements we propose a new state-of-the-art spectrometer with excellent particle identification and calorimetry, capable of standing beam intensities of up to $2 \cdot 10^8$ particles/spill. Dedicated triggers and a fast read-out complement the outstanding performance of the spectrometer. The natural location for this experiment is the EHN2 hall. The muon M2 beam line can easily be modified to transport hadrons of momenta up to 300 GeV/c as well. A technical run in 1999 will be followed by five years of data taking. The resulting statistics will provide a good basis for further evaluation of the programme.

In the following section we first give an overview of the various physics objectives we intend to pursue using hadron and muon beams. Next we present an overview of the proposed spectrometer.

2 OVERVIEW

2.1 Physics Objectives

Physics with hadron beams. With hadron beams we will address three main issues: studies of *charmed hadrons*, spectroscopy of *light quark systems and glueballs*, and an investigation of the hadronic structure of unstable particles using *Primakoff reactions.*

Charmed hadrons will be used to study *semi-leptonic decays* (semi-inclusive and inclusive), *doubly charmed baryons*, and the systematics of their *production mechanism.* These investigations are unlikely to be addressed by current or future fixed target experiments.

The knowledge of *semi-leptonic decay widths* is one of the most important issues in charm physics. They provide the best test for our understanding of charmed baryon decays since precise theoretical predictions on rates and form factors are available. In particular, the q^2 dependence of form factors attracted recently much attention within the framework of HQET calculations. Although the charm quark mass is at the lower limit of applicability of the theory corrections are believed to be of the order of only 20 %.

In the absence of a precise knowledge of charmed hadron production rates, semi-leptonic decays provide a link between lifetime and hadronic branching ratio: the theoretical semi-leptonic decay width together with the experimental ratio of semi-leptonic to hadronic branching fractions allow a determination of hadronic partial widths for comparison with theory predictions. The absolute hadronic branching ratio results from multiplication with the measured lifetime.

Almost all $1/2^+$ states of singly-charmed baryons were observed to date, but nothing is known about *doubly-charmed baryons.* Their structure probably resembles a heavy meson: a heavy cc-diquark in the centre surrounded by a light quark. Such states are expected in the mass range from 3.6 GeV (ccu, ccd) to 3.8 GeV (ccs). In addition to spectroscopical interest, their lifetimes offer insights into decay dynamics. If the decays are dominated by the spectator diagram their lifetime is expected to be about 1/2 that of the Ξ_c^+ (about 200 fs). Each doubly-charmed baryon lifetime may be affected by at most one additional decay diagram, thus allowing an independent study of each individual contribution.

However, the study of ccq-baryons is hindered by very low production cross sections. Currently, estimates for this quantity are rather uncertain. With reasonable assumptions we conclude that only a high rate experiment will allow the production of about 100 fully reconstructed events.

Finally there is the unsolved phenomenon of unexpected production yields observed in earlier experiments. This seems to be closely connected to the baryon number flow. A systematic investigation requires acceptance over the largest possible solid angle extending to negative values of x_F $(= 2p_L^{cm}/\sqrt{s})$, variable beam energies and projectile type.

Owing to its non-Abelian character one fundamental prediction of QCD is the existence of states containing valence gluons: *glueballs and hybrids.* Since QCD cannot predict the spectrum of non-$\mathrm{q\overline{q}}$ states we have to resort to models, which yield a rich spectrum of such states. Still, the models are incapable of providing narrow range predictions that would unambiguously identify glueballs and hybrids. Lattice calculations give wide limits for the probable mass of the lightest glueballs: from 1500 to 1800 MeV for the 0^{++}, i.e. in a region where scalars and other mesons abound.

For many years experiments tried to establish the existence of glueballs and hybrids, with the best candidate coming from LEAR, a scalar glueball $\mathrm{f_0}(1500)$. In order to make a large step towards a positive identification of exotic states the detection of as many decay modes and production mechanisms as possible is required. A new high-statistics, high-quality experiment can solve the problem. We will benefit from the better understanding of the expected glueball decay pattern and will have the advantage of building on the elaborate analysis techniques developed by GAMS, WA76/91/102, Crystal Barrel, OBELIX and other experiments currently working in this field.

To obtain a data sample enriched with $q\overline{q}$ states, we will exploit two production mechanisms: central production and diffractive scattering of mesons by nuclei. We will be able to detect many decay modes that contain photons as well as charged and neutral pions and kaons, with special emphasis on the glueball-preferred final states containing η and η'.

The study of nucleon structure gained considerable interest owing to the progress in the description of non-perturbative QCD. In particular, chiral perturbation theory allows to make definite predictions for a number of quantities such as polarisabilities and cross sections in $\pi\gamma$ interactions. Currently such studies are almost solely addressed at low energy electron accelerators. High energy pion, kaon, and hyperon beams allow complementary measurements using the *Primakoff reaction mechanism*, which is Compton scattering with virtual photons in inverse kinematics.

Physics with a muon beam. After confirmation of the original EMC result by recent experiments at CERN and SLAC it is now firmly established that the spin content of the nucleon is not entirely due to the quark spins. Competing explanations exist for this result. In the gluon interpretation it is the *polarised glue* ΔG which lowers the quark's contribution to the nucleon spin, whereas in an alternative model negatively polarised strange quarks are responsible. Several ways exist in which a new muon experiment can resolve these ambiguities in interpretation.

Inclusive measurements of $g_1^{\mathrm{p}}(x)$, $g_1^{\mathrm{n}}(x)$ and $g_2(x)$ do not allow to distinguish the role of each individual parton distribution function. It is therefore mandatory to either study polarised proton–proton collisions or to perform polarised semi-inclusive lepton scattering experiments, which are proposed here.

For the measurement of the *gluon polarisation* $\Delta G/G$ we use the photon-gluon fusion process leading to open charm production as a clean tool to access ΔG. We will also access ΔG by determining *asymmetries* in single or correlated large p_T particle production in deep-inelastic scattering.

Semi-inclusive data obtained the SMC experiment lead to a first measurement of Δu_v, Δd_v, and $\Delta\bar{u} + \Delta\bar{d}$. Similar measurements were proposed for the HERMES experiment at DESY. A high statistics experiment at CERN will benefit from higher beam energies (100–200 GeV), which assures a cleaner separation of current and target fragmentation.

The self-analysing properties of the $\Lambda(\bar{\Lambda})$ make this particle particularly suited for spin physics. The question of whether the spin of the strange sea-quarks is really anti-correlated with the proton spin as proposed by some models, can be decided by measuring the *polarisation of* Λ's from the target fragmentation. The use of a polarised muon beam with an unpolarised target selects reactions where quarks are oriented anti-parallel to the virtual photon's helicity. If strange quarks are oriented predominantly anti-parallel to the proton spin, then Λ 's from the target fragmentation region should carry a negative polarisation (assuming negatively polarised muons).

The observation of $\Lambda(\bar{\Lambda})$ in the current fragmentation region addresses the problem of spin dependent fragmentation functions. The measurement of the polarisation of a forward produced Λ or $\bar{\Lambda}$ directly determines the *spin dependent fragmentation function.* This function has close relations to the spin structure functions.

The probability that a quark spin in a transversely polarised nucleon is oriented parallel or antiparallel to the nucleon spin can in principle be measured in deep-inelastic scattering. Such a measurement requires a transversely polarised target and the knowledge of the spin dependent fragmentation functions for the transverse case. As in the longitudinal case the contribution of certain quark flavours can be enhanced by selecting the corresponding hadrons. This *twist-2 distribution function* $h_1(x)$ is different from its longitudinal counterpart $g_1(x)$ and is – like the transverse spin dependent fragmentation function – not yet measured. The difference between g_1 and h_1 depends among other things on the role of polarised gluons, which do not contribute to h_1.

Another method to access h_1 uses the (transverse) *spin dependent azimuthal asymmetries* of leading hadrons around the virtual photon direction. The analysing power of this process is not yet known but it is probably large, as suggested by the size of typical asymmetries in soft hadronic processes. We propose to measure these transverse spin asymmetries which, due to factorisation, can determine both, the distribution function and the fragmentation function, up to a normalisation factor.

In summary we propose a rich spin physics programme which can be completed in a running time of four years. First answers can be obtained already after about two years of running time. Therefore the estimates given in this proposal refer to a one year's measurement with a proton target and a one and a half year's with a deuteron target. The two target materials are needed to separate the helicity distributions of the different quark flavours. All the longitudinal spin measurements will be done simultaneously, while the transverse spin measurements can be performed between consecutive blocks of opposite target polarities. Taking into account the exploratory character of the transverse spin measurements, we presently envisage a 4:1 share of the beam time between the longitudinal and the transverse target polarisation mode.

2.2 Apparatus Overview

In this section we present an overview of the experimental set-ups foreseen for the different measurements. Emphasis will be given to general aspects and requirements. Details on the various components can be found in section 5.

The proposed experiment comprises measurements of rather different nature which require their own optimised set-up. Nevertheless, the global structure of the different experiments bares a lot of similarities, namely the use of a modern, high rate forward spectrometer with two independent magnetic spectrometer stages, each equipped with tracking, particle identification, calorimetry and muon detection. Despite the rather different requirements we designed a scenario in which a large fraction of the apparatus can be in common. This applies in particular for the section downstream from the first magnetic spectrometer. Owing to very different target set-ups the part upstream of the first Cherenkov counter has to be designed individually. This includes the use of different large angle spectrometer magnets. Figure 2.1 shows the two major experimental configurations used for the hadron and muon beam programme.

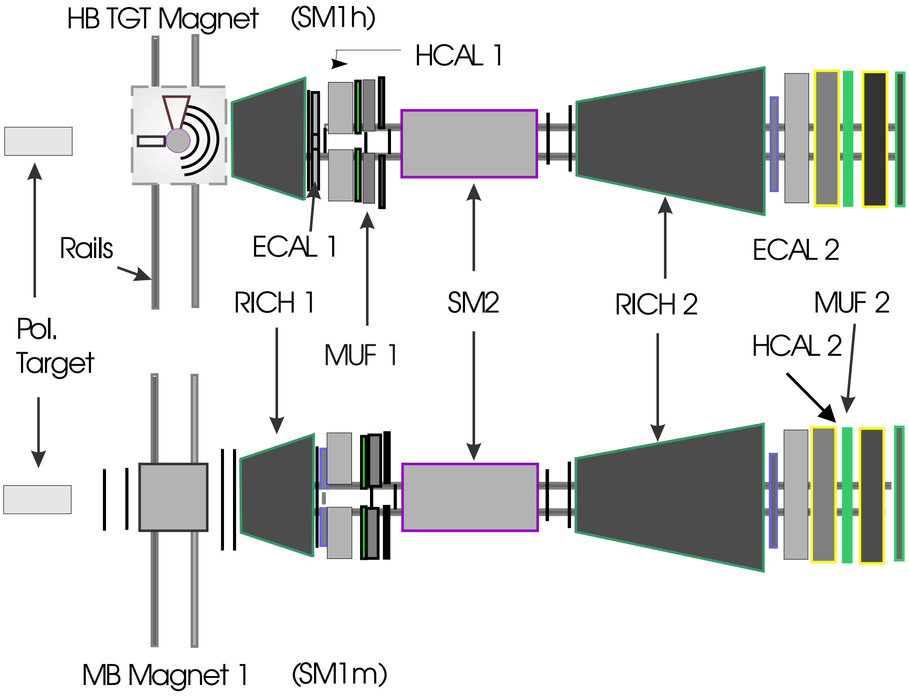

Figure 2.1: Schematic view of the apparatus set-ups for hadron (HB) and muon beam (MB) operation

The requirements for the various detectors are given by the maximum requirements for the different measurements. The most stringent ones are coming from the intensity of the muon beam (100 MHz) and the large interaction rate in the hadron beam (1 MHz). These large rates impose particular care in the choice of detector materials as radiation damage in silicon detectors or calorimeter crystals can be severe. High demands on the speed of the detectors and the read-out are put by the hadron beam programme in particular by the requirements for a very fast and efficient trigger for charmed events. Therefore fast front-end electronics, multi-buffering, and a large and fast storage of events are essential. This makes the use of LHC-type technology mandatory and constitutes a very challenging task$^{1)}$.

The set-up includes existing equipment where possible. This is the case for the second spectrometer magnet SM2 (MEP45) and the SM1h magnet (MEP48) in the hadron beam set-up. The polarised target of the muon programme will re-use the dilution refrigerator and the infrastructure of the NA47 experiment. The largest fraction of the electromagnetic

---

[1] Some of these problems were already encountered by the HERA-B experiment at DESY and solutions found can be used.

calorimeters will be made from existing equipment including the GAMS detector currently used in WA102, the OLGA calorimeter used in WA91, and the WA89 calorimeter. The beam particle identification (not shown in Fig. 2.1) can be performed by a CERN CEDAR system or by the HYPOLIT beam RICH originally built for the WA89 experiment.

In the following we will present a brief description of the various detector components starting with the common equipment. The spectrometer consists of a large and a small angle spectrometer stage. The design of the two stages is similar and comprises along the beam a spectrometer magnet, SM1/2, a ring imaging Cherenkov counter, RICH1/2, an electromagnetic calorimeter, ECAL1/2, a hadron calorimeter, HCAL1/2, and finally a muon filter, μF1/2, where 1 and 2 refer to the large and small angle stage of the spectrometer respectively

The first ring imaging Cherenkov counter, RICH1, is designed to separate pions, kaons, and protons in a momentum interval of about 3–65 GeV/c. The angular acceptance is about ± 200 mrad in the vertical and ± 250 mrad in the horizontal direction. The key part of this RICH is the fast photon detection system. It will be made of multi-wire proportional chambers with a CsI photo cathode segmented in pads. About 69000 pads will be needed to cope with the large particle multiplicities associated with hadronic interactions and with the photon halo of the muon beam. The Cherenkov photons will be reflected by mirrors in a way that the photon detectors can be mounted in the shadow of the first magnet. The same detector technique will be used for the second RICH in the small angle spectrometer. This counter will be 8 m long and separate pions, kaons, and protons up to momenta of 120 GeV/c. The photon detectors are segmented in 46000 pads.

The electromagnetic calorimeters will be made of lead glass using existing equipment. However, the central part of the downstream calorimeter will be constructed from new radiation hard $PbWO_4$ crystals. A challenging task is the construction of a very fast read-out device meeting the high resolution requirement put by the light quark spectroscopy and the Primakoff scattering programmes. The first hadron calorimeter serves mainly triggering purposes for both experimental programmes and a moderate energy resolution is sufficient. For this calorimeter we will re-use existing equipment from the WA102 experiment and from Dubna. The small angle hadron calorimeter should be a compensated calorimeter with a high resolution. It will be constructed as lead scintillator sandwich calorimeter with $10 \times 10 \times 1200$ cm^3 modules. For the hadron calorimeters the same read-out electronics is foreseen as for the electromagnetic ones.

The muon filters serve the identification and detection of the scattered muon in the muon programme and of the muons from semi-leptonic decays in the hadron programme. The muon track will be linked with the tracking information upstream of the absorber. Due to the multiple scattering in the absorber only limited spatial resolution is required. After the first muon wall the tracking is performed by plastic Iarocci tubes and after the second muon wall by drift tubes of 3 cm diameter. The information from muon hodoscopes behind the absorber will be used in the triggers of both set-ups.

For the large area tracking throughout both stages of the spectrometer drift chambers will be used. A possible choice are honey-comb chambers with drift cells of 0.5 cm diameter upstream of RICH2 and of 1 cm diameter downstream from RICH2. Smaller drift chambers will be installed in the tunnel formed by the first set of calorimeters and the first muon wall just upstream of the spectrometer magnet SM2, which provides a bending power of up to 4.4 Tm. These chambers serve in particular the identification of decays of neutral kaons and hyperons in the region between the two spectrometer magnets. Inside the magnet SM2 multi-wire proportional chambers will be used for pattern recognition. In order to minimise interactions of the proton beam all large size tracking detectors will have a beam hole of about 4×4 cm^2. These holes will be complemented by microstrip gas chambers and silicon detectors in the hadron beam set-up and by scintillating fibre or ordinary hodoscopes in the muon set-up, where beam interaction is not an issue. Where needed also the spatial resolution can be improved by these detectors.

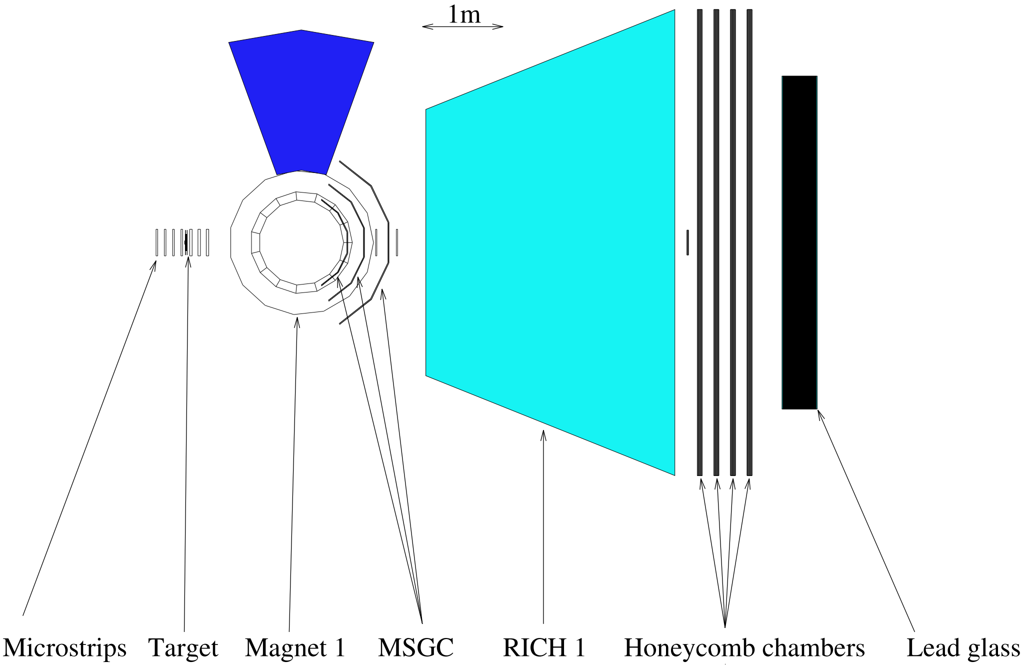

Figure 2.2: Top view of the large angle spectrometer set-up for the charm programme.

We will now describe the parts of the set-up specific to each experimental sub-programme. Figure 2.2 depicts the set-up for the hadron beam. Several different measurements will be performed, differing only in the section upstream of the magnet SM1h. The first spectrometer consists of a series of tracking chambers upstream of the cylindrical magnet, which provides a bending power of up to 1.8 Tm. In order to cope with the high particle fluxes and to obtain the necessary spatial precision they will be made from microstrip gas chambers. The same detector type will also be used inside and downstream from the magnet. In the latter case they will be arranged in cylindrical geometry, mounted on three concentric circles covering a large angular range (±50°). In total, more than 200 detectors of this type (15×25 cm^2) will be used. This provides an almost constant momentum resolution of about 0.4 % up to momenta of 20 GeV/c. For the measurement of charmed hadrons a special target detector will be built in order to allow partial track reconstruction of charged charmed hadrons. We will use a very dense arrangement of target material, trigger counters, and 10 μm pitch silicon detectors spaced by 1 mm followed by more standard double sided large area silicon detector telescopes. Such silicon detectors will also be employed upstream of the target for beam definition. For the light quark spectroscopy using central production this detector will be replaced by a liquid

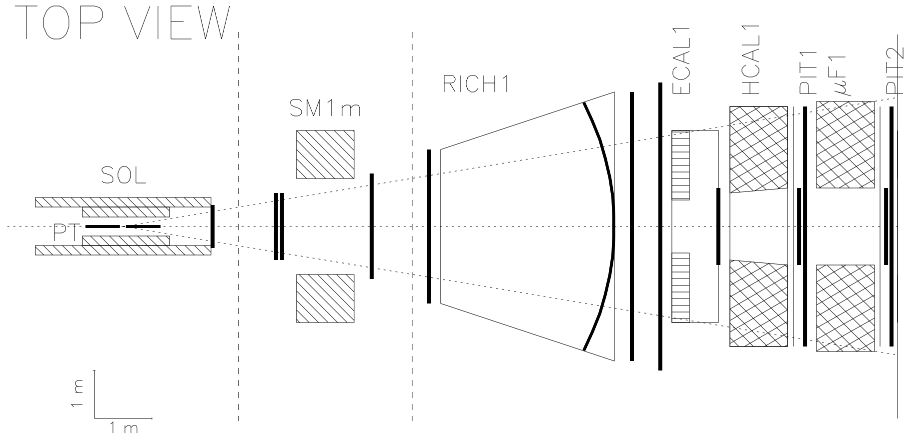

Figure 2.3: Schematic layout of the large angle spectrometer for the muon beam programme.

40 cm long hydrogen target followed by a silicon telescope. In order to identify the slow recoil proton a time of flight system will surround the target cylinder. It consists of an array of scintillation counters mounted on a cylinder with a radius of about 40 cm. For Primakoff measurements and diffractive meson production only a heavy target followed by silicon telescopes will be mounted.

Figure 2.3 shows the target and first spectrometer for the muon beam set-up. The polarised target system will comprise the SMC dilution refrigerator and infrastructure. However, in order to obtain sufficient acceptance for hadrons a solenoid with an inner diameter larger by more than a factor two compared to the existing super-conducting solenoid (26 cm) will be constructed. Essential for the measurements is the double cell target design, in which two oppositely polarised target cells can be exposed to the beam simultaneously. We will use two different target materials, NH_3 as proton target and ^{6}LiD as deuteron target. Polarisations of 85 % and 50 % can be reached, respectively. In ^{6}LiD both nuclei can be polarised to about the same extent yielding the favourable dilution factor of 0.5 assuming that ^{6}Li is composed of a deuteron and an alpha particle. The first spectrometer magnet SM1m has an angular acceptance of ± 200 mrad for particles originating in the target centre and provides a bending power of 1 Tm. To reduce the fringe field in the target region the magnet has to be at least 1.5 m distant from the end of the solenoid requiring an aperture of 2×1.6 m^2. The bending power can be achieved with a pole depth of at least 1 m. Such a magnet is not available and has to be constructed. Tracking upstream of this magnet will be performed using three stations of multi-wire proportional chambers with 2 mm pitch, while downstream from the magnet two stations of drift chambers will be used. In order to ensure high efficiency in the beam region, these chambers will be complemented by scintillating fibre or scintillator hodoscopes. For the determination of the reaction parameters it is essential to measure the momentum of the incoming muon. This will be performed by four scintillating fibre hodoscopes located up and downstream from the last vertical bending magnets in the beam line tunnel (not shown here) similar to the present set-up.

From the above description it becomes clear that a change-over from one experimental set-up to the other one requires considerable modifications of the detector. The first spectrometer magnets, SM1m and SM1h, including the surrounding detectors must be mounted on rails to allow their lateral movement. The large and unmovable polarised target system was chosen as a fix point. Its target cells will be emptied for runs with hadron beams. Thus to obtain flexibility in the longitudinal arrangement also other equipment including the magnet SM2 should be mounted on rails.

The beam line should be versatile to allow high intensity muon, pion, kaon, and proton beams of variable momenta up to 300 GeV/*c*. For the hadron programme a possible continuation of the experimental programme beyond the scope of this proposal would require proton beams of up to 450 GeV/*c* and charged hyperon beams of up to 360–400 GeV/*c*.

3 PHYSICS WITH MUON BEAM

The projected results for the muon programme presented in this chapter were estimated for incident muons of 100 GeV and 2×10^8 muons per SPS spill and muon a polarisation of 80 %. A total running of one and a half years with a ^{6}LiD (deuteron) target with 50 % polarisation and of one year with a NH_3 target (proton) of 85 % polarisation were assumed for the estimates. The luminosity is $4.3 \times 10^{37}\mathrm{cm}^{-2}\mathrm{day}^{-1}$. Taking into account an estimated combined efficiency of 0.25 for the SPS operation and the spectrometer and reconstruction efficiences, we obtain an effective luminosity of 1.9 fb^{-1}/year assuming a total SPS proton operation of 150 days/year. With an SPS performance as good as in 1995 the overall efficiency could be considerably larger than 0.25.

The programme with longitudinal target polarisation comprises the measurements for the gluon polarisation, the longitudinal spin distributions, and for part of the lambda programme. The programme with transverse target polarisation includes the measurements for the transverse quark distributions and part of the lambda programme. The experiments with the same target polarisation will be performed in parallel. The running time will be split in 80 % with longitudinal and 20 % with transverse target polarisation.

3.1 GLUON POLARISATION $\Delta G/G$

One of the current theoretical explanations [1–3] for the violation of the Ellis–Jaffe sum rule requires a substantial amount of polarised glue in the nucleon. Figure 3.1 shows some of the recently proposed parametrisations [4] of the gluon helicity distribution in the nucleon, $\Delta G(\eta)$, where η is the momentum fraction carried by the gluon. The first moment is $\int \Delta G(\eta)\,\mathrm{d}\eta \approx 2$ at $Q^2 = 4$ GeV^2 and corresponds to $\Delta\Sigma \simeq 0.30$ for the case that the violation of the Ellis–Jaffe sum rule is entirely due to the axial anomaly. The currently best value for $\Delta\Sigma$ is about 0.20 which implies a somewhat higher value of $\int \Delta G(\eta)\mathrm{d}\eta$. Common to all recent parametrisations of $\Delta G(\eta)$ [4–7] is their large positive integral $\int \Delta G(\eta) d\eta = 1$–$2$ at $Q^2 = 4$ GeV^2. This first moment increases in NLO with Q^2 like $1/\alpha_s(Q^2)$. At $Q^2 = 10$ GeV^2, which is the scale at which we will probe the gluons in the proposed experiment, this corresponds to $\int \Delta G(\eta) d\eta \geq 3$. It appears that $\eta\Delta G(\eta)$ has a maximum around $\eta = 0.1$ where the unpolarised gluon distribution $G(\eta)$ starts to drop significantly. Typical predictions at $\eta = 0.1$ are $\Delta G/G = 0.5$.

Among the various suggestions to measure $\Delta G/G$ [8–12] we consider a study of the longitudinal spin asymmetry of open charm leptoproduction as the best option for experiments at the CERN muon beam. In the following we examine the feasibility of such a measurement. We follow the suggestion [2, 8] to use the full virtual photon spectrum down to quasi-real photons. At muon energies of 100–200 GeV the contribution of the resolved photon process to the total charm photoproduction cross section is negligible.

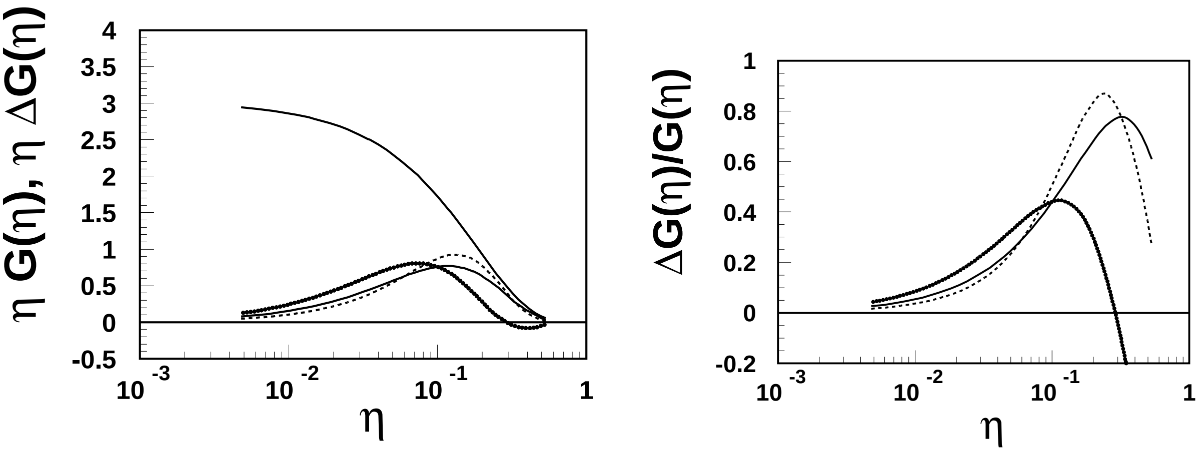

Figure 3.1: Three possible shapes of the gluon helicity distribution function $\eta\Delta G(\eta)$ as a function of the gluon momentum fraction η from Ref. [4]: set A (solid), B (dashed), and C (thick). a) upper curve: $\eta G(\eta)$ (Duke & Owens set 1.1); lower curves: $\eta\Delta G(\eta)$. b) the gluon polarisation $\Delta G(\eta)/G(\eta)$.

The proposed measurements are based on the reconstruction of D° mesons from their hadronic decay products which was already studied by the EMC with an unpolarised target [13]. Here and in the following charge conjugate states and their decays are implicitly included. Special attention received the evaluation of the combinatorial background from other inelastic interactions of quasi-real photons. The possibility of tagging D^{*+} decays to suppress the combinatorial background was also investigated [14].

3.1.1 Open charm leptoproduction

Heavy quarks are produced in leading order via the photon-gluon fusion (PGF) process shown in Fig. 3.2. The cross section for muoproduction of open charm is given by

$$\frac{\mathrm{d}^2\sigma^{\mu\mathrm{N}\to\mathrm{c}\bar{\mathrm{c}}X}}{\mathrm{d}Q^2\mathrm{d}\nu} = \Gamma(E;Q^2,\nu)\,\sigma^{\gamma^{\star}N\to\mathrm{c}\bar{\mathrm{c}}X}(Q^2,\nu) \tag{3.1}$$

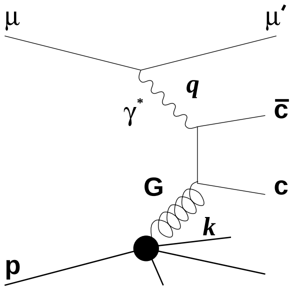

Figure 3.2: The photon-gluon fusion diagram.

ν GeV	$\sigma^{c\bar{c}}$ nb	Q^2_{min} GeV^2	Q^2_{max} GeV^2	$\Delta\nu \int_{Q_{\mathrm{min}}}^{Q_{\mathrm{max}}} \frac{\mathrm{d}\sigma^{c\bar{c}}}{\mathrm{d}Q^2\mathrm{d}\nu}\mathrm{d}Q^2$ nb	D	$\int \sigma_\gamma$ μb	$R = \frac{\int \sigma^{c\bar{c}}}{\int \sigma^{\gamma}}$
35–45	186	0.0029	15.0	0.543	0.470	0.184	$2.95 \cdot 10^{-3}$
45–55	234	0.0055	12.5	0.456	0.600	0.117	$3.90 \cdot 10^{-3}$
55–65	276	0.0089	10.0	0.375	0.724	0.077	$4.87 \cdot 10^{-3}$
65–75	309	0.0180	7.5	0.298	0.835	0.052	$5.73 \cdot 10^{-3}$
75–85	341	0.0353	5.0	0.229	0.923	0.033	$6.94 \cdot 10^{-3}$
35–85				1.9	$\overline{D}$=0.66	0.463	$\overline{R}=4.1 \cdot 10^{-3}$

Table 3.1: Cross sections for charm production as a function of the photon energy ν for a 100 GeV muon beam.

with the virtual photon flux

$$\Gamma(E;Q^2,\nu) = \frac{\alpha_e}{2\pi} \frac{2(1-y)+y^2+Q^2/2E^2}{Q^2(Q^2+\nu^2)^{1/2}}, \tag{3.2}$$

where E and ν are the muon and photon energies and $y = \nu/E$. The virtual photon cross section for charm production, $\sigma^{\gamma^\star N \to c\bar{c}X}(Q^2,\nu)$, is related to the photoproduction cross section, $\sigma^{\gamma\mathrm{N}\to c\bar{c}X}(\nu)$, by

$$\sigma^{\gamma^\star N\to c\bar{c}X}(Q^2,\nu) = \frac{\sigma^{\gamma\mathrm{N}\to c\bar{c}X}(\nu)}{(1+Q^2/M_0^2)^2}. \tag{3.3}$$

The mass parameter $M_0 = 3.9$ GeV is known from a fit to experimental data [13]. The photoproduction cross sections, $\sigma^{\gamma\mathrm{N}\to c\bar{c}X}(\nu)$, were measured in several experiments (cf. Ref. [15] and references therein) and the values used for the rate estimates are listed in Table 3.1 as $\sigma^{c\bar{c}}$ in column 2.

We propose to measure the spin dependent asymmetry, A^{exp}, for charm muoproduction, which is given by the number, $N_{c\bar{c}}$, of charm events for anti-parallel and parallel muon and target longitudinal spin orientations by

$$A^{\mathrm{exp}} = \frac{N^{\uparrow\downarrow}_{c\bar{c}} - N^{\uparrow\uparrow}_{c\bar{c}}}{N^{\uparrow\downarrow}_{c\bar{c}} + N^{\uparrow\uparrow}_{c\bar{c}}} = P_B \cdot P_T \cdot f \cdot A^{c\bar{c}}_{\mu\mathrm{N}}(y), \tag{3.4}$$

where P_B and P_T are the beam and target polarisations and f is the fraction of polarisable nucleons in the target material.

The asymmetry $A^{c\bar{c}}_{\mu\mathrm{N}}$ is related to the virtual photon asymmetry $A^{c\bar{c}}_{\gamma\mathrm{N}}$ by

$$A^{c\bar{c}}_{\mu\mathrm{N}} = D \cdot A^{c\bar{c}}_{\gamma\mathrm{N}}\ , \tag{3.5}$$

where the depolarisation D of the virtual photon with respect to the muon is given by $D(y) \approx \{1-(1-y)^2\}/\{1+(1-y)^2\}$. The asymmetry $A^{c\bar{c}}_{\gamma\mathrm{N}}$ is given by the ratio of the helicity dependent and helicity averaged cross sections for charm production, $\Delta\sigma^{\gamma\mathrm{N}\to c\bar{c}X}$ and $\sigma^{\gamma\mathrm{N}\to c\bar{c}X}$. They can be expressed as a convolution of the elementary photon-gluon cross sections [11], $\Delta\sigma(\hat{s})$ and $\sigma(\hat{s})$,

$$\Delta\sigma(\hat{s}) \quad = \quad \frac{4}{9}\frac{2\pi\alpha_e\alpha_s(\hat{s})}{\hat{s}}\left[3\beta - \ln\frac{1+\beta}{1-\beta}\right]$$

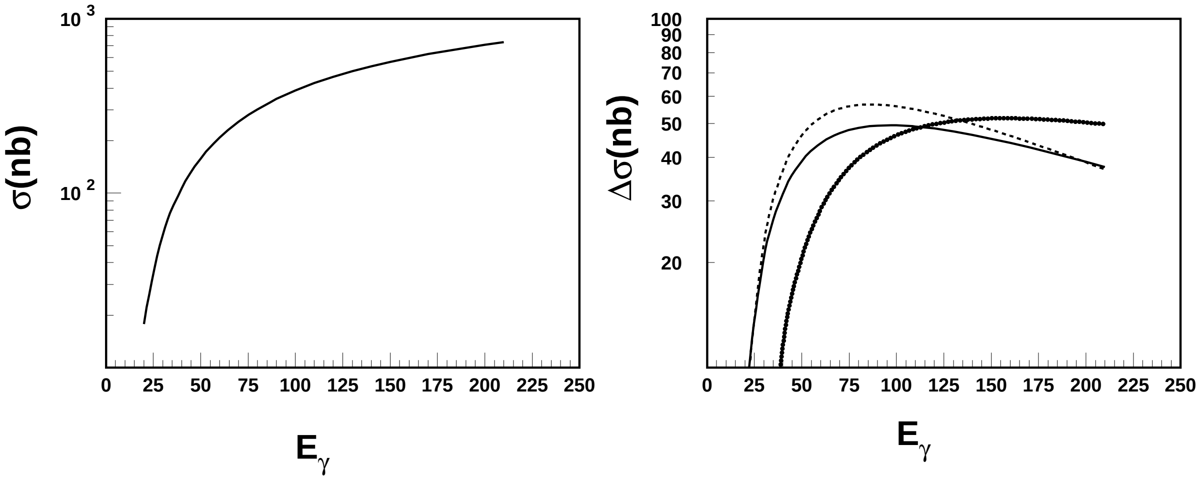

Figure 3.3: Charm photoproduction cross sections as a function of the photon energy E_γ. a) unpolarised cross section $\sigma^{\gamma \mathrm{N} \to \mathrm{c\bar{c}}X}$, b) polarised cross section $\Delta\sigma^{\gamma \mathrm{N} \to \mathrm{c\bar{c}}X}$. For the different lines see Fig. 3.1.

$$\sigma(\hat{s}) \;=\; \frac{4}{9}\frac{2\pi\alpha_e\alpha_s(\hat{s})}{\hat{s}}\left[-\beta(2-\beta^2)+\frac{1}{2}(3-\beta^4)\ln\frac{1+\beta}{1-\beta}\right], \tag{3.6}$$

with the gluon distributions, ΔG and G,

$$A_{\gamma\mathrm{N}}^{\mathrm{c\bar{c}}}(E,y)=\frac{\Delta\sigma^{\gamma\mathrm{N}\to\mathrm{c\bar{c}}X}}{\sigma^{\gamma\mathrm{N}\to\mathrm{c\bar{c}}X}}=\frac{\int_{4m_c^2}^{2M_NEy}\mathrm{d}\hat{s}\,\Delta\sigma(\hat{s})\,\Delta G(\eta,\hat{s})}{\int_{4m_c^2}^{2M_NEy}\mathrm{d}\hat{s}\,\sigma(\hat{s})\,G(\eta,\hat{s})}. \tag{3.7}$$

Where $\beta=\sqrt{1-4m_c^2/\hat{s}}$ is the c.m. velocity of the charm quark, $\hat{s}=(q+k)^2$ is the invariant mass of the photon-gluon system, q and k are the the photon and gluon 4-momenta, and $\eta=\hat{s}/2M_NEy$ is the gluon momentum fraction. The asymmetry for transverse virtual photons is assumed to be described also by Eq. (3.7) [8].

As discussed in Refs. [10, 12] the spin dependent cross section $\Delta\sigma^{\gamma\mathrm{N}\to\mathrm{c\bar{c}}X}$ in Eq. 3.7, depending on the model chosen, is maximal for photon energies around 80 GeV and decreases for higher energies whereas the spin averaged cross section $\sigma^{\gamma\mathrm{N}\to\mathrm{c\bar{c}}X}$ increases with energy.

According to the arguments given in [8] we assume that this asymmetry is independent of Q^2. The largest contribution to the PGF cross section comes from the very low Q^2 region (see column 3 of Table 3.1). We chose an incident muon energy of 100 GeV for which the depolarisation factor D is large in the relevant photon energy range $35 < \nu < 85$ GeV.

The fifth column of Table 3.1 shows the charm cross section (Eq. 3.1) integrated over the full Q^2 range in ν bins of 10 GeV. The lower integration limit is given by $Q^2_{\mathrm{min}}=m_\mu^2\frac{\nu^2}{E(E-\nu)}$ and the upper one by $Q^2_{\mathrm{max}}=E(E-\nu)\cdot\sin^2\frac{\theta_c}{2}$, where $\theta_c \le 50$ mrad is the scattered muon acceptance. The integrated cross section for charm leptoproduction in the range $35 < \nu < 85$ GeV is 1.9 nb and the average weighted depolarisation factor is $\overline{D}=0.66$.

The total quasi-real cross section $\sigma^{\gamma^*\mathrm{N}\to X}$ can be parametrised by the inelastic real photon cross section of 100 μb and a formfactor $(1+Q^2/M_0^2)^{-1}$ with $M_0^2=0.31$ GeV^2 [16]. With the virtual photon flux Γ given by Eq. 3.2 we calculate the muon cross sections shown in Table 3.1, column 7.

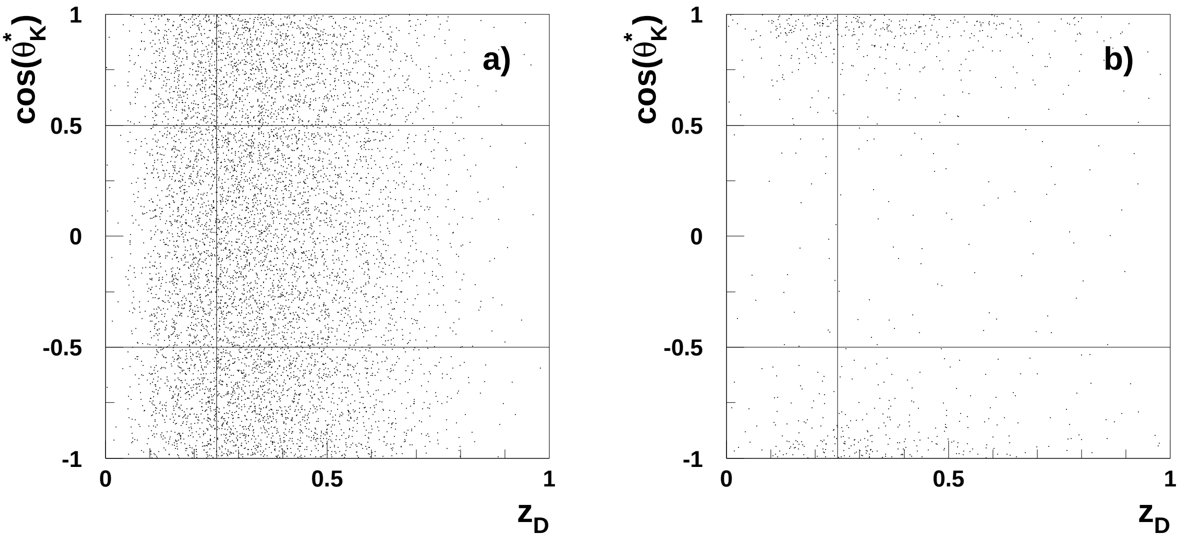

Figure 3.4: The distribution of events as a function of $\cos\theta^*_{\mathrm{K}}$ and z_{D} for (a) events from D° decays and (b) background events.

3.1.2 Monte Carlo studies

For the total cross section we rely on the experimental data as discussed in the previous sub-section, while for the shape of the differential distributions we use a Monte Carlo simulation, which was tuned to data where available. The exact spin-averaged leading-order matrix elements and the c.m. kinematics of the PGF process were calculated with Aroma [17] using massive quarks and the Q^2 dependence. This program was written for Desy to study PGF processes in the energy range of Hera. However, the evaluation of exact matrix elements makes it also valid at energies of fixed target experiments. In combination with Lepto [18], which simulates the underlying muon scattering event, and Jetset [19] for the simulation of the hadronisation process, it reproduces quite accurately the x_F (or z) and p_T differential distributions for D° photoproduction measured by E691, E687 and NA14/2 [15,20,21]. With the choice of $\mu_F = 2m_T$ and $\mu_R = m_T$ ($m_T^2 = m_c^2{+}p_T^{*2}$) for the factorisation and renormalisation scales, we find also a good agreement with the cross sections calculated from measured data (Table 3.1), since the NLO corrections for this process are expected to be moderate [22].

We implemented different polarised gluon distributions in our Monte Carlo program to get a realistic range of predictions for $A^{\mathrm{c\bar{c}}}_{\mu\mathrm{N}}$. We also used the polarised version of our event generator to study possible effects on the asymmetry introduced by the apparatus' acceptance and analysis cuts, since the PGF elementary asymmetry is a function of the c.m. energy, $\hat{s}$, and the scattering angle between the photon-gluon fusion axis and the outgoing $\mathrm{c\bar{c}}$ pair axis in the c.m. frame [23], which are correlated with the laboratory observables z and p_T of the produced D° meson. We found that these effects are negligible when considering the whole accessible range for these observables. Conversely, by selecting large z and small p_T ranges, which correspond to small c.m. scattering angles and lower values for $\hat{s}$, where the analysing power of the PGF process is larger, we observed that the sensitivity on the measurement of $\Delta G/G$ can be appreciably increased with a modest loss of events. For instance, for $p_T < 1.0$ GeV we found that the sensitivity on $\Delta G/G$ is

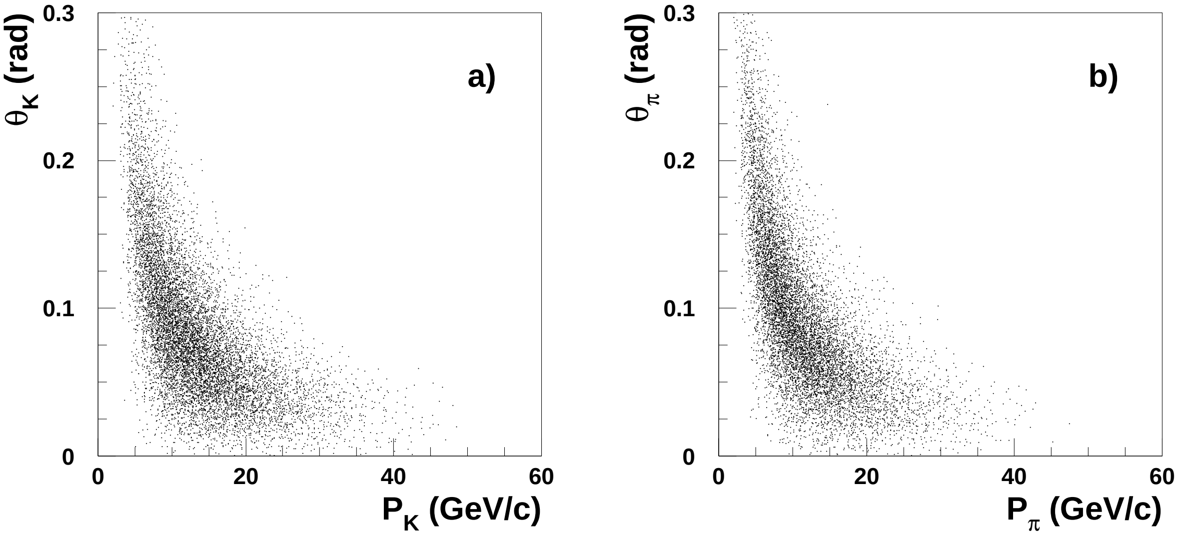

Figure 3.5: Angle vs. momentum in the laboratory frame for K's (a) and π's (b) from the decay $\mathsf{D}^\circ \rightarrow K^- + \pi^+$. The z and cosine cuts described in the text are applied.

increased by 20 to 30 %. This point will be elaborated later.

A serious problem for our measurement is posed by the combinatorial background from inelastic events not involving charm production. We studied these events in two different kinematic regions. At $Q^2 > 0.4$ GeV^2 we rely on the DIS event generator LEPTO using parton distribution functions appropriate for low Q^2, e.g. those from Ref. [24]. For real photons we studied the background with PYTHIA [19]. For the transition region of quasi-real photons $0 < Q^2 < 0.4$ GeV^2 we assumed that the event topologies and particle multiplicities are similar to those of real photons. For both kinematic regions we were able to reproduce reasonably well the existing data.

3.1.3 Reconstruction of open charm events

Typically about 60 % of charm quarks fragment into a D° and 20 % to a D^+ yielding in average to $N^{\mathsf{D}^\circ}/N^{c\bar{c}} = 1.23$ D° mesons per charm event. We therefore concentrate on the reconstruction of the D° meson. Our detection strategy is based on the combinatorial search for the hadronic decay products. A detection of the decay vertex, usually required to reduce the background, cannot be used in this experiment because of the multiple scattering in the thick target.

The simplest decay of the D° meson is the two-body decay $\mathsf{D}^\circ \rightarrow \mathsf{K}^- + \pi^+$ with a branching ratio of (4.01 ± 0.14) % [25]. The number of accidental combinations in this channel is lower than in three or four-body decays. An important property of this decay is the large momentum of the outgoing particles in the c.m. frame, $p^* = 861$ MeV$/c$. In the D° c.m. system the decay particles emitted at large angles, θ^*, with respect to the D° line of flight, have large transverse momenta with respect to the D° line of flight in the lab. frame (for instance, for $|\cos\theta^*| < 0.5$, $p_T > 750$ MeV). Conversely, ordinary fragmentation into K or π prefers low p_T, and most combinatorial background reproduces the kinematics of an almost collinear decay. Thus, by rejecting collinear decays we considerably reduce the number of accidental combinations. The distribution of charmed and background events in the variables $z_\mathrm{D} = E_\mathrm{D}/\nu$ and $|\cos\theta^*_\mathrm{K}|$ is shown in Fig. 3.4, where $z_D = E_\mathrm{D}/\nu$ is the fraction of the virtual photon energy, ν, carried by the D° meson. A mass window of $m_\mathrm{D} \pm 20$ MeV was assumed for this plot requiring a mass resolution of $\sigma_M = 10$ MeV. The concentration of the background events at large $|\cos\theta^*_\mathrm{K}|$ is clearly visible whereas the distribution for real D° decays is independent of the decay angle. An optimum background rejection with an acceptable loss of good events was found for $z_\mathrm{D} > 0.25 \pm 0.05$ and $|\cos\,\theta^*_\mathrm{K}| < 0.50 \pm 0.1$. The lines in the Fig. 3.4 indicate the applied cuts. The cut on z_D reduces the D° meson sample by a factor 0.71 and the cut of $|\cos\,\theta^*_\mathrm{K}|$ reduces it by another factor of two.

Figure 3.5 shows the laboratory angle vs. momentum distribution of the K and the π mesons for the accepted D° decays. It can be seen that particle momenta are larger than 3 GeV and that an acceptance of $\theta_{\mathrm{K},\pi} \leq 200$ mrad is needed. Table 3.2 shows the geometrical acceptances for these decays. It is required that both particles pass through the first large acceptance magnet and that the K's decay downstream of the RICH1. These acceptances for $z_\mathrm{D} > 0.25$ are better than 90 % except for the two lowest momentum bins, where the geometrical acceptance is reduced most by the polarised target solenoid. The geometrical acceptance of the apparatus is larger than 84 % for $z_\mathrm{D} > 0.25$. From the two standard deviation mass window we get another acceptance factor of 0.95. Combining these acceptance factors we get an overall acceptance of $a_\mathrm{D} = 0.29$ and find for the detection probability of a charmed event via the reconstruction of a D° meson

$$\varepsilon^{c\bar{c}} = \frac{N^\mathrm{D}}{N^{c\bar{c}}} \cdot BR \cdot a_\mathrm{D} = 0.014\,. \tag{3.8}$$

For the probability to accidentally find a Kπ pair in the mass window after applying the cuts discussed above we find

$$\varepsilon^\mathrm{BG} = (2.27 \pm 0.16) \times 10^{-4} \tag{3.9}$$

normalised to the total number of inelastic muon scattering events with $0.4\ \mathrm{GeV}^2 < Q^2$ and $35 < \nu < 85$ GeV using the LEPTO event generator. A similar value was found with PYTHIA for real photoproduction events with a photon beam energy of 60 GeV for the point-like and resolved photon components separately. We did not observe any appreciable variation of ε^BG when varying the energy of the real photon. Therefore, for the intermediate region $0 < Q^2 < 0.4\ \mathrm{GeV}^2$, we assume the same value for ε^BG.

3.1.4 The measurement of the asymmetry $A^{c\bar{c}}_{\gamma\mathrm{N}}$

With the luminosity of $4.3 \times 10^{37}\ \mathrm{cm}^{-2}\mathrm{day}^{-1}$ and the cross sections given in Table 3.1 we calculate the number of open charm events in the range $35 < \nu < 85$ GeV to $N^{c\bar{c}} \approx 82 \cdot 10^3$ per day. The total number of inelastic events $N^\mu \approx 20 \cdot 10^6$ per day. The statistical accuracy of the measurement of $A^{c\bar{c}}_{\gamma\mathrm{N}}$ (Eq. 3.4) is given by

$$\delta A^{c\bar{c}}_{\gamma\mathrm{N}} = \frac{1}{P_T P_B f \overline{D}} \frac{1}{\sqrt{N^\mathrm{S}}} \sqrt{1 + \frac{N^\mathrm{B}}{N^\mathrm{S}}}, \tag{3.10}$$

where N^S is the number of events in the signal and $N^\mathrm{B}/N^\mathrm{S}$ is the background-to-signal ratio.

Before we can calculate the rates we have to consider re-interactions in the target. If the K or π meson from a D° decay re-interacts the event is lost. The length of target

$z_{\mathrm{D^\circ}}/P_{\mathrm{D^\circ}}$(GeV)	10–15	15–20	20–25	25–30	30–35	35–40	40–45	45–50	50–55
0.7–0.8			91	91	92	93	94	94	95
0.6–0.7			88	91	92	93	94	94	95
0.5–0.6		83	88	91	92	93	94	94	95
0.4–0.5	65	80	87	91	92	93	93		
0.3–0.4	58	79	87	90	92				
0.2–0.3	51	78	87	90					

Table 3.2: $\mathrm{D^\circ} \to \mathrm{K^-} + \pi^+$ geometrical acceptance as a function of the $\mathrm{D^\circ}$ energy fraction z vs. its momentum in per cent taking into account the K decay probability and the cosine cut as discussed in the text.

material traversed by each of the two decay particles is on average about 20 cm. With the target parameters given in Table 5.10 we obtain an acceptance reduction of $\varepsilon^{\mathrm{S}}_{\mathrm{target}} = 0.76$. Also the background can be reduced if secondary interactions can be detected. We find a reduction for the background of $\varepsilon^{\mathrm{BG}}_{\mathrm{target}} = 0.80$. The shadowing in the photoproduction cross section of $\mathrm{NH_3}$ and ^{6}LiD also reduces the background. We assumed a reduction of $r_s^{\mathrm{NH_3}} = 0.9$ for the $\mathrm{NH_3}$ target and of of $r_s^{\mathrm{LiD}} = 0.95$ for the ^{6} LiD target.

Summarising the above discussion we obtain

$$N^{\mathrm{S}} = N^{\mathrm{c\bar{c}}} \cdot \varepsilon^{\mathrm{c\bar{c}}} \cdot \varepsilon^{\mathrm{S}}_{\mathrm{target}} = 877 \ \mathrm{day}^{-1} \tag{3.11}$$

and for the background rates

$$\begin{aligned} N^{\mathrm{BG}} &= N^{\mu} \cdot \varepsilon^{\mathrm{BG}} \cdot \varepsilon^{\mathrm{BG}}_{\mathrm{target}} \cdot r_s &= 3269 \ \mathrm{day}^{-1} \qquad & (\mathrm{NH_3}) \\ N^{\mathrm{BG}} & &= 3450 \ \mathrm{day}^{-1} \qquad & (^6\mathrm{LiD}). \end{aligned} \tag{3.12}$$

The projected number of events for the running time as planned in section 3, is $N^{\mathrm{S}} \approx 66$k and $N^{\mathrm{BG}} \approx 250$k with $\frac{N^B}{N^S} \approx 3.7$ for the $\mathrm{NH_3}$ target and ≈ 3.9 for the ^{6}LiD target. With a carefully designed and operated apparatus as well as offline analysis programs we expect a reconstruction efficiency per single charged track in excess of 90%, yielding to a reconstruction efficiency higher than 80% for a $\mathrm{D^\circ}$. This factor was taken into account in estimating the overall spectrometer efficiency. This leads to a statistical error on the asymmetry of

$$\delta A^{\mathrm{c\bar{c}}}_{\gamma \mathrm{N}} = 0.076\,. \tag{3.13}$$

3.1.5 $\mathrm{D^{*+}}$ tagging

The background in the above analysis can be significantly reduced by tagging the $\mathrm{D^{*+}}$ decay into a $\mathrm{D^\circ} + \pi^+$, by requiring an additional soft pion, π_S^+, in the event. The method relies on the tight kinematic constraints of the decay chain

$$\mathrm{D^{*+}} \to \mathrm{D^\circ}\pi_S^+ \to (\mathrm{K^-}\pi^+)\,\pi_S^+ \tag{3.14}$$

The mass difference $\Delta M = m(\mathrm{K^-}\pi^+\pi_S^+) - m(\mathrm{K^-}\pi^+) = 145$ MeV can be measured much more accurately than the $\mathrm{D^{*+}}$ mass itself. A large contribution to ΔM comes from the π^+ mass itself ($M_{\pi^+} \approx 140$ MeV), and hence even a modest resolution of the π_S^+ momentum vector will allow a measurement of ΔM within a few MeV. This decay yields a prominent

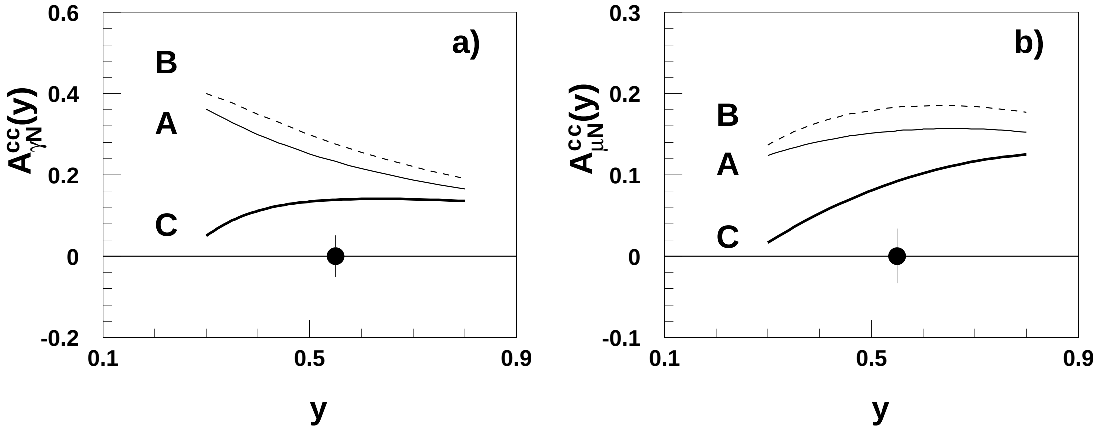

Figure 3.6: a) Asymmetry $A^{c\bar{c}}_{\gamma\mathrm{N}}$ and b) asymmetry $A^{c\bar{c}}_{\mu N}$ for open charm as a function of y. The curves refer like in Fig. 3.1 to the three sets of ΔG from Ref. [4]. The projected precision of the measurement in the range $0.35 < y < 0.85$ is indicated by the error bars of the data points shown at $A = 0$.

signal at the threshold of the ΔM distribution, which is otherwise a suppressed phase space kinematic region (see for instance Ref. [14]).

For the study of this decay channel we released some of the cuts imposed above in the analysis of the $\mathrm{D}^\circ \to \mathrm{K}^- + \pi^+$ decay, namely we require $z_\mathrm{D} > 0.20$ and $|\cos\theta^*_\mathrm{K}| < 0.85$. These cuts reduce the D° sample by a factor 0.70.

Our Monte Carlo studies showed that the background in this sample is less than 10 % in a mass interval $\Delta M \pm 5$ MeV, where we have used a mass resolution of 2.5 MeV for ΔM, which is well within the reach of our apparatus. The only serious problem for the efficient detection of this decay mode is posed by the detectability of the soft pion from the D^{*+} decay which traverses a considerable length of the target material. We find that 89 % of the soft pions have momenta larger than 1 GeV/c of which 73 % do not re-interact in the target. On the other hand we do not find any losses of π^+_S in the apparatus geometrical acceptance.

Combining these numbers we find an acceptance of 0.22 for the decay chain of Eq. 3.14, where we have already included the apparatus acceptance, the losses of events from the interactions of the decay products with the target material and required in addition that the momentum of the π^+_S is larger than 1 GeV. The branching ratio for this decay chain is 2.73 ± 0.11 % [25], while the number of D^{*+} mesons per charm event is 0.60. We expect then a reconstruction rate of

$$N^\mathrm{S}_{\mathrm{D}^{*+}} = 295\,\mathrm{day}^{-1} \tag{3.15}$$

for a total of $N^\mathrm{S}_{\mathrm{D}^{*+}} \approx 22\mathrm{k}$ reconstructed D^{*+} with almost no background ($N^\mathrm{BG} < 2.5\mathrm{k}$). This leads to a statistical error on the asymmetry, assuming a 15% background of

$$\delta A^{c\bar{c}}_{\gamma\mathrm{N}} = 0.064\,, \tag{3.16}$$

which is slightly better than the statistical accuracy that we found for the $\mathrm{D}^\circ \to \mathrm{K}^- + \pi^+$ decay channel.

Now we divide the D°'s sample analysed in the previous section in two categories, one containing D°'s that were not attached to a D^{*+} reconstructed decay, the second containing D°'s that gave a D^{*+}, and perform the analysis described in the previous section only on the events in the first category. About 33 % of all D°'s come from the decay of a D^{*+} resonance. The additional cuts applied to the D^{*+} sample were $p_{\pi_S^+} > 1$ GeV, mass cut on ΔM, interaction probability in target. This leads to a smaller fraction of D°'s in this sub-sample, which represents only 20 % of the total D° sample. The untagged sub-sample leads to an accuracy on the asymmetry measurement of $\delta A^{c\bar{c}}_{\gamma N} = 0.085$. Adding this sample with the D^{*+}'s studied in this section we find

$$\delta A^{c\bar{c}}_{\gamma N} = 0.051\,. \tag{3.17}$$

In Fig. 3.6 this error is shown together with the the expected asymmetries $A^{c\bar{c}}_{\gamma N}$ and $A^{c\bar{c}}_{\mu N}$. The sensitivity to the polarised gluon distribution in the accessible η range is then

$$\delta\left(\frac{\Delta G}{G}\right) \approx 0.14\,. \tag{3.18}$$

As discussed in section 3.1.2 the sensitivity on the measurement of $\Delta G/G$ can be increased by selecting D° mesons produced at low p_T. For $p_T \leq 1.0$ GeV we have a loss of events of about 30 %, while the analysing power of the PGF process increases by about 50 %. This increases the sensitivity and yields to

$$\delta\left(\frac{\Delta G}{G}\right) \approx 0.11\,. \tag{3.19}$$

3.1.6 Reconstruction of the D meson from other decay channels

For the more complex three and four-body decays,

$$\begin{array}{lcll} D^\circ & \rightarrow & K^-\pi^+\pi^\circ & (13.8\pm1\ \ )\ \% \\ D^\circ & \rightarrow & K^-\pi^+\pi^+\pi^- & (\ 8.1\pm0.5)\ \% \\ D^+ & \rightarrow & K^-\pi^+\pi^+ & (\ 9.1\pm0.6)\ \% \end{array}$$

the kinematical constraints on the outgoing particles are not so tight, and the kinematical cuts used above are not so effective in rejecting the background. Most hadrons, however, decay through an intermediate resonance, like a ρ or a K^*, thus partially simulating the two body decay kinematics, and the above discussed method can be applied also to these decays. The decay multiplicity, however, is higher and some particles may have very low momenta.

We studied these decays in some details. With cuts on z_D and cos θ^*_K we already get a substantial background reduction. Additional cuts were applied on the invariant masses of the $K^-\pi^+$ and $\pi^+\pi^\circ$ sub-systems. With these cuts these channels lead to an error $\delta A^{c\bar{c}}_{\gamma N} \approx 0.15$. The D^{*+} tagging method discussed in the previous section is under study also for these channels.

3.1.7 Measurement of g_1 and estimate of $\Delta G/G$ from its Q^2 evolution

In parallel with the measurements of $A^{c\bar{c}}_{\mu N}$, data for the inclusive spin dependent structure function g_1 of the proton and the deuteron will be collected. Assuming one year running with each target and taking into account the different target materials (NH_3, ^6LiD) compared to the SMC experiments (butanol), we will obtain three times smaller

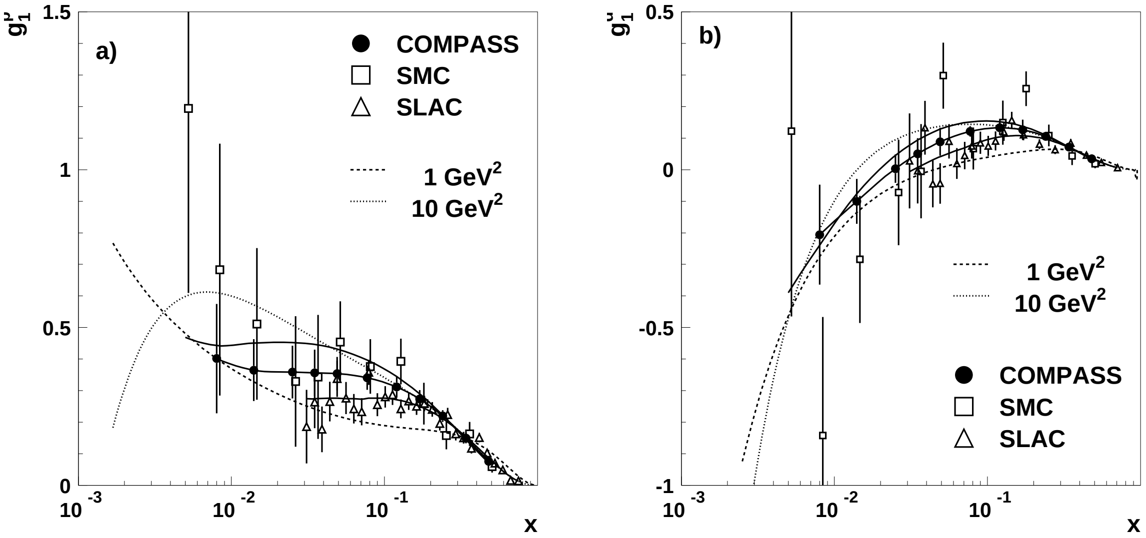

Figure 3.7: Projected accuracy of $g_1(x)$ data for the proton (a) and the deuteron (b) compared to the results from the SMC and E–143. The lines show the NLO fits for $Q^2 = 1$ GeV^2 and 10 GeV^2, as well as for the Q^2 of each experiment.

statistical errors for the proton and five times smaller statistical errors for the deuteron g_1 compared with the SMC data taken 1992–1994 [26,27]. Fig. 3.7 shows the accuracy expected for the data measured by our future experiment; also shown are the existing SMC and SLAC [28,29] data. The data taken 1995 and those expected for 1996 may double the SMC statistics but were not taken into account for this comparison. In addition the acceptance will improve for large x due to an increase of the angular acceptance by the new first muon wall. On a point-by-point basis the systematic and statistical errors of $g_1(x)$ will be of about equal size while for the first moments $\int g_1(x)\,\mathrm{d}x$ the systematic error will dominate. In the Bjorken sum rule part of the systematic error cancels and the error will improve from 0.036 (SMC) to 0.026.

These high precision data will be most important for studies of the much debated small-x behaviour of g_1 and its Q^2 evolution, which is linked to the gluon helicity distribution ΔG via the GLAP equations. We performed two next-to-leading order QCD fits using the code and the parametrisations for the parton distribution functions of Ref. [6]. One fit uses the presently available proton and deuteron data from the SMC [26,27] and the SLAC experiment E-143 [28,29] and the second fit includes also the projected data from the proposed experiment. The fit results are also shown in Fig. 3.7. The error of the first moment $\int \Delta G(\eta)\,\mathrm{d}\eta$ is reduced by the COMPASS data from 0.61 to 0.35. Although the method might to some extent depend on the parametrisations chosen for the parton distributions, this clearly shows the strong impact of more precise data at large Q^2.

3.1.8 Comparison with other experiments on ΔG

Recent results of the fixed target experiment E704 at Fermilab on polarised pp scattering [30] put restrictions on the size of the gluon polarisation, $\Delta G/G$, in the region $0.1 < \eta < 0.3$. It appears that large values of $\Delta G/G \approx 1$ at $\eta \approx 0.15$ can be ruled out. However, smaller values like the ones proposed more recently [4] cannot be excluded due to the quadratic dependence of the asymmetry on $\Delta G/G$. Furthermore, it appears that there are additional assumptions, like the relative contribution of various sub-processes and the neglect of NLO corrections which make the restriction on the size of $\Delta G/G$ less stringent.

The future polarised hadron experiments at RHIC consider direct photon production, $\mathsf{pp} \to \gamma X$, as a suitable process for measuring the gluon polarisation [31]. Data can be taken at high p_T ($P_T \simeq 30$ GeV) and therefore no ambiguity in the interpretation connected with the effects of intrinsic k_T will exist. However, the role of the NLO contributions and how they might affect the asymmetry is not yet clear. The sub-process $qg \to q\gamma$ leads to a positive contribution to A_{LL} which, in first approximation, is proportional to the product $\Delta G/G$ and $\Delta u/u$. In polarised pp collisions there are contributions to A_{LL} from different sub-processes and different Δq's which have to be known from other experiments. Background contributions from real photons, from π° decay for instance, will decrease the sensitivity. With high luminosity and high polarisations in the two beams the RHIC spin experiment expects a statistical errors in A_{LL} of 0.015 corresponding to a sensitivity $\delta\frac{\Delta G}{G} = 0.075$.

Other polarised deep inelastic lepton scattering experiments which could be considered as candidates for a measurement of the gluon polarisation are at HERA and SLAC. The energy of the HERMES experiment ($E < 30$ GeV) is probably to low [32] to investigate ΔG via the photon-gluon fusion process. There have been discussions to probe $\Delta G/G$ in J/ψ production by 50 GeV real photons at SLAC, but the short duty cycle of 10^{-5} will present a formidable problem with regard to combinatorial background in the reconstruction. Both experiments however will probe the gluon only in the region $\eta > 0.2$.

At HERA polarisations of the electron beam of 0.70 have been achieved. Presently the feasibility to polarise also the proton beam is under investigation by a study group within the Future Physics at HERA workshop. In particular a measurement of $g_1(x)$ in the region $x \simeq 10^{-4}$–10^{-3} would be of interest. Such a measurement was studied by the polarisation sub-group of the workshop and earlier at a workshop in Zeuthen. It appears to be interesting only with luminosities in excess of 200 pb^{-1} [33, 34]. Even then the determination of the Q^2 evolution of g_1, from which in principle $\Delta G(\eta)$ can be determined in a QCD analysis, is marginal. Presently the unpolarised integrated luminosity is about 10 pb^{-1} per year and with machine upgrades one hopes to finally reach 170 pb^{-1}/year. The time scale for a polarised proton beam at HERA, if feasible at all, could be: 1996 theoretical studies, 1998 conceptional design, 2004 polarised protons in HERA [35]. Polarised deuteron beams are presently considered to be infeasible. Due to the small magnetic moment of the deuteron Siberian snakes will work only for deuteron energies larger than 200 GeV and spin rotators are much more difficult than for the proton case.

3.2 LONGITUDINAL SPIN DISTRIBUTION FUNCTIONS

In view of the different explanations for the violation of the Ellis–Jaffe sum rule and the existence of various models for the spin structure of the nucleon it appears logical and tempting to decompose the nucleon spin into the valence and the sea components and to determine the spin distribution functions of the different flavours for the valence and

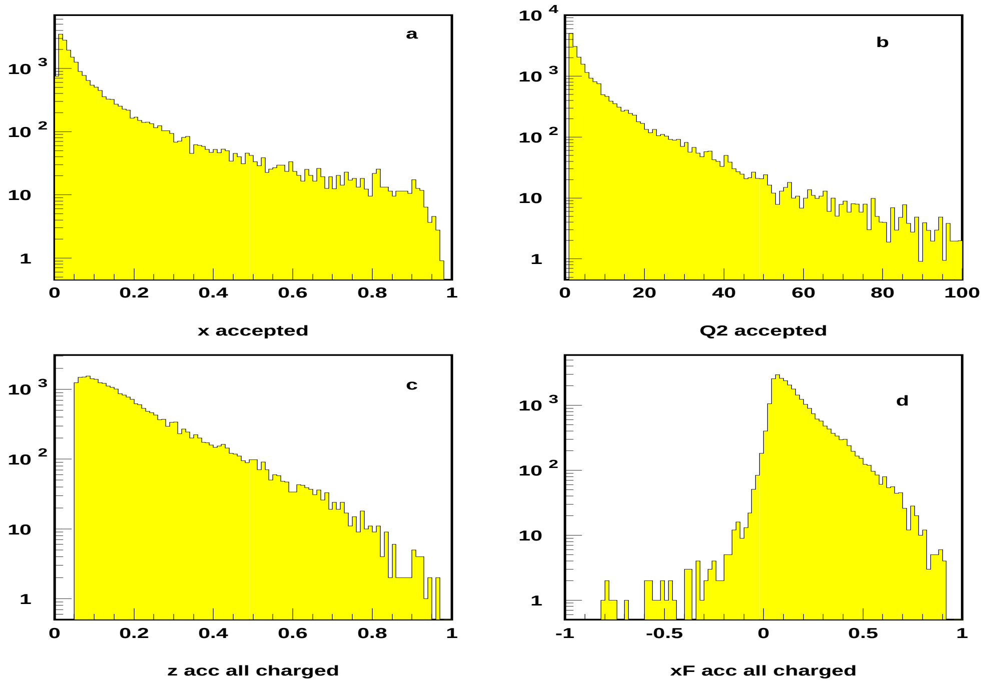

Figure 3.8: Distributions of (a) x, (b) Q^2, (c) z, and (d) x_F. The variables z and x_F refer to charged hadrons.

the sea quarks. This can be achieved by semi-inclusive measurements of deep inelastic scattering of polarised leptons on polarised proton and deuteron targets.

The first measurements of the semi-inclusive hadron asymmetries were performed by the EMC [36,37], and the SMC recently presented the first determination of spin distribution functions of the valence, Δu_v, Δd_v, and of the non-strange sea quarks, $\Delta\overline{q}$ [38]. These measurements were limited by statistics as well as by the angular acceptance of the EMC/SMC spectrometer for hadrons and the lack of particle identification. We propose here to take in parallel with the measurement of ΔG, a large sample of deep inelastic events with identified hadrons.

Estimates for the impact of such data on our knowledge of Δq_v and $\Delta\overline{q}$ are given mostly on the basis of the acceptance of the current SMC experiment scaled to the projected acceptance and luminosity of the proposed experiment. The simulation focused on π^+, π^-, K^+ and K^-.

In addition to the combination of asymmetries for the different hadrons and different targets, which is the basis for projecting out a given distribution function, we can analyse the azimuthal effects in asymmetries, the topology of the hadron jets at high $p_\perp$ and particle correlations.

For these measurements the muon energy of 100–200 GeV is important in order to cleanly separate the current and the target fragmentation. In addition, the particle identification, necessary for the flavour and the valence and sea separation, is easier if particles have momenta higher than 5 GeV.

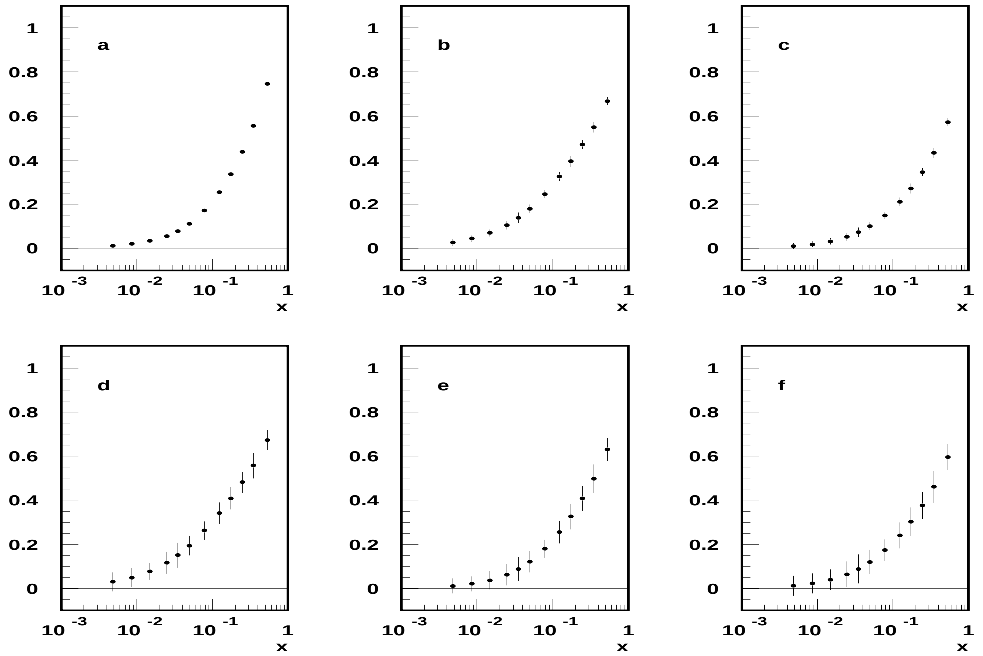

Figure 3.9: Inclusive asymmetry (a) and semi-inclusive asymmetries for muoproduction of (b) π^+, (c) π^-, (d) K^+, (e) K^- and (f) K° for longitudinally polarised proton target.

3.2.1 Rate estimates

We assume that the event rate in the future experiment amounts to 5 times that of the SMC experiment. For a two year running with polarised targets 60 million events after analysis cuts are expected from the experience of the NA47 experiment. We further assume that the statistics is divided in 30 million events for the proton and the same for the deuteron target. The total number of accepted charged hadrons from the proton target is 52.7 M, where the shares of the different species of hadrons are 23.0 M, 20.7 M, 2.9 M, and 2.9 M for π^+, π^-, K^+, and K^-, respectively. For the deuteron target these numbers are roughly the same. The distributions of the kinematic variables x, Q^2, z, and the Feynman variable, x_F, of the events with detected hadrons are shown in Fig. 3.8.

The present estimate was made for muons staying in the acceptance of the SM2 magnet and causing a physics trigger. Muons too close to the beam were thus excluded from the SMC analysis. These requirements, however, are being re-discussed for this experiment. Recently, it was shown [39] that using a trigger based on a the hadron calorimeter the x region can be extended down to $x = 10^{-4}$.

The hadron asymmetries are given by

$$A^h = \frac{1}{P_B P_T f D} \frac{N_h^{\uparrow\downarrow} - N_h^{\uparrow\uparrow}}{N_h^{\uparrow\downarrow} + N_h^{\uparrow\uparrow}}, \tag{3.20}$$

where P_B, P_T, f, and D are defined in Sect. 3.1, and N_h are the numbers of events for (anti)parallel orientation of muon and target spin for hadrons of type h.

The accuracy expected for the asymmetries A^{π^+}, A^{π^-}, A^{K^+}, A^{K^+}, and A^{K° for two years of running at 100 GeV are shown in Fig. 3.9 for the proton target and $z > 0.2$. All points are shown on curves calculated using the Durham parametrisation of the polarised quark distribution functions [4]. Also shown are the inclusive asymmetries measured in parallel leading to errors of 0.004 for the proton and 0.007 for the deuteron first moments of g_1, respectively.

3.2.2 Flavour decomposition of the distribution functions

The measurement and the identification of the final state hadrons in the full range of momentum allows a detailed study of the fraction of the nucleon spin carried by the valence and sea quarks, respectively. In the current fragmentation region semi-inclusive cross sections factorise into the z independent quark spin distribution functions and the x independent quark fragmentation functions. The asymmetries of the spin dependent virtual photon cross sections for muoproduction of π^+, π^-, K^+, K^-, and K° are given by the ratios of different linear combinations of quark distribution functions from which then flavour separated distribution functions can be derived as a function of x, see App. A.

The quark spin distributions determined from the asymmetries in Fig. 3.9 are shown in Fig. 3.10. The errors of the integrals over x of the quark polarisations are

$$\begin{array}{lcl} \delta\int\Delta u_v\,\mathrm{d}x & = & 0.05, \\ \delta\int\Delta d_v\,\mathrm{d}x & = & 0.07, \\ \delta\int\Delta\overline{q}\,\mathrm{d}x & = & 0.02, \\ \delta\int\Delta\overline{s}\,\mathrm{d}x & = & 0.11. \end{array} \tag{3.21}$$

Compared to the recent SMC results [38] the statistical errors are by a factor of three to four smaller for the valence quarks and by a factor of three smaller for the non-strange sea quarks, $\Delta\overline{q} = \Delta\overline{u} = \Delta\overline{d}$.

A selection of events with a leading ($z > 0.4$) K^{*0} or $\overline{\mathsf{K}^{*0}}$ enhances the relative amount of interactions on $\overline{\mathsf{s}}$ or s quarks by a factor of about 8. These events appear in the $\mathsf{K}^+\pi^-$ ($\mathsf{K}^-\pi^+$) decay mode with a signal to background ratio of about one to one and can thus be efficiently selected by effective mass cuts. Asymmetries in these samples enriched in interactions on $\overline{\mathsf{s}}$, s quarks are expected to provide an improved determination of $\int\Delta s(x)\,\mathrm{d}x$.

The expected statistical accuracy for the valence quark polarisation is competitive to that planed by the HERMES Collaboration [40]. The accessible x range is one order of magnitude wider and can be pushed down by almost a factor of 10 using the hadron trigger. This eliminates the source of systematic error for the integral coming from the small x extrapolation. With high statistics in the small x region a test of the the spin-isospin symmetry of the sea by separate determination of spin distributions of $\overline{\mathsf{u}}$ and $\overline{\mathsf{d}}$ quarks becomes feasible.

The proposed apparatus, which foresees a wide angular acceptance spectrometer close to the target gives a unique opportunity for exploratory study of semi-inclusive cross sections in the target fragmentation region. As seen in Fig. 3.8d a substantial fraction of hadrons with low z comes from the target fragmentation region ($x_F < 0$). In this kinematic range the semi-inclusive cross sections do not factorise and one has to determine differential cross sections as functions of x and z simultaneously. These quantities, recently dubbed *fracture functions* [41], were proposed to be used for a study of the target (in)dependence of quark spin suppression. It is conjectured that quark polarisation

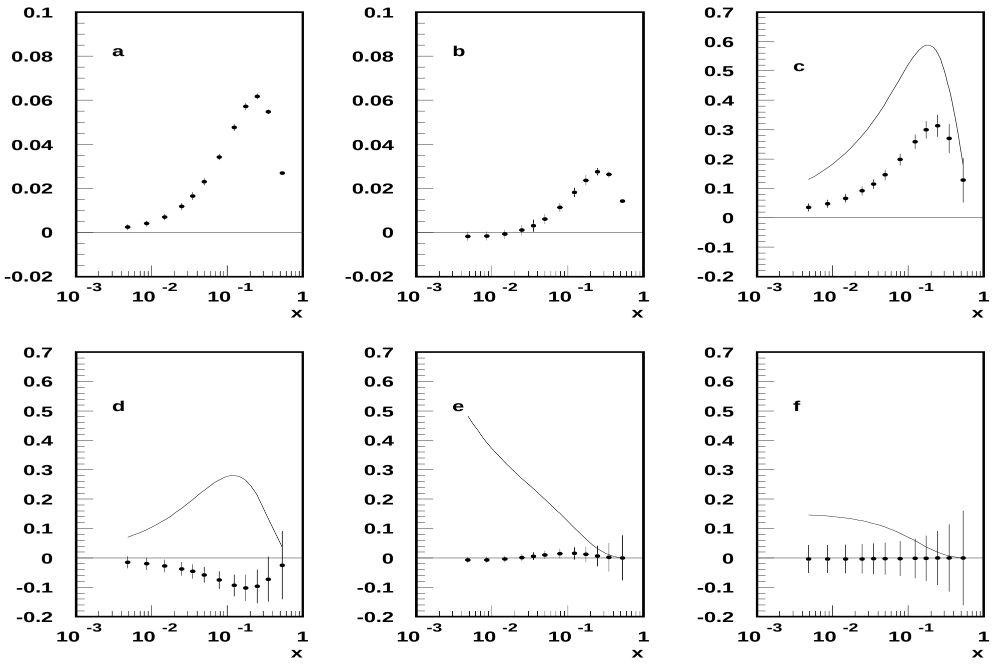

Figure 3.10: Spin dependent structure functions (a) xg_1^{p} and (b) xg_1^{d} and quark spin distributions (c) $x\Delta u_v$, (d) $x\Delta d_v$, (e) $x\Delta\overline{q}$ and (f) $x\Delta\overline{s}$. The solid curves represent unpolarised quark distributions.

is a universal feature of the axial current and does not depend on the target structure. To examine this idea one has to measure semi-inclusive asymmetries for different final state hadrons and thus control the "target" quark contents. In particular, by selecting a final proton one probes the spin structure of the gluon-rich object with vacuum quantum numbers. The experiment is well suited for such a study because of high statistics of low z particles in the sea region of low x.

Wide angular acceptance for hadrons enables a study of a dependence of the longitudinal inclusive asymmetry on the transverse momentum of a hadron. As suggested in Refs. [3, 9] the photon-gluon fusion becomes dominant in events with high p_T and a sizeable gluon polarisation could give an observable $\Gamma_1^{\mathrm{p,d}}(p_T)$ dependence.

3.3 MEASUREMENT OF Λ AND $\overline{\Lambda}$ POLARISATION

In Sect. 3.1 we propose to measure the asymmetry in the production of open charm by photon-gluon fusion as a clear method to distinguish between the polarised strange quark [42] and gluon interpretation of the EMC spin effect. We will obtain complementary information on the polarisation of strange quarks and/or antiquarks also by measuring the longitudinal polarisation of Λ and $\overline{\Lambda}$ baryons.

In this experiment we will access Λ's and $\overline{\Lambda}$'s produced in both target and current fragmentation regions. The measurement of the Λ longitudinal polarisation in the current fragmentation region is a way to determine the spin transfer function from the struck quark to the Λ hyperon. Recently it was pointed out [43] that the measurement of the Λ polarisation and of the Λ–$\overline{\Lambda}$ spin correlations in the target fragmentation region can help to discriminate between models with polarised strange quarks and gluons.

3.3.1 The target fragmentation region

The basic idea of the longitudinal polarisation transfer from the polarised lepton to the unpolarised target fragments is that the polarised virtual boson will strike preferentially one quark polarisation state inside the target nucleon, and that the fragment left behind will contain some memory of the angular momentum removed. This may be transfered to the final state in the target fragmentation region, specifically in non-trivial longitudinal polarisation for Λ hyperons with $x_F < 0$.

Measurements of Λ polarisation in the target fragmentation region were in fact made previously in neutrino experiments on unpolarised target [44–47]. Large negative[1] longitudinal polarisations of the order of 0.7 were measured by the WA59 collaboration [44]. The sign, the order of magnitude, and the x dependence of these data are well reproduced

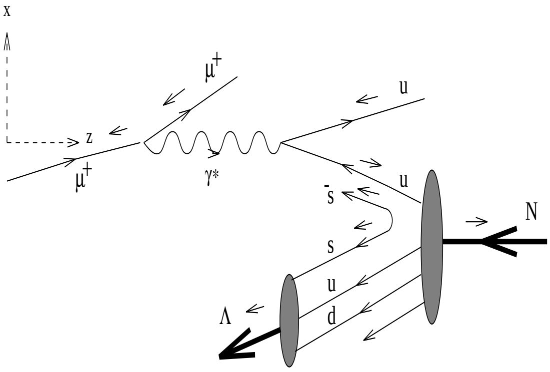

Figure 3.11: Λ polarisation according to the polarised $s\bar{s}$ sea model.

by the polarised $s\bar{s}$ model [43], which also was used successfully [48] to interpret data on ϕ and Λ-$\overline{\Lambda}$ production in proton-antiproton annihilation at LEAR.

When applied to target fragmentation in deep inelastic scattering of a negatively polarised muon from an unpolarised or polarised proton this model predicts large negative longitudinal polarisations of the produced Λ's and $\overline{\Lambda}$'s. More specifically the mean polarisation of a remnant s or $\bar{s}$, and hence the Λ or $\overline{\Lambda}$, produced in the target fragmentation region, should be net *negative*, as diagrammatically shown in Fig. 3.11. This is due to the preference of the negatively polarised virtual photon to interact with a u quark with positive helicity, which in average is aligned with the proton. Using this model the negative Λ polarisations of the order of -0.4 to -0.6 were predicted [48] in the accessible range of the target fragmentation region, $-0.3 < x_F < 0$. The effect is large and can be detected in this experiment. The calculation was performed for NH_3 target and kinematical cuts

---

[1] Here and in the following the sign of polarisation is given with respect to the direction of the momentum transfer, i.e. the z direction in Fig. 3.11.

Λ's parent	$P_{\mathrm{d}} \to P_{\lambda}$	$P_{\mathrm{u}} \to P_{\lambda}$	$P_{\mathrm{s}} \to P_{\lambda}$
Quark	0	0	+1
Σ^0	−2/9	−2/9	+1/9
$\Sigma(1385)$	+5/9	+5/9	+5/9
Ξ	−0.3	−0.3	+0.6

Table 3.3: Spin transfer coefficients according to BGH.

$x > 0.15$ and $0.5 < y < 0.9$ were applied. Note that the expected dependence of the Λ polarisation on the target polarisation is negligible for ammonia target.

It is interesting to contrast the above predictions of the polarised $\mathrm{s\bar{s}}$ sea model with the expectation for the meson cloud model of DIS [49]. In such a model the Λ polarisation in the target fragmentation region is expected to be zero for unpolarised target (in contradiction to the WA59 data) and very strongly anti-correlated with the target polarisation.

3.3.2 The current fragmentation region

Recently, an experimental programme to measure the polarised fragmentation function ΔD_q^{Λ} in $\mathrm{e^+e^-}$ was proposed by Burkardt and Jaffe [50] (see also [51, 52] and [53]). The Λ polarisation in Z decays was recently measured by the ALEPH collaboration [54]. The measured longitudinal polarisation (-0.39 ± 0.07) is well described by constituent quark model predictions implemented in JETSET [53]. We propose to investigate the same quantity in semi-inclusive deep inelastic scattering of longitudinally polarised muons on unpolarised and longitudinally polarised nucleons.

In the current fragmentation region, $\Lambda/\overline{\Lambda}$'s acquire their longitudinal polarisation during polarised quark fragmentation. The complete twist-three level description of this process is presented in [55].

At leading twist the magnitude of longitudinal Λ polarisation is given by simple parton model expression

$$P_{\Lambda}(x,y,z) = P_{\|}^{\Lambda}(x,y,z) = \frac{\sum_q e_q^2 \left[P_B D(y) q(x) + P_T \Delta q(x)\right] \Delta D_q^{\Lambda}(z)}{\sum_q e_q^2 \left[q(x) + P_B P_T D(y) \Delta q(x)\right] D_q^{\Lambda}(z)}, \tag{3.22}$$

where P_B and P_T denote the beam and target longitudinal polarisations, respectively, and $D(y)$ is the depolarisation factor. For the unpolarised target case, the only unknowns in formula (3.22) are the polarised fragmentation functions $\Delta D_q^{\Lambda}(z)$.

We studied the longitudinal Λ polarisation using the following assumptions of spin transfer mechanisms in the quark fragmentation process:

- Spin transfer according to the Bigi-Gustafson-Häkkinen [53,56] prescription (BGH). In this approach, the Λ polarisation is described by the SU(6) non-relativistic quark model. Therefore, the polarisation of directly produced Λ's is just determined by that of the s-quark, while Λ's coming from other hyperon resonances also inherit part of the parent's polarisation from other quark flavours. The non-zero spin transfer coefficients we used for this model are shown in Table 3.3. As we mentioned this model provides a good description of the ALEPH data [54].

model	$P_d \to P_\lambda$	$P_u \to P_\lambda$	$P_s \to P_\lambda$
NQM	0	0	+1
BJSR	−0.23	−0.23	+0.58

Table 3.4: Spin transfer coefficients according to NQM and BJSR.

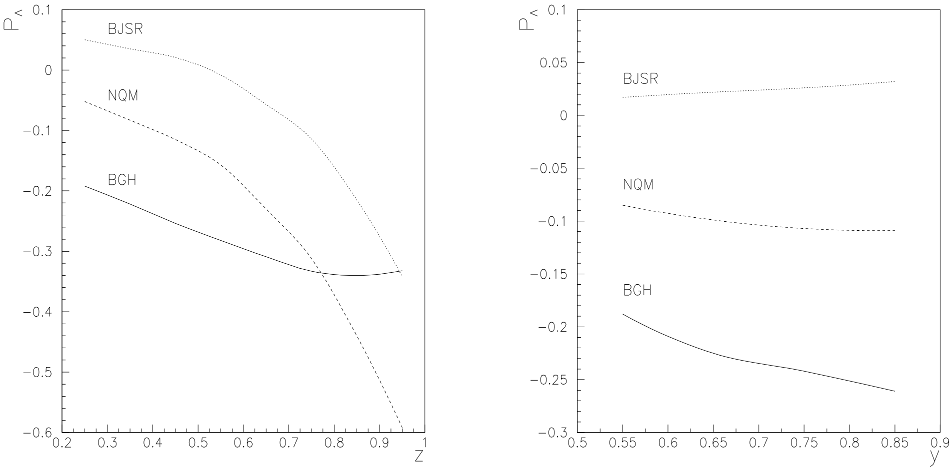

Figure 3.12: Λ polarisation in the current fragmentation region for different mechanisms of spin transfer.

- Spin transfer according to Burkardt-Jaffe [50]. It was assumed that spin transfer from quarks to Λ's have to be the same as the first moment of the polarised quark distribution functions in polarised Λ's. Λ's produced by strong decays of hyperon resonances are included in the Λ fragmentation function, while background of Λ's coming from Σ^0 electromagnetic decays are neglected. The reason for this, is that this channel is rather suppressed and that Λ's are depolarised by a factor 1/3 compared to the initial Σ^0's.

  In Table 3.4, we present the non-zero spin transfer coefficients for the naive quark model expectation (NQM) and the ones related to the the Burkardt-Jaffe sum rule (BJSR) [50], which was evaluated using the experimental value of the first moment of g_1^p.

We studied the sensitivity of the longitudinal $\Lambda/\overline{\Lambda}$ polarisation in the current fragmentation region to different mechanisms of spin transfer. The result for the unpolarised target case is shown in Fig. 3.12, and it indicates a large sensitivity to ΔD_q^Λ. The differences are quite significant between different spin transfer models and the effect could also be enhanced by flipping the beam polarisation. However, negative muon beams have an about three times lower intensity for the same number of primary protons and it has to be evaluated

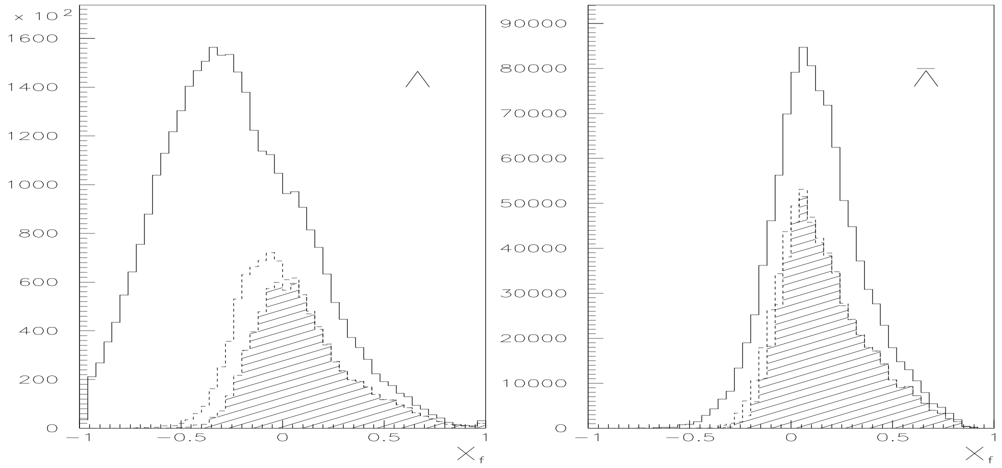

Figure 3.13: x-Feynman distributions of generated (solid line) and accepted by full spectrometer (hatched histogram) Λ (left) and $\overline{\Lambda}$ (right) samples with vertex cut .

3.3.3 Simulation of the detector efficiencies for Λ production

We investigated the possibilities of the proposed apparatus for the measurements of $\Lambda/\overline{\Lambda}$ polarisation considering the interactions of a 100 GeV 80% negatively polarised μ^+ beam with ^{6}LiD target. To simulate the DIS events the standard codes of LEPTO6.2 and JETSET74 [57] with their default values of parameters were used. To ensure high spin transfer in the lepton-quark scattering a cut on y was applied $0.5 < y < 0.9$ in addition to the standard kinematical cut $Q^2 > 1$ (GeV/c)^2 .

For the expected luminosity of $L = 4.3 \cdot 10^{37}$ cm^{-2}d^{-1}, the cross section of DIS events $\sigma = 37.8$ nb and $\Lambda/\overline{\Lambda}$ mean multiplicity of $W(\Lambda) = 0.12$ determined from the LEPTO6.2 one could estimate the total statistics of $\Lambda/\overline{\Lambda}$ with these kinematical cuts. In 38 days (one year 25% efficient SPS × spectrometer) the total number of produced $\Lambda/\overline{\Lambda}$ in charged decay mode is $N(\Lambda) \approx 3.7 \cdot 10^6$ and $N(\overline{\Lambda}) \approx 1.1 \cdot 10^6$.

The acceptance of the proposed apparatus for the $\Lambda/\overline{\Lambda}$ detection was investigated using the GEANT code. We generated a sample of $1.25 \cdot 10^5$ $\Lambda/\overline{\Lambda}$ events (1.0×10^5 Λ's and 0.25×10^5 $\overline{\Lambda}$'s) with the primary vertex in the target downstream target cell.

An event is considered as accepted if the pion and proton tracks from Λ decay pass through MWPC1–3 chambers upstream and the HC1–2 chambers downstream of SM1m magnet. The following cut on Λ decay vertex was implemented to suppress the background: $r/3\sigma_r > 1$ and $z/3\sigma_z > 1$, where r and z are the radial and longitudinal distances between the primary and the Λ decay vertices and $\sigma_r = 3$ mm and $\sigma_z = 30$ mm were assumed as errors of the primary vertex reconstruction. Figure 3.13 shows the x-Feynman distribution of both generated (solid line) and accepted $\Lambda/\overline{\Lambda}$ hyperons (hatched histogram) with the vertex cut.

The advantage of the proposed apparatus is the possibility to use information from the RICH counters for the proton identification. A cut on the proton momentum of $p > 5$ GeV/c was imposed.

To demonstrate the possibilities of the Λ polarisation measurement we considered the angular distribution of decay proton for unpolarised Λ sample. For longitudinally

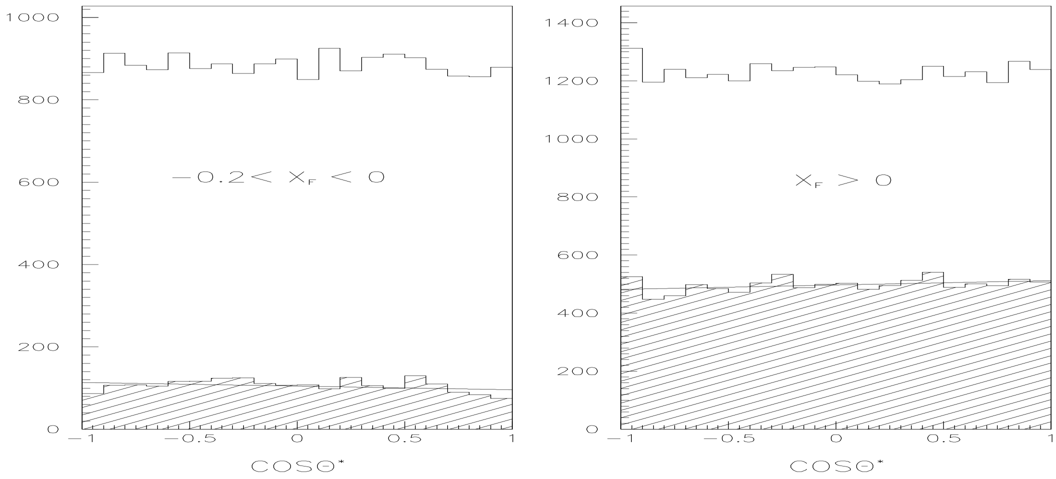

Figure 3.14: Λ decay angular distribution for the target fragmentation region ($-0.2 < x_F < 0$) (left) and the current fragmentation region ($x_F > 0$) (right). The solid lines correspond to the generated distributions and the hatched area to accepted events.

polarised Λ the relevant angle Θ^* is the angle between the decay proton and the virtual photon directions in the Λ rest frame. We compare in Fig. 3.14 the angular distributions of a unpolarised Λ sample for generated (solid lines) and accepted events passing the cut discussed above (hatched area).

For the current fragmentation region (Fig. 3.14, right) the prospects for a polarisation measurements are rather good. Even without any correction on the apparatus acceptance the angular distribution is rather flat and the false polarisation is estimated to be $P_\Lambda = (5 \pm 2)$ %. Due to the high geometrical acceptance of the apparatus about $190 \cdot 10^3$ events with $x_F > 0$ can be collected in one year of data taking.

For the target fragmentation region (Fig. 3.14, left) the acceptance is smaller due to the loss of events with pion momenta $p < 250$ MeV/c in the target solenoid and the SM1m magnet. If it will be possible to measure the momenta of low energy pions before the SM1m magnet the acceptance for events in the target fragmentation region will increase significantly and a measurement for $-0.4 < x_F < -0.2$ will also be possible (dotted line in the Fig. 3.13). Nevertheless, as one could see from the inspection of Fig. 3.14 (left), the distortion of the angular distributions by apparatus is not large and the false polarisation is $P_\Lambda = (-12 \pm 4)\%$. The expected statistics after one year running is $43 \cdot 10^3$ events for $-0.2 < x_F < 0$.

In conclusion, this experiment could provide a $\Lambda/\overline{\Lambda}$ polarisation measurement in DIS processes with high statistics which exceeds the existing data by about two orders of magnitude.

3.4 TRANSVERSE SPIN DISTRIBUTION FUNCTIONS

We propose to measure in semi-inclusive DIS on transversely polarised proton and deuterium targets the transverse spin distribution functions $\Delta_T q(x) = q_\uparrow(x) - q_\downarrow(x)$, where $\uparrow$ ($\downarrow$) indicates a quark polarisation parallel (antiparallel) to the transverse polarisation of the nucleon. Hadron identification allows to tag the quark flavour.

As shown by Jaffe and Ji [58, 59], the momentum distributions $q(x)$, the helicity distributions $\Delta q(x)$, and the transverse spin distributions $\Delta_T q(x)$ completely specify the quark state inside the nucleon at the twist-two level. The functions $\Delta_T q(x)$ have never been measured up to now. Recently, it was proposed to measure them using the LEP beam at CERN [60] and the electron beam at HERA [40]. Complementary measurements can be done in Drell-Yan processes at RHIC [61]. Several model calculations exist for $\Delta_T q(x)$. A naive covariant *quark+scalar diquark* parton model gives $\Delta_T q(x) = \frac{1}{2}[q(x) + \Delta_L q(x)]$ [62–64]. The MIT bag model calculation [58, 59] gives a $\Delta_T q(x)$ which has the same shape as $\Delta q(x)$ but is slightly larger. The QCD sum rule calculation of Ioffe and Khodjamirian [65] yields in the range $0.3 < x < 0.6$ a constant $\Delta_T q(x)$, which is smaller than the bag model value. Another interesting aspect of transversity distribution is the sum rule derived by Jaffe and Ji [58]:

$$\int_0^1 [\Delta_T q(x) - \Delta_T \bar{q}(x)]\, dx = \delta_T q,$$

where $\delta_T q$ is the so called tensor charge, which is defined in terms of the nucleon matrix element of the quark tensor current. In a non-relativistic quark model, $\delta_T q$ is equal to the axial charge Δq; in the MIT bag model, it was derived that $\delta_T u = 1.17$ and $\delta_T d = -0.29$ [66]. QCD sum rule calculations yield $\delta_T u = 1.00 \pm 0.5$ and $\delta_T d = 0.0 \pm 0.5$ [65, 66]. Finally, the recent calculation in the chiral soliton model produced $\delta_T u = 1.07$ and $\delta_T d = -0.38$ [67].

Thus, in all existing estimates $\Delta_T q(x)$ is nonzero at least for u-quarks and it is different from $\Delta q(x)$.

In analogy to $g_1(x)$, it is customary to construct from $\Delta_T q(x)$ a new structure function

$$h_1(x) = \frac{1}{2}\Sigma_q e_q^2 [\Delta_T q(x) + \Delta_T \bar{q}(x)].$$

At variance with $g_1(x)$ which can be obtained directly from the lepton-nucleon cross-section asymmetry, $h_1(x)$ can not be measured in a single inclusive process, due to its odd chirality nature. On the other hand, $h_1(x)$ has a specific signature in semi-inclusive deep inelastic scattering on transversely polarised nucleons. Since the various hadronic channels are sensitive to different quark flavours, it is important to measure many different channels to address the various flavour contributions to h_1 .

3.4.1 Measurement of $\Delta_T q(x)$

Jaffe and Ji [68] have shown that the transversity distributions can be investigated by measuring the difference of the semi-inclusive DIS cross section with longitudinally polarised leptons on transversely polarised target. However, they have integrated over the transverse momentum of the produced hadron, obtaining an expression where $\Delta_T q(x)$ is combined with a twist-three fragmentation function. Thus, this asymmetry appears only at the twist-three level and is suppressed in the deep-inelastic limit as $\sim 1/Q$. It is likely to be very small and hard to detect.

Alternatively, we propose to measure $\Delta_T q(x)$ in semi-inclusive DIS at the leading twist, by analysing the polarisation of the 'struck' quark. This is possible, because in the fragmentation process the leading hadron is expected to have a polarisation or exhibit an asymmetry related to the spin of the fragmenting quark.

Several methods have been suggested to measure the quark transverse polarisation. One method relies on the measurement of the transverse polarisation of Λ's ('baryon polarimeter') as proposed originally in Ref. [69], and later rediscovered by Artru and Mekhfi [63, 64]. In an other method, one can measure the azimuthal dependence of the plane containing the leading and next-to-leading hadrons [70], or the azimuthal distribution of the leading π's around the jet axis ('mesonic polarimeters') [71].

In all these methods the final hadronic asymmetries are given by the product of three terms, the distribution function $\Delta_T q$, the (known) quark spin transfer coefficient in the hard scattering D_{nn}, and the analysing power of the fragmentation process. Since the spin dependence of the different fragmentation functions is not known, only the product of the distribution functions (DF) and the fragmentation functions (FF) can be measured. On the other hand, due to the factorisation of the x and z dependence in the hadronic asymmetries, we will measure for the first time the x dependence of the DF's $\Delta_T q$. An absolute calibration of the analysing power of the fragmentation process might come from the analysis of two-jets events at LEP experiments. A preliminary study [72] of the transverse spin correlation of quarks in the decay of the Z^0 has provided only an upper limit to this analysing power ($\simeq 0.3$). The method is not very sensitive, since the correlation depends on the square of this quantity. On the contrary, the large inclusive pion asymmetries observed in polarised proton-proton scattering at FNAL [73] suggest for the products of the DF and FF of the light quarks values larger than 0.4 of the unpolarised quantities [74].

Using the proposed experimental apparatus, all the known 'quark polarimeters' will be exploited. In the following we will concentrate on the Collins effect, i.e. on the spin dependence of the azimuthal asymmetry of the leading pion.

3.4.2 Collins effect for leading pions

As suggested by J. Collins [71], the fragmentation function for transversely polarised quarks should exhibit a specific azimuthal dependence. The transversely polarised quark fragmentation function $\mathcal{D}_q^h$ should be built up from two pieces, a spin-independent part D_q^h, and a spin-dependent part ΔD_q^h:

$$\mathcal{D}_q^h(z, \vec{p}_q^{\,h}) = D_q^h(z, p_q^h) + \Delta D_q^h(z, p_q^h) \cdot \sin(\phi_h - \phi_{S'}), \tag{3.23}$$

where $\vec{p}_q^{\,h}$ is the final hadron's transverse momentum with respect to the quark direction (i.e. the virtual photon direction in DIS), ϕ_h ($\phi_{S'}$) is the final hadron's (final quark's spin) azimuthal angle around the quark direction. In the reference frame with the z-axis along the virtual photon momentum and the $x - z$ plane defined by the lepton scattering plane (see fig. 3.15), from first order QED, the azimuthal angle of the final quark's transverse spin is given by

$$\phi_{S'} = \pi - \phi_S,$$

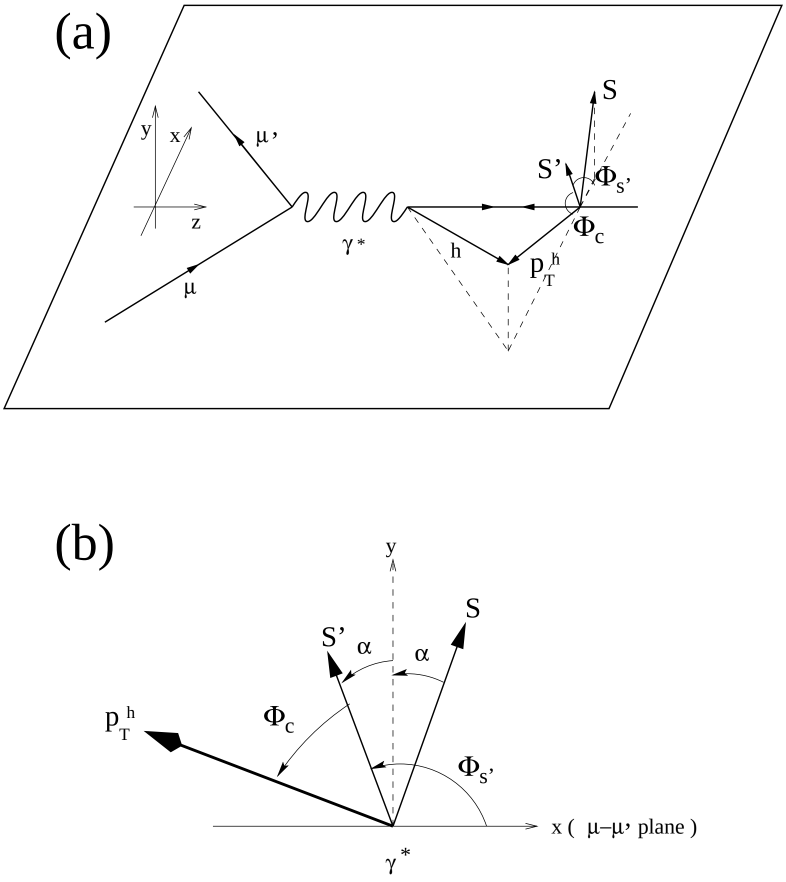

Figure 3.15: Definition of the Collins angle $\phi_c = \phi_h - \phi_{S'}$ in the Breit frame of the muon deep inelastic scattering: (a) perspective view, (b) front view (the virtual photon is coming out of the page).

where ϕ_S is the azimuthal angle of initial quark's transverse spin. Thus, in the parton model, the transverse-spin-dependent part of the cross-section has a specific dependence on the sine of the 'Collins angle' $\phi_c = \phi_h - \phi_{S'} = \phi_h + \phi_S - \pi$. The amplitude of this azimuthal modulation is proportional to both the transversity distribution and the analysing power of polarised quark fragmentation.

The ratio of the polarised to the unpolarised part of fragmentation functions (the 'analysing power') can not be calculated in perturbative QCD. This analysing power has been calculated in two different models: string fragmentation model [75] and low energy effective theory (linear sigma model) [71], [76]. The two approaches have shown that the effect can be very large.

In Ref. [71] the spin effects connected with the intrinsic transverse momentum k_T of the initial quark in the nucleon are neglected. In the case of polarised nucleons, the effect of k_T has been studied by A. Kotzinian [77] and independently by R.D. Tangerman and P.J. Mulders [78]. At the twist-2 level the quark state in a polarised nucleon is described by six distribution functions (instead of three distribution functions when k_T effects are neglected), and the semi-inclusive DIS cross section has a more complicated dependence on ϕ_S and ϕ_h. The contributions of the various distribution functions can in principle be disentangled by properly integrating on the azimuthal angles. For example, the distribution function $g_{1T}(x, k_T^2)$ describing the quark longitudinal spin in the transversely polarised nucleon appears in the cross section in combination with ordinary unpolarised fragmentation function and can be directly measured at leading twist [79].

The complete tree-level description of polarised semi-inclusive DIS up to order $1/Q$ including twist-three distribution and fragmentation functions has recently been derived by Mulders and Tangerman [55]. Although the twist-three effects are expected to be small, in principle we will have access to them, in particular to the $g_2(x)$ as well as to the semi-inclusive transverse-spin asymmetry integrated over hadron transverse momentum as proposed by Jaffe and Ji [68].

3.4.3 Statistical accuracy

Several flavour combinations of the $\Delta_T q$ can be measured, using DIS events with a leading π on transversely polarised proton and deuterium targets. A few of them are given in Appendix B, to which we refer for the notation.

To estimate the accuracy of these measurements, we have considered the asymmetry 2):

$$\epsilon = f_p \cdot P_T^p \cdot D_{nn} \cdot H(x) \cdot a_c$$

where

$$H(x) = \frac{4\Delta_T u + \Delta_T \bar{d} + 4\Delta_T \bar{u} + \Delta_T d}{4u + \bar{d} + 4\bar{u} + d} \simeq \frac{2 \cdot x \cdot h_1(x)}{F_2(x)},$$

$$a_c = \frac{\Delta D_1 + \Delta D_2}{D_1 + D_2},$$

P_T^p is the target polarisation, f_p is the target polarisation dilution factor and D_{nn} is the quark spin transfer coefficient in the hard scattering. This asymmetry can be estimated from the number of leading charged pion events on a proton target

$$\frac{(N_p^{\pi^+ +} + N_p^{\pi^- +}) - (N_p^{\pi^+ -} + N_p^{\pi^- -})}{(N_p^{\pi^+ +} + N_p^{\pi^- +}) + (N_p^{\pi^+ -} + N_p^{\pi^- -})}$$

where the $+$ and $-$ refer to the two spin orientations of the proton.

We have used a Monte Carlo program based on the JETSET-LEPTO code. The events are generated in the kinematical region $0.006 \le x \le 1.$, at 100 GeV incident μ momentum. If the leading hadron (i.e. the most energetic particle between π's and K's) is a charged pion satisfying Berger's criterion [80], an asymmetry in the Collins angle ϕ_c is generated according to the distribution $N^{h\pm}(\phi_c) = N_0(1 \pm \epsilon \cdot \sin\phi_c)$. In the Monte Carlo program for $h_1(x)$ we have used a parametrisation [81] very closed to the one of $g_1(x)$. The function we have used is shown in fig. 3.16. together with the measured values if $x \cdot g_1$ from SMC and SLAC experiments [26,28]. For a_c we have assumed the model of Ref. [75], which reproduces the π asymmetries measured by E704 [73]. It gives $a_c = z \cdot p_q^h \cdot \sqrt{p_q^{h\,2} + M^2}/(M^2 + p_q^h \cdot \sqrt{p_q^{h\,2} + M^2})$, with $M = 0.3$ GeV. This parametrisation gives an analysing power of about 0.2 at p_q^h =0.6 GeV and z =0.4, which is smaller than the upper limit given by the DELPHI analysis.

In the analysis, only events with $\nu \ge 15$ GeV, $E' \ge 5$ GeV and a leading pion with $z \ge 0.1$ are accepted. The statistical errors on $x \cdot h_1$ in the 'ideal' case (π and K identification, no interaction in the target, no reconstruction errors, no large angle acceptance cut) are given in Tab. 3.5. They have been calculated assuming a luminosity

---

[2] similar considerations hold for all the proposed asymmetries

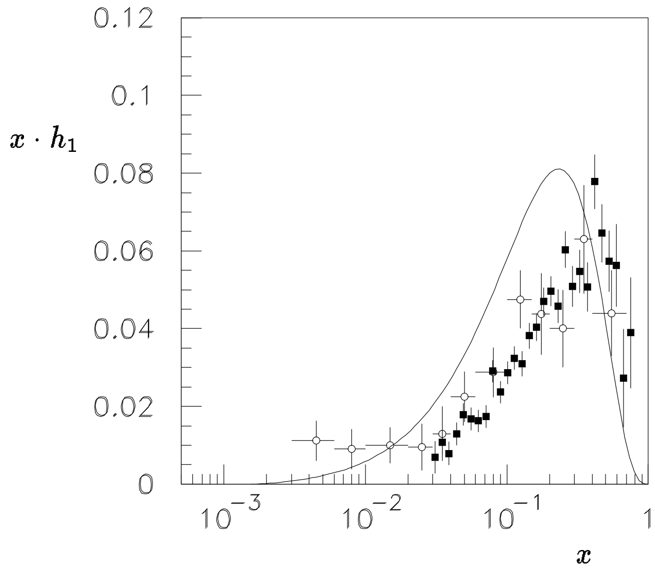

Figure 3.16: Parametrisation for $xh_1(x)$ used in the Montecarlo program compared with the measured values of $xg_1^p(x)$

x	$z \geq 0.1$		$z \geq 0.3$	
	ϵ	$x \cdot h_1$	ϵ	$x \cdot h_1$
0.006−0.01	0.0004±0.0011	0.005 ±0.013	0.0003±0.0013	0.005 ±0.019
0.01−0.02	0.0016±0.0006	0.010 ±0.004	0.0019±0.0007	0.010 ±0.004
0.02−0.03	0.0035±0.0006	0.017 ±0.003	0.0041±0.0007	0.017 ±0.003
0.03−0.04	0.0053±0.0007	0.024 ±0.003	0.0062±0.0008	0.024 ±0.003
0.04−0.06	0.0075±0.0007	0.032 ±0.003	0.0087±0.0008	0.032 ±0.003
0.06−0.10	0.0110±0.0007	0.048 ±0.003	0.0129±0.0008	0.048 ±0.003
0.10−0.15	0.0154±0.0010	0.065 ±0.005	0.0180±0.0012	0.065 ±0.004
0.15−0.20	0.0192±0.0015	0.077 ±0.006	0.0220±0.0017	0.077 ±0.006
0.20−0.30	0.0216±0.0016	0.081 ±0.006	0.0248±0.0018	0.081 ±0.006
0.30−0.40	0.0239±0.0027	0.071 ±0.008	0.0264±0.0030	0.071 ±0.008
0.40−0.70	0.0249±0.0036	0.046 ±0.007	0.0271±0.0038	0.046 ±0.007

Table 3.5: Statistical errors for the asymmetry ϵ and $x \cdot h_1(x)$ in the different x-bins, for 30 days of data taking, and $E' \geq 5.$, $\nu \geq 15$.

of $4.3 \cdot 10^{37}$ cm$^{-2} \cdot$ d^{-1}, the NH$_3$ target with polarisation $P_T^p = 85\%$ and dilution factor $f_p = 0.176$, 30 days of data taking, and an overall efficiency of 0.25. The expected asymmetries (also shown in fig. 3.18a) are many standard deviations from zero: even if the Collins analysing power should be a factor of 4 smaller than the parametrisation we have used, it is apparent from the table that the measured ϵ would still be 2 to 5 standard deviations from zero in the seven x-bins between 0.03 and 0.7.

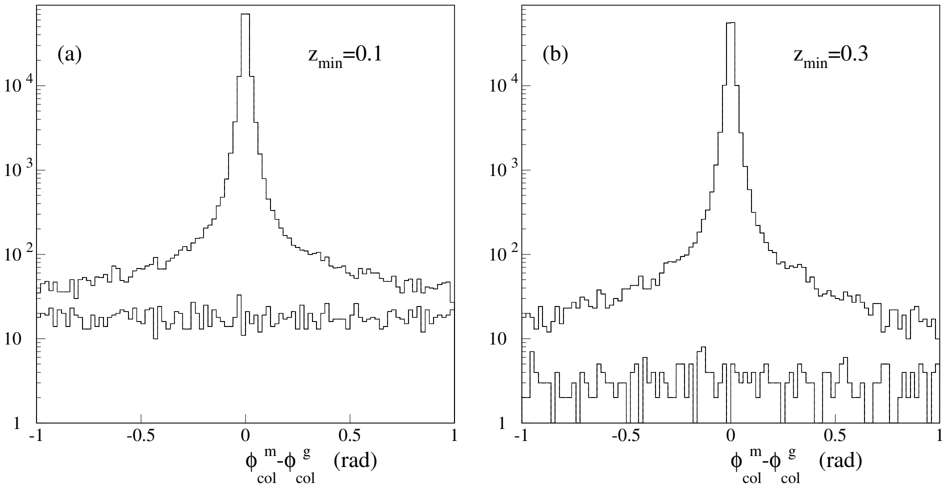

Figure 3.17: Difference between measured and generated Collins angle $\phi^m_{col} - \phi^g_{col}$ for "good" events and "background" events (lower histogram) as defined in the text. (a) refers to the cut $z_{\mathrm{min}} = 0.1$, (b) to the cut at $z_{\mathrm{min}} = 0.3$.

3.4.4 Systematics uncertainties

The dilution of the Collins analysing power due to hadron interactions in the target material has been studied using a Monte Carlo program based on Geant 3.21; the secondary hadronic interactions were simulated by the Gheisha package.

The effect of the secondary interactions in the target on the Collins asymmetry is shown in Fig. 3.17, where the reconstructed Collins angle ϕ_c is compared with the generated one for:

1. events where the reconstructed leading pion has the same charge as the generated leading pion ("good" events);

2. events where the reconstructed leading pion has a charge opposite to the one of the generated leading pion ("background" events).

It is apparent from Fig. 3.17 that the information on the Collins angle is completely lost for the "background" events and it is safe to assume that they show no asymmetry. It is also apparent, that for most of the "good" events the Collins angle is essentially unaffected. A cut at $z_{\mathrm{min}} = 0.3$ reduces the "background" events by almost an order of magnitude, as suggested by the comparison of Fig. 3.17(a) and 3.17(b).

The measured asymmetry for 30 days of running time has been estimated without and with the interactions in the target for the two cuts $z_{\mathrm{min}} = 0.1$ and $z_{\mathrm{min}} = 0.3$, and is shown in Fig. 3.18 and 3.19 respectively. The dilution of the asymmetry is not very large, it depends on the z cut, and can be estimated reliably.

To conclude, it has to be stressed that the present simulation overestimates the effect of the dilution of the asymmetry because only charged mesons are identified after the interactions in the target. The π^0 identification will help to cut down the most important source of background, namely the events with a leading π^0. In the Monte Carlo the π^0 is not identified and a sub-leading $\pi^\pm$ can be identified as the leading particle, and contributes to the "background", but clearly a good π^0 identification will reduce considerably this effect.

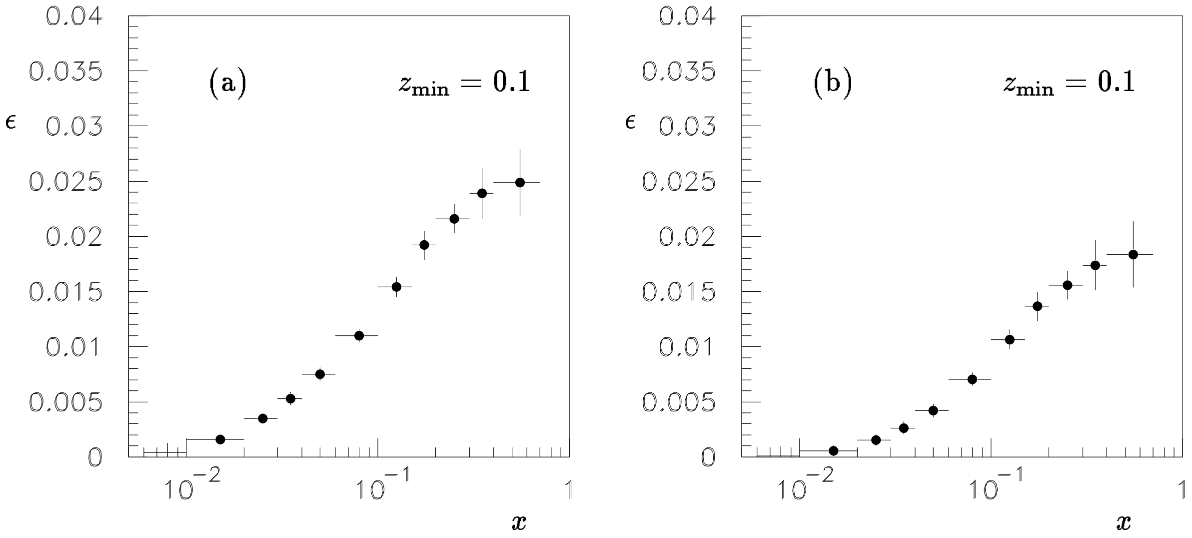

Figure 3.18: Measured asymmetry $\epsilon(x)$ in 30 days of running time, for $z_{\rm min} = 0.1$. (a) shows the errors expected without target interactions; in (b) the effect of target interactions has been included.

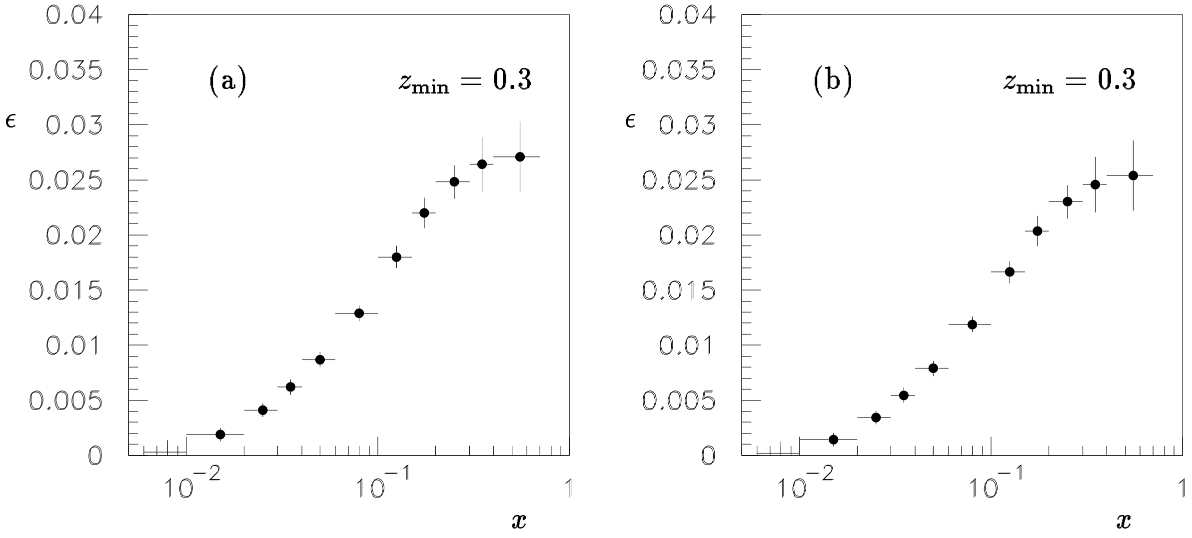

Figure 3.19: Measured asymmetry $\epsilon(x)$ in 30 days of running time and $z_{\rm min} = 0.3$. (a) shows the errors expected without target interactions; in (b) the effect of target interactions has been included.

3.4.5 Measurement of $g_2(x)$

In addition to the evaluation of $\Delta_T q$ from semi-inclusive asymmetries the data obtained with transversely polarised targets will also provide an improved evaluation of the spin structure function g_2. This function was measured for the proton and the deuteron by experiment E-143 at SLAC [82]. The data cover the range $0.03 < x < 0.7$ and show that in this region g_2 is compatible with its twist-2 part g_2^{WW} which is directly calculable from g_1

$$g_2^{WW}(x,Q^2) = -g_1(x,Q^2) + \int_x^1 \frac{g_1(y,Q^2)}{y} dy. \tag{3.24}$$

In the transverse configuration, g_2 is obtained from the asymmetry between the number of muons scattered at angles ϕ and $\phi + \pi$ with respect to the plane containing the beam and target polarisation vectors. In the case of the E143 measurements, the statistical error on this asymmetry is generally of the order of 0.2–0.3.

During the proton run of 1993 the SMC collected a small sample of data in transverse mode extending to $x = 0.006$. The results show that $g_2^p(x)$ is compatible with zero within large statistical errors [83]. Data with transverse polarisation of the deuterium target were also taken during one SPS period in 1995 and are presently being analysed. Additional runs with a transversely polarised proton target are foreseen in 1996. The statistical accuracy of these data will remain lower than for the E-143 data in the kinematic region covered by both experiments.

Half a year of running in transverse mode with a five times larger beam intensity and a more efficient spectrometer will provide transverse muon asymmetries with statistical errors comparable to those of E-143. In the low x region, $0.006 < x < 0.03$, these data will test the presence of higher-twist contributions to g_2 with a much improved accuracy.

4 PHYSICS WITH HADRON BEAM

In the following section we will layout in more detail the physics issues which can be addressed with the proposed experiment using hadron beams. They also comprise subjects not mentioned in the introduction.

4.1 STUDIES OF CHARMED HADRONS

The studies of charmed hadrons cover a wide spectrum from the investigations of charm production itself, spectroscopy, decay studies up to searches for rare processes.

The physics at a high intensity charm experiment (CHARM2000) has been discussed recently at Fermilab [84]. However, most of the discussion centred on charmed mesons. Aiming in its initial phases at a beam intensity about a factor 10 lower than discussed for CHARM2000 the proposed experiment puts more emphasis on charmed baryons and hopes to collect about ten times more charmed hadrons than the two planned Fermilab experiments E781 and E831.

4.1.1 Status of charmed baryons and previous experiments

Many years after the first discovery of charmed baryons still little is known about the properties of these objects (see fig. 4.1 for the overview on baryon ground states). Not even all $1/2^+$ ground states have been observed: The $\Xi_c^{0'}$ is still missing and the $\Xi_c^{+'}$ [85] needs confirmation. Of all the $3/2^+$ baryons only the Ξ_c^{0*} has been observed and in the past two years, two excited states of the Λ_c^+ have been discovered. Although the lifetime of all weakly decaying c-baryons have now been determined there is a lack of accuracy (see fig. 4.2). Except for the Λ_c^+ the precision on τ is about 30%. Semileptonic decays of charmed hadrons are just beginning to be tackled. Measurements now exist on the formfactors of charmed meson decays. For baryons, s.l. decays have been observed for the Λ_c^+, Ξ_c^+ and Ξ_c^0. But only for the Λ_c^+ first measurements of the decay asymmetry, directly related to the formfactors in these decays, have been obtained.

4.1.2 Charmed Baryon Decays

The study of charmed baryon decays can be divided into three mutually connected categories:

- semi-leptonic decays
- lifetimes

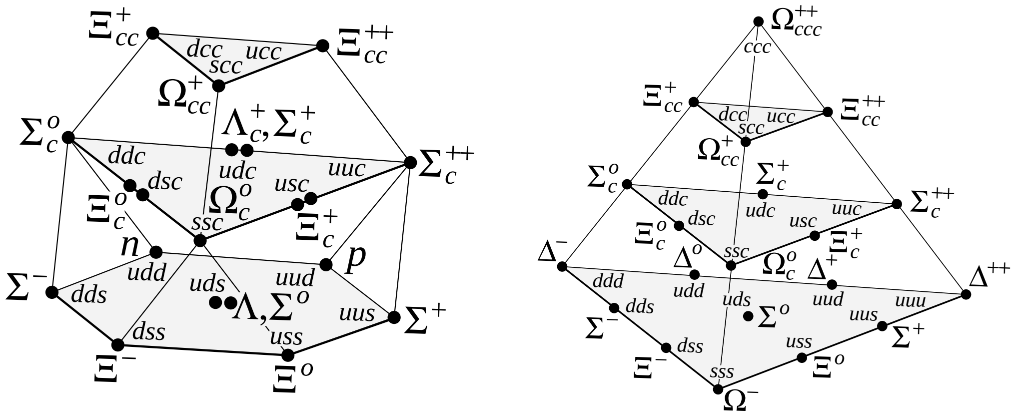

Figure 4.1: SU(4) representation of the ground state baryons

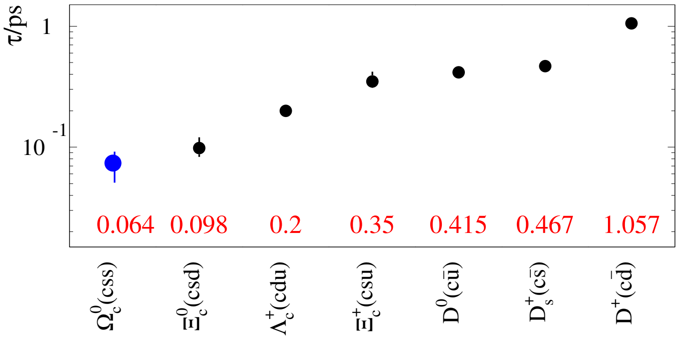

Figure 4.2: Overview of all measured c-hadron lifetimes

- non-leptonic decays

Semi-leptonic decays. The semileptonic decay rates of charmed mesons and baryons can be calculated theoretically with good precision since only the free c-quark decay rate has to be evaluated with form factors, which can be obtained using the Heavy Quark Effective Theory (HQET) [86]. Effects of the finite c-quark mass are estimated to be on the order of 20%. Furthermore, symmetries in the light quark degrees of freedom can be utilised in these calculations, such as for the semileptonic decays of Λ_c and Ξ_c.

To date, the study of semileptonic decays of charmed baryons has been the domain of experiments at e^+e^- colliders because of a high relative yield of hadronic events containing charm. Recently, CLEO for the first time has measured decay asymmetries in semileptonic decays of Λ_c using about 500 Λ-lepton pairs [87]. At low q^2, where the predictions on the baryon form factor ratios from HQET are most trustworthy [88], they observed good agreement between decay asymmetry and predictions. From a bigger sample of about

700 Λ-lepton pairs they extracted [89] the ratio of two form factors, averaged over q^2 for reasons of small statistics. A full test of HQET requires, however, the individual observation of both form factors as a function of q^2 or at least a measurement of the asymmetry at different values of q^2 which then should allow an extrapolation to q^2=0. The required large statistics of many thousand semileptonic decays will be accumulated by the proposed high intensity experiment.

We can use the theoretical semileptonic decay width Γ_{sl}^{th} together with the experimentally accessible ratios of branching fractions B_{had}/B_{sl} to determine the hadronic partial widths: $\Gamma_{had} = \Gamma_{sl}^{th}\, B_{had}/B_{sl}$, for which different models give widely differing results$^{1)}$. From the measured lifetime we can calculate *absolute* hadronic branching ratios by multiplying with the above determined hadronic width: $B_{had} = \Gamma_{had}\,\tau$.

Theoretical uncertainties in short distance corrections to the free decay rate are small and expected to be very similar for the various charmed hadrons. However, large uncertainties exist in the long distance effects, described by the w.f. overlap of initial and final states. Nevertheless, various possibilities exist to relate such effects for different hadrons giving reasonably reliable predictions for the ratios of the s.l. decays rates [90].

The method: Modern fixed target experiments have become very competitive with e^+e^- experiments. In the D-meson sector, the background reduction needed is achieved by selecting D-s coming from decays of D*-s, as $D^{+*} \rightarrow D^0\pi^+$. A right–sign lepton-kaon pair is selected for the D decay candidate. Despite the momentum of the candidate is not fully reconstructed since the neutrino is not observed the mass splitting spectrum $D^* \rightarrow D$ stays relatively narrow allowing to reduce the background considerably. In the baryon sector one may use the transition $\Sigma_c \rightarrow \Lambda_c^+$. A similar tagging technique should be also applicable for charmed–strange baryons. Here, most of heavier charmed–strange baryons have still to be discovered. The easiest to detect semileptonic decay of Ξ_c seems to be $\Xi_c^0 \rightarrow \Xi^- e^+ \nu$. An observation of Ξ_c^{0*} decaying to $\Xi_c^+\ \pi^-$ has been recently reported by CLEO [91]. Another possible signature would the observation of the decay photon from the transition $\Xi_c' \rightarrow \Xi_c\ \gamma$ [85], where Ξ_c' is the partner of Ξ_c with symmetric light-quark content. These transitions can be identified with sufficient precision even though the neutrino is not observed, to discriminate against background from processes with uncorrelated Ξ^- and positrons in the final state. In order to obtain clean charm samples one either requires the full (or partial) reconstruction of an associated $\overline{D}$-meson or the decay vertex of the c-baryon to lie a few mm downstream of the first interaction counter. For s.l. Λ_c^+ decays both techniques lead to similar efficiencies while for shorter living baryons only the requirements of an associated $\overline{D}$ may be used.

On what concerns the measurement of inclusive s.l. decay widths the measurement is far more difficult than the semi-inclusive one and the precision may only be estimated after first measurements have been done. The technique is described below. Again we use a sample of D-tagged events combined with a μ of "right" sign (a $\overline{D}$ should be accompanied by a μ^+ and vice versa). We then compare this rate for D and $\overline{D}$-mesons. Under the assumption of a pronounced c-baryon/$\overline{c}$-baryon production asymmetry the difference can then be attributed to s.l.c-baryon decays. The charge of the baryons is tagged via the charge in the decay vertex. This will give the rate of s.l. decays of charged and neutral c-baryons to which the hadronic decays can be normalised. Using the rate of their exclusive

---

[1] Note that the experimental determination of B_{sl} has to be inclusive, i.e. include *all* hadrons produced along with the lepton and neutrino.

decays and tagging techniques we thus obtain a handle on the inclusive s.l. decays of the different c-baryons.

Lifetimes. Charmed hadron lifetimes constitute a good testing ground for the understanding of the effects of the hadronic environment on the decay of the naked charm quark. These effects are about a factor 10 larger for charmed hadrons than for beauty hadrons – as evidenced by the factor 10 spread of lifetimes for charmed hadrons – but significantly smaller than in strange hadrons. Due to the small Q-value in the decays of strange hadrons not many different decay channels exist and they are subject to strong selection rules (imposed by non perturbative effects). The lifetime of strange hadrons is thus determined by one or two different decay channels. Thus it is this intermediate region of charmed hadrons which offers the best chance for studies of strong interactions in a regime where perturbative and non perturbative effects overlap. Finally, a better understanding is also needed to better predict and interpret results for beauty lifetimes, where differences are expected only at the 10% level.

Two concurring processes govern the lifetimes of charmed baryons: W-emission and W-exchange, with further modifications due to the wave function overlap between initial and final hadronic states, yielding large uncertainties. The relative strengths and phases give the predicted – and in part already confirmed – lifetime hierarchy. Theoretical uncertainties stem mainly from the determination of the coefficients for the two operators involved and uncertainties in the overlap of the quark wave functions.

To aid theory in its understanding of these hadronic effects requires precise measurements of the lifetime of all charmed baryons to better than 5% (see e.g. [92]). Current precision for the lifetimes of charmed mesons and Λ_c^+ is of the order of a few percent, whereas those of the charmed-strange baryons is around 20% and about 40% for the Ω_c^0, with improvements expected within the next few years to a level of 10%. The main difficulty lies in the short lifetimes of the charmed-strange baryons and their small production rate, which also yields rather large systematic uncertainties. A dedicated set up with a high intensity beam should allow improvement of the situation.

A precise knowledge of charmed hadron lifetimes can also be used to determine absolute charm branching ratios with sufficient precision, as discussed above. These branching ratios are needed in order to interpret beauty hadron decays.

The proposed experiment will make use of a high granularity high resolution vertex detector which should give lifetime resolutions much superior to existing or planned experiments. Excellent resolutions ($\Delta\tau$ 20-30fs) are needed to reduce the systematic error on the measurement of the shortest lifetimes ($\tau \leq 100$ fs). With about 100 (500) reconstructed events assuming a lifetime of 50 fs and a signal/background ratio (SB) of about 1, the accuracy in τ should be about 6 (3) fs. The high resolution is needed to reduce the systematic error which might arise from fluctuations in SB or the precise estimation of the resolution itself.

Non-leptonic decays. To gain insight into the interplay of the different decay diagrams for hadrons with different light-quark contents we must compare absolute decay rates of non-leptonic decays. Such absolute decay rates can either be obtained from ratios of branching ratios together with the theoretical semileptonic decay width (see above) or from observing as many final states as possible for an estimate of single branching ratios and using the measured lifetime. From a theoretical point of view it is the decay width to *two-body* final states that allows a comparison with calculations. In particular, the assumption of factorisation has yet to be tested in baryon decays.

To date, absolute decay rates have not been obtained in fixed target experiments since the observation of semileptonic branching ratios is rather difficult. Only for the Λ_c^+ exist absolute rates from the e^+e^- experiments MARK II [93] and CLEO / ARGUS [94]. The first experiment observed a change in proton production rate at the Λ_c^+production threshold, whereas the latter experiments tag Λ_c^+ from B-meson decays. Both results, however, are not consistent. As discussed in the section on semileptonic decays, a high statistics fixed target experiment would utilise the ratio of hadronic to semileptonic branching ratios together with the theoretical semileptonic width to obtain absolute branching fractions.

4.1.3 Studies of Charm Hadroproduction

The process of hadroproduction of charmed particles can be subdivided into two different subprocesses, namely the production of charmed quarks and the process of their hadronisation into charmed particles. The former defines the full cross–section of charm while the latter is responsible for the relative production of different types of charmed particles and their kinematic distributions. Perturbative QCD might be applicable to the estimations of the cross–section of charmed quark production, however the mass of the charmed quark is not large enough to limit the calculations to low order diagrams. On the other hand the process of hadronisation of charmed quarks is soft and is beyond the scope of perturbative calculations.

Previous experiments : Production cross–section of charmed particles has been measured in several experiments. Many of the old experiments were capable to detect only D-mesons produced in a limited range of x_F. Most of the experiments were performed on nuclear targets. In order to derive the full charm cross–section on nucleon one has to scale the values measured thus introducing additional systematic errors due to uncertainties of:

- contribution of unobserved charmed particles;
- extrapolation to the full kinematic range;
- A-dependence of the cross–section;
- branching ratios of observed decay modes.

These systematic errors may differ for different experiments. Estimates of the full charm cross–section based on results of existing measurements extrapolated to the full kinematic range of x_F are shown on figure 4.3. The details of the method used are explained in [95].

Only two measurements allow a direct comparison of cross–sections at different energies. One was performed in a pion beam with energies of 200 and 230 GeV [98] and another in a proton beam with energies of 200 and 360 GeV [100]. Both indicate a rapid rise of the cross–section with energy. For lower energies there are several measurements of upper limits on a level of 5-20 μbarn [101]. In contrast, there are two measurements [102, 103] reporting a very high cross–section of the order of magnitude of 10 μbarn for charmed baryons produced by baryon beam in the forward hemisphere at about x_F>0.5.

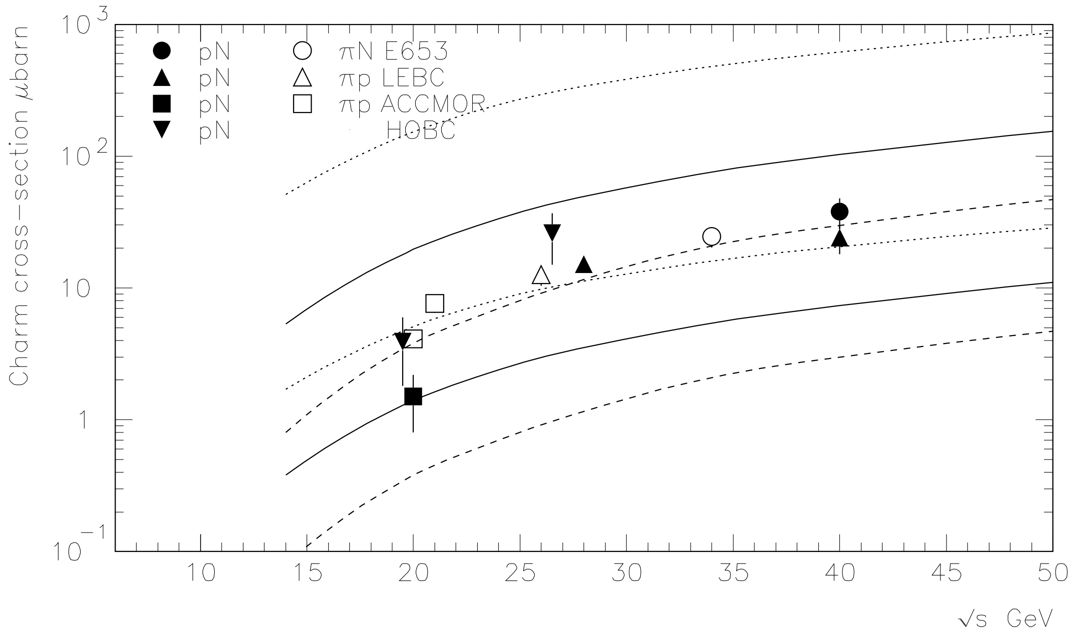

Figure 4.3: Energy dependence of the full charm production cross–section. The measurements from LEBC [96, 97], ACCMOR [98], E653 [99] and HOBC [100] experiments are scaled in order to obtain the values of $\sigma_{c\bar{c}}$. The full symbols present the proton beam data while the hollow ones present the pion beam data. The curves are obtained with next-to-leading order calculation for p-p collisions within Perturbative QCD [95] for different charm quark masses (1.2 GeV for the dashed curves, 1.5 GeV for the solid curves and 1.8 GeV for the dotted ones) and reflect the calculation uncertainties. Cross–section in pion beams is expected to be slightly higher than in proton beams due to the different partonic structure functions.

Kinematic parameters of charmed particles may probe the process of hadronisation. The measurements from CERN and FERMILAB [104] observed a considerable "leading effect" of D-mesons produced in a pion beam, namely an excess of about 50% of "leading" D-s over "non-leading" ones produced at x_F>0.5. This effect can not be explained by the distributions of charmed quarks produced within the NLO calculations. This underlines the important role of the hadronisation process. One of the most popular hadronisation models involving a "colour flow" concept and implemented in the PYTHIA program predicts strong leading effects, however its prediction for a very strong leading in diquark fragmentation processes were not confirmed by the results of WA89 experiment on charmed baryons produced in a Σ^- beam.

In summary, a number of measurements of the full charm cross–section at $\sqrt{s}$ of 20-30 GeV are mutually consistent within 50-70% tolerance. Generally, different energies were covered by different experiments which prevents one to derive the energy dependence of the charm cross–section with an accuracy better than 50%. The data at lower energies are scarce or not convincing. In the near future more results on the charm hadroproduction are expected from the experiments WA89 (Σ^- beam at 320 GeV/c), WA92 (π^- beam at 350 GeV/c) and from E791 (π^- beam at 500 GeV/c). In several years one expects to see results from E781 (Σ^- beam at 600 GeV/c). None of these measurements will cover the lower energy region.
Today, theoretical uncertainties of the cross–section prediction are at least as wide as the experimental uncertainties. There are "leading particle effects" observed which have not been explained by the popular hadronisation models.

New measurements proposed: Due to the very high beam rate the experiment proposed is capable of a systematic study of the charm production in a range of CM energies from 14 to 25 GeV, i.e. for beam momenta from 100 to 300 GeV/c. The systematic errors of the charm cross–section determination are expected to be better than in other experiments due to a higher acceptance to x_F and ability to detect different types of charmed particles. The high statistics of charmed signals also helps to study possible systematic errors. The study can be performed both with proton and π^- beam. The following points are important for the measurement:

- A-dependence of the cross–section measured in the same experiment;
- detection the decay modes with reliable branching ratios;
- detection of all types of charmed particles which may contribute to the cross–section;
- the high acceptance for $x_F > -0.1$;

In order to diminish the uncertainty coming from the A-dependence of charmed particle production the target may include a copper plate 2mm thick and a carbon plate build of diamond powder 2mm thick of a density of 3.25g/cm^2. These diamond plates have been used in WA89 experiment. The branching ratios of the major decay modes of charmed mesons are known within an accuracy of about 3%. For Λ_c^+ the accuracy of branching ratios is not better than 15%, however since its contribution to the full cross–section is about 20% the associated systematic error of the cross–section measurement does not exceed 3%. Branching ratios of charmed–strange baryons are not known at all, [2] but they are not expected to contribute more than a few percent to the full charm cross–section in proton or pion beams. Therefore a systematic error associated with the branching ratios used should not exceed 5%.

The prospects of the measurements proposed were evaluated using the Monte-Carlo simulation. The details are given in the subsection 4.1.7 and the results are summarised in the table 4.1. In order to evaluate the full cross–section charmed particles of all types have to be measured. Thus the time needed for a measurement at a certain energy is defined by the weakest signal. At 100 GeV/c we expect to observe about 30 Λ_c^+ per day. 10 days of effective running should provide enough statistics to determine its contribution to the $\sigma_{c\bar{c}}$. A comparable measurement at 200 GeV can be accomplished in about 5 days. The measurement at the highest energy (about 300 GeV) does not need a dedicated run and can be carried out along with the other charm program. Since the efficiency at a beam energy of 60 GeV is lower than at 100 GeV no measurement at this energy is considered at the moment. Kinematic distributions of charmed particles will be also studied. Furthermore, at the highest energy the expected statistics of about 10^5 events with both charmed particles fully reconstructed is high enough to study their correlations.

4.1.4 Double-Charmed Baryons

The topic of doubly charmed baryons has not yet been addressed by any running experiment. The study of such systems is an experimental challenge owing to the very low cross sections and small branching ratios expected.

---

[2] However the experiment proposed should contribute to this field (see the section on semileptonic decays).

Masses of *ccq* baryons. Bjorken [105] in 1986 estimated M(ccq) $\sim$ 3.7 - 3.8 GeV for J=3/2, by assuming an "equal-spacing" rule for J=3/2 baryon masses, and by interpolating between estimated ccc and bbb masses, and those of ordinary baryons. More recently, Roncaglia et al. [106] used the Feynman-Hellmann theorem and semi-empirical mass formulae to fit known hadron masses, and to estimate ccq masses. Those estimates [106] are given here to three significant figures:

Ω_{cc} (ccs): $1/2^+$, 3.74 $\pm$ 0.08 GeV,
Ω^*_{cc} (ccs): $3/2^+$, 3.82 $\pm$ 0.08 GeV,
Ξ_{cc} (ccu), (ccd): $1/2^+$, 3.66 $\pm$ 0.07 GeV,
Ξ^*_{cc} (ccu), (ccd): $3/2^+$, 3.74 $\pm$ 0.07 GeV.

The cc diquark is a colour antitriplet with spin S=1. The spin of the third quark is either parallel (J=3/2) or anti-parallel (J=1/2) to the diquark. We see that the masses of ccq baryons with J=1/2 are expected to be lower than the J=3/2 value by roughly 80 MeV. The potential model estimates of Richard et al. [107, 108] are in agreement with these to within 30 MeV. Bagan et al. [109] studied Ξ_{cc} masses using QCD spectral sum rules, and find values some 150 MeV lower.

Lifetimes of *ccq* baryons The Ξ^{++}_{cc} and Ω^{+}_{cc} decays may be dominated by spectator diagrams [105,108,110–115] with lifetimes about 200 fs, roughly half of the D^0 or Ξ^+_c. The main effect for ccq decays is that there are two c quarks rather than only one that may decay. Fleck and Richard [108] suggest that positive interference will occur between the s-quark resulting from c-decay, and the pre-existing s-quark in Ω^+_{cc}. Its lifetime would then be less than that of Ξ^{++}_c. Bjorken [105] and also Fleck and Richard [108] suggest that internal W exchange diagrams in the Ξ^+_{cc} decay could reduce its lifetime to around 100 fs, roughly half the lifetime of the Λ^+_c. Such considerations for charmed hadron lifetimes [110–118] have been extensively discussed. The most recent calculations [119–123] of these lifetimes are based on a QCD expansion in inverse powers of M_c. In the decay of each of the three ground state ccq baryons, only one additional process occurs together with the free c-quark decay (W-exchange or u-quark or s-quark interference). This should allow a much cleaner investigation of these processes and their effects on the lifetimes of ccq baryons. It should be possible to determine the lifetimes of doubly charmed baryons reasonably well even without their full reconstruction. The lifetime data may then have improved statistics compared to the yields given later for completely reconstructed decays. An interesting question is whether the binding of the cc pair leads to an increase of the ccq lifetime. This is discussed in the appendix.

One expects that doubly charmed hadrons should be predominantly produced with small Feynman x_f near threshold in the centre of mass of the colliding hadrons. They would then have sufficient energy in the laboratory frame to be conveniently observed. We give an estimate in the appendix for the lifetime boost γ in the laboratory frame for a ccq baryon that is produced at the centre of rapidity via a high energy hadron beam of momentum p_b^{lab} and energy E_b^{lab}. We obtain $\gamma \approx \sqrt{E_b^{lab}/2M_N}$, where M_N is the mass of the target nucleon. For a CERN experiment with $p_b \approx 400$ GeV/c, one obtains $\gamma \approx 15$, so that the expected ccq energies are near 55 GeV.

Decay modes and branching ratios of *ccq* baryons. The semileptonic and nonleptonic branching ratios of ccq baryons were estimated by Bjorken [105] in 1986. He uses a statistical approach to assign probabilities to different decay modes. He first considers the most significant particles in a decay, those that carry baryon or strangeness number. Pions are then added according to a Poisson distribution. The Bjorken method and other approaches for charm baryon decay modes are described by Klein [124]. Sanchis-Lozano [125] studied semi-leptonic decays of doubly heavy baryons. Savage and Springer [126] examined the flavour SU(3) predictions for the semileptonic and nonleptonic ccq weak decays. They give tables of expected decay modes, where the rates for different modes are given in terms of a few reduced matrix elements of the effective Hamiltonian. In this way, they also find many relationships between decay rates of different modes. Savage and Springer discuss the fact that the SU(3) predictions for the decay of the D-mesons can be understood only by including the effects of final state interactions [127]. They suggest that FSI effects should be much less important for doubly charmed baryons (ccq) compared to charmed mesons.

We describe some decay chains considered by Bjorken [105]. For ccq decays, Bjorken in 1986 estimated [105] that roughly 40% are semi-leptonic and 60% are hadronic. Considering that the D^0 semi-leptonic decay rate [25] is given as 17%, one may instead estimate 17% semi-leptonic and 83% hadronic for ccq decays. Bigi evaluates semileptonic decay rates for c quarks [122,123] in B_c and D^0 in a $1/M_c$ expansion. Such calculations are not available for ccq decays. Bjorken estimates that as many as one-third of the hadronic decays lead to final states with all charged hadrons. We quote from Bjorken's decay rate estimates. For the Ξ_{cc}^{++}, one may have $\Xi_{cc}^{++} \to \Sigma_c^{++} K^- \pi^+$ followed by $\Sigma_c^{++} \to \Lambda_c^+ \pi^+$. A $\Lambda_c^+ \pi^+ K^- \pi^+$ final state was estimated by Bjorken [105] to have a 5% branching ratio. Bjorken also estimated:

$\Xi_{cc}^{++} \to D^0 \Lambda \pi^+ \pi^+$ (5%); $\Xi_{cc}^{++} \to \Xi_c^+ \pi^+$ (1.5%); $\Xi_{cc}^{++} \to \Xi_c^0 \pi^+ \pi^+$ (4.5%);
$\Xi_{cc}^{++} \to D^+ \Lambda \pi^+$ (3%); $\Xi_{cc}^{++} \to \Lambda_c^+ K^- \pi^+ \pi^+$ (5%); $\Omega_{cc}^+ \to \Omega_c^0 \pi^+$ (5%);
$\Omega_{cc}^+ \to \Omega_c^0 \pi^+ \pi^+ \pi^-$ (4%); $\Omega_{cc}^+ \to \Xi^- D^+ \pi^+$ (2%); $\Omega_{cc}^+ \to \Xi_c^+ K^- \pi^+$ (1.5%);
$\Omega_{cc}^+ \to \Xi_c^0 K^- \pi^+ \pi^+$ (4%); $\Xi_{cc}^+ \to \Xi_c^+ \pi^+ \pi^-$ (2%); $\Xi_{cc}^+ \to \Xi_c^0 \pi^+$ (1.5%);
$\Xi_{cc}^+ \to D^+ \Lambda$ (2.5%); $\Xi_{cc}^+ \to \Lambda_c^+ K^- \pi^+$ (3%); $\Xi_{cc}^+ \to D^+ K^- p$ (1%);
$\Omega_{ccc}^{++} \to \Xi_{cc}^{++} K^- \pi^+$ (2.5%); $\Omega_{ccc}^{++} \to \Xi_{cc}^+ K^- \pi^+ \pi^+$ (5%); $\Omega_{ccc}^{++} \to \Omega_{cc}^+ \pi^+$ (5.5%).

Following the decay of one of the two c quarks, the resulting state has typically a singly charmed baryon or meson, which may also decay hadronically or semileptonically. The decay event therefore has either two hadronic, two semi-leptonic, or mixed decays. The experiment must identify the two secondary vertices. For events with no neutrino in the final state, the mass resolution will be superior.

Can one distinguish experimentally between the production of the ccq $1/2^+$ ground and excited 3/2+ states? Considering that the $3/2^+$ to $1/2^+$ mass difference for ccq baryons is expected [106–108] to be roughly 80 MeV, the $3/2^+$ states would decay electromagnetically to the $1/2^+$ states, in a two-body decay. For ccq decay, the coincidence detection of the GeV decay gamma ray, together with the weak decay products of the $1/2^+$ decay, can distinguish $1/2^+$ from $3/2^+$ production. Such a gamma-ray coincidence technique was reported by CERN WA89 [128] in their low statistics observation of the symmetric $1/2^+$ $\Xi_c^{+'}$ charmed baryon, which is expected [106, 129] to decay electromagnetically to the antisymmetric $1/2^+$ Ξ_c^+.

Production of two c-quarks. The production of two c-($\bar{c}$-) quarks can result either in two charmed (anticharmed) hadrons or in a doubly charmed (anti) baryon. For the first case the kinematic correlations between the two charmed hadrons will give insight into the production mechanisms, in particular concerning the question whether these quarks are created in separate processes or come from a single parton-parton interaction. The production of doubly charmed baryons will depend very much on the details of the fragmentation process. The study of their properties - masses and lifetimes - has been discussed above.

If we assume that $\sigma(ccq)/\sigma(cqq) \approx \sigma(c)/\sigma_{tot} \cdot k$ where k describes the probability that both c-quarks are present in the same baryon we can estimate the production cross section of ccq-baryons to be about $10^{-6} - 10^{-7} \cdot \sigma_{tot}$. For details on these estimates, we refer to the Appendix C.

4.1.5 Studies with D-mesons

Using high intensity beams a large sample of a few 10^6 D-mesons can be obtained. They can be used to study rare processes like leptonic decays which are the key to the determination of the charmed meson decay constants.

The measurement of f_D and f_{D_s} via $D \rightarrow \mu\nu$ is extremely difficult due to the poor definition of the D-meson. CLEO has tried to observe the decay $D_s \rightarrow \mu\nu$ tagging the presence of the D_s via the decay photon from the process $D_s^* \rightarrow D\gamma$. A few events have been observed in the missing mass spectrum $M(\mu\gamma)$-μ [130], the branching ratio has been estimated to be about .6%. For D-mesons, the leptonic decay is Cabibbo suppressed and only appears with a branching ratio of about 10^{-4}.

In the proposed set up the decay can be identified as follows: The decay muon from the associated D-meson is identified in the muon wall and extrapolated to the target detector. There it has to join with the track piece stemming from the charged D-meson before its decay. We thus get a decay vertex and the direction of the D-meson. $D_s \rightarrow \mu\nu$ is the most favourable case, since it is not Cabibbo-suppressed. The p_T-spectrum of the muons peaks at 980 MeV/c, i.e. 75 MeV/c (115 MeV/c) beyond the endpoint of the spectrum from $D_s \rightarrow \eta\mu\nu$ ($D^{\pm} \rightarrow K^0\mu\nu$) decay. This feature was exploited in the emulsion experiment WA75 at CERN [131], where a sample of 6 decays with $p_T(\mu) > 900$ MeV/c was observed, from which a value $f_{D_s} = 232 \pm 69$ MeV was obtained. In the proposed setup, $p_T(\mu)$ can be measured with sufficient accuracy for D_s decay tracks of $\geq$5 mm length. Background from other charm decays will be reduced by tagging the D_s through the $D_s^* \rightarrow D_s\gamma$ decay chain.
A measurement of $D^{\pm} \rightarrow \mu\nu$ decay is more difficult, since it is Cabibbo-suppressed. Here the $p_T(\mu)$ peak from the leptonic decay at 932 MeV/c is 67 MeV/c above the endpoint of the $p_T(\mu)$ spectrum from $D^{\pm} \rightarrow K^0\mu\nu$ decay, which has a branching ratio larger by a factor of $\approx$200. The shape of this spectrum can be studied in muonic two-prong $D^0 \rightarrow K^-\mu^+\nu$ decays. Background can be suppressed again by tagging the decay $D^{*\pm} \rightarrow \pi^0 D^{\pm}$.

Other studies of D-mesons include semileptonic decays in a manner described above for baryons, spectroscopy of orbitally and radially excited states and the search for rare or forbidden D-decays. Details on these subjects have been worked out for CHARM2000. The upper limits achievable have to be scaled to the lower beam fluxes foreseen in the first stage of this experiment.

4.1.6 The technical challenge

Measurements of semi-exclusive s.l. decays (reconstruction of a lepton and associated baryon with a common origin) are difficult since the charmed baryons cannot be fully reconstructed (due to the missing neutrino). This leads to enhanced backgrounds which are difficult to understand and are the cause of systematic errors. In order to reduce such backgrounds the detection of the associated charmed meson would be very helpful since it provides a good tag for a charmed baryon. This, however, requires a spectrometer with large solid angle and acceptance extending to the backward hemisphere. Other charmed baryon tagging methods also require large solid angles for low energy decay photons or pions (see chapter A.1 and B.5). For the measurements of inclusive decays of charged charmed baryons it is necessary to observe the decay process itself. This might be achieved if the parent baryon can be tracked and the kink angle between the charmed baryon and the outgoing lepton can be observed. The short flight path of a charmed baryon turns this into an experimental challenge. For neutral charmed baryons, s.l. decays will always leave a charged multi prong vertex and the accuracy and background depend strongly on the vertex quality achieved.

For full reconstruction of *ccq*-baryons we must observe the full decay chain. This involves an intermediate singly charmed hadron (baryon or meson). This decay chain is overlaid by decays of the associated anticharmed hadrons. Clearly, a high efficiency for detecting singly charmed hadrons is mandatory in order to observe such states.

4.1.7 Yields

In the following we describe the yields to be expected for some of the above mentioned processes. At this stage such estimates are crude since in particular the detailed production properties of charmed baryons are not known.

The number of observed charmed particles was estimated using the following assumptions:

- beam rate:	$4 \cdot 10^7$ particles/s
- target thickness:	2.5%
- spill duration:	2.0 s
- $\sigma_{c\bar{c}}$	$\approx$ 10 μbarn/nucleon at a beam momentum of 300 GeV/c
- charm enhancement:	a factor of 3, assuming A^1 dependence of the charm cross–section on Cu/C target
- one day of running:	5000 spills (10^7 $c\bar{c}$ events produced)
- beam time:	100 days of effective running with 100% beam delivery efficiency

From this we derive :

- charm events/interaction:	$1 \cdot 10^{-3}$ in a π-beam and $0.7 \cdot 10^{-3}$ in a proton beam
- total number of interactions	10^{12}
- $c\bar{c}$ pairs produced	$1.0 \cdot 10^9$ in a π-beam and $0.7 \cdot 10^9$ in a proton beam.

In order to estimate the expected number of reconstructed charmed particles we may use results from existing experiments. The Fermilab experiment E791 had a relatively high acceptance for $x_f > -0.1$ and used a weak, unbiasing trigger and observes about one charmed particle per $2 \cdot 10^5$ interactions. The experiment proposed should have a higher efficiency for charm reconstruction than E791 due to better tracking, but may have a lower trigger efficiency.

Using the expected number of interactions and the charm yield of $0.5 \cdot 10^{-5}$ we estimate the expected number of all charmed particles reconstructed to be about $5 \cdot 10^6$.

In the following we describe an estimate based on MC simulation:

Simulation :

In order to estimate the acceptance of the spectrometer and the beam time needed we performed a MC simulation based on the assumptions listed below. Due to the large uncertainties in the production characteristics with proton beams, we mostly rely on the results obtained with π-beams. It should be noted that we may expect higher relative baryon yields operating with protons beams. This, however, is not accounted for in the present rate estimates.

- We assumed relative yields of the weakly decaying charmed particles D^0:D^+:Λ_c^+:D_s^+ of 45%:20%:20%:10% with the remaining 5% going to charmed–strange baryons; we also assumed that the types of two associated particles are not correlated.
- Production of two associated charmed particles was supposed to be uncorrelated in x_F while a correlation in the transverse plane was imposed in accordance with a measurement from WA92 [132].
- x_F distributions of a form of $(1 - |x_F|)^n$ were used for both charmed particles where a value of n=5 was used for most of simulated processes
- The mean transverse momentum for a charmed particle was 1 GeV/c.
- All possible combinations of associated charmed particles were simulated and all known and dominant decays of D-mesons have been included comprising about 90% of the full decay rate; the rate of decays with no additional charged multiplicity was taken into account for the trigger simulation.
- No pattern recognition was performed at this stage but the MC association of hits and tracks was used.
- A charmed particle was considered to be detected if the following conditions were fulfilled: The effective mass has to be reconstructed and charged kaons from the decay have to be identified with the Cherenkov counters. The corresponding efficiency is called ε_{acc} (acceptance). The charged multiplicity should be increased by at least 2 particles in between two trigger counters (see the section on triggering) and the separation between the decay vertex and the interaction point should exceed 1mm, which corresponds to about 8-10σ of the space resolution. The corresponding efficiency is called ε_{sep}. The resulting efficiency calculated is called ε_{MC}.
- The efficiency of pattern recognition was assumed to be 80% per charged track and independent of track parameters.
- We assumed additional losses of ε_{loss}= 50% because of a trigger imperfection in the real experimental environment, or other reasons.

In the following we present the yields of selected processes for each of the different measurements.

- *Energy dependence of the c-quark cross section:* Detection efficiencies were estimated for the following processes: $D^0 \to K^-\pi^+$, $D^0 \to K^-\pi^-\pi^+\pi^+$, $D^+ \to K^-\pi^+\pi^+$, $\Lambda_c^+ \to K^-p\pi^+$and $D_s^+ \to K^-K^+\pi^+$ including the dominant decays to charged particles easier to reconstruct and also decays involving neutral particles: $D^0 \to K^-\pi^+\pi^0$ and $D^0 \to K_S^0\pi^+\pi^-$. The results are summarised in the table 4.1. The yields in a proton beam are expected to be about 30% lower. We assumed a ratio of charm production cross–sections at 300, 200 and 100 GeV of 10/5/1. No estimate was done for 60 GeV. The value of ε_{tot} includes a reconstruction efficiency of 80% per track and a loss of 50% assigned for trigger implementation. An interaction rate of $2 \cdot 10^6$ per spill was assumed (see the section 4.1.3).

  The acceptance practically does not depend of the p_T of charmed particles. The dependence of ε_{acc} on the longitudinal momentum averaged for all processes is shown on figure 4.4. The dependence of ε_{MC} on x_F for beam energies of 300 and 100 GeV is demonstrated on the same figure. The integrated value of ε_{MC} at 300 GeV does not depend strongly on the x_F distribution of charmed particles within a range of the slope of $3 < n < 6$. Associated charmed particles contribute about 15% to ε_{MC} for D-mesons via the trigger efficiency. For Λ_c^+ the corresponding number is about 40%
  The yields are estimated for $c = +1$ charmed particles only. Nearly the same yield should come from the charge conjugated particles. 100 days of effective running at 300 GeV should provide a statistics of about $1 \cdot 10^7$ of all charmed particles reconstructed in the decay modes mentioned. Using the data from table 4.1 we estimated that in about 2% of events with a reconstructed charmed particle the associated charmed particle can be also fully reconstructed. We assumed that strong separation cuts are not needed for the identification of the second particle. Thus we may expect to obtain a sample of about 10^5 of fully reconstructed charmed pairs.

- *semileptonic c-baryon decays:*

  For the moment we are considering the semileptonic decays to muons only. Assuming 100 days of running with 300 GeV/c protons we generate $1.4{\cdot}10^9$ charmed hadrons. About 20% of those may contain a Λ_c^+(or $\overline{\Lambda_c^+}$). Assuming $BR_{s.l.}(\Lambda_c^+) \approx 0.5 \cdot BR_{s.l.}(D^0) \approx 8\%$ [3] we produce

  $$1.4 \cdot 10^9 * 0.2 * BR_{s.l.} = 1.1 \cdot 10^7 \qquad \text{s.l. decays of } \Lambda_c$$

  Semileptonic decays of Λ_c may include various combinations of baryons and mesons in the final state. However, CLEO has measured [87] the ratio of the $\Lambda_c^+ \to \Lambda\mu^+\nu$ decay rate to the full semileptonic rate to muons to be about $B.R._{\Lambda\mu\nu}=0.8$. Thus this decay is the dominant one. Two different schemes are discussed for the isolation of such decays. The first one relies on a clean identification of a Λ_c^+decay outside the target including tagging via Σ_c. We require the decay points to lie at least 2-3 mm downstream of the first multiplicity counter. The second one uses D-tagged events (thus clean) where the $\Sigma_c$can be considered as an additional option.

---

[3] it is generally assumed that hadronic effects although dominating the total width do not strongly effect the semi-leptonic decay widths.

Process production yield BR	Beam Energy GeV	ε_{acc}	ε_{sep}	ε_{MC}	ε_{tot}	Yield per day
$D^0 \rightarrow K^-\pi^+$	300	0.458	0.366	0.168	0.054	10000
0.45	200	0.471	0.263	0.124	0.040	3600
0.04	100	0.299	0.156	0.047	0.015	270
	60	0.177	0.071	0.0126	0.0040	
$D^0 \rightarrow K^-\pi^-\pi^+\pi^+$	300	0.449	0.370	0.166	0.034	12000
0.45	200	0.432	0.284	0.123	0.025	4500
0.081	100	0.229	0.161	0.037	0.0076	280
	60	0.096	0.110	0.011	0.0022	
$D^0 \rightarrow K^-\pi^+\pi^0$	300	0.138	0.352	0.048	0.0155	9600
0.45	200	0.142	0.281	0.040	0.0127	4000
0.138	100	0.084	0.167	0.014	0.0045	280
	60	0.035	0.113	0.0040	0.0013	
$D^0 \rightarrow K^0_S\pi^+\pi^-$	300	0.179	0.429	0.077	0.0157	1300
0.45	200	0.137	0.334	0.046	0.0094	380
0.053×0.34	100	0.057	0.173	0.010	0.0020	16
	60	0.022	0.092	0.0020	0.0004	
$D^+ \rightarrow K^-\pi^+\pi^+$	300	0.471	0.550	0.259	0.066	12000
0.20	200	0.441	0.501	0.221	0.057	5200
0.091	100	0.259	0.421	0.109	0.028	500
	60	0.127	0.306	0.039	0.010	
$\Lambda_c^+ \rightarrow K^-p\pi^+$	300	0.594	0.141	0.084	0.0215	1900
0.20	200	0.588	0.088	0.052	0.0132	600
0.044	100	0.419	0.030	0.0124	0.0032	30
	60	0.245	0.009	0.0021	0.00054	
$D_s^+ \rightarrow K^-K^+\pi^+$	300	0.526	0.376	0.198	0.051	2400
0.10	200	0.505	0.279	0.141	0.036	800
0.048	100	0.314	0.179	0.056	0.0144	70
	60	0.152	0.102	0.016	0.0040	

Table 4.1: Detection efficiencies and estimated yields of charmed particles per day in a pion beam of various energies. The yields in a proton beam are expected to be about 30% lower. We assumed a ratio of charm production cross–sections at 300, 200 and 100 GeV of 10/5/1. No estimate was done for 60 GeV. The value of ε_{tot} includes a reconstruction efficiency of 80% per track and a loss of 50% assigned for trigger implementation. An interaction rate of $2 \cdot 10^6$ per spill was assumed (see the section 4.1.3). The yields given are estimated for $c = +1$ charmed particles. The $c = -1$ yields are expected to be nearly the same.

We have simulated the s.l. decays of $\Lambda_c^+ \rightarrow \Lambda\mu^+\nu$ using a decay distribution described in [88] and a dipole type formfactor for the q^2 dependence. Fig. 4.1.7a depicts the acceptance for Λ_c^+ as a function of momentum. Fig. 4.1.7b shows the q^2 dependence of the integrated acceptance.

a) The efficiency ε_{life} to find a Λ_c^+ 2-3mm downstream of the multiplicity detector is about 2%. The trigger efficiency for such events is given by the trigger efficiency of the associated charmed meson ($\varepsilon_{meson-trig} \approx 25\%$) or by the efficiency of the μ-trigger (a μ is considered as triggerable if $p_\mu \geq 5$ GeV/c). The reconstruction

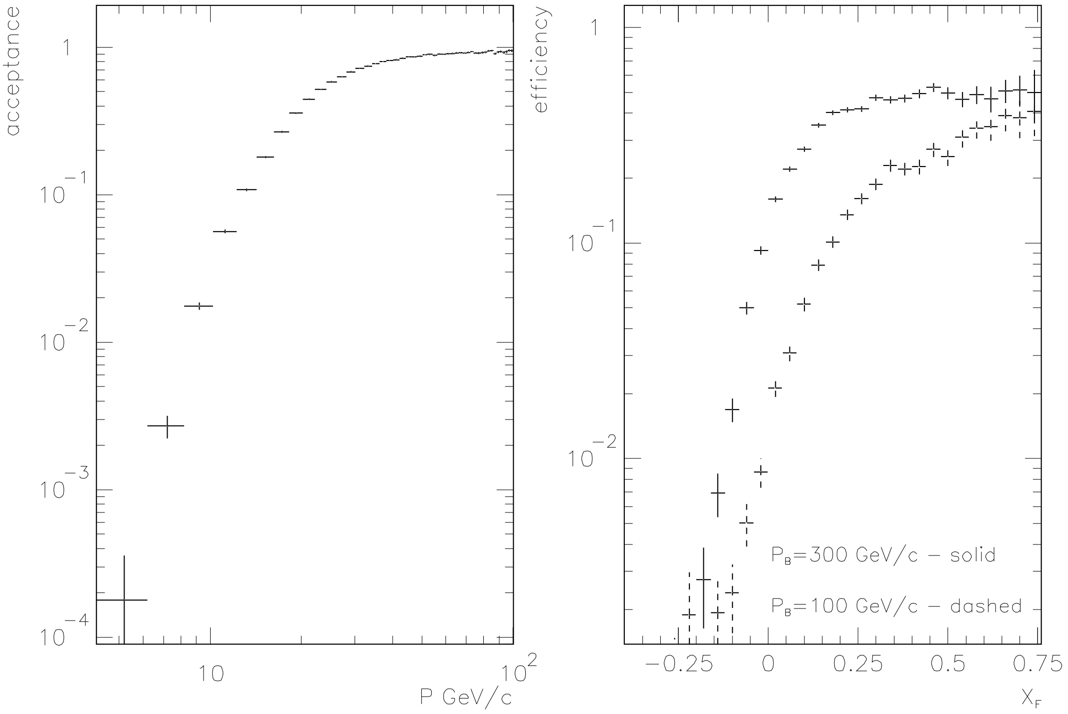

Figure 4.4: The dependence of ε_{acc} on the longitudinal momentum averaged for all processes considered; the dependence of ε_{MC} on the x_F for beam energies of 300 and 100 GeV.

efficiency for Λ_c^+-decays downstream of the multiplicity counter is high ($\varepsilon_{rec} \approx 50\%$). For those events, the loss rate due to the μ-momentum cut is small ($\varepsilon_{muon-trig} = 90\%$). Thus the trigger efficiency is close to 100% mainly supported by the muon. We assume a global track reconstruction efficiency $\varepsilon_{track} = .8$ The number of reconstructible semileptonic decays is thus given by :

$$1.1 \cdot 10^7 * B.R._{\Lambda\mu\nu} * \varepsilon_{life} * \varepsilon_{rec} * \varepsilon_{meson-trig} * B.R._{\Lambda\to p\pi}(= .66) * \varepsilon^3_{track} * 0.5 = 1.3 \cdot 10^4.$$

In order to clean this sample further we can employ the tagging techniques using Σ_c-decays. We assume that about half of Λ_c stem from Σ_c. The tagging efficiency for such decays is large ($\approx 50\%$). Thus we expect :

$$1.3 \cdot 10^4 * .5 * .5 = 3 \cdot 10^3 \text{ useful semileptonic } \Lambda_c \text{ decays.}$$

b) The estimated efficiency for the full reconstruction of charmed D-mesons ε_{tag} is estimated to be about 0.25% (see table 4.1). Using also a μ-trigger we can compensate for trigger inefficiencies contained in ε_{tag} and gain a factor of about 2. Since these events contain a reconstructed charmed particle only a weak separation cut on the Λ_c decay path of about 1mm should be sufficient. The efficiency ε_{rec} for this cut and for the reconstruction of the $\Lambda\mu$-mass is about 10%. Thus about

$$1.1 \cdot 10^7 * B.R._{\Lambda\mu\nu} * 2 \cdot \varepsilon_{tag} * \varepsilon_{rec} * B.R._{\Lambda\to p\pi}(= .66) * \varepsilon^3_{track} * .5 = 700$$

D-tagged decays can be identified.

Clearly, the above estimates depend strongly on the decay length required for the Λ_c^+which can only be estimated using a full simulation including pattern recognition. We think, however, that the assumptions made above are conservative enough to accommodate for additional losses not taken into account at present. These candidates can be used to extract the formfactors in semi-inclusive ($\Lambda_c^+ \to \Lambda\mu$X) Λ_c^+-decays. It should be noted, that less stringent selection criteria have been used by previous experiments to determine formfactors in semileptonic D-decays.

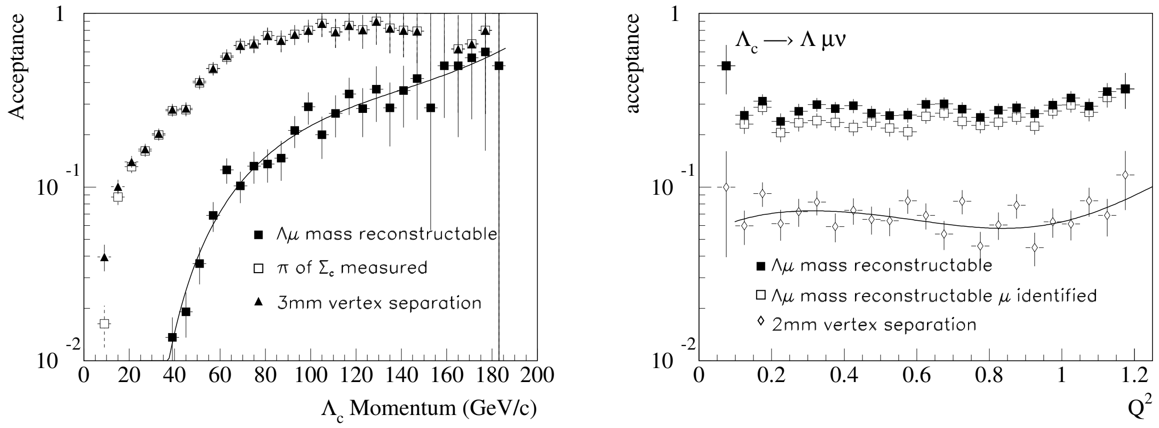

Figure 4.5: Acceptance for semileptonic Λ_c^+ decays as function of the Λ_c^+momentum. Upper curve: Λ and μ are reconstructible, lower curve : Additional requirement for a 2mm separation of production- and Λ_c^+-decay vertex. Also shown are the effects for the detection of the decay π from Σ_c-decays (left) and the inclusion of triggerable $\mu(p_\mu \geq 5$ GeV).

For the determination of inclusive s.l. decay rates we have to require the Λ_c^+-decay point to be about 5 silicon planes downstream of the interaction counter. The acceptance is reduced by a factor 7 as compared to the numbers quoted above for case a) leaving us with about 500 such decays.

- Leptonic D-decays: Out of the $1.4 \cdot 10^9$ charmed hadrons mentioned above we assume that about 20% contain $D^{*\pm}$ of which 30% subsequently decay into $D^\pm \pi^0$:

$$1.4 \cdot 10^9 * 0.2 * B.R._{D^{*\pm} \to D^\pm} = 8.4 \cdot 10^7$$

We assume that 10% of all charmed particles are $D_S^\pm$-mesons and about 50% of them stem from $D_s^{*\pm}$. We also assume a leptonic decay B.R. of $6 \cdot 10^{-3}$. Our starting sample is thus

$$1.4 \cdot 10^9 * 0.1 * 0.5 = 7 \cdot 10^7 \qquad D_S^\pm \text{ from } D_s^*,$$
$$7 \cdot 10^7 * B.R. = 4.2 \cdot \ 10^5 \text{ leptonic decays.}$$

	$D_s^* \to D_s\gamma$ $D_s \to \mu\nu$	$D^{+*} \to D^+\pi^0$ $D^+ \to \mu\nu$
μ in acceptance and $p_\mu > 5GeV/c$	38.2%	41.4%
D track reconstructed (min. 5 planes crossed)	3.3%	12.4%
D tagged with pi^0 or γ resp.	2.4%	3.7%
Kink detectable	0.9%	1.9%

Table 4.2: Efficiencies for detection of leptonic charm meson decays. The values correspond to a simulated π^--beam at 300GeV/c with $d\sigma \sim (1-x_F)^5$. The efficiencies are cumulative. There are cuts of $E >$ 1GeV on the energy of the photons from π^0 and for the tagging photon from D_s^*.

In order to identify these decays we gave to require the $D_S^\pm$ track to traverse at least 5 planes of target silicon before its decay, μ to have a momentum greater than 5 GeV/c and to be reconstructed in the spectrometer and π^0 or the photon from the D* decay to be reconstructed. Additionally, we require a detection of a clear kink between the tracks of D and μ. The efficiencies associated to these requirements are summarised in table 4.2. We should also take into account a reconstruction efficiency per track of 0.8 and a general loss of 50%. We can thus reconstruct

$$4.2 \cdot 10^5 * 0.009 * 0.8 * 0.5 = 1500 \quad \text{muonic } D_S^\pm \text{decays.}$$

It should be noted that only the muonic decay channel has currently been considered. We also have to foresee a μ-trigger efficiency (high for the preselected sample) as well as a number of analysis cuts. In order to reduce the background from semileptonic D-decays, only about 50% of the μ sample will be kept, namely the part decaying with high p_T. We expect a $\mathrm{D}_s \to \mu\nu$ sample of 500-800 events, which should bring the total error on f_{D_s} below 10%.

The estimates for $\mathrm{D}^\pm \to \mu\nu$ are similar since the Cabibbo-suppression of $\mathrm{D}^\pm \to \mu\nu$ is largely compensated for by the larger production cross-section. As mentioned above, stronger cuts on the p_T of μ might be employed. We can expect a sample of 100 or more reconstructed leptonic decays at high $\mathrm{p}_T(\mu)$, which should enable us to extract their number from a fit to the $\mathrm{p}_T(\mu)$ spectrum. From this, f_D could be determined with an error well below 20%.

- *doubly charmed baryons:* For doubly charmed baryons such an estimate is even more difficult. Based on the arguments discussed in the appendix C we estimate $\sigma(ccq)$ to be $\approx 1 - 25$ nb/nucleon, i.e. about 10^{-4}-10^{-3} of the full $c\bar{c}$ cross section.
  Weak decays of ccq include a single charmed particle. We assume that about 10% of these decays could be reconstructed for cases when the daughter charmed particle is reconstructed. Thus the yield of double charmed particles is expected to be about 10^{-4}-10^{-5} of the yield of single charmed particles, yielding about 100-1000 of reconstructed events.
  We may also consider the expected efficiency for the charm events, by comparison to E781 estimates [133]. The E781 efficiencies for cqq decays include a tracking efficiency of 96% per track, a trigger efficiency averaged over x_F of roughly 18%, and

a signal reconstruction efficiency of roughly 50%. The trigger efficiency of the proposed experiment may be higher than in E781, if low x_F events are included. However, the signal reconstruction efficiency is low for low x_F events. The reconstruction efficiency may be lower for double charm events, since they are more complex than single charm events. Yet, using the proposed type of vertex detector multi-vertex events can be reconstructed with good efficiency [134]. Considering all these effects, we assume here an overall average *ccq* reconstruction efficiency of $\varepsilon \simeq 2\%$, about one-quarter the average expected E781 value for *cqq* detection. The expected yield is then 150 charm events for each pb per nucleon of effective cross section (for nucleons in A $\approx$ 64 nuclei), where $\sigma_{eff} = \sigma BB\varepsilon$. Here ε is the overall efficiency for the experiment. For σBB $\sim$ 20-500 pb/N, one has $\sigma_{eff} < 0.4 - 10.\ pb/N$, and therefore an upper limit of N(ccq) $\approx$ 60-1500 events for this experiment. This is the maximum total expected yield for ccu,ccd,ccs production for ground and excited states. It should be noted, however, that lifetime measurements can also be performed using a *ccq*-decay chain involving a semi-leptonic *cqq*-baryon decay. In addition, the production of a ccq state will probably be accompanied by two associated $\overline{D}$-mesons, which will increase the trigger efficiency considerably. Thus, the number of useful events could be larger.

The rate of events where two uncorrelated *c*-quarks are produced, should be larger by about a factor 10.

Summary: Table 4.3 summarises the estimated yields for different processes assuming 100 days of effective data taking at maximal beam intensity.

Process	beam	energy	estimated yield	running time [days]
c-production	π	100 GeV	24,000	10
c-production	proton	100 GeV	18,000	10
c-production	π	200 GeV	200,000	5
c-production	proton	200 GeV	140,000	5
c-production	Kaon	200 GeV	15,000	5, with π
c-production	π	300 GeV	500,000	5
total:			about $0.9 \cdot 10^6$	
c-production	proton	300 GeV	$4.5 \cdot 10^6$	65
c-baryon s.l. decays	proton	300 GeV	3000	65
cc-baryons	proton	300 GeV	25-250	65
$D_S^{\pm}$-leptonic decays	proton	300 GeV	500	65
D-leptonic decays	proton	300 GeV	100	65
c or $\bar{c}$-total:			about $5.4 \cdot 10^6$	

Table 4.3: Summary of estimated yields for the different measurements with charmed hadrons

Competition

The main advantage of the experiment proposed in comparison with other experiments in the field is a very high statistics of charmed particles (about $1 \cdot 10^7$) reconstructed in combination with a very high spatial resolution for secondary vertices (about $100\mu m$ longitudinally) of the vertex detector which also allows to observe tracks of charged charmed particles before their decays. A comparison with fixed target experiments is straightforward while a comparison with collider experiments in e^+e^- is less clear since possible systematic errors and backgrounds are different. In the following we present a list of experiments which might do part of the proposed program before a new CERN experiment can be established.

Fixed target experiments in hadron beams

- E791
  This pion-beam experiment at 500 GeV/c has accumulated about 40 times as many interactions as WA89. The expected sample of charmed particles reconstructed is about $2\cdot 10^5$. The experiment might contribute to charmed baryon decay studies with a yet unknown quality/quantity. The spatial resolution of the vertex detector was about 10 times worse than in the experiment proposed. The experiment proposed should have an advantage of a higher statistics and better vertex resolution.

- WA92
  The main goal of this pion-beam experiment at 350 GeV/c was to observe semileptonic decays of beauty particles, but it has detected a considerable amount of charmed particles as well. The vertex detector used was comparable to the one proposed, though a high spatial resolution was provided in one projection only. The expected sample of charmed particles fully reconstructed is about $2\cdot 10^4$. Since the experiment used a muon trigger it may contribute to the studies of semileptonic and leptonic decay modes of charmed particles. The new experiment should have a much higher statistics.

- SELEX
  This is by far the most important competition in the charmed–strange baryon sector. Scheduled since many years, this Fermilab experiment will probably run in 1996-1998 for about 15 months. It is similar to the WA89 experiment with a higher beam energy (which is an advantage unless some leading particle effects are more prominent at lower energies), an acceptance down to almost $x_F=0$ due to the use of a triple magnetic spectrometer, and a higher beam flux. The higher flux is obtained in part by the higher duty cycle of the Fermilab Tevatron and in part by the higher proton flux possible in the high intensity area at FNAL. The DAQ relies on a software charm trigger. Assuming that the trigger will provide the efficiency planned one may expect a yield of charmed particles of about $1\cdot 10^6$, which is 10 times lower than in the experiment proposed, however the yields of charmed–strange baryons may be comparable. The vertex detector does not provide tracks for charmed particles and has a resolution 4-10 times worse than the vertex detector proposed. Thus the experiment proposed should gain a higher statistics for non–strange charmed particles and also a much better ability to study short–living particles and not fully reconstructible decay modes.

  It is not clear how well Primakoff physics can actually be addressed by SELEX as this requires a non-trivial trigger to be installed and a dedicated set up.

- HERA-B
  The HERA-B experiment is designed to detected as many B-meson decays as possible using 800 GeV protons from the HERA proton beam halo impinging on a wire target within the ring. Although much charm will be produced in these interactions it is not yet clear how well it can be used as their trigger will be highly selective for B-meson decays and at the current stage charm physics will only constitute a by-product.

None of these experiments will study the energy dependence of the cross–section of charm hadroproduction.

Fixed target experiments in photon beams

- E831
  The FNAL tagged-photon beam experiment has been approved to run again for the next fixed target period in 1996 with an upgraded detector and DAQ. The predecessor experiment E687 was very successful in all sectors of charm studies, including charmed and charmed-strange baryons. E831 is planning to gain a statistics of about $1 \cdot 10^6$ charmed particles. The new experiment should gain a higher statistics and also should provide a superior vertex resolution.

Collider experiments

- CLEO
  This experiment clearly will be very competitive for charm studies. The apparatus has undergone a major upgrade and has shown in particular an excellent photon reconstruction capability. From 1999 onwards CLEO III will run with a five-fold increase in luminosity. Obviously, CLEO will produce large numbers of charm particles. For instance, they have already reported a sample of 40 observed decays $D_s \rightarrow \mu\nu$. After 1999 they will have almost one order of magnitude more events per year, and thus be on the same level as the proposed experiment. The latter, however, will have the possibility to observe the D and D_S decay tracks directly, which will allow full kinematic reconstruction and thus provide a powerful means of background rejection. CLEO has already observed the Λ_c^+ in many final states and have seen clear signals from two Λ_c^+-resonances. They have also obtained interesting results for semileptonic decays of Λ_c^+, but their "tagging" technique leads to systematic errors very different from the ones expected in a fixed target experiment. In contrast to fixed target experiments, however, they have not yet observed the Ω_c^0.

- SLAC-B
  This e^+e^- collider experiment [135] is scheduled to run from the beginning of 1999. The main physics issue is CP violation in the B-system. However, they will also use the expected large sample of D-mesons ($\approx 10^7$ of each species) to perform precision measurements of semileptonic D-decays and their form factor, measurements of the D-decay constants f_D and f_{D_s} and e search for possible direct CP violation in the D-system. Like CLEO III they will also constitute a competition in the non–strange charmed baryon sector.

4.2 STUDY OF GLUONIC SYSTEMS

Quantum Chromodynamics (QCD), the theory of the strong interactions, is certainly most successful as its viability has been confirmed by many experiments. However, one of its most striking predictions – the existence of new classes of non-$q\bar{q}$ mesons – still awaits definite experimental confirmation: Glueballs ought to exist [136], objects composed entirely of valence gluons, as should hybrids [137], states in which a color-octet $\bar{q}q$ pair is neutralized in color by a constituent gluon.

A major difficulty in the search for glueballs and hybrids arises from the proliferation of mesonic states with $q\bar{q}$ structure in the mass range in which states with constituent glue are expected. The quark model certainly helps in the identification of $q\bar{q}$ states. It has proven unexpectedly successful in the interpretation of the mass-spectrum of mesons and their decay properties [138]. The main features of all mesons, from those comprising the light-quark sector to the members of heavy-quark systems, can be explained within a comprehensive description based on a simple ansatz including relativistic effects as well as spin-spin and spin-orbit interactions. Unfortunately, these achievements are of only limited help in the glueball search since, up to now, the light scalar and pseudoscalar mesons have resisted an unambiguous understanding. Yet it is just here that the lowest-lying glueballs are expected. The proper classification, therefore, of the scalar and pseudoscalar mesons demands the highest of research priority and dedication.

From an experimental point of view, the spectroscopy of scalar and pseudoscalar states is particularly difficult, since higher-spin mesons are often produced more abundantly than are states with $J = 0$, and scalar contributions remain unrevealed. The situation has improved considerably in recent years due to the efforts of experimental groups working at CERN; the present collaboration comprises a strong fraction of physicists from this community. But an unambigous answer to the question: "do glueballs exist and what is their mass spectrum" has not yet been given.

It must be stressed that light-meson spectroscopy is a broad field. Many states and many decay modes of conventional high-mass states are not known; we estimate that a much more profound knowledge of the field is required before hybrid states can be identified and differentiated from four-quark states. The proposed experiment will make many significant contributions to this field. Here, we highlight only the program aiming at an unambiguous identification of glueballs.

4.2.1 The existence and signatures of glueballs

Considerable progress has been made in the understanding of the anticipated properties of glueballs. Lattice QCD calculations now not only predict that a 0^{++} glueball should exist, but also that it should be observed with a width of about 100-150 MeV. The mass estimate for the 0^{++} glueball still varies according to the results of different groups and ranges from 1500 to 1800 MeV. The masses of the 2^{++} and 0^{-+} glueballs are estimated to be 2360 and 2300 MeV, respectively.

Glueballs can be identified by their production characteristics, their decay patterns and their relations to other mesons carrying the same spin and parity. All three signatures have to be considered in a consistent way before an identification as a glueball becomes secure. Production of glueballs should be enriched in gluon-rich channels such as:

- Pomeron-Pomeron scattering, since the Pomeron is an object which can be described as a multi-gluon state. The Pomeron-Pomeron scattering contribution is enriched in central production.

- Proton-antiproton annihilation; the annihilation region of quarks and antiquarks is a source of gluons where glueballs and hybrids could be produced.
- J/ψ decays are believed to be highly glue-rich, both in hadronic and radiative decays.

The decay pattern of a mesonic state may reveal its glueball nature or a strong glueball component. The discussion of a glue component in the η and η' wave functions [139] is the best-known example for this approach. We note that:

- Glueballs are predicted to be flavor blind, i.e. their decay branching ratios should not be dependent on the quark composition of the final-state mesons, once phase space effects have been taken into account. However, flavor symmetry may be broken due to mixing with neighboring $q\bar{q}$ mesons having the same J^{PC}.
- Glueballs may decay preferentially into states containing large glue components or large SU(3) singlet components like the η' or the η.

A glueball is likely to be embedded in a $q\bar{q}$ nonet of the same J^{PC}. If mixing is possible, identification of all three states – the glueball and the two near-by isoscalar mesons – is required in order to constrain the mixing scheme. The determination of the mixing scheme of three states with $q\bar{q}$-, $s\bar{s}$- and glueball-contents would provide strong evidence that the search for a glueball has been completed successfully.

4.2.2 Status of the search for glueballs

The GAMS collaboration was the first to demonstrate the discovery potential of a detector specialized in neutral-particle detection. Many new states were observed; of outstanding importance was the discovery of the $f_0(1590)$ with anomalous decay properties [140] which identified it as a prime glueball candidate. A state at a similar mass, 1500 MeV, and with similar decay properties was found by Crystal Barrel at LEAR to decay into $\pi^0\pi^0$ [141], $\pi^+\pi^-$, $\eta\eta$ [142], $\eta\eta'$ [143], and 4π (with additional $\sigma\sigma$, $\pi\pi(1300)$ contributions) [144] and into $K\bar{K}$ [145]. The small rate of the $K\bar{K}$ decay mode excludes the possibility that the $f_0(1500)$ is the 1^3P_0 mainly-$s\bar{s}$ state which might otherwise be the most natural interpretation for a meson at this mass. The WA91 collaboration reported evidence of a scalar state at 1454 MeV and a width of 54 MeV decaying into 4π [146]; a reanalysis [147] has demonstrated that the data are also compatible with the Crystal Barrel state, provided interferences are allowed for.

For the moment we assume the three states, $f_0(1454)$, $f_0(1500)$ and $f_0(1590)$ to be the same object which we call $f_0(1500)$. In a recent paper, Amsler and Close have shown that $f_0(1500)$ is incompatible with being the member of the scalar $q\bar{q}$ nonet [148]. This statement is true independent of the nonet mixing angle, the only assumption being the validity of the OZI rule. This state is therefore a prime candidate for the ground state of the glueball spectrum. Instanton induced interactions violate the OZI rule; the possibility can therefore not yet be excluded that the $f_0(980)$ and $f_0(1500)$ are the flavor-singlet and -octet states of the 1^3P_0 nonet [149] and that OZI violation leads to the anomalous decay pattern of the $f_0(1500)$ [150]. Such an interpretation would exclude the existence of a glueball in this mass range. The existence or non-existence of a "narrow" $f_0(1370)$

[144, 151–153] (with a width of $\sim$ 300 MeV) plays a decisive role in the interpretation of the scalar mass spectrum. Of course, the $f_0(1370)$ and the $f_0(1500)$ must be seen in the same experiment and in the same data sets. In addition the $a_0(1450)$ observed by Crystal barrel must be confirmed as the isovector state in the scalar nonet and the still missing $s\bar{s}$ scalar identified. This requires high statistics data in $K\bar{K}$ production between 1000 and 1500 MeV.

With the $f_0(1500)$ assigned to the glueball ground-state we expect, from lattice gauge calculations, which predict a tensor to scalar glueball mass ratio 1.5 ± 0.1 [154], a tensor glueball with a mass of 2.2 to 2.3 GeV. It is exciting that GAMS does, indeed, observe a good candidate having a mass of 2175 MeV, produced in central production at 300 and 450 GeV, [155] and decaying into $\eta\eta$. The problem is that the total statistics in that mass range amounts to less than 100 events. So, even the spin-parity analysis is not unambiguous and rare decay modes are unaccessible.

There are several further intriguing observations in light meson spectroscopy which have been discussed in the glueball context. The $\Theta(1690)$ – seen in radiative J/ψ decays in its $\eta\eta$, K_sK_s and $\rho\rho$ decay modes – was originally suggested to be a tensor glueball but its spin is also compatible with zero [156]. Central production data favor spin 2 ; the clear $\eta\eta$ resonances at 1500, 1750 and 2100 MeV seen in $p\bar{p}$ annihilation in flight at Fermilab [157] motivated a reanalysis of radiative J/ψ decays into 4π, where similar peaks had been observed. It was shown that the data are fully compatible with all three states having $I^G(J^{PC}) = 0^+(0^{++})$. The production rates – as observed in 4π – are similar but, clearly, since three scalar glueballs in a narrow mass gap are unlikely, one has to state that the situation needs clarification. This statement also holds true for the $\xi(2220)$ with its unusually narrow width [25].

A question which still remains open, is that of the $\iota(1440)$. This state was first reported as the E-meson in $\bar{p}p$ annihilation at rest [158] and then discussed as a first glueball candidate (glueball number ι) due to its large production rate in radiative J/ψ decays [159]. Later experiments suggested that the $\iota(1440)$ might be split into two states, an $\eta(1400)$ and an $\eta(1500)$. The Obelix and Crystal Barrel experiments have recently confirmed these findings: in the $K\bar{K}\pi$ channel two pseudoscalar states are seen , in the $\eta\pi\pi$ channel there is only one state at 1400 MeV [160]. A further state with about the same mass and width but quantum numbers $I^G(J^{PC}) = 0^+(1^{++})$ and also referred to as the E-meson was identified [25] and is now called the E/$f_1(1420)$.

In spite of its long history, the E/$\iota(1440)$/$f_1(1420)$ puzzle is far from being resolved: the 1^3P_1 nonet is rather well understood with $a_1(1260), f_1(1285), f_1(1510), K_{1A}$ as members. Possibly, the E/$f_1(1420)$ is composed of a $K\bar{K}$ center and an orbiting pion forming K^* and $\bar{K}^*$ [161]. The pseudoscalar sector is much less clear: the Particle Data Group assigns the states $\pi(1300), \eta(1295)$, ?? , $K(1460)$ to the 2^1S_0 nonet; the two states $\pi(1300)$ and $\eta(1295)$ suggest ideal mixing and that the $s\bar{s}$ state should have a mass of about 1500 MeV. This matches with the proposed splitting of the E/$\iota(1440)$ into an $\eta(1400)$ and an $\eta(1500)$ but, if this is indeed the case, what is the nature of the $\eta(1400)$? Its large rate in radiative J/ψ suggests a gluonic nature; lattice gauge calculations can no longer accommodate a glueball at such a low mass.

4.2.3 Study of glueballs within the scope of this proposal

The main lesson that has been learned from previous experiments is that the identification of glueballs requires complete information on all neighboring states, in particular:

- Availability of high-statistics data samples
- Reconstruction of final states containing both neutral and charged particles
- Observation of the same meson in many different channels
- Production of mesons in different reactions

The detector proposed here is ideally suited to satify all of the above requirements. In particular we plan to extract the following final states from data on central production, on nondiffractive scattering and on Coulomb excitation (using a high-Z nuclear target): $\pi^0\pi^0, \eta\eta, \eta\eta', 4\pi^0, K^+K^-, K_s^0K_s^0$, amongst many others. The data will allow us to verify the existence and identity of the $f_0(1500)$ and $f_0(1590)$, to determine the decay branching ratios and to compare them with Crystal Barrel and GAMS results, and to extend the spectroscopy to 2.5 GeV. Hence the states at 1500, 1750 and 2100 MeV and the tensor glueball, if it exists in the predicted mass range, would be observed in the same final states and under identical conditions. The three different running conditions – central production, nondiffractive scattering and Coulomb excitation – may be used to select, preferentially, states with a large glue content or mesons with $\bar{q}q$ structure; glueballs should be absent in data produced by Coulomb excitation. We anticipate that the pseudoscalar glueball may be seen best in the channel $(\pi\pi)_{S-wave}\eta'$ due to large couplings of glue to $(\pi\pi)_{S-wave}$ and to η' while conventional $\bar{q}q$ mesons will prefer to decay into $(\pi\pi)_{S-wave}\eta$.

The performance of the proposed detector is illustrated by comparing Monte Carlo simulations with the data obtained by the WA102 experiment, running at the CERN Ω-spectrometer. The WA102 experiment was conceived to search for non-$\bar{q}q$ mesons centrally produced in proton proton interactions at 450 GeV/c. The setup was designed to study reactions of the type

$$pp \rightarrow p_{fast}X^0p_{slow} \tag{4.1}$$

where X^0 represents the object that is presumed to be produced by a double pomeron exchange process. The detector is optimized for the detection of X^0 decays into $\eta\eta$ and $\eta\eta'$, allowing all possible neutral and mixed decay modes of the η and η'.

The most essential differences between the proposed setup scheme and that used in WA102, in the way in which they affect the reaction (1) detection efficiency, are:

- The large angle spectrometer will provide a factor of 5 greater geometrical acceptance ($\approx$ 100%) for the slow particles, when compared to that of WA102 ($\approx$ 20%). That gain will be partly offset by the loss in the the acceptance for the X^0 decay products due to the larger distance between the target and the first tracking device (a factor $\approx$ 30%).
- The beam intensity for the proposed experiment will be a factor of 10 greater than the limit imposed by the Ω-spectrometer.
- The double spectrometer scheme will provide a good mass and angular resolution for the X^0 decay products in the full energy range. This, in turn, will significantly improve the quality of the spin analysis.

Once the central production program will utilize a pion beam of 300 GeV/c, rather than the proton beam of 450 GeV/c used by WA102, the Double Pomeron cross-section energy dependence [162] should be taking into account. The ratio of the reaction (1) detection efficiency for the proposed setup to that of WA102 is estimated to be ≈ 12 This number includes all factors mentioned above and a pessimistic assumption for the tracking and photon reconstruction efficiency of 50%.

We expect to acquire, in 2 "SPS years" (2 × 120 days) of running, 100000 $\eta\eta$, 30000 $\eta\eta'$ and 15000 $\eta'\eta'$ decays, fully reconstructed. Statistics similar to those obtained for the case of $\eta\eta$ are expected for objects decaying into the $\pi\pi$ and KK channels.

4.2.4 Production of mesons through diffractive processes

Interesting in the context of the search for exotics (such as glueballs and hybrids) is the study of diffractively produced meson systems through the use of pion and kaon interactions with a nuclear target. Pomeron exchange would be a process complementary to central production in the quantum numbers of the produced states – $I = 1$ with $J^P = 0^-, 1^+$, and so on. States with strong gluon coupling can be produced by means of such an exchange, leading to glueballs and ordinary mesons as their decay products. Objects with other quantum numbers are accessible through formation processes. So far such experiments have been performed only at energies below 40 GeV with moderately intense beams of $10^6\pi$ /spill.

A new generation experiment such as that proposed – using a high-intensity pion beam of momentum 200-300 GeV/c has the following advantages:

- The diffractive cross section remains rather constant as a function of energy, in contrast to those for concurrent processes (e.g. charge-exchange) which drop with increasing energy. This allows a more effective rejection of background. One example of such a background reaction to the diffractive $\pi^+\pi^-\pi^-$ production is the coherent production of $\omega\pi^-$ where the π^0 is not seen by the detector.

- Operating with higher beam energies, a higher mass range (3 GeV) is accessible with reasonable sensitivity than is currently the case [163],(see fig.4.6a.) An object (possibly hybrid) of mass 2.5 GeV could be a source of both 0^{++} and 2^{++} glueballs.

- The acceptance of the two-magnet spectrometer is large up to this higher mass in the full range of the kinematical variables. This is crucial for the study of high angular momentum states.

- The γ energy resolution of the electromagnetic calorimeter is better in the high energy range, resulting in superior mass resolution. Furthermore, the losses of γ's which lie below calorimetry threshold are fewer. Both of these factors lead to higher efficiency and an enhanced signal/background ratio for channels with neutral mesons.

- With a total diffractive cross section of about 1 mb (per nucleon), a fast DAQ, an intense beam and a minimum bias trigger (with a veto on nucleon excitation and track multiplicity, yielding a by a reduction factor of 20) an event sample with 10 times higher statistics than that currently available can be expected to be recorded during a 3 month run period. For a rare system such as $\eta\eta\pi^-$ [164], (fig. 4.6b) with 4 γ's in the final state, an additional gain of the order of 2-3 can be expected (see above). An even greater gain should be available through the use of a more specialized trigger.

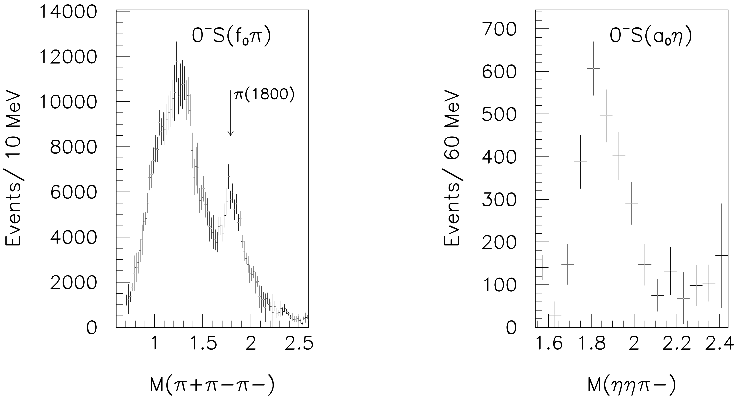

Figure 4.6: 0^- wave intensities in diffractively produced systems : a)$\pi^+\pi^-\pi^-$ b)$\eta\eta\pi^-$.

- Utilising the 2-3 % kaon fraction in the pion beam, we will collect a competitive high statistics event sample even in the strange sector, with the additional advantages of both secondary particle identification and neutral particle detection.

A program studying diffractive production poses no additional requirements to the design of the apparatus. It can be fulfilled with the use of a second trigger, running in parallel.

4.3 HADRONIC STRUCTURE WITH VIRTUAL PHOTONS

The study of hadron structure has gained considerable new interest owing to progress in the description of non-perturbative QCD. It is generally believed now that spontaneously broken chiral symmetry is essential for the existence of particles and nuclei. It is therefore important to check the predictions of the QCD chiral Lagrangian in the laboratory. Tests of quantum chromodynamics in low energy processes [165, 166] require checking QCD predictions for the decay rates and interactions of the nine pseudoscalar mesons (the small-mass Goldstone bosons in the approximation that quark masses and the chiral anomaly are neglected). Rigorous predictions were made using an effective field theory, with a QCD chiral Lagrangian which unambiguously follows from the assumption of spontaneously broken chiral symmetry. A low-energy expansion of the effective (Weinberg) Lagrangian establishes unambiguous relationships between different processes. The effective chiral Lagrangian includes a chiral anomaly (Wess–Zumino–Witten) term [167,168]; which provides the mechanism for the generation of the large mass of the η'. Experimental investigations to determine how well chiral perturbation theory works in the normal [165,169] and anomalous parity sectors [168,170,171] seem to be very important. Thereby we test fundamental predictions of QCD. In particular, chiral perturbation theory now allows one to make definite predictions for a number of measurable quantities such as pion and kaon polarizabilities, and chiral axial anomaly amplitudes.

PRIMAKOFF REACTIONS. Using high energy π or kaon or Sigma beams, we can make important measurements using the well-tested Primakoff effect. This effect relates processes involving real photon interactions to production cross sections involving the exchange of virtual photons. All studies will make use our spectrometers to measure final-state hadrons (pions, Sigmas, kaons) and gamma rays. We cite two reasons why research on gamma-hadron interactions now plays an important role in studies of hadron structure. First, progress in experimental techniques now makes these experiments feasible. Second, hadron-photon interactions supply information on the distribution of quark configurations in hadronic matter, via the photon interactions with the electric charges of quark fields.

Several physics aspects can be addressed by studying such small-angle radiative scattering of hadrons. In general, Primakoff experiments require high Z targets, low mass tracking detectors, good charged-particle momentum resolution and high resolution (spatial and energy) electromagnetic calorimetry.

As part of the trigger for Primakoff reactions, it is important to use a veto system around the target to reject events with an excitation and break-up of nuclei. Such a veto requirement is also important for studies of coherent diffractive cross sections. To the extent that the triggers are similar to each other, it will be possible to have parallel running of these two programs. For both diffractive and Primakoff studies, it would also be of interest to use an active silicon target, to guarantee that the target nucleus recoils coherently. Without the use of a veto system, delta rays can also be troublesome. One may get 10% knock-on electrons with energies of several MeV leaving the target, events which may be rejected with a veto scintillator.

π and Σ and kaon polarizabilities. Primakoff scattering of beam particles from a high-Z nucleus accompanied by the emission of photons (bremsstrahlung) can be used to test the structure of these particles. For the hadron polarizability, the γ hadron scattering can be measured with 200-400 GeV hadrons via radiative pion scattering in the nuclear Coulomb field (hadron + Z $\rightarrow$ hadron + Z + γ), where the incident hadron undergoes Compton scattering from a virtual photon in the Coulomb field of a nucleus of atomic number Z, and the final gamma ray and hadron are detected in coincidence. For Compton scattering on composite systems the expression for the cross section has to be modified to take into account their internal structure. These additional terms depend on the electric and magnetic polarizabilities. The magnitude of the polarizability tests the response of the particle's charge distribution to an exposure of a high electromagnetic field. Naively one expects larger values of the polarizability for systems made from quarks with opposite charge (like $\Sigma^+(uus)$) as compared to those made from equal charge quarks (like $\Sigma^-(dds)$) as the electromagnetic fields exert forces in opposite directions for Σ^+ and in the same direction for Σ^- [172, 173]. We will measure pion and Sigma and kaon polarizabilities. Compton scattering is also of interest [174] for higher energy gamma rays, higher than allowed for polarizability studies.

Electric and magnetic polarizabilities are described by two terms each, one term reflecting the action of the electromagnetic field on the charge and magnetic moment of individual partons and the other term being a form factor of the composite system. From a study of the magnetic moments of Σ^- and Σ^+ we can infer that the main difference between these two isospin partners comes mainly from the intrinsic structure and less from a global form factor. Various predictions have been made for the polarizabilities of neutron, proton and pion, but little work has been done for hyperons or the kaon.

For the γ-π interaction at low energy, chiral perturbation theory establishes a relationship [165,175] between the pion axial vector and vector coupling constants and the pion polarizabilities. The experimental ratio of these coupling constants leads [165] to $\bar{\alpha}_\pi = -\bar{\beta}_\pi = 2.7 \pm 0.4$, expressed in units of 10^{-43} cm^3. Antipov et al. [176] measured the $\gamma\pi$ scattering with 40-GeV pions at Serpukhov. This reaction is equivalent to $\gamma + \pi \rightarrow \gamma + \pi$ scattering for a laboratory gamma ray of 200-1000 MeV incident on a target pion at rest. It is otherwise impossible to carry out experiments on a pion target. The Sigma and kaon polarizability measurements proceed similarly. A detailed description of this physics has been given at the recent MIT Chiral Dynamics Workshop [169,177–180].

The pion electric polarizability $\bar{\alpha_\pi}$ was deduced in this low statistics experiment ($\sim$ 7000 events) to be $\bar{\alpha}_\pi = -\bar{\beta}_\pi = 6.8 \pm 1.4 \pm 1.2$. The data, not counting the large error bars, are some three times larger than the chiral symmetry prediction. Higher quality pion polarizability data are therefore needed for a serious quantitative test of the QCD chiral Lagrangian.

The Kaon polarizabilities are of complementary importance to pion polarizabilities for chiral symmetry tests away from the chiral limit. To date, there are no kaon data. For kaon polarizabilities, kinematics reduces [180] the polarizabilities compared to the pion by a factor $m_K {F_K}^2 / m_\pi {F_\pi}^2 = 5.4$, where the F terms are the pion and kaon decay constants. Until now, only an upper limit [181] at 90% confidence was measured (via energy shifts in heavy Z kaonic atoms) for the K^-, with $\alpha_{\bar{K}^-} \leq (200.0) \times 10^{-43} cm^3$. The Kaon beam energy must be low, to have good Kaon PID. With a positive beam energy, one obtains data simultaneously for protons, kaons, pions.

We consider the uncertainties achievable for the pion polarizabilities, based on Monte Carlo simulations. Estimates for the kaon and Sigma cases are made in the same way. We will achieve a significant improvement in statistics compared to Antipov's 7000 events. The improvement in statistics will allow binning the data in fine steps for the incident virtual photon energy E(V) in the incident pion rest frame; which will be valuable for reducing systematic errors.

Σ and pion and kaon Radiative Transitions. In addition to polarizability measurements, one may also study radiative transitions of the incident hadron to higher excited hadron states. This is possible for pion, kaon, proton, hyperon beams. These widths are also related by theory to the polarizabilities.

Measurements of the Primakoff production of hyperon resonances (spin 3/2 states) which proceed by spin flip of the incoming spin 1/2 hyperon are easier to interpret than polarizabilities. The cross section constitutes a complementary measurement of the hyperon's magnetic moment. The observed pattern of static magnetic moments in the baryon octet cannot exactly be described by any model. Small but significant deviations from the predictions occur for the Σ^+ and Ξ^-. Different cross sections are for example expected for the Primakoff production of Σ^{-*} by Σ^- and Σ^{+*} by Σ^+. This may be used to single out the role of the strange quark concerning the magnetic moment in the various hyperons. If polarized hyperon beams are available one can disentangle the M1/E2 contributions in this process by analysing asymmetries in the final states. In the SU(3) symmetry limit, the magnetic moments of the d and s quarks are equal. However, an analysis [172] shows that the strange quark contribution to the magnetic moment of the Σ is suppressed by an order of magnitude compared to that of the d-quark in the proton or the s-quark in the Lambda.

In a description of SU(3) symmetry breaking in the Σ^- to Σ^{*-} transition, the ratio of M1 decay widths for the Σ^- and proton can be estimated to be [172]:

$$\frac{\Gamma(\Sigma \to \Sigma^{*-})}{\Gamma(p \to \Delta^+)} \approx \frac{1}{9}(1 - \frac{\mu_s}{\mu_d})^2 \ .$$

Here μ_s and μ_d are empirical magnetic moments of s and d quarks. Within the validity of the constituent quark model the size of the Σ^- M1 transition determines directly the relative magnitudes of s- and d-quark magnetic moments.

New high-statistics data are also needed for radiative transitions [182–186] leading from the pion to the ρ, to the $a_1(1260)$, and to the $a_2(1320)$; and similarly for kaon transitions. Data for Kaon radiative transitions are very scarce [187], and such data would be particularly valuable. These radiative transition widths were studied in the past, but there are large uncertainties in the results, so that independent data would still be of value. For $\rho \to \pi\gamma$, the widths obtained [182–184] range from 60. to 81. KeV. For $a_1(1260) \to \pi\gamma$, the width given [185] is $\Gamma = 640. \pm 246.$ KeV, and for $a_2(1260) \to \pi\gamma$, the width given [186] is $\Gamma = 295 \pm$ 60 KeV. Xiong, Shuryak, and Brown [188] and Holstein [165] show that the pion polarizability and this width are related. A remeasurement of the $a_1(1260)$ width and of the pion polarizability will allow checking the consistency of their expected relationship. There is a clear need for new and improved radiative transition data to help check unambiguous predictions of chiral symmetry, and to increase our understanding of the magnetic moments of hyperons.

We consider now the cross section estimates for the Σ radiative transition experiments. Similar estimates can be made for the other transitions. We first give the signal and background estimates for a C^{12} target, and then extrapolate to Pb. To approximate real pion Compton scattering, the virtual photon must be almost real; corresponding to $t < 6.0 \times 10^{-3}(GeV/c)^2$ [169]. We compare the Σ expected cross sections to data and calculations [182] for the $\pi \to \rho$ radiative transition measurement at 156 GeV on a C^{12} target. For the ρ to π transition, for this t-interval, the Primakoff cross section was 2.4 μb. and the strong background cross section was 0.75 μb, which gives a signal to background ratio of 3. At 300 GeV, the hadronic cross section falls as 1/E (factor=1/2), while the Primakoff cross section rises as ln(E) (factor = 1.1) [169]. In addition, the Primakoff cross section for $a \to a^*$ [169] has a coefficient K, given by:

$$K = \frac{2J_a^* + 1}{2J_b^* + 1}(\frac{M_a^*}{M_{a*}^2 - M_a^2})^3 \Gamma_{a^* \to a\gamma}.$$

Considering mass and spin values, the coefficient K is 7 times larger for the $\Sigma^* \to \Sigma$ transition, compared to the $\rho \to \pi$ transition, assuming the same $\approx$ 70 KeV width. However, we will use the estimated widths $\Gamma(\Sigma^+) = 1000$ KeV and $\Gamma(\Sigma^-) = 25$ KeV [169]. We also assume that the strong backgrounds for the ρ transition are of the same order as those of the Σ transition. We obtain therefore the rough estimate of signal cross sections of 265 microbarns (Σ^+), 6.6 microbarns (Σ^-), with a background cross section of 0.4 microbarns. This is a very promising first estimate, and we are working to improve this. For a Pb target, the corresponding Primakoff cross sections are 49. mb (Σ^+), 1.2 mb (Σ^-), with a background cross section of 2.7 μb.

Chiral anomaly tests. The chiral anomaly term describes abnormal parity transitions between an even and odd number of mesons in the initial and final states; describing for example the well known decay $\pi^0 \rightarrow 2\gamma$. For the γ-π interaction, the abnormal intrinsic parity component of the effective chiral Lagrangian also leads to interesting predictions [168] for the process $\gamma \rightarrow 3\pi$ at threshold; described by the amplitude $F_{3\pi}$. The $O(p^4)$ $F_{3\pi}$ prediction [168] is: $F_{3\pi} \sim 9.7 \pm 0.2\ GeV^{-3}$. The amplitude $F_{3\pi}$ has been measured by Antipov et al. [189] at Serpukhov with 40 GeV pions. They studied pion production by a pion in the nuclear Coulomb field, which is equivalent to $\pi^- + \gamma \rightarrow \pi^{-\prime} + \pi^0$. The Antipov et al. data sample yielded $F_{3\pi} = 12.9 \pm 0.9(stat) \pm 0.5(sys)\ GeV^{-3}$. This differs [168] from the $O(p^4)$ expectation by at least two standard deviations. Bijnens et al. [170,171] studied $O(p^6)$ χPT corrections in the anomalous sector. The need for high quality experimental tests of such higher order predictions (with different reactions) was stressed at the recent MIT Chiral Dynamics workshop [168]. We can make a quality chiral anomaly test by a precision measurement of the amplitude $F_{3\pi}$.

We need to isolate the π + virtual photon $\rightarrow \pi + \pi$ Primakoff production of the final state $\pi\pi$ configuration from other processes. Here we are helped by G-parity conservation, as the diffractive process π^- pomeron $\rightarrow \pi^-\pi^0$ is not allowed; with G-parity negative for the initial state, and positive for the final state. Other strong backgrounds are associated with meson exchange, but such cross sections are known [169] to fall rapidly with increasing energy. Therefore, the cross section using a 300 GeV pion beam should be dominated by photon exchange for the $\pi\pi$ final state.

The $\gamma\pi \rightarrow \pi\pi^0$ reaction is also approved for study at CEBAF [190] by measuring $\gamma p \rightarrow \pi^+\pi^0 n$ cross sections near threshold using tagged photons. This is a major experiment set up with this one objective, in contrast to the chiral anomaly component of this experiment, which represents a very modest cost effective effort. Even for perfect data, the accuracy of the CEBAF method is limited by the uncertainties associated with the needed Chew-Low extrapolation to the pion pole. Comparison with CEBAF data will be very important to understand systematic uncertainties.

The chiral anomaly also leads to predictions [191] of the amplitudes for radiative non-leptonic kaon decays: $K_L \rightarrow \pi^+\pi^-\gamma$, $K^+ \rightarrow \pi^+\pi^0\gamma$. The bremsstrahlung amplitude is suppressed for these decays, making verification of the anomalous amplitude easier. These complementary measurements are planned for $DA\Phi NE$.

Yields. The number of expected events for the pion polarizability measurement was estimated using the following assumptions:

- beam rate:	$2 \cdot 10^7$ particles/s
- target thickness:	0.5% λ_I Pb target
- spill duration:	2.0 s
- σ_{total}	$\approx$ 0.8 barn/nucleus at a beam momentum of 300 GeV/c
- beam time:	5 days of effective running with 100% beam delivery efficiency, 10^{12} beam pions
- total number of interactions	$5 \cdot 10^9$

We consider the Primakoff cross section (750 μb) for the s-range of 2 - 10 m_π^2, where $\sqrt{s}$ is the invariant energy of the final $\gamma\pi$ system. This s-range corresponds to very low γ-ray energies of E(V) = 70 - 630 MeV in the pion rest frame (pion target). We derive:

- $\sigma_{primakoff}$ $\approx$ 750 μbarn/nucleus at 300 GeV/c
- Primakoff events/interaction (R) : $9.4 \cdot 10^{-4}$
- Total number of Primakoff events $4.7 \cdot 10^{6}$ in a π-beam.

We estimate the accuracy for the measurement of $\bar{\alpha}$ and $\bar{\beta}$. As for the case of charm yields, we assume a track reconstruction efficiency of $\varepsilon_{track} = 80\%$. We assume also a photon detection efficiency (geometric acceptance, γ conversion) of $\varepsilon_{\gamma} = 50\%$. We thus obtain:

$$4.7 \cdot 10^{6} * \varepsilon_{track} * \varepsilon_{\gamma} = 1.9 \cdot 10^{6} \text{ useful events.}$$

With these projected statistics, $\gamma\pi$ Compton scattering angular distributions can be determined separately for different ranges of s. We will analyse data in restricted s-t_1 regions (t_1 is the incident π four-momentum transfer in the $\gamma\pi$ system) for polarizability purposes, and at higher energies and angles for other physics [174] involving multi-loop effects or the ρ meson properties. We did a Monte Carlo simulation for the 300 GeV Primakoff experiment assuming the dispersion sum rule result $\bar{\alpha}+\bar{\beta} = 0.4$ and also $\bar{\alpha}=6.8$. For $4.8 \cdot 10^{5}$ events in an s interval (2 - 10)m_{π}^{2}, less events than projected above, we find by fitting simulated data that $\bar{\alpha} = 7.1 \pm 0.4$, $\bar{\alpha}+\bar{\beta} = 0.3 \pm 0.1$. We will simultaneously obtain data in the sensitive s-interval 10.-15.3 m_{π}^{2}. Data in different s-t_1 intervals will give independent values for the polarizability, which will help control the systematic uncertainties. These independent values will have comparable error bars, because the cross section falls while the polarizability sensitivity increases with increasing s-value [169]. Our Monte Carlo simulations show that the objective of obtaining pion polarizabilities with significantly smaller statistical and systematic uncertainties than the work of Antipov et al. is realistic.

More run time is planned in the experiment with negative than with positive beam. The backgrounds are different in the two cases, considering the large proton flux with the positive beam. The proton data should give the proton polarizability, whose value has been accurately measured with gamma ray beams [178,192]. The proton data are of value for helping determine the Σ^{+} polarizabilities and for checking experimental techniques. But it is not our objective to improve the known proton polarizability measurements.

Chiral anomaly. Using the above mentioned beam conditions we now derive the projected accuracy for the chiral anomaly amplitude $F_{3\pi}$: From this we derive :

- $\sigma_{primakoff}(\pi\pi^{0})$ $\approx$ 18.7 μbarn/nucleus at 300 GeV/c
- Primakoff events/interaction (R) : $2.3 \cdot 10^{-5}$
- Total number of Primakoff events $1.2 \cdot 10^{5}$ in a π-beam.

We use the Primakoff cross section formula [169, 189, 190] with the O(p^{6}) $F_{3\pi}$ value, to calculate the expected cross section for an incident 300 GeV energy. The 18.7 μb cross section above is for a Pb^{208} target for an s interval (s is invariant energy of final $\pi\pi$ system) of 4-10 m_{π}^{2}. The beam and target conditions are as given above for the pion polarizability estimates. We estimate an 8% efficiency, five times lower than the $\gamma - \pi$ efficiency assumed above, due to the π^{0} reconstruction efficiency.
We thus obtain:

$$1.2 \cdot 10^{5} * \varepsilon_{track} * \varepsilon_{\pi^{0}} = 9200 \text{ useful two-pion events for this s-interval.}$$

This is far superior to the 200 events of the previous experiment of Antipov et al.

This number of events will allow analysis of the data separately in different intervals of s. This is important because uncertainties [189] due to ρ and ω contributions increase with s; and to control systematic uncertainties. The ρ contributions (near the ρ-resonance s-value, and near the two-pion threshold) can be seen in the data of Jensen et al. [182] for the Primakoff reaction $\pi^- + \gamma \rightarrow \rho^- \rightarrow \pi^- + \pi^0$. Our own results for this radiative width will also provide a test of our experimental apparatus and analysis techniques, which will be valuable for the $F_{3\pi}$ determination. Backgrounds from the tails of the ρ distribution can be better controlled if we also understand the $\pi^-\pi^0$ contribution at the ρ invariant mass. For events in the s interval from 4-6 m_π^2, we find roughly an order of magnitude less events than in the interval to 10 m_π^2. But this number of events is still large enough to give excellent statistical error.

Sigma radiative transitions. The number of expected events for the Sigma radiative transition measurement was estimated using the following assumptions:

- beam rate:	$2 \cdot 10^7$ particles/s
- target thickness:	0.5% λ_I Pb target
- spill duration:	2.0 s
- σ_{total}	$\approx$ 0.8 barn/nucleus at 300 GeV/c
- beam time:	5 days of effective running with 100% beam delivery efficiency, 10^{12} incoming Σ's
- total number of interactions	$5 \cdot 10^9$

We consider now the event rate expectations and backgrounds for the Σ^- radiative transition experiment. The produced Σ^{-*} is observed via the $\Lambda\pi^-$ decay. For a Pb target, we use Primakoff cross sections of 49 mb (Σ^+) and 1.2 mb (Σ^-), and a background cross section of 2.7 μb. We derive:

- $\sigma_{primakoff}$	$\approx$ 1.2 mb/nucleus at 300 GeV/c
- Primakoff events/interaction (R) :	$1.5 \cdot 10^{-3}$
- Total number of Primakoff events	$7.5 \cdot 10^6$.

Assuming 50% experimental efficiencies, we see that the expected event rates are very good. More details on these estimates and expected backgrounds have been given elsewhere [169].

Colour Fluctuations. Soft coherent diffractive dissociation of an incident hadron by a nuclear target can provide important experimental tests of the idea of size fluctuations in the projectile wave function [193–198]. The target remains in its ground state, as the incident hadron diffractively dissociates. The incident hadron can be considered as a superposition of different configurations, having different sizes. Large inelastic diffractive cross sections arise only if there are significant differences in the absorption cross sections of the different configurations, as described in references [193,197] and references therein. The term *colour fluctuations* is used to describe how the hadron fluctuates between its various configurations, and how colour dynamics affects the interaction strengths of the different configurations [193].

Consider experiments with a pion projectile, for which the pion wave function can be expanded into states of $q\bar{q}$, $q\bar{q}g$, $qq\bar{q}\bar{q}$, $qq\bar{q}\bar{q}g$, $q\bar{q}gg$, etc. Some of these Configurations such as $q\bar{q}$ have Small Size (SSC). The time scale for fluctuations of the incident pion of mass m into an excited state of mass M is long. The excited state M can move a considerable distance, the coherence length, before decaying. This coherence length $l_c \approx 2p_{lab}/(M^2 - m^2)$ can be significantly larger than the diameter of a target nucleus [193]. The interactions occur between the excited configuration and target material over the coherence length, so that the amplitudes from the entire target for the diffractive dissociation add coherently and constructively. The incident pion, entering the nucleus in a specific initial configuration, can be treated as frozen in that configuration as it passes through the entire nucleus.

4.3.1 Diffractive Cross Sections

High energy diffractive processes have been described [193] in terms of a probability $P(\sigma)$ that a configuration interacts with a cross section σ. $P(\sigma)$ estimated from data is broad; in line with the view that different size configurations interact with widely varying cross sections. One can describe $P(\sigma)$ in terms of its moments: $\langle\sigma^n\rangle = \int \sigma^n P(\sigma)d\sigma$. The zeroth moment is unity, by conservation of probability, and the first corresponds to the total hadron-nucleon cross section σ_{tot} (hN). The second moment has been determined from available diffractive dissociation data. Different determinations [193, 197] give the variance of the distribution: $\omega_\sigma \equiv \left(\langle\sigma^2\rangle - \langle\sigma\rangle^2\right)/\langle\sigma^2\rangle$, with $\omega_\sigma(p) \sim 0.25$ and $\omega_\sigma(\pi) \sim 0.4$, for incident momenta near 200 GeV/c. The part of the pion total cross section associated with small size is roughly 2-5%, the integral of P(σ) for σ values less than 5 mb [193].

The total diffractive cross section for an incident pion and proton was calculated via the colour fluctuation approach [193] using realistic $P(\sigma)$. The FMS calculation for the total diffractive cross section leads to $\sigma_{diff}^{pi-A}(A) \propto A^{1.05}$ for $A \sim 16$ and $A^{0.65}$ for $A \sim 200$. The FMS calculation predicts [193] very large diffractive cross sections; 40-50 mb for π-Nucleus interactions at 200 GeV at A $\sim$ 100 and $p_\pi \sim$ 200 GeV/c.

A proper demonstration of the success of the colour fluctuation predictions requires experimentally measuring the cross section and A-dependence of the total diffractive cross section. The FMS calculation agrees well with the A-dependence of semi-inclusive data of [199] on $\pi^+ + A \rightarrow \pi^+ + \pi^+ + \pi^- + A$ for $p_{\pi^+} = 200$ GeV. However, this 3-pion channel corresponds only to roughly 20% of the predicted cross section [193]. Coherent diffractive cross section emulsion data for 400 GeV protons on A $\approx$ 50 nuclei give large cross sections (20 mb) in line with the colour fluctuation expectations [200], but higher quality data are needed. It is important to get improved data compared to Zielinski et al. [199] for the three-pion case, and new data for the many other channels. Recently, Strikman and Guzey [201] have shown that the colour fluctuation cross section expectations are in good agreement with cross section data for $p + He^4 \rightarrow X + He^4$ data. Soft diffractive dissociation cross section data for other hadrons are also of great interest; as for $\Sigma^- \rightarrow \Lambda\pi^-$ and other Σ channels that can be studied.

Experimental Aspects. Total inelastic diffractive cross sections may be measured for proton and silicon targets. Consider first that we measure the total cross sections on these nuclei in the standard transmission setup for total cross sections. The downstream silicon tracking detectors allow one to make the Coulomb corrections, by the usual extrapolation to small angles. Now we consider that we use an active silicon target, as described by Bellini et al [202] and Kodama et al [203]. With such a target, one may require that the recoil energy is consistent with coherent scattering. This requirement, applied to the total inelastic cross section data, determines the total inelastic diffractive cross sections. The reactions can also be studied on the proton target, where a measure of the final state proton assures coherence. Aside from the extension of the A-dependence to A=1, such data is the natural input for competing theoretical approaches for hadron-Nucleus interactions, based on the usual quasi-free approximations.

4.4 CHARM EXOTICS

4.4.1 Singly Charmed Pentaquark

The strange-anticharmed Pentaquark is a $uud\bar{c}s$ or $udd\bar{c}s$ five-quark baryon that is expected to be either a narrow resonance, or possibly even stable against strong and electromagnetic decay. This subject has been recently reviewed [204]. Lipkin [205] and Gignoux et al. [206] showed that 5-quark "anticharmed" baryons (Pentaquarks), or analogous "anti-beauty" baryons, are the most bound in the 5-quark sector. Experiments with $10^6 - 10^7$ reconstructed charmed baryon events, should have sensitivity to determine whether or not the Pentaquark exists.

Pentaquark Binding Energy If the Pentaquark is a bound state (ND_s^-) with the mass $M(P) < M(D_s^-) + M(N)$, such a state would decay only via weak interactions and would be quasi-stable. Tightly bound pentaquarks have been extensively studied theoretically [108, 207–209] [210–212]. A very weakly bound D_s^-p deuteron-size bound state just below threshold with a structure very different from that of the strongly bound proton size Pentaquark might still be consistent with these recent calculations, considering all the model uncertainties.

Pentaquark Structure and Decay Modes The wave function of the Pentaquark may contain two-particle cluster components, each corresponding to a pair of known colour singlet particles; and also a direct five quark component. The Pentaquark production mechanism and its decay modes depend on these components. Pentaquark searches in progress in E791 [213,214] are based on the charged particle decay components of different Pentaquark decay modes: $D_s^- p \to \phi\pi^- p$ (B=3.5%), $D_s^- p \to K^{*0}K^- p$ (B=3.3%), $D^-\Lambda \to K^+\pi^-\pi^-\Lambda$ (B=8%), $\overline{D^0}\Lambda \to K^-\pi^+\Lambda$ (B=4%) and $\overline{D^0}\Lambda \to K^-\pi^+\pi^+\pi^-\Lambda$ (B=8%). The indicated branching ratios are those of the on-shell D-meson. Such Pentaquark branching ratios are plausible in a model where the D meson decays weakly, while the proton and Λ act as spectators.

Experimental Pentaquark Search Reaction mechanisms described elsewhere [204] have estimated $\sigma(P)/\sigma(D_s^-) \sim 10^{-3} - 10^{-2}$. In actual measurements, the product $\sigma \cdot$ B for a particular decay mode is measured, where B is the branching ratio for that mode. If a Pentaquark peak is not observed, assumptions on the values of B and on the P lifetime may be necessary in order to set limits to the Pentaquark production cross section.

We proceed with count rate estimations for the expected yields of Pentaquark baryons. Given the need to search for both quasi-stable and resonant Pentaquark baryons in different regions of X_f, estimates have been given [204] for $X_f > 0$ and in the fragmentation region $X_f > 0.5$, where one expects an improved signal to background ratio. Here, we assume [204] that quasi-stable P^0 baryons would be reconstructed in selected visible weak

(w) decay modes with a combined effective branching ratio B_w, based on a $[D_s^- p]$ bound state model for the quasi-stable P pentaquark:

$$\begin{aligned} B_w =& \ B[P^0 \to p\phi\pi^- + p\phi\pi^-\pi^+\pi^- + pK^{0*}K^-] \\ B_w = \simeq& \ 0.05 \ ; \ \textit{based on } \phi \to K^+K^- \textit{and } K^{0*} \to K^+\pi^-. \end{aligned} \tag{4.2}$$

Our objective is a search that will have improved signal to background, by concentrating on final states having resonances, such as the narrow ϕ or the K*(890).

Both weak and strong decay modes coming from the $D_s^- p$ component of the P are currently being studied in E791, where the data were taken with a 500 GeV π^- beam. Analysis of a part of the E791 data already yielded a preliminary upper limit at 90% confidence level:

$$\frac{\sigma(P^0) \cdot B(P^0 \to \phi\pi p)}{\sigma(D_s^-) \cdot B(D_s \to \phi\pi)} < 2.6\%, \tag{4.3}$$

for quasi-stable Pentaquark production (not including systematic uncertainties) [215]. In the analysis, it was assumed that the Pentaquark has the same lifetime as a real D_s^- and a mass of 2.75 GeV. It was assumed that its production characteristics are the same as other charmed baryons. This limit was based on a part of the data and measured D_s^- yield. With the full data sample and more decay modes analysed, several Pentaquarks may be observed if the cross section is in the range estimated in the previous section, or else the limit may be further lowered.

We estimate the expected cross sections for Pentaquark production in $\Sigma^- N$ interactions for a hyperon beam. Similar cross sections are expected with pion or proton beams. We take [204] $\sigma_{\Sigma^-}(P^0)/\sigma_{\Sigma^-}(D_s^-) \simeq 10^{-2} - 10^{-3}$ and $\sigma_\Sigma(D_s^-)|_{X_f>0} \simeq 5\ \mu b/N$; and obtain $\sigma(P^0) \approx 50 - 5\ nb/N$. We consider also the expected efficiency for Pentaquark detection, by comparison to estimated E781 [133] efficiencies for cqq decays. Considering all the unknown variables, we use the upper value of 8% for the global efficiency [204]. We assume 1.3×10^{11} target interactions [204]. This gives [204] for quasi-stable Pentaquark baryons, the maximum expected statistics of 280-2800 events. This may be adequate for their observation, if they really exist.

4.4.2 Doubly Charmed Tetraquark

Experimental searches of doubly charmed tetraquarks are considered here. Estimates are given of masses, lifetimes, internal structure, production cross sections, decay modes, branching ratios, and yields.

A tetraquark $(cc\bar{u}\bar{d})$ structure (designated here by T) was described by Richard, Bander and Subbaraman, Lipkin, Tornqvist, Ericson and Karl, Nussinov, Chow, Maonohar and Wise, Weinstein and Isgur, Carlson and Heller and Tjon, and Jaffe, [107,205,210,216–223]. Tetraquarks with only u,d,s quarks have also been extensively studied [107, 224]. The doubly charmed tetraquark is of particular interest, as the calculations of these authors indicate that it may be a narrow resonance. The main reason is that binding in a 1/r quark-quark potential is proportional to the mass, which must lead to a bound state in the limit of infinite mass quarks. A less important reason for increased should binding is that the kinetic energy of a high mass charmed diquark is low. Some authors [107,210,216,219] compare the tetraquark structure to that of the antibaryon $\bar{Q}\bar{u}\bar{d}$, which has the coupling $\bar{Q}_{\bar{3}}(\bar{u}\bar{d})_3$. In the T, the tightly bound $(cc)_{\bar{3}}$ then plays the role of the antiquark $\bar{Q}$. The tetraquark may also have a deuteron-like meson-meson weakly bound component, coupled to 1^+, and bound by a long range one-pion exchange potential [217, 219], which corresponds to light quark exchanges in the quark picture. Such a structure has been referred to as a deuson by Tornqvist [217], since it is a **deu**teron-like **meson**-meson bound state. A D^*D narrow resonance may be more likely than a DD bound state or resonance, considering the extra binding associated with the pion exchange. The discovery of an exotic tetraquark would have far reaching consequences for QCD, for the concept of confinement, and for specific models of hadron structure (lattice, string, and bag models).

Should only the $cc\bar{u}\bar{d}$ $(D^{*+}D^0)$ be bound; or should the $c\bar{c}d\bar{u}$ $(D^{*-}D^0)$ also be bound? The $D^{*+}D^0$ state, if above the DDπ threshold, would likely decay strongly to doubly charmed systems. It is easier to produce only one $c\bar{c}$ pair, as in $D^{*-}D^0$. However, this state has numerous open strong decay channels. These include charmonium plus one or two pions and all the multi-pion states and resonances below 3.6 GeV, and it is therefore not strong interaction stable. Shmatikov [225] explicitly studied the widths and decay mechanisms of $D^{*-}D^0$, including some bound possibilities. In a $D^{*+}D^0$ search, it would be of value to also look at $D^{*-}D^0$ data. Even if no peak is observed, the combinatorial backgrounds may help understand those for $D^{*+}D^0$.

Mass, Lifetime, Production Cross Section Fleck and Richard [108] estimated the tetraquark mass. Fleck and Richard, and Nussinov [219] have shown that $cc\bar{u}\bar{d}$ masses near 3.7 GeV are consistent with expectations from QCD mass inequalities.

The lifetime of the T should be very short, since it is set by the D^{*+} lifetime.

For the T, we assume the same production cross section as for the ccq, based on the thermodynamic equation used for ccq estimates.

Decay Modes and Branching Ratios of the T The $J^\pi = 1^+$ $cc\bar{u}\bar{d}$ T structure may be a direct four-quark bound state, or a $D^{*+}D^0$ bound deuson. It can have a narrow width, since it can not decay directly to DD, which can only couple to 0^+, 1^-, 2^+. For the deuson case, the binding is via a π^+ exchange potential, which is twice that of a π^0 exchange potential. Consequently, the $cc\bar{u}\bar{d}$ $D^{*+}D^0$ may be bound, even while the $cc\bar{u}\bar{u}$ $D^{*0}D^0$ and $cc\bar{d}\bar{d}$ $D^{*+}D^+$ are not [219]. Due to the (D^*-D-π) mass difference of only 5.7 MeV, the exchange potential acts at very long range [217, 219]. The heavy c quarks make the kinetic energy of these quarks in the T small, thereby increasing the chances for binding. Here we consider the likely decays of a $D^{*+}D^0$ state, described as a binding of a virtual D^* and a D. One can search for the decays T → π D D and T → γ D D, as discussed by Nussinov [219]. The pion or gamma are emitted at the primary interaction point, where the virtual D^* decays immediately. The two D mesons decay downstream, with the γ-ray and the two D's nearly co-linear in the laboratory frame [219]. The D^* decay branching ratios [25] are 99% for πD and 1% for γD, where these values depend strongly on the (D^*-D-π) mass difference. If the T has a D^*D structure, the mass of the virtual D^* may be lower than that of a real D^*. In that case, one expects different branching ratios for T decay to DDπ versus DDγ, compared to D^* decay to Dπ versus Dγ [219]. If the T mass is below the DDπ threshold, only electromagnetic decay would be possible.

The T decays to πDD and γDD may be useful for a search, if these branching ratios are sufficiently large. One should get better resolution for the reconstruction of the T mass for the pion decay channel. If the T has a mass higher than DD^*, it may be a narrow resonance, not strong-interaction stable. In that case, one may search for a peak in the reconstructed DD* mass spectrum.

4.5 OUTLOOK

All physics yields described above have been estimated on the basis of a 300 GeV/c proton or π beam. However, in order to obtain higher c-cross sections and yields (owing to the larger Lorenz-boost) particularly for short living states it is advantageous to raise the beam energy to 450 GeV/c. The yield increase for detectable Λ_c^+ is about a factor 2 assuming the same cross section as for 300 GeV/c. For shorter living states like Ω_c^0 yields almost 4 times higher could be achieved.
The open question of the energy dependence of the c-cross section is particularly crucial for the production of cc-baryons. Although nothing is known about its energy dependence it is likely that the shape is similar as for c-hadrons, shifted however to higher values of $\sqrt{s}$.

Another subject is the use of a hyperon beam for more efficient studies of strange and cs-systems. WA89 using a 330 GeV/c Σ^--beam has observed high yields of cs-baryons showing no clear suppression in the production of cs-baryons as compared to c-mesons or Λ_c^+. More quantitative results will be known soon, and also E781 will measure the production properties of c-baryons using a 600 GeV/c hyperon beam at FNAL,

Discussions with the CERN EBS group [226] have revealed that the necessary modifications in the beamline are possible, though man power extensive. The number of change overs should thus be limited and have therefore not been foreseen in the first years of running. The estimated yield increase, however, makes this modification very attractive.

5 THE EXPERIMENTAL APPARATUS

5.1 COMMON EQUIPMENT

5.1.1 Beam Considerations

Both, the muon and the hadron programme of this proposal would largely benefit from a modified SPS cycle similar to the lead cycle. A proton beam of 400 GeV corresponding to a lead beam of 158 GeV/nucleon could operate with an 18.9 s period and an about 5 s long extraction. Thus the duty factor for the standard operation of 14 % (14.4 s, 2 s) could be raised by almost a factor two. This option must be seriously considered and possible draw-backs for other experiments (Neutrinos, NA48) will be studied.

5.1.2 General layout

The detection of particles over a large acceptance and a large dynamical range requires the use of a two-stage spectrometer. As already mentioned, the different requirements of the hadron and muon programs, mainly dictated by the different target systems, impose two options for the first spectrometer, to be described in sections 5.3 and 5.2 respectively. The small angle spectrometer (SAS), on the other hand, is common to all experiments, and it comprises:

- the spectrometer magnet SM2
- tacking detectors HC3 - HC7 before the magnet
- tracking detectors MWPC4 - MWPC7 inside the magnet
- tracking detectors HC8 - HC11 after the magnet

Location and transverse dimensions of the tracking detectors are given in Tab. 5.1. Honeycomb (HC) drift chambers are indicated as a viable option, since they combine high location accuracy with simplicity of construction, but other types of drift chambers are also being investigated. Multi-Wire Proportional Chambers (MWPC) are used where the particle flux is high and there are no special requirements on the positional accuracy. The spectrometer magnet SM2 is the CERN MEP45, presently used in the SMC experiment. It is a dipole magnet with a gap of 200×100 cm^2 (horizontal$\times$vertical) and provides an integral field of 4.4 Tm.

Particle identification is a distinctive feature of the proposed experiment. It is performed both in the large angle spectrometers, and in the small angle spectrometer, and

detector	position	transverse dim (h×v)	comment
	0 cm	Polarised target centre	
	152.5 cm	End of solenoid	
RICH1	550 cm	320×240 cm^2	entrance window
RICH1	850 cm	560×400 cm^2	rear window
HC3	880 cm	560×380 cm^2	
HC4	930 cm	600×400 cm^2	
ECAL1	950-1030 cm	400×300 cm^2	hole 110×60 cm^2
HC5	1030 cm	160×80 cm^2	
HCAL1	1050-1150 cm	400×300 cm^2	hole 140×80 cm^2
μHOD1	1160 cm	400×300 cm^2	hole 160×80 cm^2
HC6	1170 cm	160×80 cm^2	
PIT1	1180 cm	500×400 cm^2	hole 160×80 cm^2
μF1	1200-1300 cm	500×400 cm^2	hole 160×80 cm^2
μHOD2	1310 cm	500×400 cm^2	hole 160×80 cm^2
HC7	1320 cm	160×80 cm^2	
PIT2	1330 cm	500×400 cm^2	hole 160×80 cm^2
SM2	1350-1750 cm	Spectrometer magnet MEP45	
MWPC4	1400 cm	200×100 cm^2	
MWPC5	1470 cm	200×100 cm^2	
MWPC6	1540 cm	200×100 cm^2	
MWPC7	1650 cm	200×100 cm^2	
HC8	1780 cm	220×120 cm^2	
HC9	1880 cm	240×120 cm^2	
μHOD3	1890 cm	240×120 cm^2	
RICH2	1900 cm	240×120 cm^2	entrance window
RICH2	2700 cm	440×240 cm^2	rear window
HC10	2750 cm	450×180 cm^2	
HC11	2850 cm	480×180 cm^2	
ECAL2	2900-2980	400×200 cm^2	
HCAL2	3000-3100	400×200 cm^2	Fe absorber + scintillator planes
μF2	3120-3320 cm	400×200 cm^2	Fe absorber
μHOD4	3350 cm	400×200 cm^2	Trigger Hodoscope
DT1	3380 cm	400×200 cm^2	Drift tube station
DT2	3580 cm	400×200 cm^2	Drift tube station
μF3	3800-3840 cm	400×220 cm^2	Fe absorber
μHOD5	3860 cm	400×220 cm^2	Trigger Hodoscope

Table 5.1: The elements of the common apparatus.

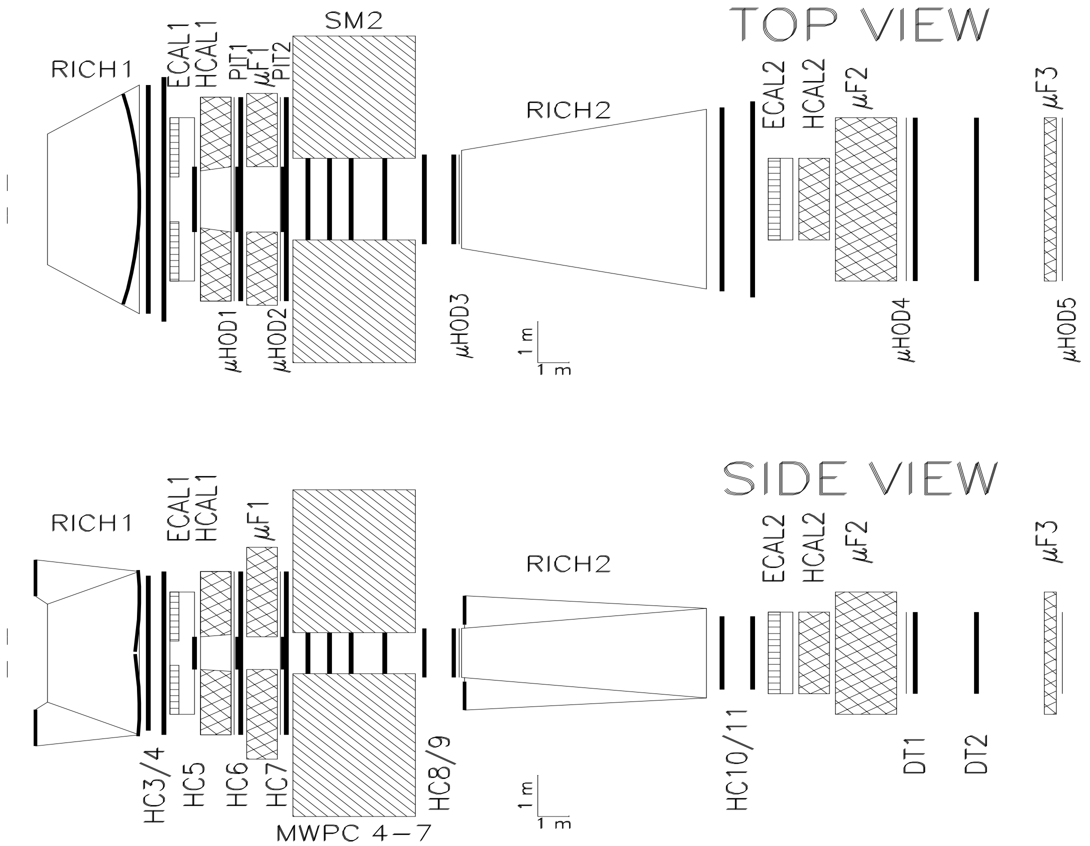

Figure 5.1: Layout of the common apparatus.

it constitutes a major part of the common apparatus. In either spectrometer it requires four different components, namely

- a Ring Imaging Cherenkov Counter (RICH)
- an Electromagnetic Calorimeter (ECAL)
- a Hadronic Calorimeter (HCAL)
- a muon filter (μF), made of Fe absorbers and Plastic Iarocci Tubes (PIT's) or Drift Tubes (DT's).

Their location and transverse dimensions are also listed in Table 5.1. The general layout of the common apparatus is shown in Fig. 5.1, with the details on the various detectors given in the following sections.

5.1.3 The Honey-Comb Trackers

Large area honeycomb drift chambers are used with high spatial resolution [227–229]. The chambers are grouped in packages, which have sufficient planes to reconstruct local tracks with unique position information and with sufficient accuracy in the reconstructed slopes to connect tracks of neighbouring packages. A chamber package consists of 6 planes (2 horizontal, 2 vertical and 2 slightly inclined), while each plane consists of two layers of cells shifted laterally by half a cell width to cover the less efficient regions of the cells, and to resolve most of the left-right ambiguity in a single cell. The planes are constructed from

150 μm thick folded conductive foils and anode wires of 30 μm diameter. The genuine honeycomb structure (Fig. 5.2) contains a minimal amount of foil, while in the structure with an extra foil (Fig. 5.3) each layer is modular.

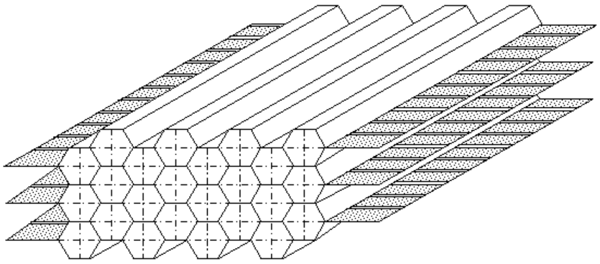

Figure 5.2: Genuine honeycomb structure.

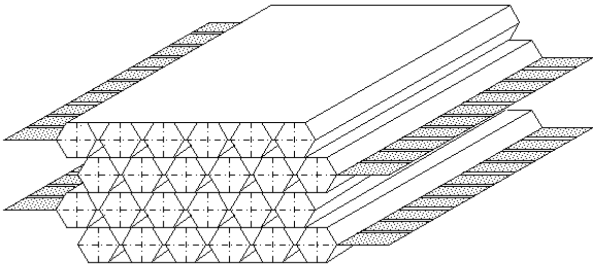

Figure 5.3: Honeycomb structure with an extra foil between cell layers.

The standard cell diameter is 1 cm. In the high particle density region a cell diameter of 0.5 cm is considered to avoid too high occupancy. The honeycomb cells are fixed at the ends by rows of plastic molds, which hold the wires in grooves and determine their lateral position with an accuracy of 10 μm over several meters. The experimental resolution of $\sigma \sim 100$ μm obtained with a relatively slow gas ($Ar:CO_2$=50:50) is shown in Fig. 5.4.

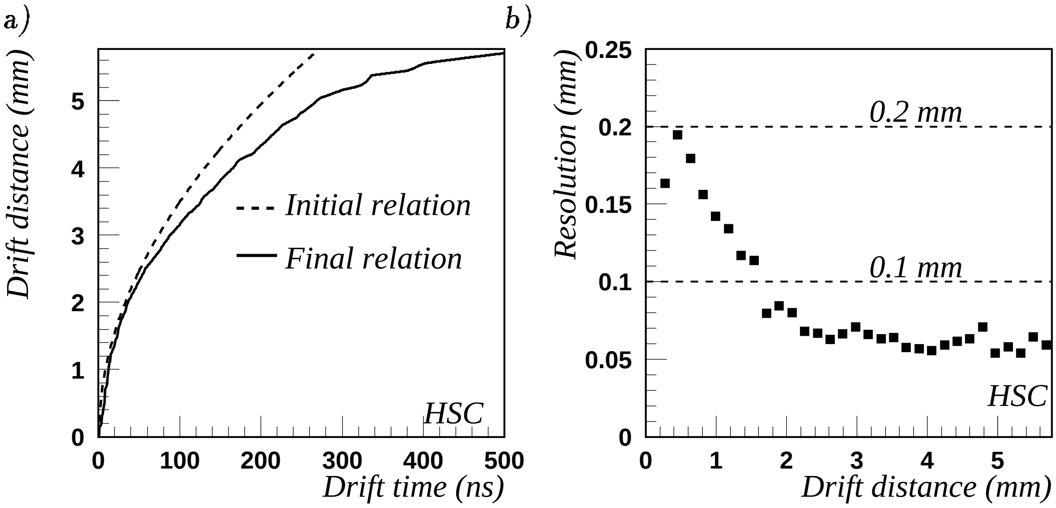

Figure 5.4: a) Drift distance vs. drift time before and after fit procedure. b) Spatial resolution as a function of the drift distance.

In the honeycomb design no heavy frames are needed to sustain the wire tension and the chambers are light. A support frame is still needed to keep the chambers in position. The positions of the planes are monitored by small CCD-cameras focused on pattern blocks via mirrors or lenses mounted on the chamber frames [230].

High voltage distribution and read-out electronics are mounted inside the gas volume. Staggered printed circuit boards are used for the electronics. The inner boards support the preamplifier-discriminator and the time-to-digital converter chips. The outer boards provide the gas containment and cable connectors.

A total number of channels of about 50000 will provide sufficient tracking redundancy for the whole spectrometer. The number of cells may still be substantially reduced by a

Chamber	Position (cm)	Size (cm^2)	Cell size (cm)	Number of cells
HC1	430	220 × 180	0.5	4960
HC2	530	320 × 240	0.5	7040
HC3	880	560 × 380	1.0	6000
HC4	930	600 × 400	1.0	6400
HC5	1030	160 × 80	0.5	3200
HC6	1170	160 × 80	0.5	3200
HC7	1320	160 × 80	0.5	3200
HC8	1780	220 × 120	0.5	4480
HC9	1880	240 × 120	0.5	4800
HC10	2750	450 × 180	1.0	4320
HC11	2850	480 × 180	1.0	4560
all				52160

Table 5.2: Distribution of honeycomb cells over the spectrometer

larger cell diameter, up to 2 cm, for the low-intensity part in HC3, HC4, HC10, and HC11. The distribution of honeycomb cells over the spectrometer is indicated in Table 5.2.

5.1.4 Multi-Wire Proportional Chambers

Multiwire proportional chambers (MWPC) will be used inside the spectrometer magnet SM2 much in the same way as in the SMC experiment, to help matching the tracks reconstructed in the tracker telescopes before and after the magnet. We plan to use the existing chambers. The front-end electronics will be upgraded to match the read-out requirements.

As described in Section 5.2.1 MWPC's will also be used in the muon programme in between the target and the first magnet SM1m, where the particle flux is too high for the honeycomb trackers. The construction of these chambers is similar to that of the existing ones (graphited kapton foils for the cathode planes). Their size and the number of planes needed is given in Tab. 5.1and in Tab. 5.6.

5.1.5 The RICH Detectors

Particle identification is performed by Ring Imaging Cherenkov (RICH) counters. Fast gas RICH detectors are capable of providing unambiguous identification of high momentum charged hadrons in large multiplicity events, occurring at high rate. To achieve pions separation above three standard deviation level from kaons and protons between 3 and 120 GeV/c, two RICH counters are needed; they are designed to provide almost complete coverage of the spectrometers acceptances.

The basic elements of each RICH counter are:

1. a gas radiator, where Cherenkov photons are produced by charged particles with velocity above threshold;

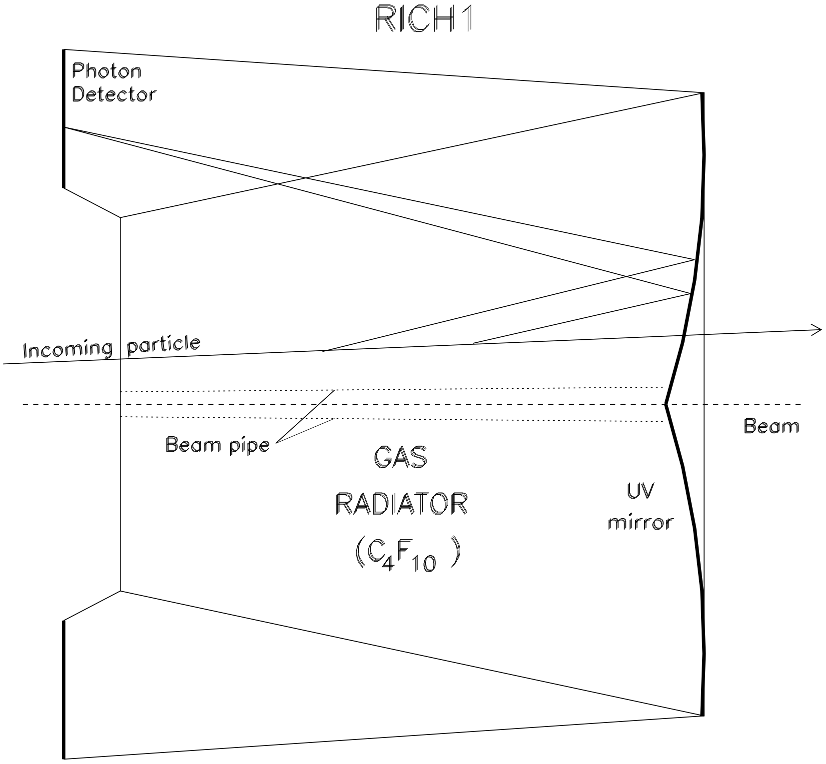

Figure 5.5: Schematic view of the detector RICH1

2. a mirror system which focuses the photons onto a ring on the detectors, outside the spectrometer acceptance;

3. a set of position sensitive photon detectors, located on the mirrors focal surface, characterised by high rate capability and good efficiency and spatial resolution.

As photon detectors we propose to use the MWPC with CsI photocathode developed by the RD26 project at CERN [231]. The Trieste group is collaborating to this work and has participated in the construction and test of prototypes.

To design the two counters, a full simulation of the RICH detectors and of the production of Cherenkov light has been implemented in a Monte Carlo program using the GEANT package.

RICH1 Design Considerations

The detector RICH1 is located between the magnets SM1 and SM2, and is designed to cover the entire acceptance of the first spectrometer, providing hadron identification in the momentum range between 3 and 65 GeV/c.

This requirement suggests the use of a heavy fluorocarbon gas as radiator. We choose C_4F_{10}, which has low chromatic dispersion [232] and can be operated at atmospheric pressure and room temperature. Its refractive index is $n \approx 1.00153$ at 7 eV, and the threshold momenta p_{th} for emission of Cherenkov photons are: $p_{th} \approx 2.5$, 8.9 and 17.0 GeV/c for π, K and p respectively.

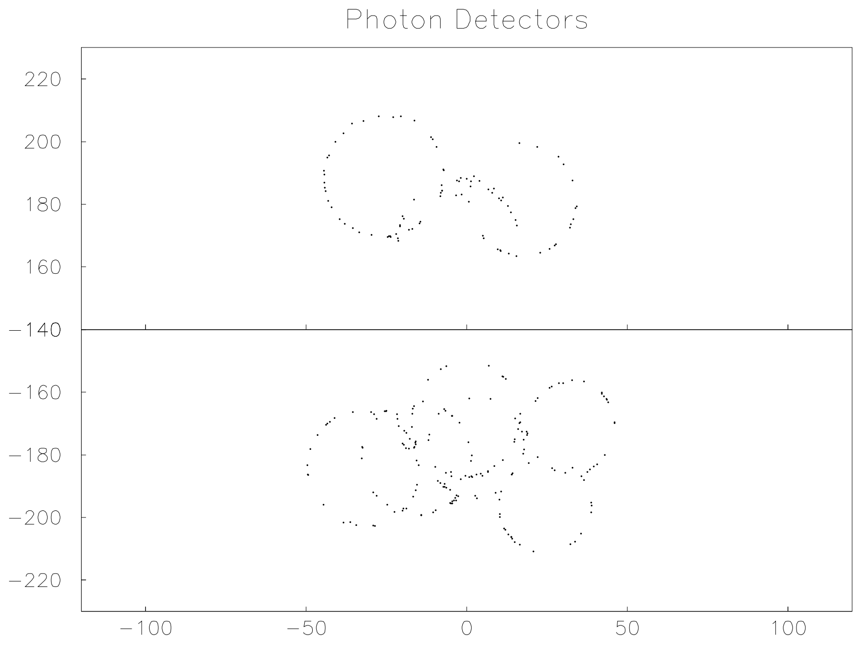

Figure 5.6: Typical DIS event on the photon detectors of RICH1.

The length of the radiator vessel is dictated by the need to produce enough photons for each ring and is set to 3 m. To cover the 400 mrad vertical and 500 mrad horizontal acceptance of the spectrometer the transverse dimensions of the active area are set to 3.2 m × 2.4 m at the upstream and 5.6 m × 4.0 m at the downstream end.

The radiator entrance is located 2 m downstream of the centre of magnet SM1 and the residual magnetic field inside the radiator volume amounts to an integral of 0.03 Tm, which poses no problem. A thin pipe around the beam region intercepts the background photons copiously produced by beam particles and their delta-rays.

The entire downstream surface is covered by mirrors with spherical geometry and a focal length of 3.3 m. Tilting the mirrors in the vertical plane allows us to place the photon detectors outside of the spectrometer acceptance. This increases the geometrical aberrations of the ring image (which nevertheless remain at a tolerable level), but it helps in reducing the background hits and in achieving stable operation of the photon chambers. Also the amount of material along the particle trajectories is reduced. The mirror surface is split in two parts by the horizontal plane on the beam axis: the upper half focuses the Cherenkov photons onto the upper photon detector, the lower half onto the lower photon detector.

The photon detectors consist of MWPC's. On one side, the MWPC is equipped with a UV transparent window and on the other side with a photocathode segmented in pads of 8 × 8 mm^2 size and covered by a layer of a photosensitive material. Each of the two photon detectors has an active area of 100 cm × 230 cm. The total number of pads of RICH1 is 69000.

The resulting design is schematically represented in figure 5.5, and is similar to the

	RICH1	RICH2
Radiator gas	C_4F_{10}	C_2F_6+Ne
Max. Cherenkov angle	55.3 $mrad$	31.8 $mrad$
π threshold mom. p^{π}_{th}	2.5 GeV/c	4.4 GeV/c
K threshold mom. p^{K}_{th}	8.9 GeV/c	15.5 GeV/c
p threshold mom. p^{p}_{th}	17.0 GeV/c	29.5 GeV/c
Focal length f	3.3 m	8 m
Radiator length L	3 m	8 m
Det. response param. N_0	37 cm^{-1}	29 cm^{-1}
Number of photons N_{ph}	34	23
Single det. area	100 × 230 cm^2	70 × 200 cm^2
Pad size a	8 × 8 mm^2	8 × 8 mm^2
Total Number of pads	2 × 34500	2 × 23000

Table 5.3: Main parameters of the proposed Cherenkov counters RICH1 and RICH2. Each counter has two photon detectors.

design of the RICH detector originally proposed for the Hera-B experiment [233]. The main parameters of the detector are summarised in tab. 5.3.

Typical ring images on the RICH1 photon detectors produced in one Monte Carlo event are shown in figure 5.6.

RICH2 Design Considerations

The detector RICH2 is located downstream of the SM2 and is designed to achieve 3 sigma π/K separation from 30 GeV/c up to 120 GeV/c. Particle identification is challenging at high momenta, nevertheless it is achievable with properly suited gas RICH detectors: kaons up to 200 GeV/c have been well identified by the RICH of the E605 Experiment at FNAL [234]. In the momentum range 30-65 GeV/c, where in RICH1 the particle identification is more demanding, RICH2 will provide additional information; most of the hadrons with such momenta enter the acceptance of the second spectrometer too.

The design of RICH2 is conceptually similar to that of RICH1. A very low chromatic dispersion gas, with a low refractive index, has to be used to identify particles at high momenta. This implies the need of a long radiation volume to produce enough Cherenkov photons.

The use of a gas mixture allows us to tune the refractive index to the desired value by changing the proportions of the mixture: we envisage to use a 50% C_2F_6 + 50% Ne gas mixture, obtaining a refractive index $n \approx 1.000506$ at 7 eV. The corresponding Cherenkov threshold momenta will be $p_{th} \approx 4.4$, 15.5 and 29.5 GeV/c for π, K and p respectively. The radiator vessel is 8 m long, and the transverse dimensions of the active area are 2.4 m×1.2 m at the upstream and 4.4 m×2.2 m at the downstream end, covering the 56 mrad vertical and 112 mrad horizontal acceptances of the high momentum spectrometer.

The optical setup of RICH2 is similar to that of RICH1. The RICH2 mirrors have a focal length of 8 m. Due to the smaller angular acceptance, the tilt of the RICH2 mirrors

	C_4F_{10}	C_2F_6	$C_2F_6 : Ne = 0.5 : 0.5$
(n-1) at 7 eV	$1530 \cdot 10^{-6}$	$938 \cdot 10^{-6}$	$506 \cdot 10^{-6}$
dn/dE at 7 eV (eV^{-1})	$53 \cdot 10^{-6}$	$23 \cdot 10^{-6}$	$12.3 \cdot 10^{-6}$

Table 5.4: The refractive index and the chromatic dispersion of the gas radiators.

contributes only marginally to the error on the measured Cherenkov angle. The photon detectors have an active area of 70 cm × 200 cm each. The total number of pads of RICH2 is 46000.

The main parameters of the detector RICH2 are summarised in table 5.3.

Gas Radiators

C_4F_{10} has been successfully employed in the DELPHI forward RICH [235]; its refractive index in the UV region [232] is presented in table 5.4. C_2F_6 has already been used in a mixture with Ne in the Omega RICH [236]. The value of the C_2F_6 refractive index shown in table 5.4 come from a recent measurement performed by Abjean et al. [237].

The intrinsic transparency of C_4F_{10} and C_2F_6 for photons in the UV region is very good at least down to photon wavelengths of 160 nm (see for example ref. [238]).

The effective transparency of the gas radiators to UV light is limited mainly by the presence of O_2 and H_2O vapor contaminations. These contaminations will be kept below the 5 ppm level by a purification and monitoring gas system. The Omega-RICH experience [236, 239] shows that it is possible to reach this low contamination level in large volume gas radiators.

Neither C_4F_{10} nor C_2F_6 exhibit appreciable emission of scintillation light in the wavelength region of interest (lower than 210 nm) [238].

UV mirrors

The standard technique for producing spherical mirrors with focal lengths of several meters with the precision necessary for RICH counters is to produce glass bodies of about 1 cm thickness, grind and polish the surface and finally coat it with a UV-reflecting layer. The process is well understood and has been used for the Omega-RICH [239] at CERN and for the SELEX-RICH at Fermilab.

Large surfaces are obtained by joining many hexagonal single mirrors with typical diameters of 40 cm.

To ensure the necessary rigidity and long-term stability, the thickness cannot be significantly smaller than 1 cm, which corresponds to 0.08 radiation lengths. The CERES RICH [240] has used an alternative technique: a carbon fibre mirror of 1 mm thickness only, corresponding to 0.005 radiation lengths; the diameter is 80 cm and the focal length is 2 m. It is not clear, whether mass production of mirrors using this technique would provide the surface quality necessary for the focal length needed here, and whether the price could become at least competitive with the glass mirrors.

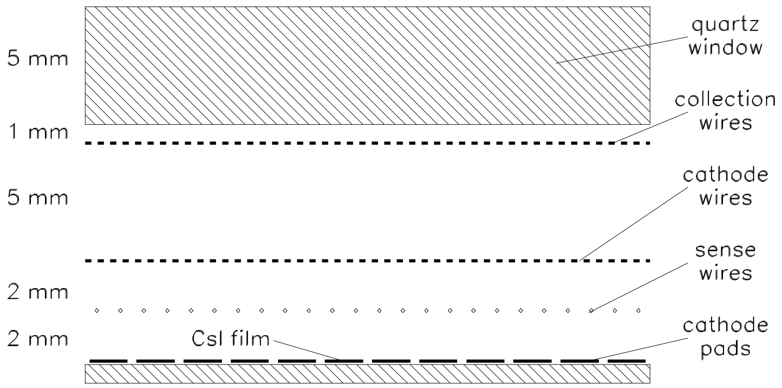

Figure 5.7: Schematic layout of the RICH photon detector.

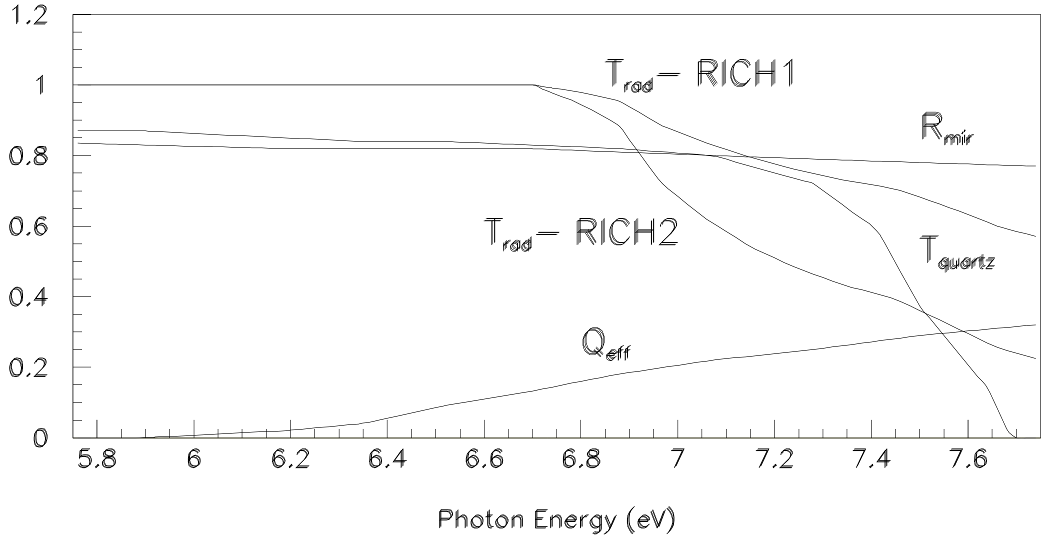

Figure 5.8: Quantum efficiency Q_{eff} [242], transparency of the gas radiator T_{rad} (scaled from ref. [239]), transparency of the quartz windows T_{quartz} and mirror reflectivity R_{mir} [239] versus photon energy.

Photon Chambers

MWPC's for Photoelectron Detection. The conversion of the UV Cherenkov photons, and the collection and detection of the photoelectrons are performed by special MWPC's, similar to those developed by experiment RD26 at CERN [241] [231].

The photon detector layout is sketched in fig. 5.7: the MWPC is symmetric, with 2 mm anode-cathode distance; the sense wires have 20 μm diameter and 4 mm spacing. One of the cathodes is made of wires, the other one consists of a printed board segmented into pads of 8 × 8 mm^2, covered by a layer of CsI. Conversion of UV photons into electrons takes place on the CsI surface.

The chamber volume is separated from the RICH radiator by a polished "Suprasil 2" quartz window; the transparency T_{quartz} of the window is larger than 80% for photons with $E_{ph} < 7\ eV$ and has a cut-off around 7.5 eV, as shown in figure 5.8.

CsI Quantum Efficiency. The quantum efficiency of CsI for UV photons has been measured several times (see, for example, ref. [243]) and is larger than zero for photon wavelengths lower than 220 nm. It depends on a variety of parameters such as, for instance, the substrate material on which the CsI is deposited, the gas to which the CsI is exposed and the level of water vapour contamination (this seriously degrades the quantum efficiency) [244,245].

In the MWPC developed by RD26 and proposed for this experiment, a ≈ 500 nm thick CsI film is deposited by evaporation in vacuum on a Ni/Au protection layer covering the conventional G10/Cu printed board of the photocathode. The CsI cathode is submitted to a heat treatment of several hours at $\approx 60^o$ C and then kept in controlled atmosphere to preserve the maximum photo-conversion quantum efficiency. It has to operate as a photo-converter in an atmosphere of CH_4 . The effective quantum efficiency in these conditions has been a matter of discussion and first measurements indicated low values [246,247].

More recently, however, the procedure of the preparation of the printed boards has been modified and the resulting measured quantum efficiency has significantly increased [242]. The use of this technique for RICH photon detectors can thus be pursued.

Read-out. It is foreseen to read the amplitude of the signal formed on the cathode pads. The main advantage of the analog read-out consists in a better control of the noise rejection which can be based on the analysis of signal amplitudes. Another advantage is the improvement in the resolution of the measured coordinates, which would no longer be determined only by the pad size.

The chip Gassiplex [248], developed in the context of the RD26 collaboration is specifically designed for this application. It is characterised by low noise (580 e^- rms at 0 pF of additional input capacitance with a slope of 15 e^-pF) and by a signal shaping that allows us to cut the long hyperbolic tail of the signal due to the motion of the ions in the MWPC. The peaking time is adjustable from 400 ns to 1 μs.

The front-end electronics will be mounted on the rear side of the MWPCs to minimise parasitic capacitance.

To match the dead-time requirements of our read-out and data taking system, the Gassiplex scheme requires modifications of its read-out logics (see section 6).

Beam Tests of RD-26 Photon Detectors. The fast CsI RICH photon detectors developed by the RD-26 collaboration have been successfully tested with photons emitted from a Cherenkov radiator traversed by a 3 GeV/c pion and proton beam at the PS/T11 CERN beam line during 1994 and 1995. The schematic lay-out of the setup used in one of the tests is presented in fig. 5.9.

The liquid C_6F_{14} radiator was contained in a cylindrical vessel with a 3 mm thick quartz window at the downstream edge. The Cherenkov photons traversed a proximity focusing lever arm between the radiator and the photon detector and produced ring images on the chamber. A wire electrode, close to the quartz window, collected the primary ionization electrons generated by the beam in the proximity gap.

The MWPC had a photocathode of 32×29 cm^2 printed board segmented into 40×36 pads; it was operated with CH_4, purified by Oxisorb and Hydrosorb filters, at room temperature and atmospheric pressure, and with a HV around 2100 V.

Five identical photocathode prototypes have been studied. They all exhibited similar behaviour and performances, and good stability of operation. Typical pion events and proton events obtained during the tests are shown in fig. 5.10.

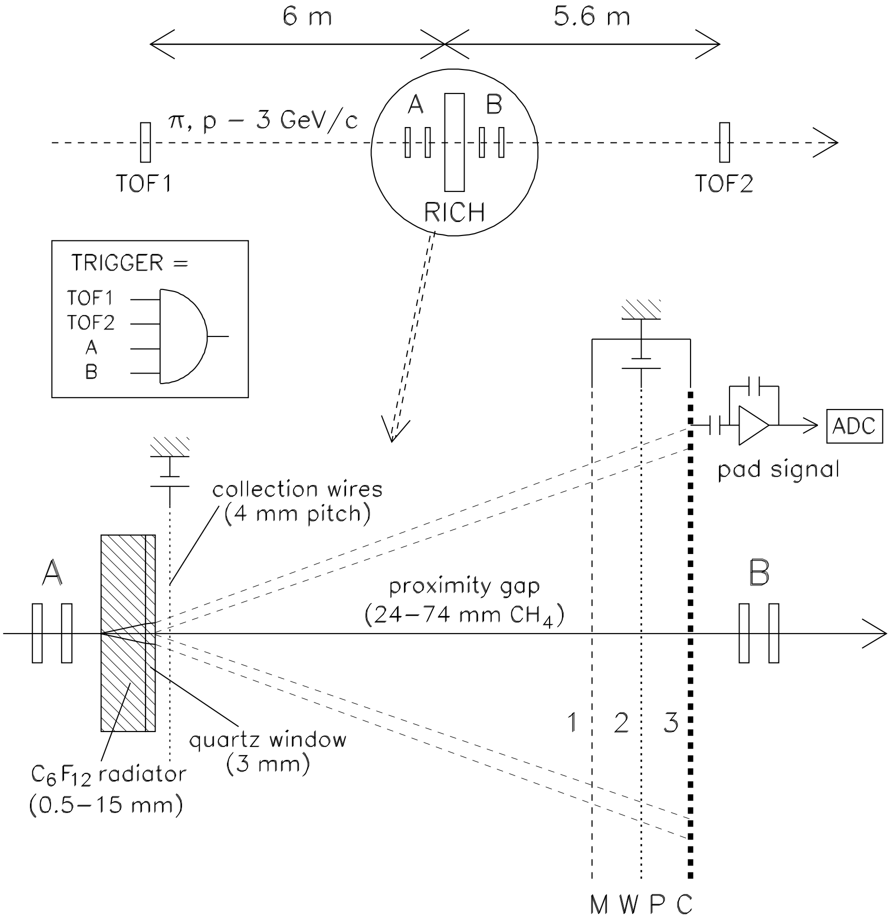

Figure 5.9: Schematic lay-out of the RD-26 CsI fast RICH module test at the CERN PS/T11 beam line. The module consists in a liquid freon radiator, a proximity gap and a 30×30 cm^2 photon chamber with: 1 = cathode mesh (50 μm diam., 0.5 mm pitch), 2 = anode wires (20 μm diam., 4 mm pitch), 3 = CsI photocathode (36×40 pads of 8×8 mm^2); the anode - cathode gap is 2 mm. A and B are $10 \cdot 10$ mm^2 scintillators.

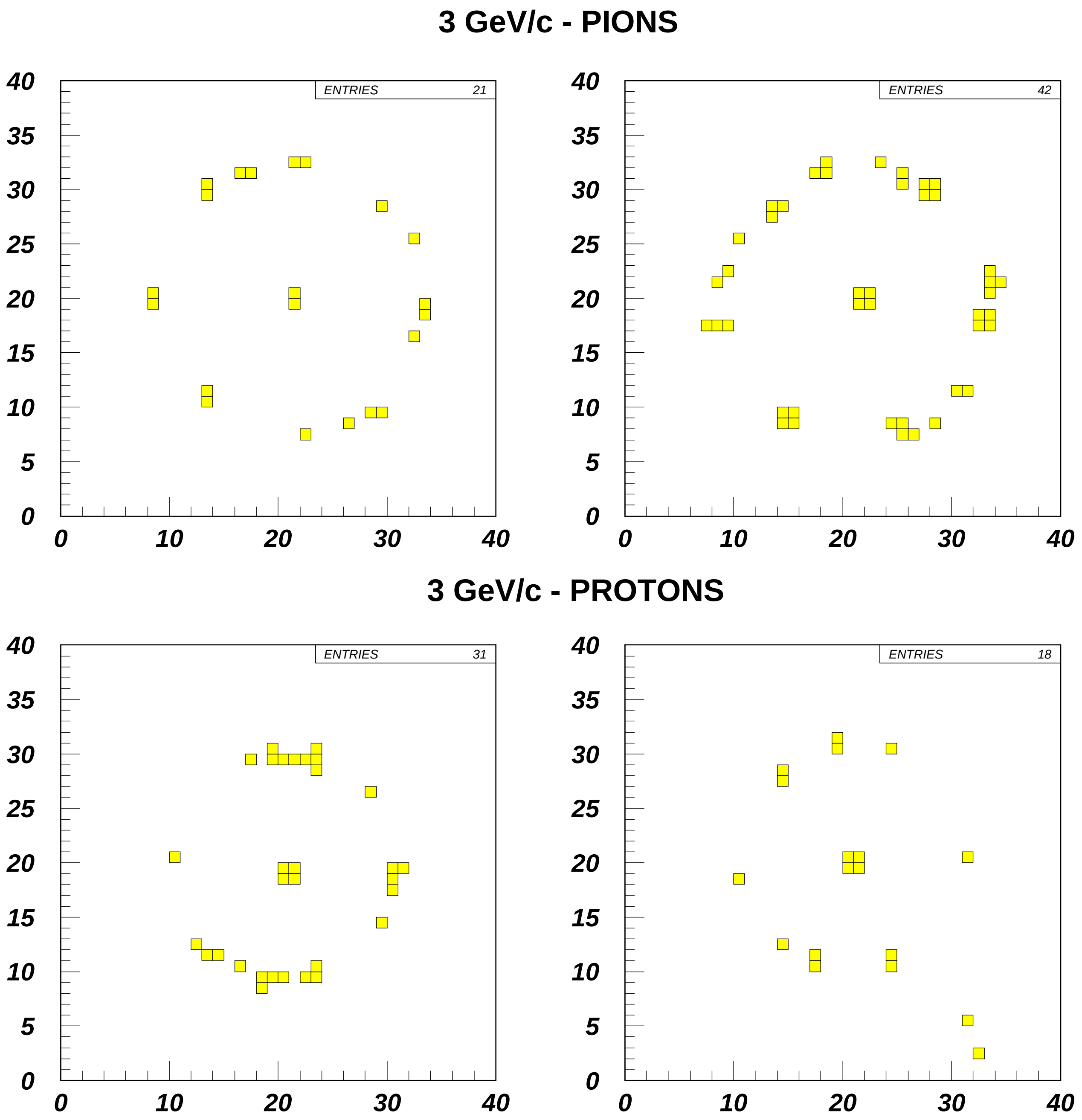

Figure 5.10: Cherenkov rings on RD26 photon chambers, generated by 3 GeV/c pions and 3 GeV/c protons crossing 10.5 mm of C_6F_{14} freon radiator.

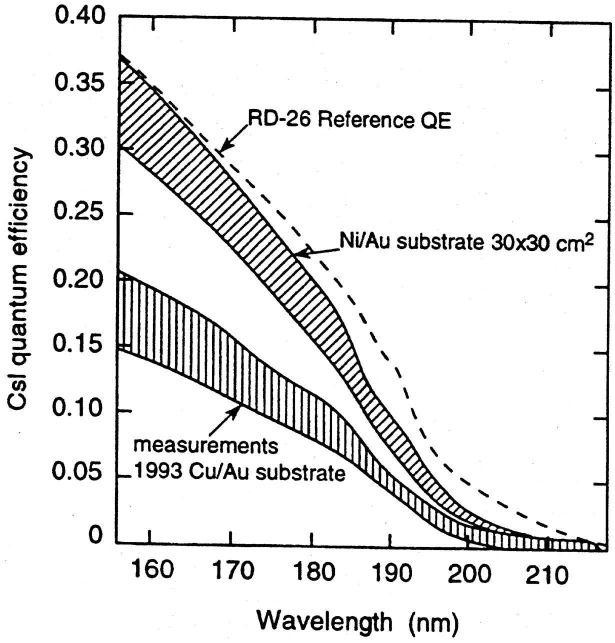

Figure 5.11: CsI quantum efficiency measured in experimental conditions by RD26 [242]. The Ni/Au substrate band represents the present typical performance of RD26 MWPC's with CsI photocathodes.

Figure 5.11 shows the effective CsI quantum efficiency determined by RD26 from these and similar tests. Also the MWPC efficiency for the single photo-electron detection has been measured to be $\approx 90\%$.

Alternatives to CsI. The photon detectors described above rely on good CsI photoconversion performance; furthermore, stability of operation in our proposed large scale system is an important issue. The R&D for this technology is well advanced and results are promising. If performance limitations appear in the near future we will develop the photon chambers following a more conventional approach, with the use of a vapour photon converter.

Number of Detected Photons

The number of detected photons has been evaluated taking into account the radiator material and length of the two RICH detectors, the effective quantum efficiency Q_{eff} of the photon detectors with CsI cathodes, the dead zones (F_{active} fraction of active area) and detection efficiency F_{eff} of these detectors, the transparency T_{rad} of the gas radiator, the transparency T_{gas} of the chamber gas (CH_4 10 mm), the transparency T_{quartz} of the quartz windows and the mirror reflectivity R_{mir} .

In figure 5.8 Q_{eff} , T_{rad} , T_{quartz} and R_{mir} are shown. T_{rad} is obtained assuming full transparency for the radiator gases and the effect of O_2 and H_2O vapor contaminations at the level of 5 ppm. For the product P of F_{active} and F_{eff} the value 0.85 has been assumed. T_{gas} has been taken equal to 1 in the wavelength region of interest.

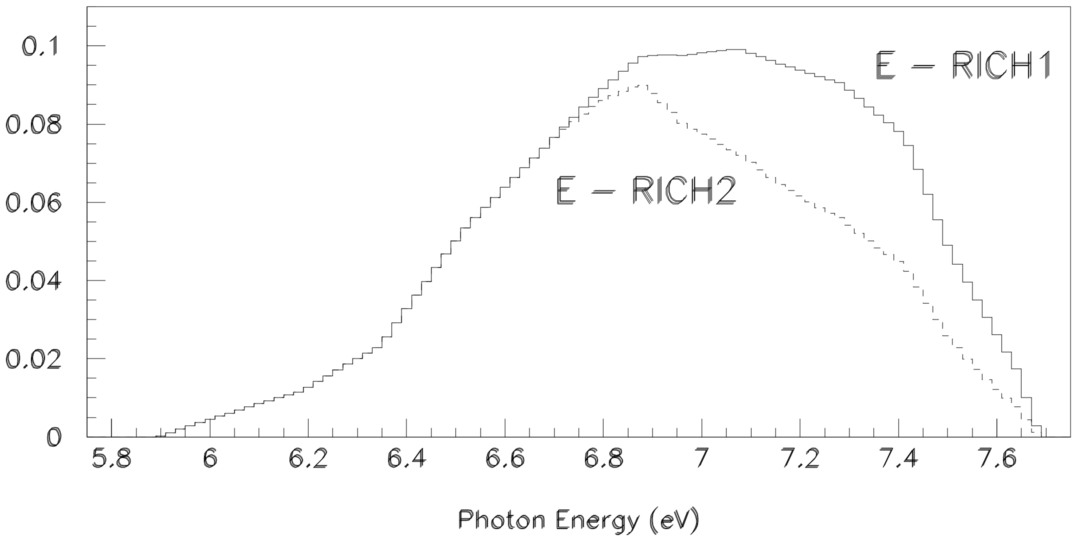

Figure 5.12: E for RICH1 and for RICH2 versus photon energy.

The product

$$E = Q_{eff} \times F_{active} \times F_{eff} \times T_{rad} \times T_{gas} \times T_{quartz} \times R_{mir}$$

is presented in figure 5.12 as function of the photon energy for the detectors RICH1 and RICH2.

The values of the figure of merit N_0 (obtained from the integral of E) and the corresponding number of detected photons N_{ph} in RICH1 and RICH2 are given in table 5.3.

RICH Resolutions

The identification of a charged particle track requires a precise determination of the Cherenkov angle, knowledge of the radiator refractive index, and measurement of the track momentum.

The main sources of error in the measurement of the Cherenkov angle θ_c for RICH1 and RICH2 are listed below. The quoted contributions to the angular error σ_θ refer to a single detected photon.

1. The finite space resolution of the photon measured coordinates is conservatively assumed as due to the full pad size, although we plan to use an analog read-out; since this is the dominant error source for both counters, any increase in space resolution will directly improve the high momentum particle identification performances. The σ_θ values based on full pad size are 700 μrad for RICH1 and 290 μrad for RICH2.

2. The error due to spherical aberrations strongly depends on the particle track incident angle θ_i. This is more critical for RICH1 and gives a value of 320 μrad for a track with the typical incident angle of 13^o. For RICH2, θ_i is not dominated by the tilt of the mirrors, and has a larger momentum dependence, because of the SM2 bending. The spherical aberrations for RICH2 are on average ≈ 70 μrad.

Error source	σ_θ^{ring}(RICH1)(μrad)	σ_θ^{ring}(RICH2)(μrad)
Detector resolution	120.	60.
Background and overlaps	66.	34.
Chromatic dispersion (1)	50.	27.
Geometrical aberrations	55.	15.
Mirr. and Det. alignement	17.	21.
Mirror quality	17.	21.
Refractive index	10.	10.
Multiple scattering (1)	8.	5.
Magnetic field (1)	5.	1.
Total	160.	80.

Table 5.5: Main sources of error in the Cherenkov angle θ_c. (1) The momentum dependent contributions have been computed at 60 GeV/c for RICH1 and at 120 GeV/c for RICH2.

3. The chromatic error is due to the dispersion of Cherenkov angles caused by the variation of the refractive index with the energy of the photons. For tracks with $\beta \approx 1$, σ_θ is calculated to be 290 μrad for RICH1 and 130 μrad for RICH2. This error increases for smaller rings, but the corresponding velocity resolution σ_β remains constant. (For RICH1 $\sigma_\beta \approx 1.6 \times 10^{-5}$ and for RICH2 $\sigma_\beta \approx 4.1 \times 10^{-6}$).

4. The error in the alignment of the mirrors and the photon chambers is estimated to be ≈ 100 μrad (from Omega experience [249]), for both RICH1 and RICH2.

5. The error due to surface imperfections of the mirrors, resulting in a distortion of the image is deduced from the average photon smearing of 0.5 mm at the photon detector reported by the WA89 experiment [249]: $\sigma_\theta = 100\mu rad$.

6. The multiple scattering of the particle in the Cherenkov radiator contributes to the angular error with a term inversely proportional to the track momentum p. For RICH1 (0.09 X_0) $\sigma_\theta = 270$ μrad at 10 GeV/c (45 μrad at 60 GeV/c), for RICH2 (0.08 X_0) $\sigma_\theta = 88$ μrad at 30 GeV/c (22 μrad at 120 GeV/c).

7. The track bending due to the residual magnetic field gives another contribution inversely proportional to p: for RICH1 $\sigma_\theta \approx 160$ μrad at 10 GeV/c, for RICH2 $\sigma_\theta \approx 18$ μrad at 30 GeV/c.

8. Background contamination and ambiguous attribution of photons due to ring overlaps degrade the resolution. A 10% increase of σ_θ was used as an estimate, based on the low electronic noise level and the small expected number of Cherenkov rings per event.

The combined single photon error obtained by summing the above errors in quadrature for a high momentum track (i.e. 60 GeV/c in RICH1 and 120 GeV/c in RICH2) is

$$\sigma_\theta^{ph.}(\text{RICH1}) = 920\ \mu rad,\ \sigma_\theta^{ph.}(\text{RICH2}) = 390\ \mu rad.$$

Taking into account the number of detected photons (see table 5.3) the Cherenkov angle resolution for the whole ring of a high momentum track is therefore:

$$\sigma_\theta^{ring}(\text{RICH1}) = 160\ \mu rad\ ,\ \sigma_\theta^{ring}(\text{RICH2}) = 80\ \mu rad$$

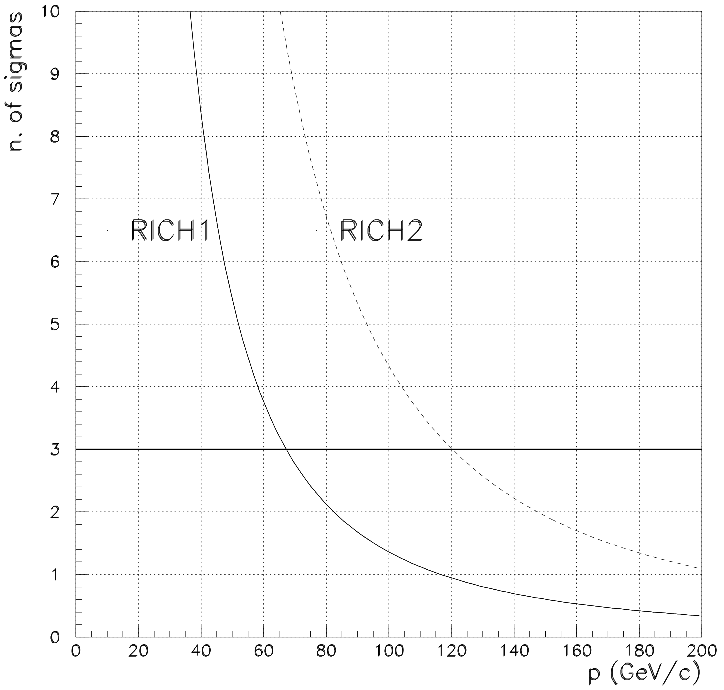

Figure 5.13: Expected resolution for π/K separation in number of standard deviations: $[\theta_\pi(p) - \theta_K(p)]/\sigma_\theta(p)$ versus momentum in GeV. The solid (dotted) curve represents the RICH1 (RICH2) response.

The other contribution to the uncertainty in the velocity measurement comes from the error in the estimate of the average refractive index. If we take as reference the analysis of Omega-RICH events, the refractive index error gives a contribution $\sigma_\theta \approx 10$ μrad, almost negligible with respect to the measured Cherenkov angle error.

The expected contributions to the error in the determination of the Cherenkov angle from the whole ring of a particle track are summarized in table 5.5: the momentum dependent contributions are computed at 60 GeV/c for RICH1 and at 120 GeV/c for RICH2.

The expected velocity measurement precision is:

$$\sigma_\beta^{ring}(\text{RICH1}) = 8.8 \times 10^{-6} \ , \ \sigma_\beta^{ring}(\text{RICH2}) = 2.6 \times 10^{-6}$$

Particle identification is obtained by comparison between the velocity measured from the Cherenkov angle and the velocity estimated from the measured momentum, on the basis of a mass hypothesis.

The error on the measured particle momentum corresponds to a velocity resolution $\sigma_\beta^{ring} = \beta m^2 c^2 \sigma_p / p^3$. This contribution is very small, due to the high momentum resolution of both spectrometers (it corresponds to an angular error of the order of 14 μrad for RICH1 at 60 GeV/c, and 5 μrad for RICH2 at 120 GeV/c).

The expected π/K resolution as function of particle momentum is shown in fig. 5.13 for the detectors RICH1 and RICH2. A π/K separation better then 3 standard deviations is expected up to 65 GeV/c in RICH1 and up to 120 GeV/c in RICH2.

5.1.6 The Electromagnetic Calorimeters

Good photon detection is mandatory to reconstruct final states which include single photons and photons from hadron decays. Following the general setup structure there will be two photon detectors downstream to the first and second magnetic spectrometers (ECAL1 and ECAL2).

The choice of a detection technique is driven by the requirements specific to the proposed experiment:

- Good photon momentum reconstruction, i.e. good energy and coordinate resolution. Typical energy resolution required for the charm decay reconstruction is few MeV for π^0 or 3-4 MeV for the mass resolution for radiative decays of exited charm hadrons. The photons energy ranges from some tens MeV to 100 GeV. Similar resolution is needed for the selection of the exclusive glueball central production using precise momentum balance.

- An unambiguous photon detection in the high multiplicity events, i.e. good two photon separation.

- Very fast response, because almost all proposed measurements require a high rate.

A cellular lead-glass electromagnetic calorimeter with photomultiplier readout is the detector which fulfil the above requirements . Typical parameters of such a detector with an optimal cell size (about Moliere radius) are:

- energy resolution: $\sigma_E/E = 5.5/\sqrt{E} \oplus 1.5$ in %;

- position resolution: $\sigma_x = 6.0/\sqrt{E} \oplus 0.5$ in mm;

- two photon separation: 50% at $r_{\gamma\gamma} = 20mm$; 100% for $r_{\gamma\gamma} \geq 40mm$.

- high rate capability: 90% of signal within 50ns gate, no dead time.

- effective light yield: about 1 photoelectron / MeV; hence low energy photons of down to 20 MeV can be reconstructed.

One of the detectors with these specifications, GAMS-4000 [250] currently in the WA102 experiment, will be used as ECAL1. It is built as a 64×64 matrix of $38 \times 38 \times 450$ mm^3 lead glass cells with FEU-84-3 PMTs for the Cherenkov light readout. The central cells will be removed to provide the second spectrometer acceptance. The area covered by GAMS-4000 is 6m^2. This is sufficient for the charm and central production version of setup. For the muon runs GAMS-4000 will be upgraded with OLGA calorimeter cells ($143 \times 143 \times 450$ mm^3) at the detector's periphery to cover 12m^2 required.

The ECAL2 specification is, in general similar to ECAL1 but differs in two essential points. First, the position resolution may be lower due to the much larger distance from the target, hence the detector with larger cell size may be used. Second, the central part of ECAL2 will be exposed to a high flux of particles produced in the target and material along the beam. This will create radiation load untolerable by the lead glass. To cope with this problems, the central ECAL2 zone (about $0.5m^2$) will be covered with a novel fine granulated calorimeter made of the $PbWO_4$ (PWO) heavy scintillating crystals [251]. These crystals have very small Moliere radius ($R_M \approx 2$ cm) and radiation length ($X_0 \approx 0.9$

cm), which results in a best possible two shower separation. An essential advantages of PWO crystals is high (megarad) radiation hardness. The detector will be built as a 50×25 matrix of the cells of $20 \times 20 \times 200\ mm^3$ with 3/4" Hamamatsu PMT readout. The energy and position resolutions of this calorimeter, according to our beam tests [252] are: of $\sigma_E/E = 2.8/\sqrt{E} \oplus 0.5$ in % and $\sigma_x = 3/\sqrt{E}$ mm ($r_{\gamma\gamma}$ is two times smaller than in GAMS). The central part of ECAL2, surrounding PWO detector, will be made of the currently available 2000 GAMS-type lead glass cells. To cover the periphery of ECAL2 we are envisaging the use of the lead glass cells of the electromagnetic calorimeter used by the WA89 experiment (cell dimensions $75 \times 75 \times 360$ mm^3) which are available for the COMPASS experiment.

5.1.7 The Hadron Calorimeters

The main task of the first hadron calorimeter HCAL1 will be the detection of neutrons from the decays of charm baryons and triggering on it. Due to the relatively low energy of the detected particles the position resolution is more important than the energy resolution in this calorimeter. A modular structure of the detector is preferable for the triggering purposes. The modular hadron calorimeter MHC-200 [253], currently in the WA102 experiment, will operate as HCAL1. It will be arranged in a 20×15 matrix of $200 \times 200 \times 1100$ mm^3 cells made of 25mm thick Fe and 5mm thick plastic scintillator sandwich. The total calorimeter thickness is 5 nuclear absorption lengths for pions and 7 such lengths for protons. The scintillating light readout is done with a 3mm thick wavelength shifter plastic connected to PMT FEU-84-3. The energy and position resolution of this calorimeter are: $\sigma_E/E = 80/\sqrt{E} \oplus 8$ % and $\sigma_x = 4$ to 14 mm at the edge and in the centre of the module respectively. A combined calorimeter ECAL1+HCAL1 will show similar resolutions, according to our beam tests. The detector is equipped with a system collecting the fast analog signals from the modules, which will be used for the fast trigger. For the muon runs it will be upgraded with the modules of the Dubna hadron calorimeter used now in the Tagged Neutrino experiment in IHEP, Protvino [254]. This calorimeter modules have the structure similar to MHC-200, size of $150 \times 150 \times 1200$ mm^3 and sampling 20mm Fe and 5mm scintillator.

For the second hadron calorimeter HCAL2 good energy resolution is the most essential requirement. The detector should be a compensated calorimeter with the fine granulation in a heavily loaded central zone. It will be built as a 40×20 matrix of $100 \times 100 \times 1200$mm^2 modules made of the "sandwich" of 16mm lead and 4mm scintillator (the Pb/scintillator ratio 4:1 is a compensation condition which provides the best possible energy resolution) with plastic wavelength shifter - PMT light readout. Based on the beam test of small prototype [255], energy resolution of this calorimeter can be estimated as $\sigma_E/E \approx 60/\sqrt{E}$ % with a few percents constant term. The appropriate mass production technology have been developed at IHEP in cource of the NEPTUN experiment R&D.

5.1.8 The Muon Filters

We need a large-area muon identifier for the muon programme and for the identification of muons from semileptonic decays in the hadron programme. This detector will make use of the higher penetration abilities of muons compared to hadrons and will be placed behind the Hadron Calorimeters at each of the two stages of the spectrometer. The muon identifier should allow us to reconstruct a muon track after its passage through 2 m of

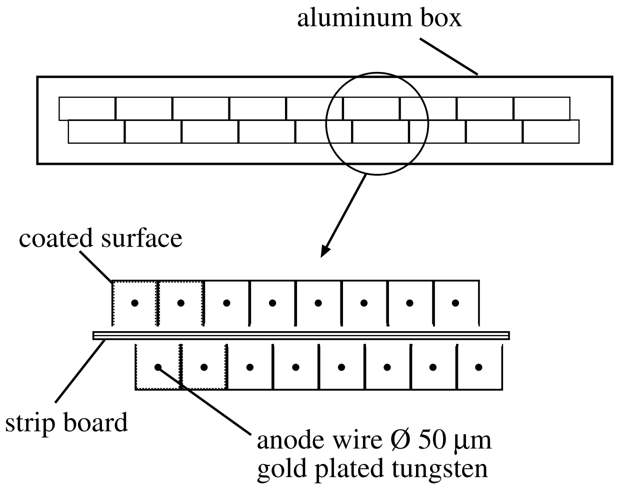

Figure 5.14: Schematic diagram: part of a PIT muon station with detail of a PIT module.

iron so that it can be matched with the associated track in the tracking devices upstream from the Hadron Calorimeters. Multiple scattering in the absorbers—which must be thick enough to prevent considerable punch-through from hadrons—has to be taken into account as well.

The experiment requires a muon system with high efficiency, so redundancy in the muon hit information is desirable. In addition to resolution requirements, background flux rates from the muon halo in the muon beam constrain the choice of detectors for the muon tracking. Estimates by the SMC collaboration show that this flux can be as high as 1 kHz/cm^2 at distances 25 cm from the beam axis, and 50–180 Hz/cm^2 almost everywhere else outside this region.

Because of space limitations in the first stage of the detector, a muon detector must be placed in the middle of the absorber to achieve sufficient tracking resolution. For the second stage, a self-supporting structure containing the tracking devices for the muons can be placed behind the absorber. The support structure has the added advantage that it ensures an automatic alignment of the chambers.

We propose the use of two different detector types for these two muon filters.

First Muon Wall For the first muon wall (MW1), located upstream from the magnet M2, we propose using Plastic Iarocci Tubes (PITs) [256] as muon chambers. The proposed PIT is a gaseous detector consisting of eight-cell tubes [257]. One cell measures 1×1 cm^2 and has a 50-micron anode wire made of gold-plated tungsten in the middle. Negative high voltage is applied to the inner coated surface of the cell, which has one open side and an internal surface resistivity of a few k$\Omega/\square$. The PITs are used in proportional mode to allow high rate capabilities of up to 10^5 particles per wire.

A module consists of two layers of these eight-cell tubes with a strip plane between them (see Fig. 5.14). The two layers of tubes are staggered by half a cell with respect to each other, to improve spatial resolution and resolve the usual left-right ambiguity. In the strip plane, the 2 cm-wide strips are 2 mm apart and run at an angle of 45° relative to the anode wires in the tubes. A muon station would then consist of one plane of several modules whose wires are all in the x-direction, and one plane of modules with wires in

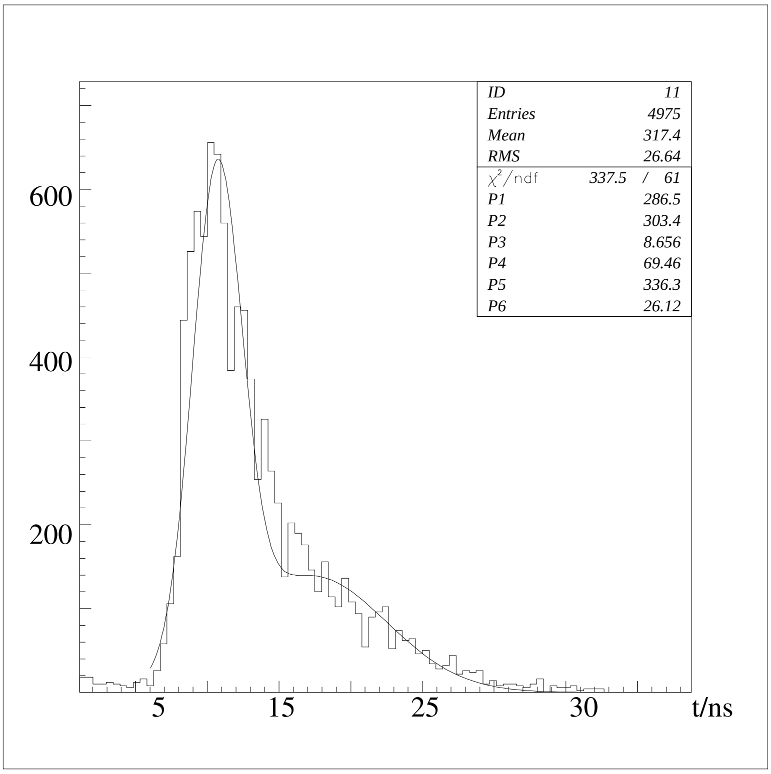

Figure 5.15: Measured time spectrum of a PIT prototype. Channels correspond to ~ 1 ns each.

the y-direction. The v-coordinate is measured with lower resolution via the strips.

Two muon stations will be placed after the hadron calorimeter HCAL1, followed by a muon absorber (1 m of iron) and two more muon stations. This gives enough redundancy for the muon track measurement. The overall coordinate precision for a station, which is limited by mechanical precision, is about 1 mm. This, together with the distance of ~ 1 m between the two pairs of muon stations, is sufficient to make the track resolution comparable to the smearing of the tracks by multiple scattering. If needed, a calibration procedure could improve the resolution to 0.5 mm.

PIT detectors with the dimensions 4×1.5 m^2 were built at the JINR (Dubna) workshop. They are used in the DELPHI experiment as surround muon chambers [258]. The time resolution was on the order of 20 ns (cf. Fig. 5.15). PITs are planned for use as a tracking muon system in the D0 experiment at Fermilab. The prototype measuring 1×1 m^2 was tested with a fast, inflammable gas mixture of 90% CF_4 and 10% CH_4.

An area of 18 m^2 has to be covered by the PITs. This makes a total of 1200 PITs for all four stations. The wires and the strips will be read out by TDCs.

Second Muon Wall For the second muon wall (MW2), at the end of the small-angle spectrometer, we propose using 2 m of iron and a system similar to the one used by the SAMUS muon spectrometer in the D0 experiment at FNAL [259]. The system consists of several layers of stainless steel drift tubes. Each drift tube has a diameter of 3 cm and a maximum rate capability of 300 Hz/cm^2, depending on the gas mixture. The maximum drift time varies between 160 ns for fast gases and 300 ns for slower ones.

Two staggered layers of drift tubes with an overlap of 10% allow the measurement of one coordinate. One station thus measures six coordinates (twice x, twice y, and twice v), each of which is measured with a precision of 0.3 mm. Putting two stations 30 cm apart allows for a track reconstruction of sufficient efficiency (the multiple scattering of 50 GeV muons after 1 m of iron is ~ 2 mrad). A total area of 20 m^2 has to be covered with drift tubes at the second muon wall, requiring ~ 3000 drift tubes in all. The drift tubes will be read out by TDCs as well.

Because the drift tubes cannot support the higher rates near the beam axis, another detector type must be used there. Proportional chambers with a wire spacing of 2 mm are the natural candidates to cover an area of 1×1 m^2 near the beam axis.

5.2 MUON PROGRAMME

In the present section we describe the parts of the apparatus which are specific to the muon programme, namely

- the μ beam
- the polarised target
- the large angle spectrometer (LAS) magnet
- the μ trigger hodoscope

and the momentum and mass resolutions of the LAS evaluated with a Montecarlo code.

The elements of the LAS which are common with the hadron program (the RICH1 detector, the HC trackers, the ECAL1, the HCAL1 and the first μ filter), as well as the elements of the SAS, have already been descibed in Section 5.1.

5.2.1 Design criteria of the LAS

To achieve the hadron acceptance which is required by the muon program ($\simeq 200$ mrad vert. and $\simeq 250$ mrad hor.), the hadron detection is split into two sections, one upstream of SM2 for hadrons at large angles, > 30 mrad, and/or low momenta, and a section downstream of SM2 for hadrons with large momenta and angles below 30 mrad.

A new large acceptance spectrometer magnet (SM1m) will characterize the LAS. Fig. 5.16 shows the horizontal and the side views of the first spectrometer. The basic elements shown in the figure are:

- the polarised target PT
- the super-conducting solenoidal magnet SOL for the PT
- the dipole magnet SM1m
- the Rich Cherenkov counter RICH1
- the Multi-Wire Proportional Chambers MWPC
- the Honeycomb drift chambers HC's

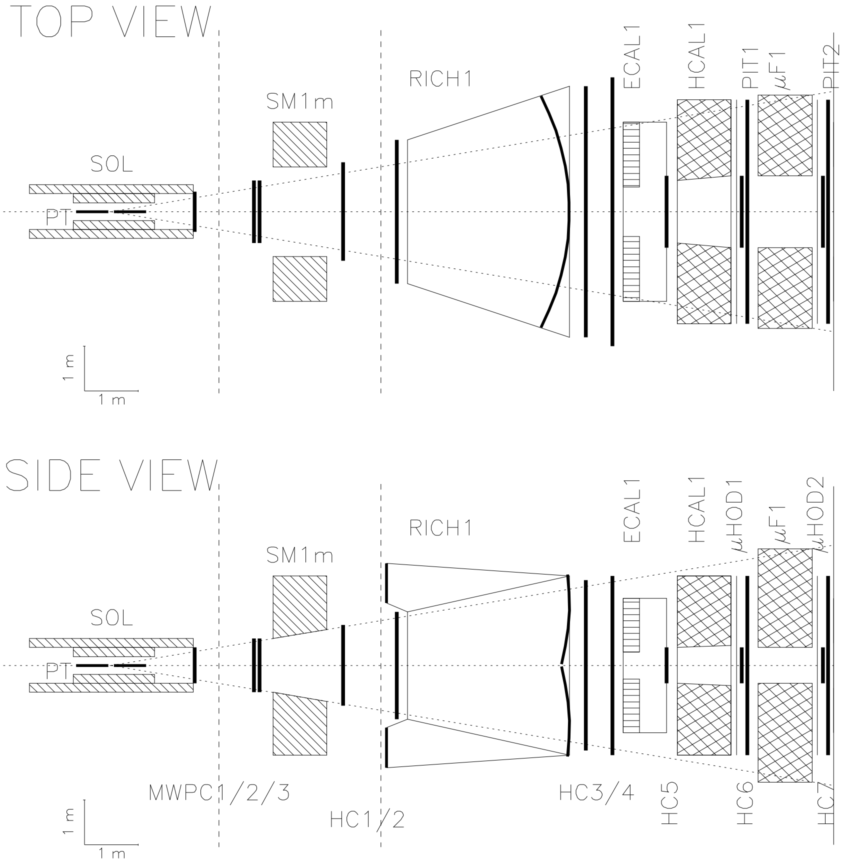

Figure 5.16: The first spectrometer (Large Angle Spectrometer) in the configuration for the μ-beam programme. The dashed lines indicate the part of the apparatus which is rolled out for the hadron-beam programme.

- the Electromagnetic calorimeter ECAL1
- the Hadron calorimeter HCAL1
- the μ-filter and the μ-trackers PIT's
- the μ-hodoscope μHOD1

Positions and transverse dimensions of the tracking elements are summarised in table 5.6. Not shown in Fig. 5.16 are the scintillating fibre beam hodoscopes located both upstream and downstream from the target (see Sect. 5.2.2).

The requirements on the target region and on the LAS were mainly determined by the D detection in the measurement of the open charm asymmetry $A_{\gamma N}^{c\bar{c}}$. The D's decay within a centimetre from the lepton vertex and their re-interaction probability is negligible. But re-interactions of mesons and photons in the target material cause losses and introduce a smearing of the measured kinematical variables via multiple scattering. This also affects the determination of the D decay vertex, which has to be used to attach the event to the correct target half. The lepton vertex cannot be determined precisely for quasi-real photon interactions because the scattering angle is too small. The strategy to minimise the losses and multiple scattering without sacrificing the luminosity is a reduction of the

Detector	position	transverse dim (h×v)	comment
	0 cm		Polarised target centre
	152.5 cm		End of solenoid
MWPC1	155 cm	90×80 cm^2	
MWPC2	265 cm	140×120 cm^2	
MWPC3	275 cm	140×120 cm^2	
	300-400 cm		SM1m position
HC1	430 cm	220×180 cm^2	
HC2	530 cm	320×240 cm^2	

Table 5.6: The tracking detectors of the large angle spectrometer.

target diameter from the 50 mm value of the SMC to 30 mm. This must be compensated by a better focusing of the muon beam to a waist of $\sigma_x = \sigma_y = 0.8$ cm at the target.

The momentum and mass resolution which are relevant to the $\mu-$program will be given in section 5.2.5.

5.2.2 The muon beam and beam detectors

The required muon beam intensity is 2×10^8 positive muons per spill for energies from 90 to 200 GeV with high longitudinal polarisation. In a measurement performed with L. Gatignon, SL division, in the end of the 1994 NA47 run [260] it was shown that this beam intensity can be obtained with a proton intensity of 1.2×10^{13} per spill for a 190 GeV muon beam. For 100 GeV an about two times smaller proton intensity is sufficient. The nominal intensity limit for the T6 production target in the M2 beam line is 10^{13} protons per spill, but this limit appears to be rather conservative and intensities of up to 40 % higher than this limit seem to be reasonable, although a careful study has to be carried out [261].

The present muon polarisation of about 0.80 for a pion to muon momentum ratio of 0.92 is assumed since no major modifications in the beam optics are foreseen. The measurements of the muon polarisation by the SMC established a good agreement with the results obtained from Monte-Carlo simulations of the beam transport [262,263]. Therefore we do not foresee to repeat the measurement of the beam polarisation.

The focusing of the muon beam in the NA47 experiment is a compromise between the size of the beam spot at the position of the polarised target and that at the beam polarimeter magnet about 75 m downstream. This results in a beam spot ($\sigma_h \times \sigma_v$) of about 16×16 mm^2 RMS size at the polarised target. Smaller spot sizes of about

instantaneous rate		10^8	μ/s
muons / spill		$2.0 \cdot 10^8$	
beam polarisation	P_B	0.80	
beam diameter	σ_x, σ_y	0.8	cm

Table 5.7: Parameters of the μ beam.

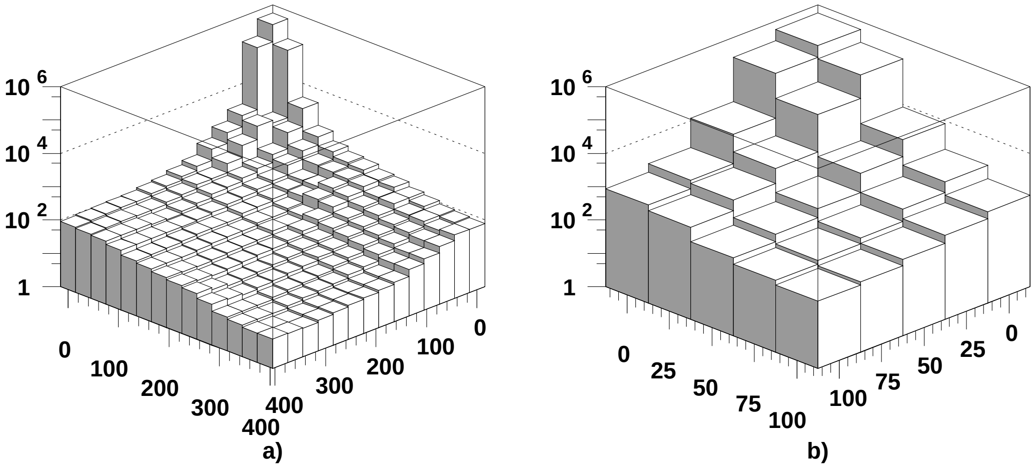

Figure 5.17: The beam halo normalised to 1 cm^2 and 10^7 muons, in a 400×400 mm^2 (a) and a 100×100 mm^2 quadrant (b).

Plane 1	180 mm	×	60 mm
Plane 2	90 mm	×	120 mm
Plane 3	100 mm	×	120 mm
Plane 4	230 mm	×	60 mm

Table 5.8: Dimensions of the present BMS hodoscope planes

12×14 mm^2 are obtained at a hodoscope 23 m downstream of the target. In order to limit the multiple scattering and re-interaction in the target its diameter must be as small as possible and therefore a better focusing of the muon beam is required. This will need stronger quadrupole magnets close to the target. With a tolerable target diameter of 3 cm the beam spot size should not be larger than 8×8 mm^2. The beam parameters are summarised in Tab. 5.7.

For the design of the trackers a detailed measurement of halo rates [264] was performed with a 190 GeV muon beam in the present NA47 set-up. The measurement of the near halo close to the position of the polarised target is shown in Fig. 5.17 with the beam centred at zero. The beam halo is normalised per unit area of 1 cm^2 and to 10^7 muons. At 100 mm from the beam centre the halo rate is still in the order of 0.1 to 1 $kHz/cm^2/10^7\mu$. The far halo outside a 0.5×0.5 m^2 region was determined over an area of 6.5×4 m^2. Rates are typically below 10 $Hz/cm^2/10^7\mu$. For a 100 GeV beam the far halo rate is known to be about three times larger.

The momentum of each incoming muon is measured at the Beam Momentum Station (BMS) consisting of four scintillator hodoscopes planes and the last dipole magnet bending the muon beam vertically into the experimental hall. The scintillator planes form two telescopes upstream and downstream of the magnet. The segmentation of the present

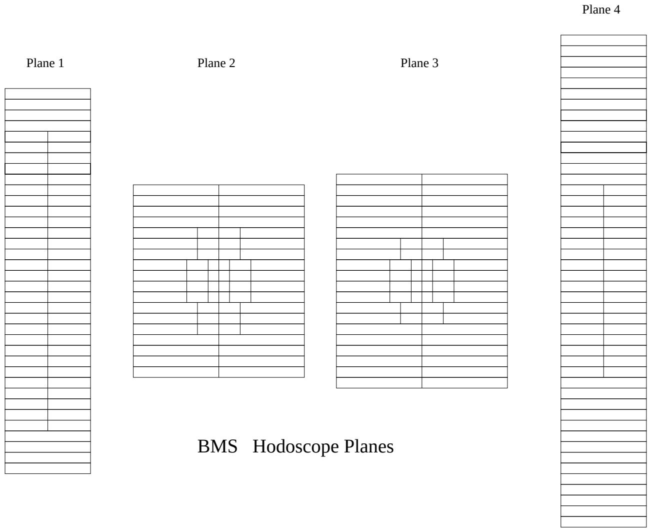

Figure 5.18: Hodoscope planes of the present beam momentum station

planes is shown in Fig. 5.18 and their sizes are given in Table 5.8. The 64 scintillator strips of each plane are 5 mm high and segmented in the non-dispersive plane to limit the rate in a single strip. Tracking of the beam is not performed between the BMS and the first beam detector at the entrance of the experimental hall about 60 m downstream.

Beam hodoscope telescopes will be located upstream and downstream of the polarised target. The two detectors of the upstream telescope located -3 m and -12 m from the target centre a size of 40×40 mm^2 is sufficient. The first downstream detector about 1 m from the target centre will be still inside the target solenoid and the second one will cover the central region of the trackers at the entrance of the large angle spectrometer magnet SM1m, 3 m downstream of the target centre. These hodoscopes should cover an area of 120×120 mm^2. The detectors have to operate at a rate of about 15 MHz/cm^2 in the beam centre. For an unambiguous correlation of the information from beam muon momentum measurement, the beam muon tracking, and the scattered muon tracking a time resolution of better than 1 ns is required.

We propose to use scintillating fibre hodoscopes for the BMS and the beam detectors similar to those developed in the CERN RD-17 project [265]. Scintillating fibre detectors combine high spatial and time resolution with a fast response of 1–2 ns which gives them also a triggering capability. The RD-17 prototypes consist of six layers of 0.5 mm diameter scintillating fibres bundled in columns of six fibres onto one pixel of a position sensitive photomultiplier tube (PSPM). A 48 channel 100 mm long prototype was tested by RD17 in 1995. The final design of the RD-17 detector and the start of construction is planned for September 1996.

For this experiment we propose to use hodoscopes with only five layers of fibres per plane, stacked in the same way as in the RD-17 prototypes. Each hodoscope consists of four planes with two pairs of orthogonal fibre orientations. Each plane corresponds to 2.25 mm of CH_2 equivalent material, 0.5 % of a radiation length, and less than 0.3 % of an interaction length.

For the BMS detectors with 0.5 mm fibres and a 5 times higher beam intensity the now twofold segmented strips need not to be segmented anymore. The presently four and sixfold segmented strips should become two and fourfold segmented. In total this amounts to 1540 channels. With four planes per detector the upstream beam hodoscopes account for 2 × 320 and the downstream ones for 2 × 960 channels. This adds up to a total of 4100 scintillating fibres channels.

5.2.3 The polarised target

The existing SMC polarised target [266] can be used for the proposed muon scattering program but a new and much larger superconducting solenoid/dipole magnet system has to be installed to allow for a sufficiently large acceptance of hadrons. This requires modifications to the dilution refrigerator, mainly to accommodate for the new position of the target cells.

The basic features of the polarised target will stay: polarisation of the nucleons (and nuclei) by the method of dynamic nuclear polarisation [267] (DNP) in a homogeneous field of 2.5 T and at a temperature below 0.5 K. Microwaves with frequencies set slightly below or above the Larmor frequency of the paramagnetic centres, present in dilute form in the material, will lead to positive or negative target polarisation. In going from the polarising mode of operation to the "frozen spin" mode, by turning off the microwaves, a base temperature below 50 mK will be reached. In this mode the nuclear spin-lattice relaxation time is several hundred hours if a holding field greater than 0.5 T is present which needs not to be very homogeneous. Thus, the high polarisation can be preserved over long times.

For the measurements with longitudinal spin settings (transverse dipole field off) the polarising mode will be used practically all the time in order to obtain the highest polarisation values. For the measurements with transverse spin settings (solenoid field off) the frozen spin mode has to be chosen.

The design of the SMC target with the material divided into two cells which are polarised in opposite directions will be kept as it is essential in eliminating systematic errors. By frequent reversals of the spin orientations the systematic error from acceptance variations of the spectrometer with time can be greatly reduced, as has been shown by the SMC. The reversals will be done in the same way as in the SMC experiment, namely rotating in the frozen spin mode the magnetic field direction by 180° in space by using simultaneously the solenoid and the dipole magnet. Polarisation losses during reversals can be kept very small. Figure 5.19 shows the spin orientations with respect to the magnetic field. The target spin and the magnetic field directions can be set in four different orientations for both the longitudinal and the transverse mode. Data will be taken in suitable combinations of these to minimise systematic errors.

Target magnet and dilution refrigerator

The present superconducting magnet [268] of the SMC polarised target has a bore of 26 cm diameter. To match the acceptance requirements of the proposed experiment a new superconducting solenoid is needed, with a bore at least twice as large.

The homogeneity of the solenoidal field is dictated by requirements of the DNP and NMR techniques in order to reach uniform polarisation and to measure it accurately. Tests done with the SMC magnet show that a homogeneity of 10^{-4} is sufficient. For the dipole a homogeneity of a few per cent is enough. The (transverse) fringe field of the first spectrometer magnet SM1m will not deteriorate the field homogeneity if it is at least 2 meters distance from the end of the solenoid.

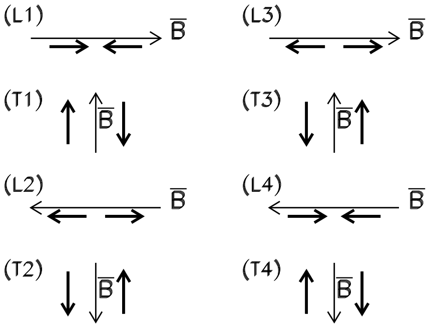

Figure 5.19: Longitudinal (L) and transverse (T) spin orientations in the two target cells with respect to the magnetic field B.

The solenoid magnet will be the biggest investment to the new target system (see Fig. 5.20). Preliminary studies show that an acceptable design is feasible and also affordable. Components of the SMC magnet instrumentation will be reused as much as possible.

The dilution refrigerator has to be modified owing to the new positions and dimensions of the target cells: The horizontal part has to be extended by 50 cm, a new plastic mixing chamber has to be fabricated with smaller diameter to minimise the amount of liquid helium around the target material, and the target holder has to be reconstructed. In addition, the pumping lines and the support structures have to be modified.

The refrigerator is using a set of 8 Root's blowers to circulate ^{3}He gas for the dilution cooling process. This set was already used by the EMC and SMC collaborations and a factory overhaul of the pumps is required to assure their reliable operation.

The planned beam intensity of 2×10^8 muons per spill and the smaller beam size results in a factor of about 12 times higher heating of the target material compared to the SMC target. Experience from other experiments with similar beam intensities [269] demonstrate that this will have a negligible effect on the polarisation in the frozen spin mode.

Minimisation of the amount of matter around the target material in the track of the outgoing particles is essential for this experiment. The material thicknesses, traversed by the particles, are listed in Table 5.9 for a scattering angle of 180 mrad. The biggest contribution comes from the liquid He coolant surrounding the target. A further reduction of this is difficult without sacrificing the cooling power of the refrigerator. The possibility to reduce the thicknesses of the other structures is being investigated.

Microwave system

The microwave field at the target is produced by two Extended Interaction Oscillator tubes having a maximum output power of 20 W each at 70 GHz. The existing tubes can probably still be used for some time but at least one spare tube has to be purchased.

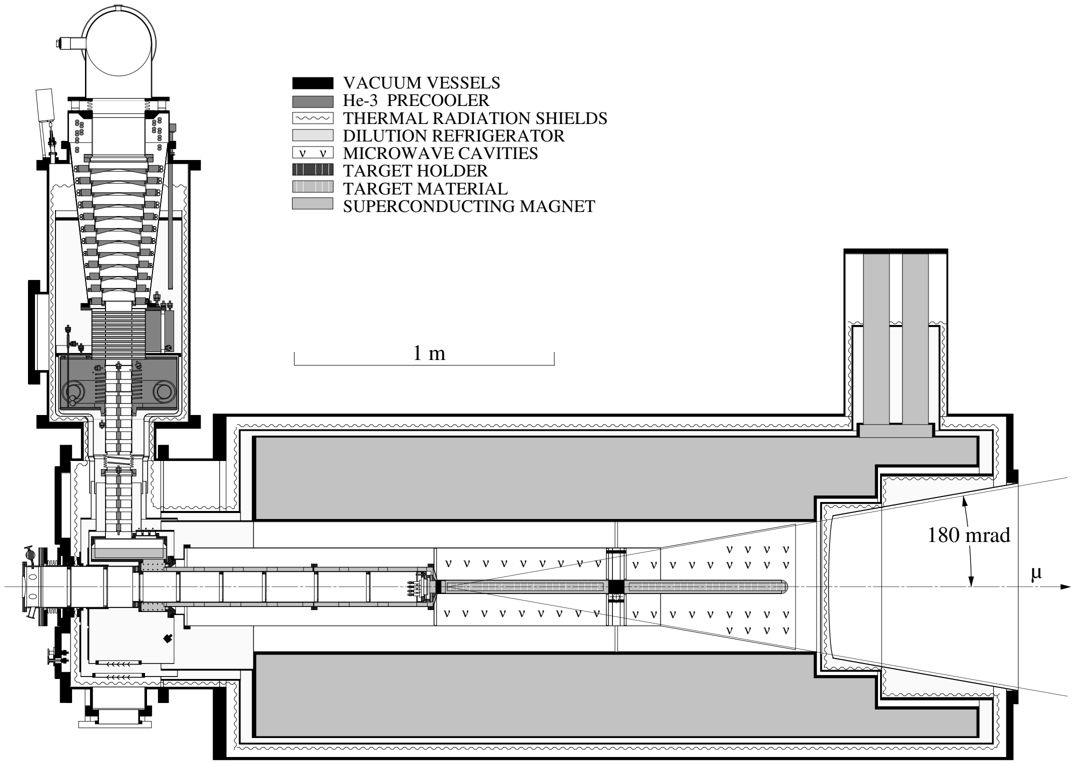

Figure 5.20: A schematic view of the new magnet, together with the modified dilution refrigerator.

location	*material*	t (mm)	ρ_v (g/cm^3)	ρ_s (g/cm^2)
Dilution refrigerator	^{3}He-^{4}He	70	0.14	0.98
Target holder	Kevlar-epoxy	3.5	1.4	0.49
Mixing chamber	Glassfibre-epoxy	3.5	1.9	0.67
microwave isolator	Cu	4x0.1	9	0.36
microwave isolator	Graphite	6x0.3	2	0.36
microwave cavity	Al	1	2.7	0.27
thermal screens	Al	2x0.2	2.7	0.11
superisolation	Mylar	30x0.02	1.4	0.08
vacuum window	Be	3	1.8	0.54
total				3.86

Table 5.9: Material thicknesses traversed by the outgoing particles with a scattering angle of 180 mrad.

Similarly, a spare high voltage supply is needed. The rest of the microwave system outside the cryostat can be used as such.

The microwave cavity and the waveguides inside the cryostat have to be reconstructed due to the increased length of the refrigerator and the larger opening angle. The present cavity is made out of 1 mm thick Cu sheet which would severely absorb the hadronic fragments. A very careful design of the new cavity is necessary to minimise the wall thickness, to obtain a high quality factor, and to ensure rigidity.

NMR system

The nuclear spin polarisation of the target material P_T will be measured by NMR techniques employing commercial series Q-meters. The measurement is based on obtaining the integral of the NMR absorption signal which is proportional to the polarisation. The calibration is done by measuring the NMR absorption signal at a known polarisation when the spin system is in thermal equilibrium with the lattice. In order to probe a large fraction of the target material, 4 to 5 NMR coils will be embedded in each target half. Multiple channels provide also security against failures of individual NMR probes. The existing NMR equipment of SMC can be used but the controlling minicomputer has to be replaced by a new workstation.

Target material

The proposed polarised target materials are ammonia (NH_3) for the proton target and lithium deuteride (^6LiD) for the deuteron target. Of the possible target materials, these are superior in terms of the figure of merit $\mathcal{F} = \rho(P_T f)^2$ which is inversely proportional to the data taking time for achieving a certain statistical accuracy. Here, P_T and f have been defined in section 3.1 and ρ is the thickness of the material. Their values for the proposed materials are given in Table 5.10. The target material is in a form of small fragments for cooling reasons, and in practice a filling factor of about 0.6 is reached, the rest of the target cell volume being occupied by liquid helium and the NMR coils. The NH_3 material will be available from the SMC 1996 run but the ^6LiD material has to be acquired.

The paramagnetic centres needed for DNP are created in these materials by irradiation with an electron beam. The ammonia for SMC has been irradiated with the 20 MeV linac at Bonn and the same will be done with ^6LiD but a new irradiation cryostat is needed. The paramagnetic centres in NH_3 decay during a long-term storage in liquid nitrogen. To overcome this the material can be stored in liquid helium or re-irradiated before the use.

In the tests done with the SMC target a proton polarisation of $P_T = +80$ %/-82 % was reached in ammonia in about 24 hours and 63 % of this within 2 hours of DNP. These numbers are subject to slight improvements during the SMC 1996 run.

The measurement of proton polarisation in ammonia can be done with an accuracy of 2–3 % owing to the narrow NMR signal. The measurement of the polarisation of ^{14}N is difficult due to its very broad NMR lineshape. Recent measurements at CERN and at Bonn indicate that an accuracy of about $\pm 20\%$ can be achieved. The ^{14}N polarisation is not expected to be more than 15 % under the conditions reachable in the new target. The ^{14}N nucleus has spin 1 and in the shell model it consists of a spin-0 core plus a neutron and a proton. The uncertainty in the correction for the asymmetry from the bound polarised neutron and proton corresponds to an uncertainty in the free proton asymmetry of about 1 %.

The material for the deuteron target, ^6LiD, has a very high theoretical dilution factor f of 0.5. The argument for this high value rests upon a presumed "alpha + deuteron" picture of ^6Li, with the polarisation of the nucleus carried by the polarization of the deuteron. Recently, the polarization of the constituents of ^6Li as a three-body bound state of $\alpha + n + p$ was calculated [270] to check the assumption above. The authors find a polarization of the valence neutron and the valence proton in excess of 92 % for a fully polarised nucleus and for eight different models investigated, in effect supporting the naive expectation for the polarization. Theoretical uncertainty is around 3 %.

Maximum polarisations above 50 % have been obtained for ^6LiD (for the deuteron as

material		NH_3	^{6}LiD	
length of each cell		60		cm
gap between cells		10		cm
cell diameter		3		cm
thickness	ρ	61	59	g/cm^2
dilution factor	f	0.176	0.5	
polarization	P_T	0.85	0.5	
figure of merit	$\rho(P_T f)^2$	1.4	3.6	g/cm^2

Table 5.10: Properties of target cells and materials. The dilution factors are theoretical and neglect the other materials present in the target volume.

well as for ^{6}Li) at 2.5 T and in a dilution refrigerator. Two thirds of the maximum polarization could be reached in 16 hours and the maximum was achieved in 2 to 3 days [271]. Optimisation of the irradiation conditions [272] can, however, result in a shorter time scale. The slow built-up does not harm the experiment, as the target can be polarised practically continuously during the longitudinal measurement, and the transverse measurement will be done in between two consecutive measurements with opposite target-cell polarization.

The NMR properties of ^{6}LiD are favourable for a high-accuracy polarization measurement because the quadrupolar line broadening is quenched due to the cubic crystalline symmetry. A relative accuracy of better than 2 % can be obtained for the deuteron as well as for the ^{6}Li nucleus.

5.2.4 The Large Angle Spectrometer Magnet

A sketch of the present design of the new spectrometer dipole magnet SM1m is shown in Fig. 5.21. The magnet is located between the polarised target and SM2. It has an aperture of 2.0×1.6 m^2 and a pole depth of about 1 m, and it will provide a field integral of 1 Tm. The field is opposite to the one of SM2. A design similar to the HERMES magnet [40] is presently being studied at the D.V. Efremov Scientific Research Institute of Electrophysical Apparatus in St. Petersburg, Russia, and at CERN [273].

Tracking partly inside the magnetic field will be provided by the beam detectors discussed above and proportional chambers in the outer region. Care will be taken for the fringe field, which on the upstream side must not interfere with the highly homogeneous field of the polarised target, and on the downstream side should not disturb the ring resolution of the RICH.

5.2.5 The D° invariant mass resolution

Using the GEANT code the momentum resolution of the magnetic spectrometers and the invariant πK mass resolution for the $D^\circ \rightarrow \pi^+ K^-$ decay (and charge conjugate channel) have been investigated. The AROMA code has been used to generate the charm events at 100 GeV, as in chapter 2.1. To avoid the complications involved with tracking in the magnetic field, a simplified layout has been used, in which the fields of the two spectrometer magnets are taken as box fields and all the chambers are placed out of the

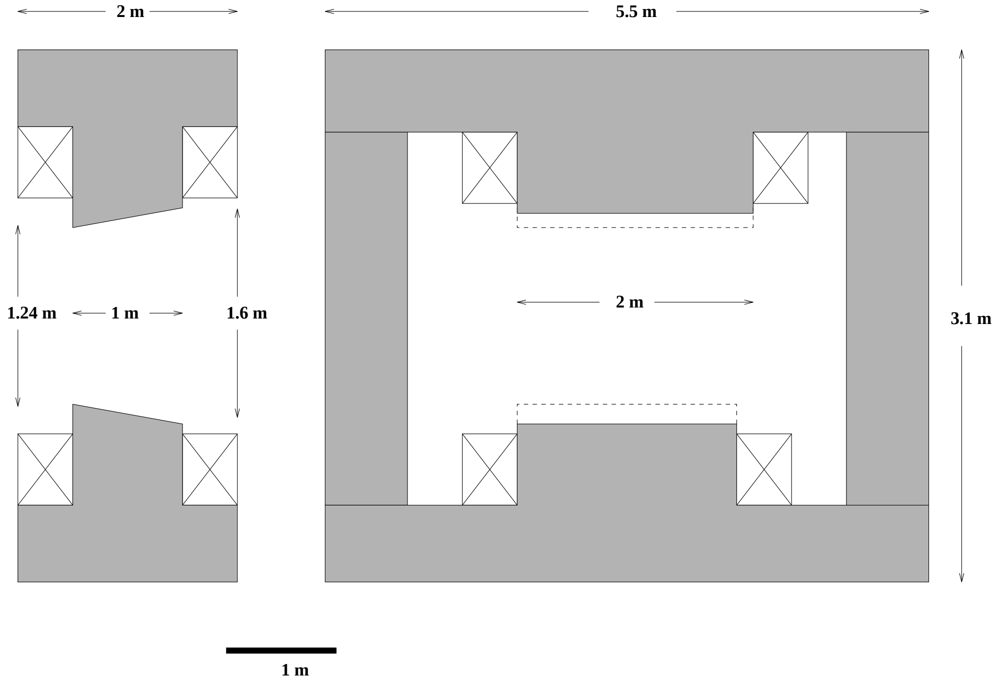

Figure 5.21: Large angle spectrometer magnet SM1m

field regions. The simplified layout is shown in fig. 5.22, together with the hits of a typical $\mathsf{D}^\circ \longrightarrow \pi^+\mathsf{K}^-$, in which, apart from the μ track, 6 more charged hadrons are produced. The dashed lines refer to γ's from the π°'s decay with $E_\gamma \geq 1$ GeV.

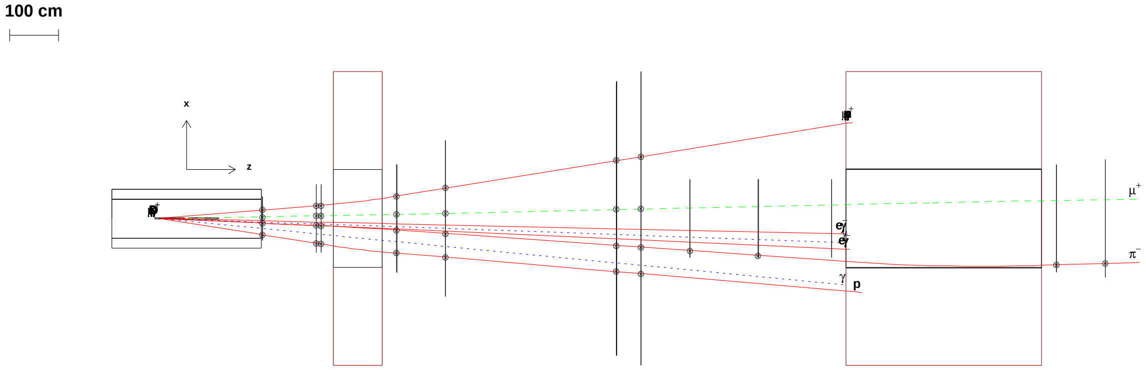

Figure 5.22: Typical DIS event

In the simulation, location errors of 100 μm have been given to the transverse coordinate of each honeycomb chamber. For the multi-wire proportional chambers MWPC1, MWPC2, and MWPC3 pitches of 0.33 mm and 1 mm have been assumed for the horizontal and the vertical coordinates respectively. They will be obtained by using several planes of 2 mm wire-spacing suitably staggered.

The mass resolution depends somewhat on the topology of the event, since the two magnetic spectrometers have different resolving powers. Fig. 5.23 gives the momentum resolution of the LAS as obtained from the simulation: $\Delta p/p$ varies from 1 to 2% in the useful momentum range. Something can be gained by improving the tracking, but the multiple scattering eventually dominates. In particular the limiting factor in the invariant mass resolution is the multiple scattering in the target, which plays no role for $\Delta p/p$, but affects the mass resolution by spoiling the measurements of the π and of the K directions.

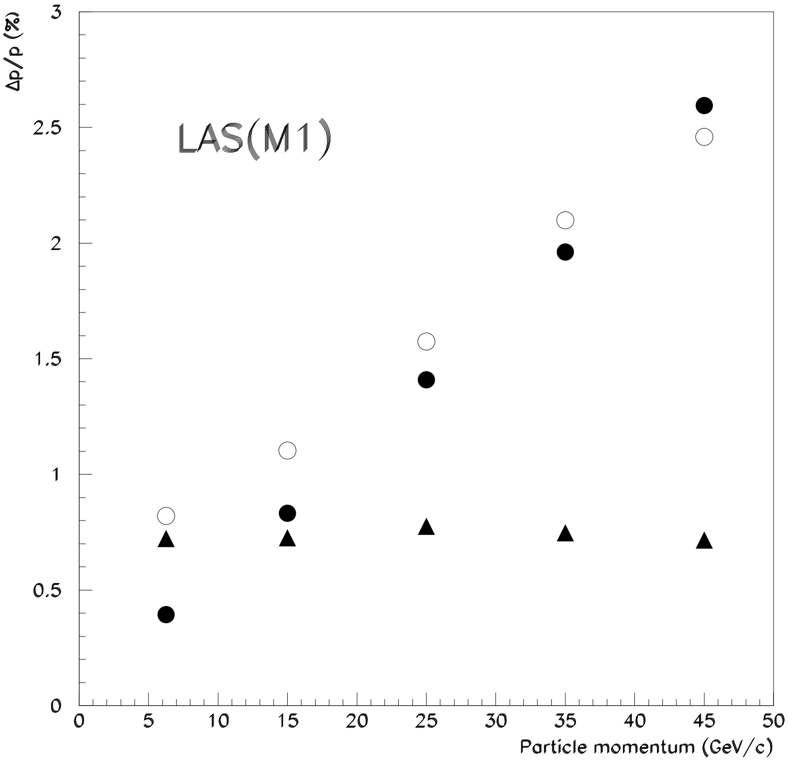

Figure 5.23: Momentum resolution $\Delta p/p$ in percent versus the particles' momentum as measured in the LAS. The full points are the measurements of $\Delta p/p$ with the location errors only, while the full triangles correspond to the case with multiple scattering only. The open points refer to the real case, with both multiple scattering and location error.

Given the large number of trackers, distributed over long lever arms, and the large bending power of SM2, the SAS momentum resolution is considerably better, $\Delta p/p \simeq$ 0.3%, as given in Section 5.3.4. Therefore the accuracy in reconstructing the D° mass depends on whether no decaying particle, or one, or two, enter the SAS.

In the following we have considered two situations, one in which neither the π nor the K enter the SAS, and the complementary one, in which at least one decaying particle enters the SAS. The relative frequency of the two classes of events depends on the D° energy as can be seen from Table 5.11.

The D° mass resolution for the first class of events can be seen in fig. 5.24 that shows the invariant πK mass for three bins of D° energy.

The resolution is about 12 MeV at low D° energy and increases with the increasing energy. On the other hand, as apparent from Table 5.11, most of the events with $E_{D^\circ} \geq 30$ GeV belong to the second category, where the mass resolution is essentially constant with energy, as shown in Fig. 5.25. From this figure, one can also notice that multiple scattering (and the dominant contribution is given by the polarised target) is the limiting factor for the resolution, and not the location errors.

	Number of events			
D° Energy	Generated	After kinematical cuts	Acceptance	Events in LAS only
0-10	1520	0	0	0
10-20	3988	882	794	711
20-30	2672	1216	1212	817
30-40	1204	621	621	252
40-50	450	216	216	48
50-60	144	73	73	3
60-70	22	13	13	1
ALL	10000	3021	2929	1832

Table 5.11: The number of D° is shown in the first column as generated by AROMA. The second column shows the effect of the cuts $z_{D^\circ} > 0.3$ and $|\cos\theta^*_K| < 0.5$. Practically all these events are then accepted by the apparatus. The last column shows the distribution of the events with both π and K tracks measured in LAS but not entering the SAS.

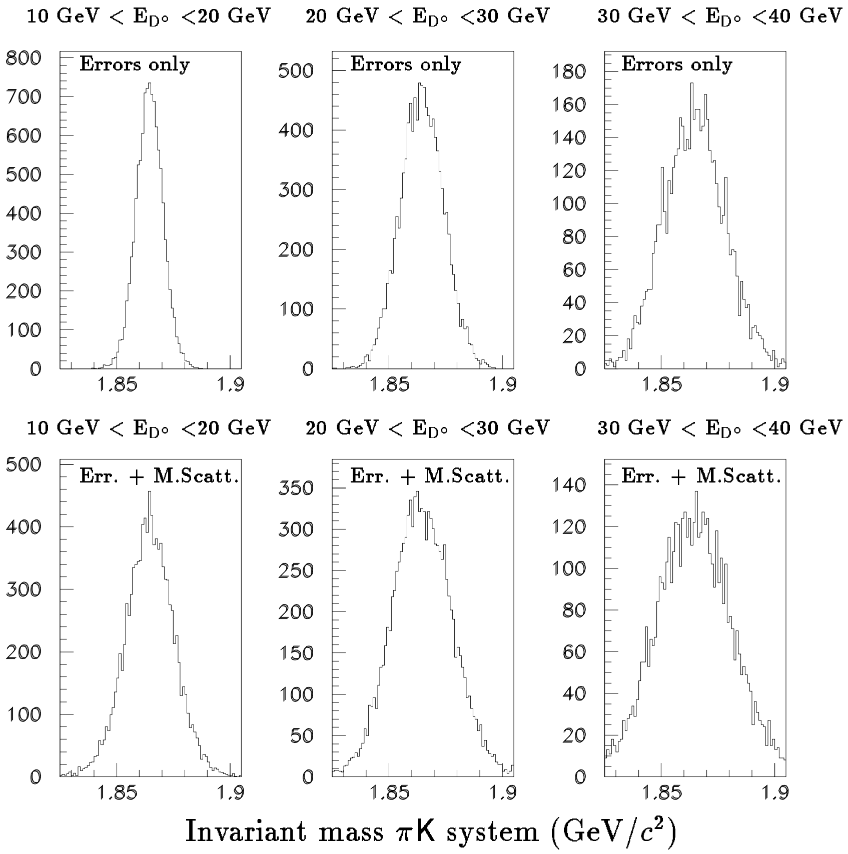

Figure 5.24: Invariant mass distribution of the πK from D° decays for three different D° energy ranges, when neither the π nor the K enter the SAS. The upper row refers to the case where location errors only are taken into account. The second row refers to the "full" case (both multiple scattering and location errors are there).

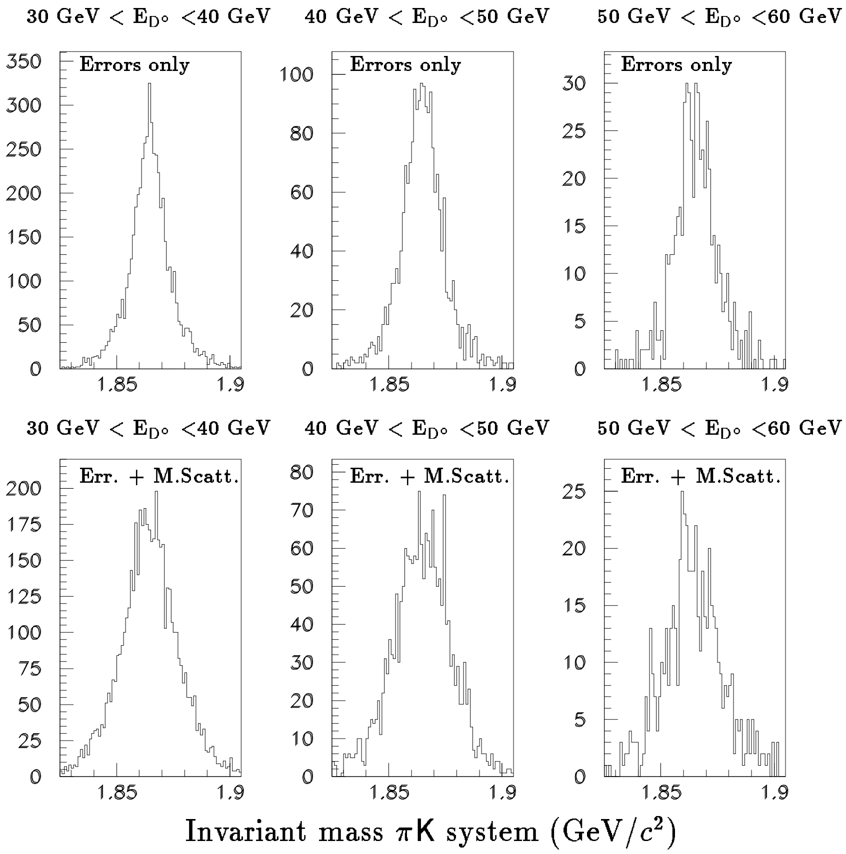

Figure 5.25: Invariant mass distribution of the πK from D° decays for three different D° energy ranges, when the π or/and the K enter the SAS. The upper row refers to the case where location errors only are taken into account. The second row refers to the "full" case (both multiple scattering and location errors are there).

Combining all the events entering the geometrical acceptance of the apparatus and within the kinematical cuts described in Section 3.1 we obtain that the invariant mass resolution for the $D^\circ \rightarrow \pi^+ K^-$ channel is essentially constant with energy and has a mean value of about 11 MeV/c^2.

5.2.6 The muon trigger hodoscopes

The trigger of the present NA47 experiment is based on horizontal and vertical hodoscope strips. Information about which strips fired is used (a) to select the kinematic region and (b) to determine whether a track points to the target. We propose using similar hodoscopes for the muon trigger of the COMPASS experiment. A muon trigger is also needed for the hadron programme, to identify semileptonic decays.

The large-angle spectrometer will contain two muon trigger hodoscopes, one (μHOD1) upstream from the muon trackers of the muon filter system and one (μHOD2) downstream from them. The hodoscopes will have 10 cm-wide scintillator strips in both the x and y directions; the strips will be read out by photomultipliers on both sides. Each hodoscope must cover an area of 18 m^2, which corresponds to about 180 channels per hodoscope.

For the small-angle spectrometer, we plan to use three muon trigger hodoscopes as a high-resolution *energy tagger* to detect muons in the deflection plane behind the spectrometer magnets. The first of these hodoscopes (μHOD3) will be located at the entrance window of RICH2. The second hodoscope (μHOD4), downstream from RICH2, will also be used to improve the target pointing. The third (μHOD5) will be located behind the muon filter system.

One problem is that this particular type of muon trigger depends on projections and is thus vulnerable to random coincidences in which signals from different particles simulate a scattered or decay muon that would be of interest. This will become much more severe at higher rates. In order to combat the problem and to withstand the higher beam rates, the hodoscopes μHOD3 to μHOD5 will require a finer granularity than NA47's present one of 10×10 cm^2. The 10×10 cm^2 area closest to the beam axis will therefore be covered by 1 cm-wide scintillator strips running in the x and y directions. The areas farther from the beam axis will be covered by 5 cm and 10 cm-wide strips, also running in the x and y directions. The hodoscope μHOD3 will cover 240×120 cm^2, while μHOD4 and μHOD5 will cover 400×200 cm^2 each. This yields a total of 532 channels for the three hodoscopes, assuming a photomultiplier read-out on both sides of every strip.

Certain regions have very high background from μ-e scattering. Including hadron information from HCAL2 in the trigger condition will help remove this background and eliminate radiative events. The New Muon Collaboration, using a similar set-up, achieved a trigger efficiency on the order of 90% (compared to the typical value of 30% when no hadron condition was involved). Requiring a muon candidate in the selected energy-loss window and a hadron with a minimum z cut will yield a trigger rate of less than 4000 events per spill. Summing up all other sub-triggers we arrive at about 10000 events per spill.

5.3 HADRON PROGRAMME

5.3.1 Beam Requirements

One of the most important issues for the hadron part of the program is the choice of beam particles. The present muon beam line can rather quickly be converted into a hadron beam by retuning after the removal of the hadron absorber. The present beam line layout, however, only allows beams up to about 300 GeV/c to arrive in the area. For most of the proposed running periods a beam energy of 300 GeV/c and an intensity of 10^8 per spill is foreseen. The particle composition has roughly been estimated by P. Grafstrom and is depicted in fig. 5.26. With rather modest modifications of the beam line it can be adapted to provide the necessary conditions to perform fast particle identification using either a set of CEDAR counters or the HYPOLIT RICH detector. In the following we will give a brief description of the needs for the different measurements:

For part of the program, mostly concerning the study of the incoming projectile, this question is easy to answer. Although a high intensity proton beam (400-450 GeV/c) is preferred to continue the study of central glueball production beam energies of 300 GeV/c should be sufficient to guarantee the expected yield. Most of the reactions based on the Primakoff effect have to be performed with π beams of various energies. For charm production, however, the choice is more difficult. Existing experimental results have already been presented in section 4.5 and will only shortly be repeated here.

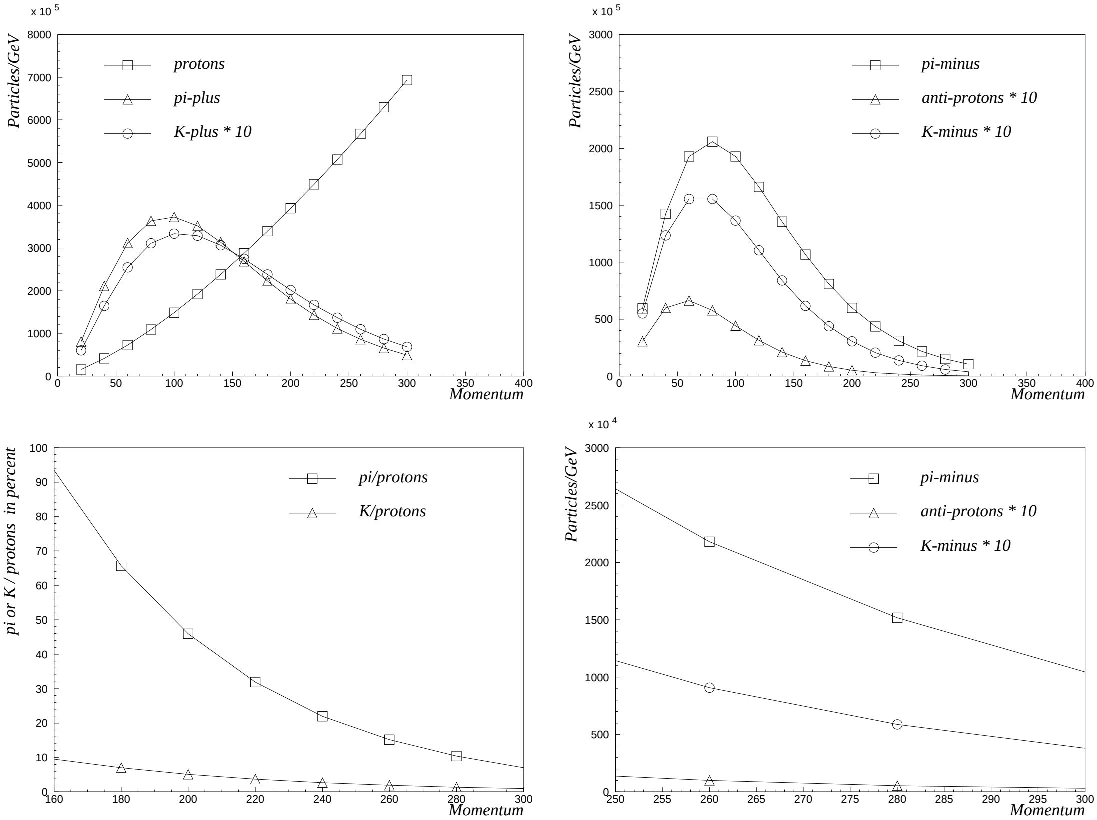

Figure 5.26: Estimate of the beam composition for the hadron beam. The figures were computed for 10^{13} protons per spill on T6 with 0.8mrad horizontal and vertical acceptance at 0mrad production angle.

According to calculations of perturbative QCD and results from π beam experiments the highest possible beam energy should be used for the production of charmed hadrons. However, there is good experimental evidence that the production of fast baryons is strongly enhanced in baryon beams. From these observations the choice of a 450 GeV/c proton beam is favourable. The choice of protons over hyperons or neutrons will probably hold for the topic of double charmed baryons. For a study of charmed hyperons, however, a Σ^- beam such as used presently in WA89 may be more useful. It should be noted, however, that the price to pay is a large background in such beams from π contamination and accompanying μ. Also the neutron and π background from beam particle decays in the detector will cause large damage to downstream calorimeters since no well defined 'beam hole' can be inserted.

Besides of the particle type, the beam energy is of great importance. Considering the results from "low energy" beams (50-70 GeV/c neutrons and 120 GeV/c Σ) where surprisingly large charmed baryon samples have been obtained, the choice of low beam momenta should be favoured. However, trigger and reconstruction of s.l. decays rely strongly on the observation of charm decays downstream of the first multiplicity counter or within the target detector, respectively. The requirement of long flightpaths can only be met by use of highest possible momenta. [1)]

---

[1] The low energy option should however be kept if possible. Smaller hyperon beam and proton beam momenta can for example be obtained by pre-extracting a lower energy proton beam from the SPS. This

While the installation of a beam line for primary and secondary beams of p, π and K does not pose any problems the construction of a 450 GeV/c proton beam or even a high intensity hyperon beam with about $2 \cdot 10^7$ Σ^-/spill is a larger effort. Although feasible, a change over involves a major modification in the full beam line and can thus not be performed on a regular basis. This is even more true for the creation of a high intensity hyperon beam which not only requires 450 GeV/c protons but also calls for large shielding to be set up in the experimental hall. Fig. 5.27 displays the rates which can be obtained if $5 \cdot 10^{12}$ protons are dumped onto the hyperon production target using a single bend hyperon beam. If the channel is designed for a maximum momentum of 400 GeV/c even primary protons (using a high duty cycle option) could be passed through after removal of the production target

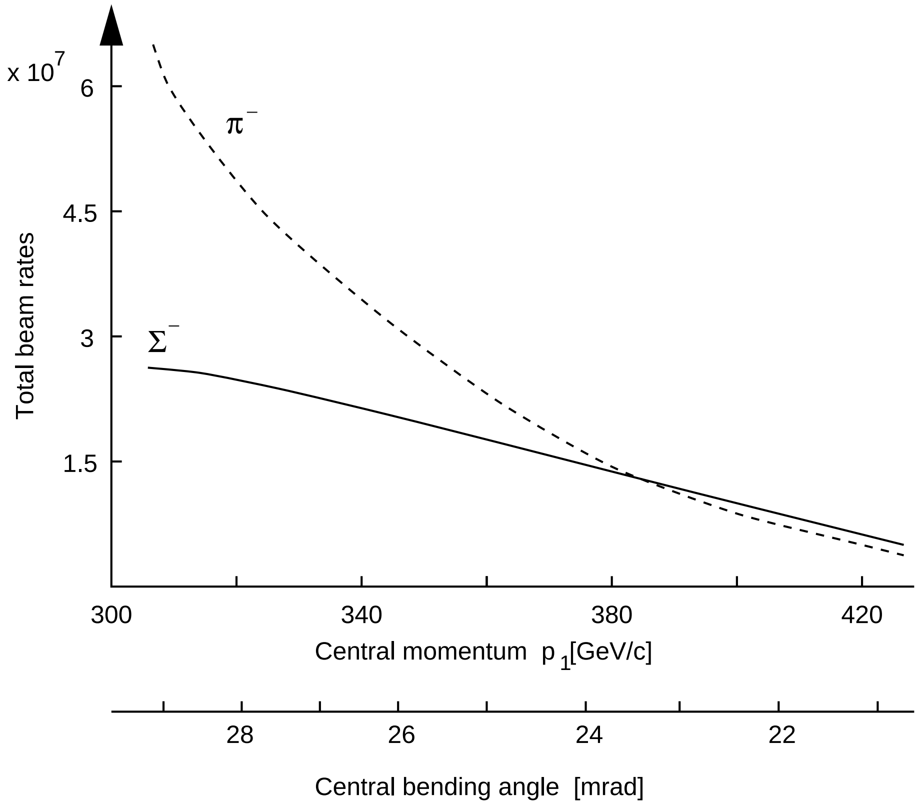

Figure 5.27: Hyperon beam rates for a single bend beam

5.3.2 Beam identification

When used in hadron mode beam particle tagging is needed to make use of the various particle species present in a mixed beam. This tagging has to be performed using fast Cherenkov counters[2)]. Two such counter systems currently exist:

The first system (CEDARs) uses a adjustable diaphragm to select only Cherenkov angles within a small range thus allowing to positively identify particles of a preselected type. At 300 GeV/c such a system shows a typical efficiency of about 50-60% rapidly increasing

---

has been done in the past and its only drawback is a 200 MHz bunch structure since no debunching can be performed.

[2] the prerequisite for their use is a section with parallel beam ($\Delta\theta \leq$ 100-150 μrad), as discussed in section 5.3.1

towards lower beam momenta. Two such counters can be used to provide tagging of two different particle species.

The other system was developed for the hyperon beam experiment WA89[3] and is a RICH allowing to measure the Cherenkov ring radii for many different particle types. To cope with large beam fluxes the system was designed such that Cherenkov light from π (typically the most abundant particle species) would not enter the photon detectors. This detector could be rejuvenated and equipped with new electronics to perform a fast ring detection (as was already provided for the WA89 experiment).

A different beam definition is needed for hyperons. It can be achieved using a fast TRD with active radiator.

A set of 9 silicon microstrip counters with 25 μm pitch reading 3 different projections is used to determine the position of the incoming beam particle (called Si-beam). Also a fast scintillating fibre hodoscope is used in order to tag the beam particle timing in case of pile up.

5.3.3 Target region

The charm vertex detector

In order to perform high precision measurements of lifetimes and to ensure a high charm tagging efficiency also for short lived hadrons, we must aim at the highest possible spatial resolution. Also highly efficient triggering on secondary vertices must be ensured. A layout of the target region is shown in fig. 5.28. The target is made from 4mm copper equivalent to about 2.5% of a nuclear interaction length and is placed about 30cm in front of the entrance of the first magnet. In order to select interactions in the target a thin silicon counter is placed at the downstream edge of the target. This counter can be segmented and is read by means of a fast preamplifier. For the detection of secondary vertices it is necessary to know the longitudinal position of the primary interaction with a precision of better than 1mm. One possibility is to replace the solid target block by a sandwich of seven 500 μm thick Cu sheets interleaved with silicon detectors of 150 μm thickness.

The target is followed by the first of two multiplicity counters (MUCs) to be used in the trigger (see trigger section). Both MUCs are made from 1mm thick MgF_2 read at all 4 edges by UV sensitive PMs also equipped with MgF_2 windows.

The design of the tracking detector following the target is based on the 'target detector' of the WA92 experiment [274]. It consists of two times 10 planes of silicon strip detectors with a pitch of 10μm and 20μm and a thickness of about 150 μm. The readout direction is alternating between horizontal and vertical (Si-target). All counters will be spaced by 1mm which will provide longitudinal vertex resolutions better than 75μm. The first counter will be located about 1mm downstream of the first MUC. The analog information from all channels will be read so that secondary interactions in the detectors can be isolated. Downstream of the 'target detector' the second MUC will be placed.

In order to obtain the desired interaction rate, two such set ups will be placed in series. They are followed by three more sets of silicon counters (Si-vertex). Each set consists of 2 double sided detectors 300 μm thick with orthogonal readout (6.3x6.3 cm^2). They are

---

[3] despite its well functioning the counter finally was never used

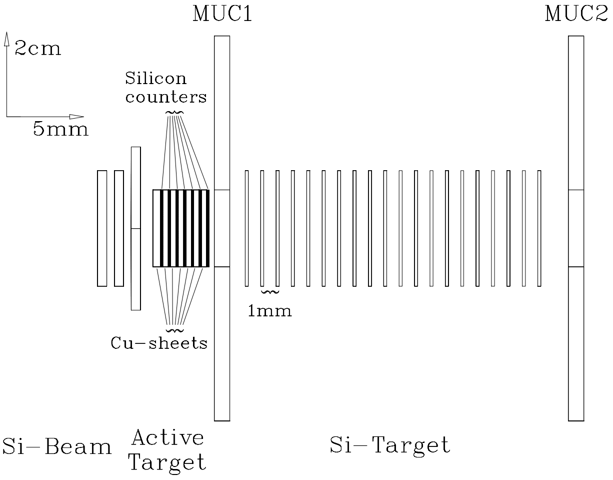

Figure 5.28: Side view of the target region

arranged in such a way that tracks are measured in 4 projections to allow track reconstruction in space. The alternative use of silicon pixel detectors is being studied. The advantage of fast and unambiguous track reconstruction in space is obvious (in particular for trigger purposes). Detectors with zero suppression and fast readout are currently being developed by RD19 [275]. However, it is not clear whether the desired readout speed can be achieved. Recently, small size pixel (500μ* 50 μ) mosaic detectors have been developed with readout at the sides allowing thin detectors ($\approx 300\mu$). If equipped with fast electronics 2 of these devices could even be used in the target detector. [276]
It should be noted that radiation damage will become a serious issue in such an experiment. Possible alternatives to silicon like GaAs or diamond are therefore being explored.

The LH_2-target system

For the central production measurements we will use the liquid hydrogen target with a recoil proton detector (RPD) used previously by the NA12/2 experiment.

The liquid hydrogen volume of the target is a 60cm long cylinder with a diameter of 6cm which will be reduced to 40cm and 4cm respectively. The side walls of the vacuum vessel are made of light composite material to minimise the undetectable energy loss of the recoil proton and decrease the momentum threshold of RPD measurement.

The recoil proton detector [277] consists of two rings of scintillating counters surrounding the target. The inner layer is made of 6 scintillator slabs of $65 \times 8.5 \times 0.5\text{cm}^3$ composed in a cylinder of 7cm radius. The outer layer is made of 24 slabs of $106 \times 20 \times 1\text{cm}^3$, the cylinder has a radius of 75cm. The scintillating light from each slab is collected by two photomultipliers (PM) attached to the opposite sides of the scintillator, Phillips PM2020 for the inner layer and PM2262 for the outer one. Both amplitude and arrival time are measured for all PM signals. The dedicated trigger electronics is used to select events with signals in both PMs of one inner and one outer slab consistent with one particle coming from the target. The difference of arrival times and amplitudes of the signals from PMs looking to the same slab provide information on the longitudinal coordinate with a precision of σ_X 3.2cm for inner and 3.8cm for outer layers respectively. The time of flight resolution is $\sigma_T = 350$ps. At a proton momentum of 350 MeV/c, corresponding to

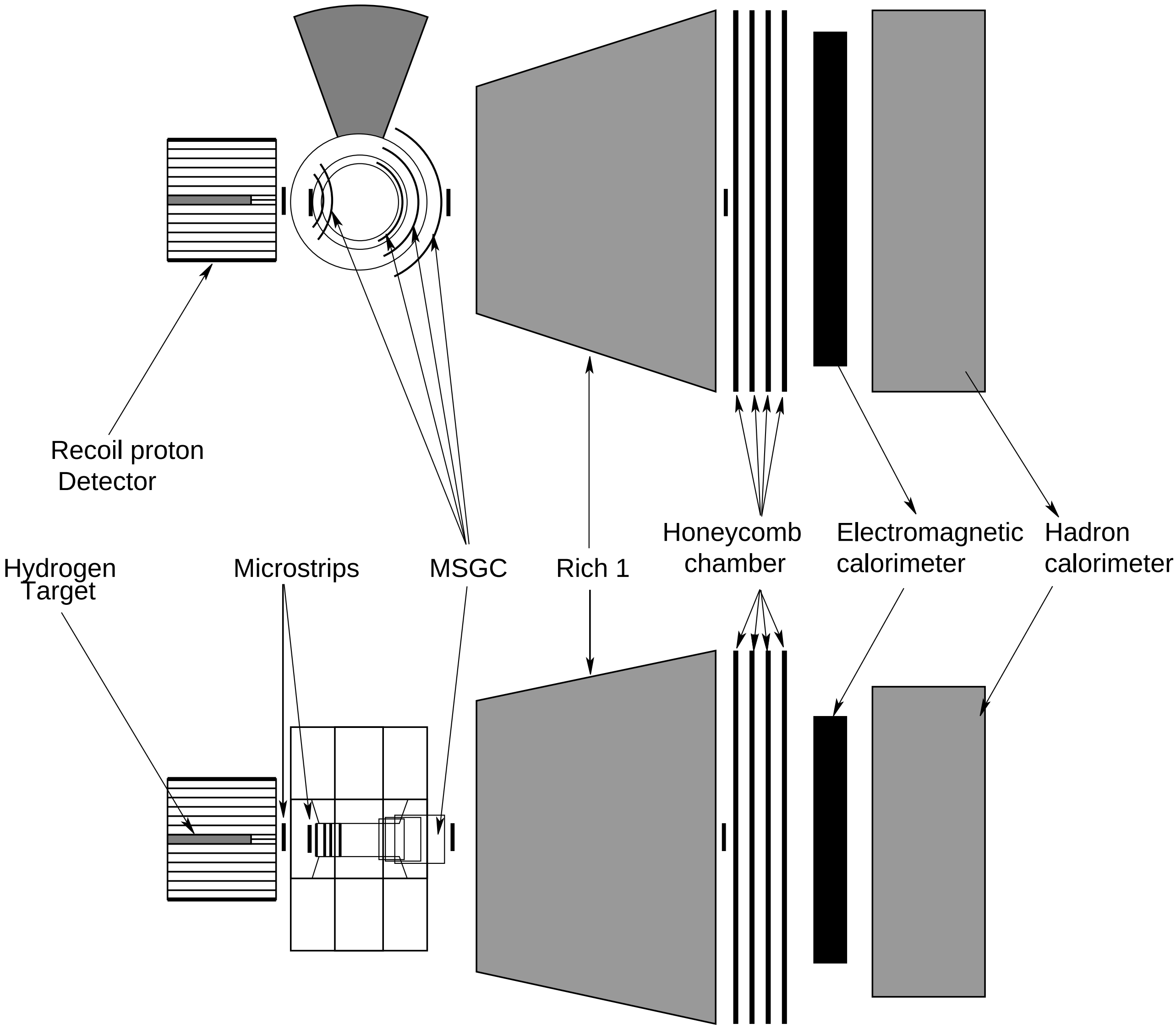

Figure 5.29: Top and side view of the large angle spectrometer for the central production setup.

the maximum in the momentum spectrum of the slow proton in the central production, momentum resolution is better that 5separation can be achieved up to 800 MeV/c.

5.3.4 The SM1h magnetic spectrometer

The SM1h magnetic spectrometer will be built around magnet MEP48, previously used in experiment PS170 at LEAR and now at SATURNE as part of the DISTO set up. It provides a field of 1.5 T in a cylindrical volume of 50 cm radius and 46 cm height. Cylindrical C-shape magnets suffer from large fringe fields leading to an effective field integral of about 1.8 Tm. On the other hand, the cylindrical form reduces the bending for low momentum tracks and thus the active area of the tracking detectors downstream of the magnet. Despite magnetic shielding the target centre has to be placed about

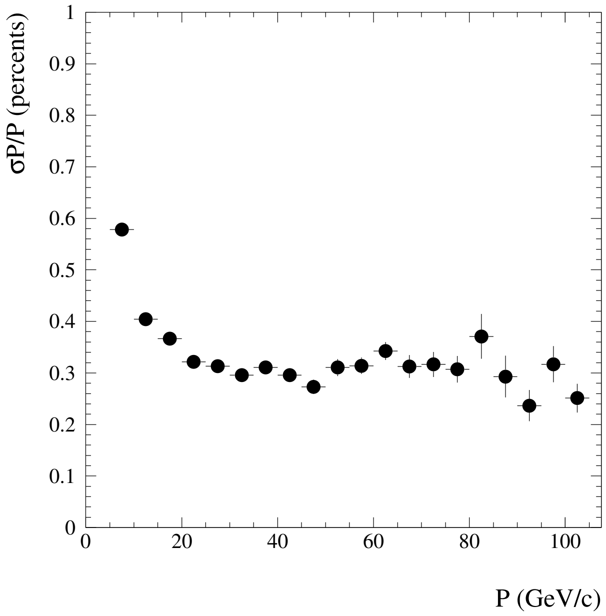

Figure 5.30: Momentum resolution of the full spectrometer in the HB setup.

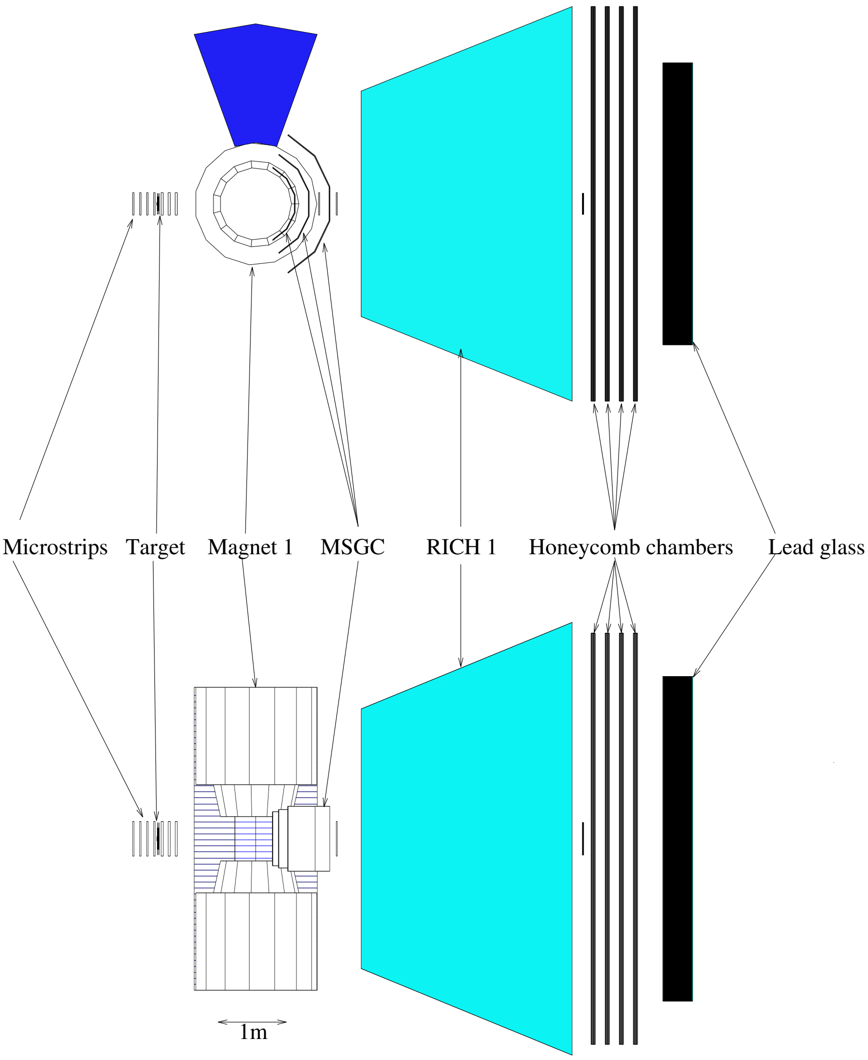

Figure 5.31: Top and side view of the large angle spectrometer for the charm programme.

1m upstream of the magnet in order to sit in a field free region. In order to keep the acceptance, we consider to raise the pole gap to about 60cm. As the field integral is rather low good spatial resolution is needed in order to obtain high momentum resolution. Upstream of the first magnet (SM1h) we intend to install large area MSGCs with 200 μm pitch and readout in three projections (MSGC-vertex). Two such MSGC-sets may be placed between Si-vertex and the entrance yoke of SM1h. The total size needed is about $50 * 25 cm^2$. MSGCs will also be used at the exit of the spectrometer to determine the angle of the outgoing particles (MSGC-SM1h). Three sets of MSGCs are mounted on concentric cylindrical surfaces. The cylinders are cut at $\pm 50^0$ and are spaced by about 50cm. MSGCs typically provide spatial resolutions of about $50 \mu m$. The cylindrical mounting reduces the number of tracks passing through the chambers at large angles for which the position resolution is considerably worse. The bending of high momentum particles with low p_T can be measured by a set of double sided silicon microstrip counters with an active area of 6.3x6.3 cm^2 (Si-SM1h). The first spectrometer accepts momenta down to below 1 GeV/c. We will also place 1-2 sets of of MSGCs in the field to help the reconstruction of low momentum Λ and K^0.

In order to improve the high rate performance of this system we also plan to place MSGCs into the central part of both detector sets (MSGC-M2). The momentum resolution obtained in the hadron beam setup using both magnetic spectrometers is shown in figure 5.30.

5.3.5 Microstrip Gas Chambers

Much progress has been done concerning the construction and operation of MSGCs for high energy physics experiments. This is documented in the status reports of the RD28 collaboration at CERN as well as in the proceedings of several workshops. MSGCs will be used extensively in the CMS experiment as well as in HERA-B.

The design of our MSGC system uses anode/cathode structures printed onto a 150 μm thick substrate made of Desag 202 glass. The anode pitch is about 200 μm, using 11 μm wide anode strips and 50μmdistance anode/cathode. In order to obtain high rate capabilities [278] the structure will be coated with a thin diamond like layer. The drift cathode will again be made from ordinary glass, again 150 μm thick. A gas gap of 3mm is envisaged. The gas used will be a mixture of Xenon/DME. In order to reduce aging effects, the MSGC structure will be made from gold strips. The drift cathode and backplane cathode will be made of thin aluminium. The size of one module will be about $10 * 25cm^2$. Using a thin glass frame the dead area can be minimised.

The anode readout will be performed at one end only allowing to stack two MSGC modules on top of each other. The readout chips will sit outside of the gas volume allowing easy mounting and a good sealing of the gas volume by glue. A total of about 250 MSGC modules will be needed to cover the required area.

In order to operate MSGC in the beam region it would be desirable to build small modules on plastic substrate thus reducing their thickness. However, not much research has been done with such substrates although their high rate capabilities using thin coatings have also been demonstrated [279]. We also consider the use of Micro Gap Chambers (MGC) [280] as an alternative. These detectors have been developed more recently and much less experience in their construction and operation exists. However, their performance, rate capabilities and aging characteristics look very promising.

5.3.6 Electron Identification

For the study of semileptonic decays, clean electron identification is very useful. Although not depicted in the layout 2.1 we are considering the implementation of a fast TRD into the set up. Such a detector would be placed between the RICH and the electromagnetic calorimeter. The TRD can be made using large area wire chambers in combination with radiator stacks. Alternatively we can use the design from RD6 [281], based on straw tubes embedded in a radiator foam. The latter scenario has the advantage that it can be used also downstream of the second spectrometer. The technique of straw tubes is very well developed and TRD-modules are now fabricated industrially for ATLAS. Typically, a 10-stage detector gives π-rejection of more than 2 orders of magnitude with high efficiency for electrons. As the inclusion of such a detector will require SM2 to be moved downstream by about 1-2m, it is again necessary to place the largest part of the detector on rails.

5.3.7 Trigger

In high intensity experiments one of the main challenges is the design of a fast trigger. Various steps are foreseen to achieve the necessary reduction. In order to avoid deadtime from complicated trigger scenarios we envisage a complete and fast buffering of all events into a large memory (see section 6). This leads to a derandomization and therefore allows deadtime free triggering as long as the trigger decision time for all events does not exceed the length of one accelerator cycle. A fast first-level trigger has to be implemented which reduces the event rate below $\approx$ 100 kHz, the limit for the serial data transfer. The size of the first stage event buffer is determined by the decision time of this first level trigger. Such a scenario is currently being installed for the NA48 experiment. Any trigger can run on the stored events and consecutive events can therefore be treated in parallel if necessary. The following section tries to sketch possible trigger scenarios for the different physics items addressed. (The term trigger is being kept although we mostly deal with event filters.) The front-end and DAQ are designed to allow trigger decision times of up to $\approx$ 800 ns of which about 300 ns are needed to accommodate for cable lengths and TOF.

Charm

This trigger clearly is one of the most challenging parts of the experiment. The very short lifetimes of charmed baryons make efficient triggering almost impossible. However, charmed baryons will mostly be produced in association with a long lived charmed meson on which such a trigger can work with higher efficiency. Some of the physics questions addressed even require the observation of the associated particle. Using high resolution silicon strip or pixel devices one can envisage a fast reconstruction of secondary vertices using either a hardwired processor as designed for WA92 or a fast high power CPU farm as currently set up for E781 at FNAL [282]. However, the foreseen interaction rate of about 1 MHz is far too large for such a system. We therefore envisage to reduce the trigger rate by about a factor 10 using other fast triggers. A simple cut on a minimum number of charged particles already reduces the number of interactions by a factor 2. Another factor 3-5 could be obtained by means of a multiplicity jump trigger depicted in fig. 5.32.

Using two thin solid Cherenkov counters right downstream of the target and spaced by a few centimetres we can detect decays of short living particles in the volume between the counters by comparing the total light produced in each counter. Such a trigger has been tested in E791 at FNAL giving very promising results [283]. The reduction is limited by two factors, one determined by concurring physical processes and the other one by the performance of the Cherenkov detectors. Considering the results from the E791 test we conclude that about 7-10 photons/PM should be observed per traversing track for high efficient multiplicity separation. The set up used can be improved using hybrid photomultipliers providing excellent single photon resolution and other crystals like PbF_2 or sapphire. The trigger rate caused by strange particle decays and secondary interactions between two Cherenkov counters is expected to be below 10% of all interactions. Since all charm decays useful for triggers lead to a multiplicity increase of 2 or more (about 60% of all D-decay modes) this jump has to be set to $\Delta\mu \geq 1.5$. Ideally, this should reject 95% of all ordinary interactions. However, the effective rejection is give by the resolution of the counters. Typical multiplicities in the detectors will be around μ=12. Assuming about 20 detected photons/particle we should thus reject about 80% of the ordinary events keeping more than 60% of the good events.

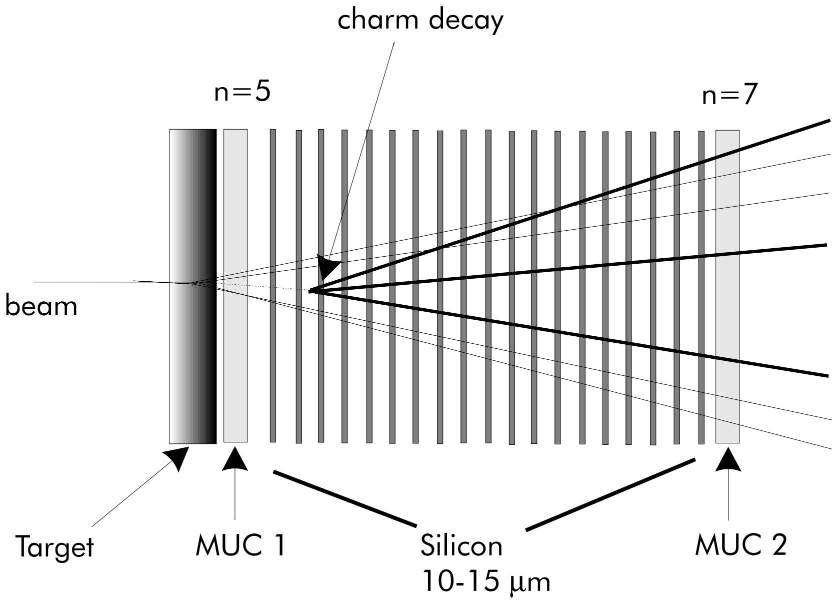

Figure 5.32: Sketch of the principle of the multiplicity jump trigger

Another quantity useful for rejection of non-charm events is the transverse energy E_t observed in calorimeters (used by E791 at FNAL [284]). A cut at about 8 GeV should retain about 70% of all charmed mesons reducing the total trigger rate by about a factor 4 [284]. Furthermore, it was studied recently that p_t could be a more powerful quantity. Further details will have to be studied also using WA89 data.
A fast beam TRD can give π rejection when used with a hyperon beam (as currently employed by WA89 [285]) resulting in another reduction of 3 for the interactions fed to a vertex processor.

In order to allow for double charm production in the silicon target, which is particularly appealing due to the short decay path expected for cc-baryons we have to complement the above trigger. Events with clear primary interactions in the target detector will be subjected to the E_t trigger. Since double charm events are expected to give larger $\overline{E_t}$ than single charmed, we can operate the E_t threshold at more than 10 GeV. Extrapolating the results from E791 we can reduce the background by about a factor 10.

Charm semileptonic decays

In addition to the two triggers mentioned above we can also use a trigger on semileptonic decays, based on the detection of the decay μ. From minimum bias events we estimated that $\leq$ 20% of all events are accompanied by a muon. Imposing a momentum cut off at 3-5 GeV (effective cut for the muon trigger) we are left with 7-5% of all events. The latter condition reduces the acceptance for semileptonic decays by only about 10-20%. WA92, searching for beauty decays, used a μ-trigger with target pointing and observed rejection powers of about 40 [134].
Using a fast TRD we may also complement this trigger by an electron trigger.

We also investigate the possibility of a multi-parameter trigger taking into account the information used for the individual triggers thus allowing a more adaptive trigger logic.

Central production

The central production trigger will be based on the specific kinematics of this reaction - fast and slow particles in the laboratory system, separated by significant rapidity gaps from all other particles. The slow particle will be detected by the RPD detector. The trigger electronics of this detector will select events consistent with only one particle coming from the target. The fast particle will be detected by the scintillating counter downstream of HCAL1. The counter will be segmented matching to the RPD segmentation and will have a hole in the beam region. These two trigger signals will provide a selection factor about 50 (estimated from the data of the central production experiments NA12/2 and WA91 using the same trigger scheme), sufficient to achieve acceptable data taking rate.

Primakoff reactions

Primakoff scattered particles emerge from the target with almost the incoming momentum and a very small scattering angle, typically 150 μrad. A fast trigger should therefore include the detection of the soft Primakoff photon to tag a reaction. A fast signal containing the energy sum of ECAL1 and ECAL2 can be obtained within 100 ns after passage of the beam particle. Together with a fast charged particle multiplicity signal from the multiplicity counters we thus arrive at a trigger rate well below the critical trigger rate of 100 kHz. We might also detect the scattering of the beam particle itself. This could be achieved using fast high resolution scintillating fibre detectors to reconstruct the beam track upstream and downstream of the target. We can require a minimum kink angle in order to select a scattering event.

6 READ-OUT ELECTRONICS AND DATA ACQUISITION

One of the features of the readout electronics and DAQ for the proposed experiment is that it will serve different physics programs with different detector setups. The amount of channels and the rate of the first level trigger (table 6.1) make the design of the system very challenging and require LHC type frontend electronics. A general structure of the DAQ system shown in the fig. 6.6. There are 250 000 channels in total (table 6.2). The frontend electronics is fully pipelined on the depth of 800ns in which the first level trigger decision takes place to achieve a rate of 100kHz. This defines the maximum bandwidth of the DAQ on the stage of frontends. The frontend system reads out all subdetectors in parallel, compresses the data reducing the size of the event to 20kB and stores it in huge dual port event buffers (6GB in total). The purpose of these buffers is to extend the readout time to the full SPS cycle and like that reduce the event building rate to 350 MB/s . The last stage of data processing is a multiprocessor machine where the data from different subdetectors is merged to complete events that will be passed through the online filter (second level trigger) with a reduction factor of 10 and written to the tape at 1.5 kHz (30MB/s). This corresponds to 2.6 TB of information being recorded each day.

PHYSICS	TRIGGER RATE kHz	DATA RATE MB/s	DATA RATE AFTER FILTER
Spectroscopy	100	3000	300
Charm	100	5000	500
Muon	4	200	200

Table 6.1: Expected trigger and data rates for the various periods.

DETECTOR	Number of channels	Occupancy %	Size, kB
Silicon & MSGC	140 000	2	9.0
RICH1 & RICH2	115 000	2	7.0
ECAL1 & ECAL2	8 000	10	3.2
HCAL	2 000	10	0.8
Honeycomb	45 000	0.5	1.0
MWPC		0.5	
Total			21.0

Table 6.2: Number of channels, average occupancy and data size per event.

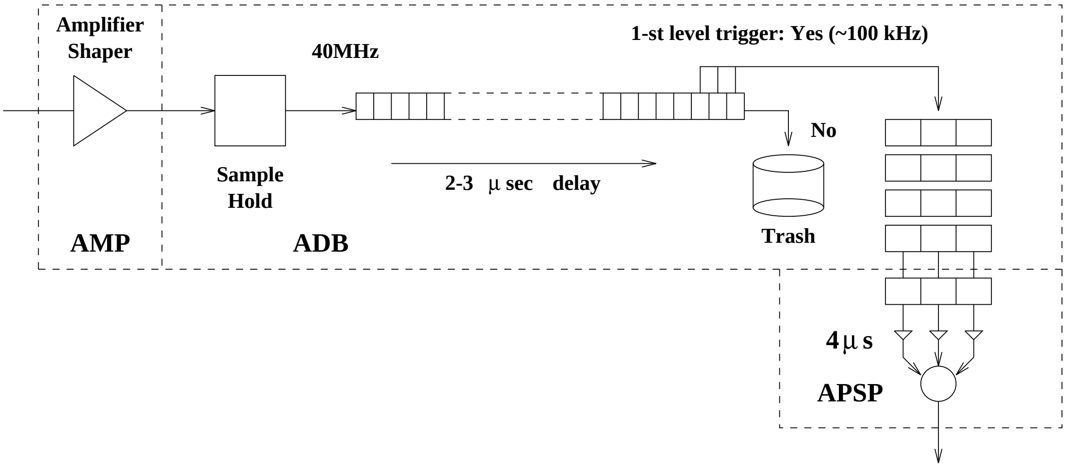

Figure 6.1: The RD20 chip layout.

6.1 Frontends

MSGC and silicon strip detectors

The high density microstrip trackers will be read out using the FELIX or APV5 chip designed within the RD-20 collaboration for silicon detectors [286]. Both chips exhibit a common architecture and practically have the same technical parameters. Here we concentrate on the description of the parameters of the APV5-RH chip.
The architecture of the chip shown in fig. 6.1. It provides full analog information important for the silicon target detectors and MSGCs. The analog buffer samples the signal at 40 MHz and delays it 1-2 μs in its pipeline in order to let the first trigger decision arrive. The signal from the detector will be distributed over 3 cells of the analog buffer due to the 50 ns time constant of the preamplifier and shaper . Detailed information on the APV5-RH chip is shown in tab. 6.3. The data from the chip (128 channels) can be transferred into a microstrip readout(MSR) board within 5 μs without deadtime using an internal multiplexer.

The MSR board will be located on the detector module itself and consists of 20 FADCs with 8 bit resolution, sparsifying logic and an optical interface (fig. 6.2). Choosing this location of the board dramatically reduces the amount of cables and simplifies the layout of the DAQ setup. The minimum functional requirements for the MSR board are digitisation of analog data received from the preamplifier chip, and compression of these data by suppressing the channels with a low pulse height. However one has to take into account that the amount of data transferred to the DAQ in one event is limited by the bandwidth of the optical link. Therefore it is necessary to implement additional functions on the MSR board to avoid overloading the interface in case of big fluctuations of the hit multiplicity:

- pedestal subtraction;
- common pedestal shift correction;
- masking of hot channels;

GENERAL	
Chip Size(WxLxH)	6.35 x 11.15 x 0.4 mm
Number of channels	128
Clock speed	40 MHz
Minimum Readout time	4.7 μs /event
Supply Voltage	$\pm 2V$
Power Consumption	256 mW
AMPLIFIER and SHAPER	
Input pad pitch	44 μm
CR-RC time constant	50 ns
Noise	550 e + 50 e/pF
Linear input range	0 - 4 MIPS
Gain	50 mV/MIP
Calibrating inputs	43 fF, every 4-th channel
PIPELINE	
Length	160 cells
Event depth	5 to 8
Trigger latency	$\leq 3\mu sec$
APSP	
Time resolution	25 ns
	3 samples at t0-1,t0,t0+1
Peak value	4-th sample
MULTIPLEXER	
Communication speeds	5,10,20,40 MHz, programmable
Output modes, selectable	- 128 channel serially
	- 128 consecutive samples
ANALOG OUTPUT	
Charge gain	50 mA/MIP
Rise time	10 ns
Type	differential current mode
DC range	$\pm 1V$
DIGITAL I/O	
Clock trigger	differential
Other inputs	$\pm 1V$
Outputs	open drain

Table 6.3: Specifications of the APV5-RH chip

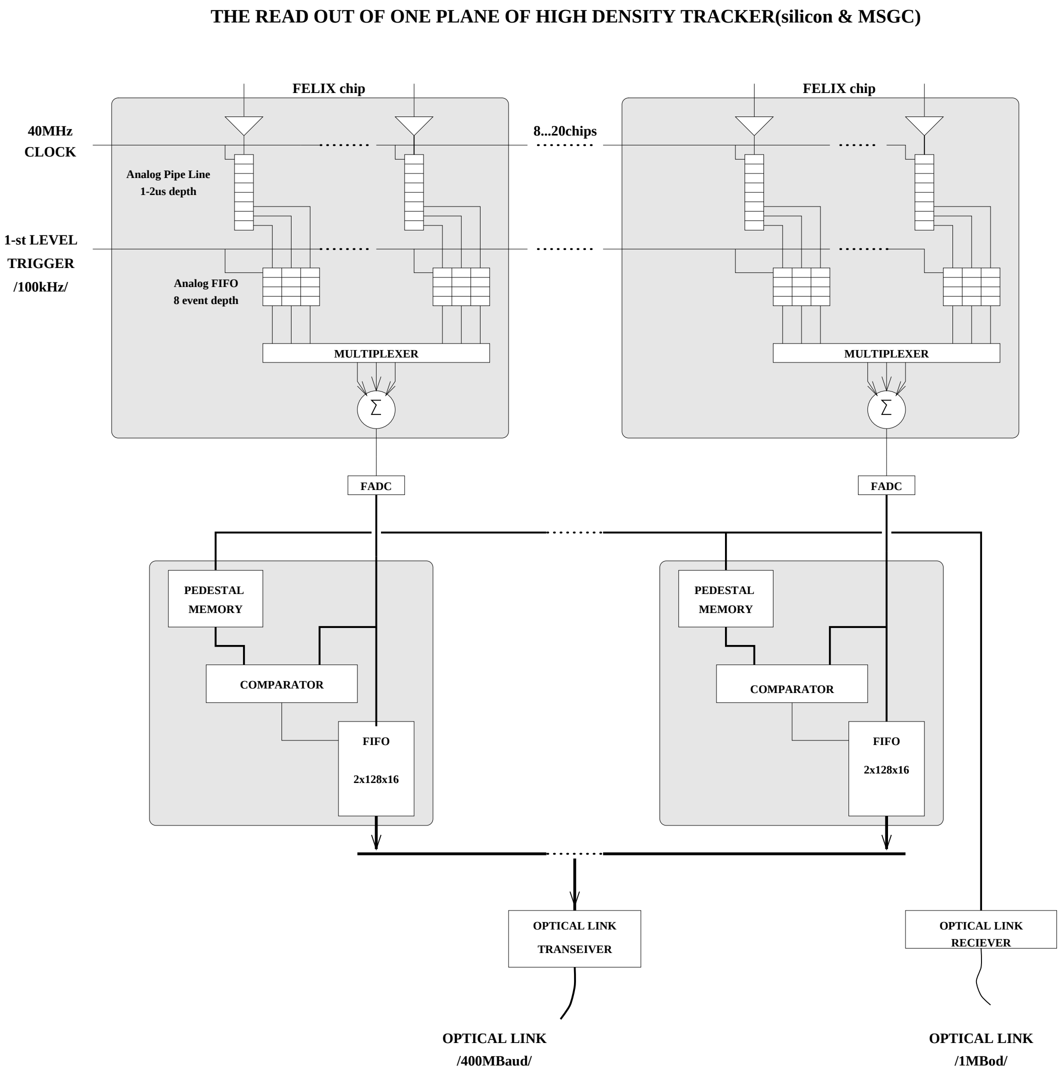

Figure 6.2: The readout scheme for MSGCs and silicon trackers.

- cluster finding and zero suppression;

We foresee the following parameters for the MSR board: The maximum number of the APV5-RH chips connected to one board should be 20 corresponding to 2560 channels. The maximum number of hits to be read out after zero suppression will be 60 or 120 depending on the bandwidth of the optical link ranging from 20 to 40 MB/s.
According to the architecture of the DAQ the data from all subdetectors will be stored in VME dual port memory (DPM) modules. In case of the microstrip detectors this will be a custom designed module with four optical links and 200 to 400 MB of memory.

RICH detectors

For the analog readout of the pads of the MWPC photon detectors, we foresee to use the frontend scheme included in the GASSIPLEX chip complementing it with:

Technology	1.0 μ m CMOS Sea-of-Gates(TC140G)
Digitisation step	1.14 ns/bit
No. of channels	4 ch
Recording range	4 μ s
Power Supply Voltage	3.3 V
Number of Gates	30 000
Feedback Circuit	Digital Phase Lock Loop
Encoding scheme	14 bit to 4 bit(rising edge only or both edges)
Double Pulse Resolution	16 ns

Table 6.4: Main features of the TMC4004 chip

- either an analog buffer integrated in the front-end chip (4 event deep)
- or with a separate analog buffer chip.

The relatively long peaking time of the GASSIPLEX can be used as a built-in delay to match the trigger timing.

The treatment of the analog information (FADC, pedestal subtraction and zero suppression) and the following buffering will be done as for the microstrip trackers.

Honeycomb chambers

The signals of honeycomb chambers have to be fed into TDCs after amplification and discrimination has been performed on detector mounted cards. Fast TDC-chips without conversion time are currently being developed. The TMC4004 [287] e.g. operates at a 40 MHz cycle. The time within a cycle can be measured with about 5 bit accuracy (1-1.5 ns). The other main features are summarised in table 6.4. After pipelined encoding the information is fed into a FIFO from where the relevant clock cycle information for valid events (1-st level trigger) is extracted into a 16 event deep buffer. This chip performs zero suppression and presents the data for a multiplexed readout of 64 channels. Currently 64 TDC channels with the described logic can fit onto one 9U VME module. Each VME crate with 16 TDC modules will be read out by a VME master module with enough memory to store all data from one spill.

Calorimeters

The total number of readout channels of the four calorimeters ECAL1/2 and HCAL1/2 is 9000. The signals are transferred via 70m long special coaxial cables to the readout electronics.

The main part of the frontend electronics is located in VME crates containing readout modules for analog signal processing and digitising, fast control distribution modules and VME master modules. The readout crates will be of the VNX9 standard with 9U size boards. We plan to mount 32 ADC channels on one board with a dimension of 9U×400 mm and have 16 readout modules per crate. There will be a total of 21 VME crates for the four calorimeters.

The actual readout module provides analog signal processing, digitising, zero suppression

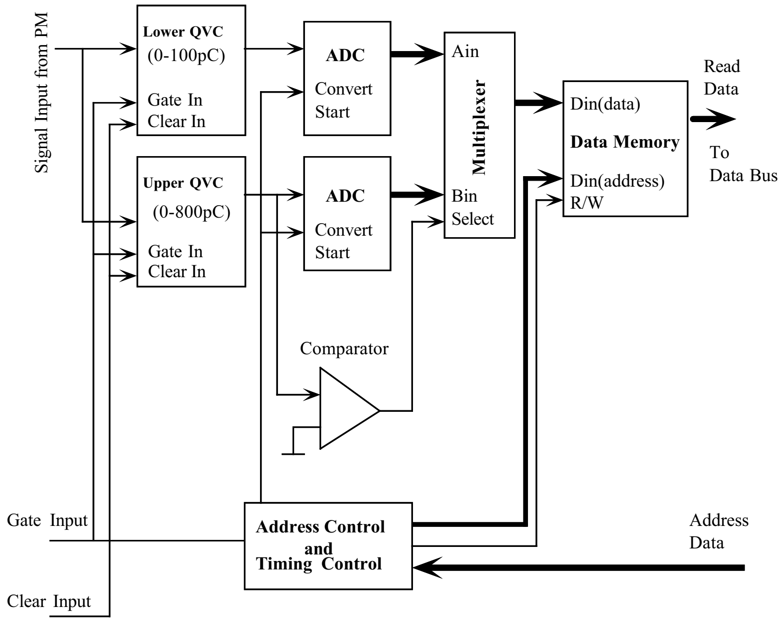

Parameters of QVCs
Lower QVC ; Relative Gain=4/1 C(hold)=100pF
Upper QVC ; Relative Gain=1/1 C(hold)=200pF
Lower QVC : Upper QVC=8 : 1

Figure 6.3: Layout of one QVC chip.

and temporary data buffering. The scheme of a readout module is shown in figure 6.4.

We are currently investigating two different approaches to realise a derandomization buffer, the analog buffering approach and the digital buffering (figures 6.5a and 6.5b). Both approaches have advantages and disadvantages and the design of the readout module depends on the choice of the derandomisation buffer. In both schemes there will be a FIFO buffer to store 8-16 events after analog processing and digitising. In the case of analog buffering it will be one FIFO memory for each channel with a depth of 8-16 19 bit words (13 data bits, 6 address bits), while with digital buffering one FIFO memory per group of 8 channels with a depth of 64-128 16 bits words (13 data bits, 3 address bits) is needed. The time until the raw data of one event is stored in the FIFOs after digitisation etc. is 2-3μs . Calibration signals for the analog part using a 16 bit DAC controlled via VMEbus is provided, as well as test and debugging lines. Zero Suppression is achieved by pedestal subtraction and selection of channels with useful information in three parallel streams. The time for the treatment of the raw information of 48 channels is approx. 2.5μs (0.15μs /word). This includes the time for the packing of 3 20 bits words to 1 64 bits word and loading into FIFOs.

To calibrate the detector all channels have to be read out for special triggers. This large amount of data is stored in a dedicated memory during the spill which is read out after the end of the burst via VME so that it does not interfere with the normal flow of data.

A fast control distribution module (FCD) provides all of the high speed timing signals required for the selection, synchronisation, and identification of data. These functions include fast reset, initialisation, synchronisation, clocking calibration, triggering and busy indications. The FCD module is a VME card that receives high-speed signals from the fast control system and repeats the signals on the crate's VMEbus. This card is designed either to drive directly the signals received from the outside or to generate these signals

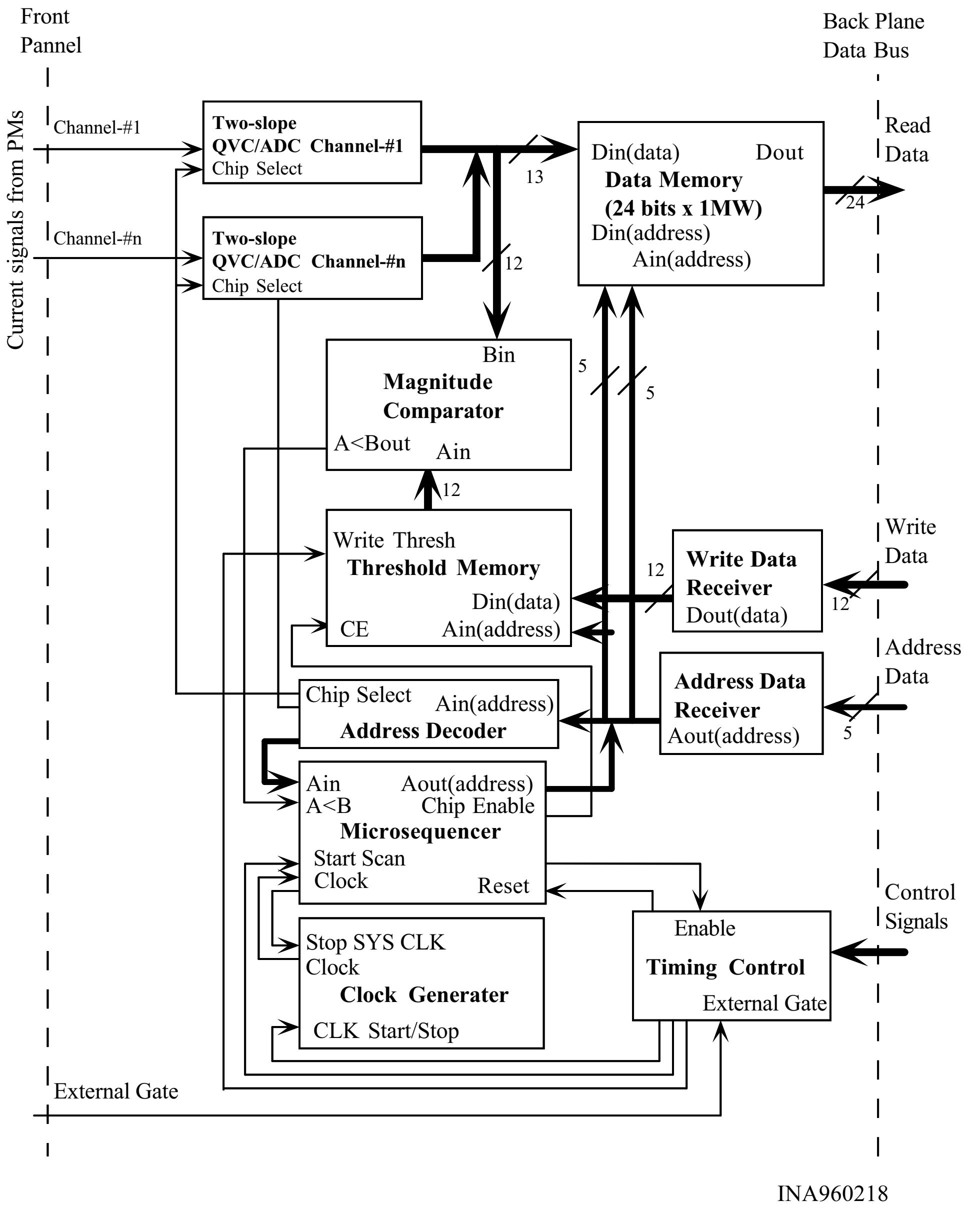

Figure 6.4: Possible layout of a QVC frontend module for the calorimeter readout. A second option would have a FIFO memory instead of the large data memory inidcated on the top right.

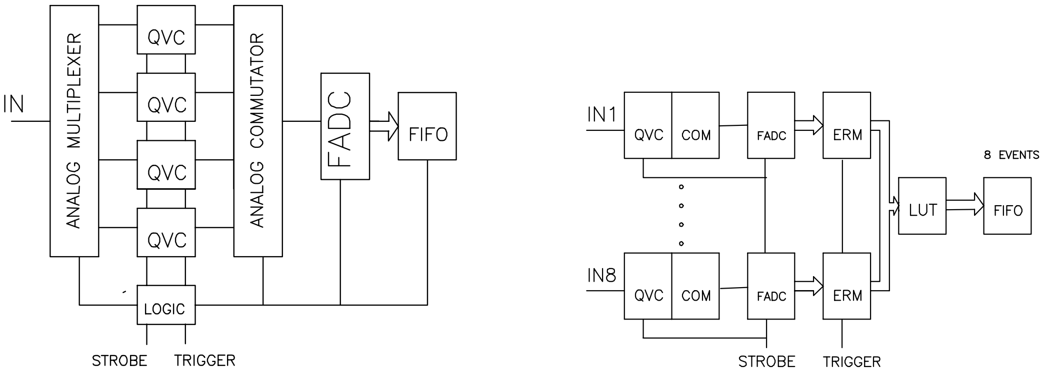

(a) Analog buffering (b) Digital buffering

Figure 6.5: Two approaches to realize a derandomization buffer for the calorimeter readout.

Number of Channels	16-ch or 32-ch.
Analog Input	Negative Uni-polar Input. 0– -300pC. DC coupled.
Input Impedance	50Ω
Dynamic Range	14 bits (combining two QVCs of different range into one)
Linearity	11 bits (consists of discrete components) 10 bits (made by Semi-custom IC)
Resolution	0.25pC/count
Conversion Time	$3\mu s$ (all channels in parallel)
Gate Input	50–200 nsec NIM standard signal
Reset Input	50 nsec NIM standard signal
Reset Time	500 nsec
Remaining Pedestal	about 50 counts

Table 6.5: Design parameters of the ADC module for Calorimeters.

under program control through VME. This latter capability is needed to perform stand-alone operation and calibration of the system.

6.2 DAQ computer

Once the data of one spill is stored in dual port memory modules it is transferred to the data acquisition machine which filters the events for valid physics topologies, performs the event building and then writes the data to tape. The advantage of putting all steps into one machine is the flexibility and transparency of the flow. The system we propose consists of components that are already now available on the market, all based on the widely used PCI standard. The basic layout of the data flow is shown in figure 6.6.

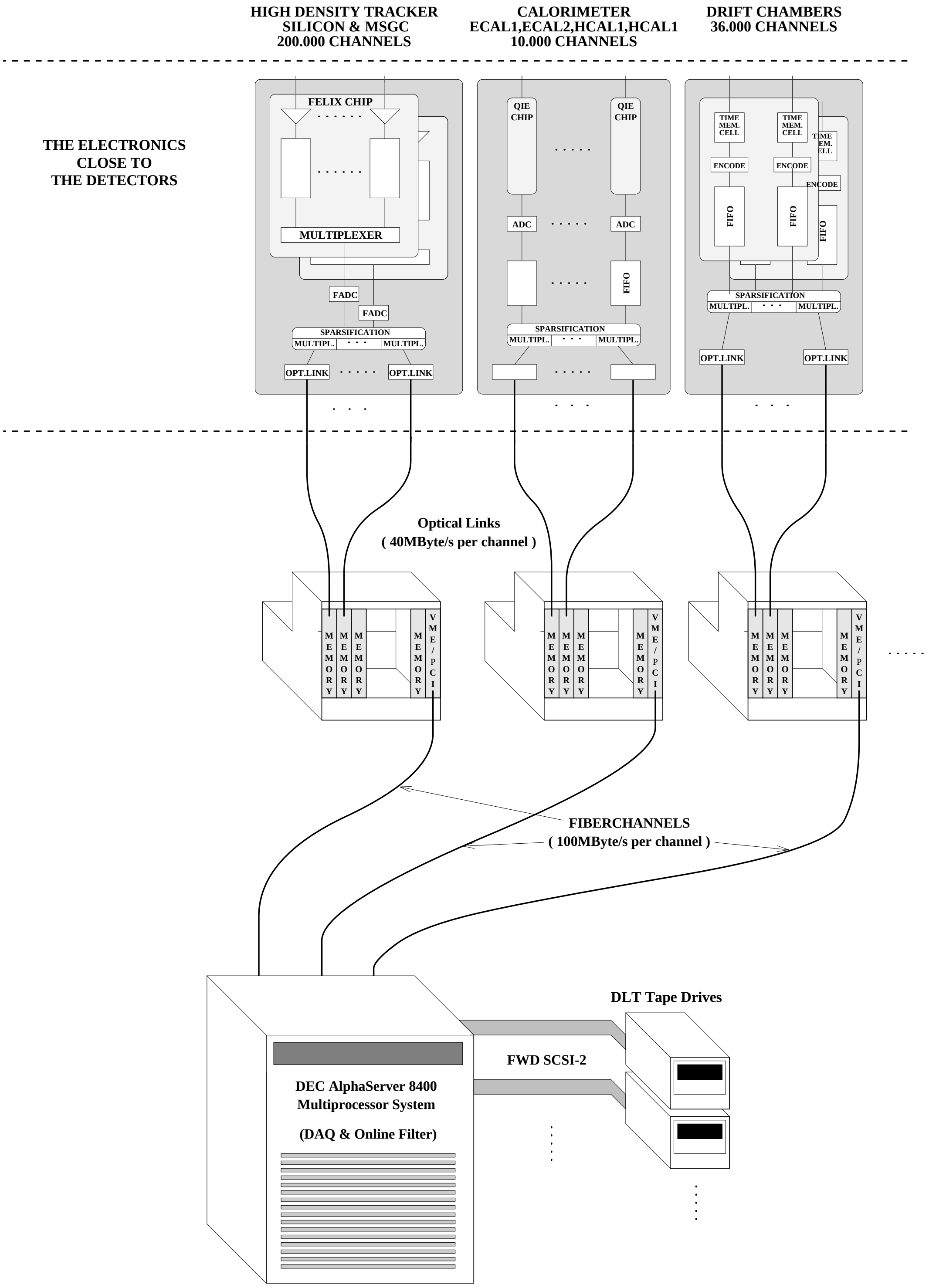

Figure 6.6: The data flow of the proposed data acquisition system.

Data transfer

The frontend readout will be performed by VME master modules providing a link to high speed interfaces via the PMC (PCI Mezzanine Card) standard. A possible master is the MIDAS 100 system developed by VMETRO Inc., Houston, which combines all necessary features:

- One module can have 4-64MB RAM expandable to up to 896MB. This allows a tailored memory architecture for all detector types and frontends.
- A fast i960RP processor provides functionality as data compactifier, memory controller and DMA controller offering a real time operating system like VxWorks.
- A VMEbus speed as high as 80MB/s allows the fast readout of standard VME TDCs and ADCs. An optional RACEway interface using the auxiliary P2 VMEbus adds another 132MB/s of bandwidth for VME readout.
- The module can hold up to 5 PMC modules serving as interface to the frontends on one side and to the DAQ computer on the other side via optical links.

Standard fibre optical links are used to connect the detector readout electronics to the memory modules. A transfer speed of 20-40MB/s is fully sufficient since there will be 50-100 of these links. Once data is available in the memory modules the VME masters will transfer the data via high speed links with a rate of up to 60MB/s to the DAQ computer. Since the data transfer can take up to 12s the total transfer rate needs not to exceed 400 MB/s.
There are currently several similar link technologies under development which achieve rates of around 100MB/s. The status of the relevant projects allows to project full availability of standard components in two years from now:

HiPPI High Performance Parallel Interface. At CERN the Digital joint project and NA48 have developed a HiPPI-PCI interface and ran benchmark tests reaching 93MB/s sustained data rates. HiPPI PMC cards are scheduled to be released this year by several companies. The HiPPI is available on copper cables for short distances and optical fibres for distance up to several kilometres.

FCS Fibre Channel Standard. This standard offers bandwidths from 133Mbit/s up to 1Gbit/s. The Fibre Channel can operate as channel interface as well as network interface and can run various higher level protocols.

SCI Scalable Coherent Interface. An even more advanced standard is SCI which is a combination of processor-memory-bus and local area network. designed for parallel multiprocessing at very high bandwidths of 1GB/s and more. The CERN project RD24 has developed a first PMC-SCI-card which operating at 200MB/s. This would be already fully sufficient for our needs although SCI aims higher.

Event filtering and storage

As the central piece of the DAQ system we propose a multiprocessor system like Digital's AlphaServer 8400 or other systems with similar performance. This machine should digest

Link	Possible output rate	Possible input rate	Required bandwidth	Readout time	Channels
Frontend - memory	20-40MB/s	20-40MB/s	20-40MB/s	2.5s	50-100
Memory - PCI slot	100MB/s	60MB/s	40MB/s	14.4s	12-48
PCI cage - internal bus	100MB/s	100MB/s	100MB/s	14.4s	4-8

Table 6.6: Data rates and band widths of the readout system. The onspill rate is 2GB/s, the offspill rate 350MB/s

Processor	Availability	Frequency	SPECint92	CERN units[1]	time/event
MIPS R4400	now	150MHz	90	19	3.7ms
MIPS R8000	now	180MHz	132	28	2.5ms
MIPS R10000	1996	200MHz	300	80	0.88ms
MIPS R10000	1997	275MHz	413	110	0.64ms
DEC AXP 21164	now	300MHz	340	90	0.78ms
DEC AXP 21164	now	350MHz	433	115	0.61ms
DEC AXP 21164A	1996	417MHz	500	125	0.56ms
DEC AXP 21264	1997	500MHz	600	150	0.47ms

[1] estimated

Table 6.7: Comparison of processors available now or in the near future.

the incoming data, process all events and filter out interesting topologies. The valid data is then written to tape. The architecture of this machine is the following: The internal bus has 9 I/O ports of which 6 will be used for the CPU boards with two AXP 21164 processors each and one for the standard I/O board connecting to networks, disk drives and tape units. One port will take a memory board with 2-4GB memory. The remaining port is used for a 400MB/s adaptor to four PCI cages with a total of 48 PCI slots. Each PCI connection can take up to 60MB/s, one cage combined can amount to 100MB/s. This architecture already allows to absorb the expected offspill rate of 350MB/s (s. table 6.6).

The next step in the data flow is the filtering of the events, which will be needed by the charm physics part of the experiment to go down a factor of ten in the number of events to record to tape. The filtering will be done in parallel by the 12 processors of the DAQ computer. Experiment E781 at Fermilab has designed a similar system. The algorithm is comparable to the one we are planning to use. The basic idea is to reconstruct tracks in the microvertex detector, locate the primary vertex and look for tracks that have an impact of 30 microns or more to the interaction point. The E781 algorithm is supposed to process one event in 3.7ms on a MIPS R4400 processor at 150MHz. First tests with a not yet fully optimised algorithm gave a processing time of 7ms per event on the same processor. Table 6.7 shows a comparison of processors available now or in the near future. It is clear that already with twelve AXP 21164A processors at 417MHz the required maximum time of 0.69ms per event can be safely kept and the margin is even bigger with the expected AXP 21264 processor. An additional advantage of the AXP processors over the MIPS R4400 which has not been considered in the calculation is the fact, that the AXP chip has 4MB on board memory allowing the storage of all necessary date and code to process an event without further I/O.

The final step is then to write the remaining 10% of data to tape, which requires to handle 500MB per spill. Currently there are two technologies on the market, that can be considered.

- The Digital Linear Tape standard currently offers tape writing speeds of 3MB/s and tape capacities of 20GB per medium with the DLT4000 drive. Quantum Inc., CA has announced for this year the DLT7000 drive with 5MB/s speed and 35GB per medium. With this type about 10 drives would be needed to safely handle the expected data flux. However it is necessary to have two to three FWD SCSI-2 interfaces to cope with the rate to be written to tape. One period of 100 days of data taking would produce 4000 DLT tapes.
- A more sophisticated solution would be to use the SONY DIR-1000 tape drive along with a driver by Myriad Logic Inc., MD which provides a 384MB buffer and a HiPPI interface to ensure the full possible rate of 32MB/s at 100GB per medium. Currently a new drive with 64MB/s is under development by SONY, which could still be safely fed by the Myriad driver via HiPPI. One would then need only one drive to store the data and have 720 large 19mm ID-1 tape cartridges from one period of data taking.

An additional option which should be considered in case of the use of 10 or more DLT drives is the buffering of the valid data on a large disk array connected to the DAQ machine via a HiPPI link. This would allow the decoupling of the data stream to tape from the DAQ stream which would be helpful in the case of tape drive failures.

Summary

Although the design of the DAQ for the proposed experiment is a challenging task, the basic components to build this system are available on the market right now or within the year. Further probable improvements will increase the safety margin of the proposed system.

7 COST ESTIMATE

The cost estimates for the parts of the apparatus that have to be either bought or newly built are given in this section, as well as the responsibilities of the various institutes for the different equipments.

7.1 Estimate for the Cost of the Equipments

The honey-comb trackers

A honey-comb detector was assumed to consist of six planes arranged in three or four orientations. each plane consisting of two layers of wires, to cover the dead regions between the cells. The total system will consist of about 50000 channels, as discussed in Section 5.1.3. The estimated cost of the system is given in table 7.1. We assumed everywhere anode wire readout (cathode readout of strips is in principle more expensive per wire). We also assumed we can benefit of the development work on the read-out, foreseen for ATLAS, which is expected to bring down the cost of the electronics/channel to from the present 100 CHF/channel (ASD8+LeCroy+cables) to 30 CHF/channel.

Equipment	Description	Cost (kCHF)
Chambers	pocalon foil	100
	wire clips	100
	blocks, wire, templates	100
	preparation manpower	200
	production manpower	300
Electronics	ASD8+TDC-chip (30 CHF/channel)	1500
	development+production manpower	500
Alignment		100
Total		2900

Table 7.1: Price estimate for the honey-comb chambers.

The Multi-Wire Proportional Chambers

The cost of multi-wire proportional chambers as presented in table 7.2 is mostly due to the purchase of new frontend electronics. Concerning the construction costs only the chambers around SM1m have to built new, the chambers for SM2 exist already.

Description	# channels	Frontend electronics	Construction	Sum
4 det. inside SM2 (à 2256 wires)	9024	720		720
1 det. downstream of target (.9x.8 m^2)	6000	480	120	600
2 det. upstream of SM1m (1.2x2.0 m^2)	12000	960	240	1200
Total				2520

Table 7.2: Price estimate for the MWPC. All values are given in kCHF.

The RICH detectors

Costs have been estimated for the various components of the RICH detectors assuming the dimensions and construction parameters described in section 5.1.5. For those items for which an alternative possibility is mentioned, the cost estimate is done assuming the default choice. Costs are scaled to 1996 price rates. They are given in table 7.3.

The costs of the radiator gas systems and the chamber gas system are derived from the Omega experience: a possible use of elements of the Omega system could lower this cost to 100kCHF.

The mirror cost is estimated to be about 40kCHF per m^2, From Fermilab (SELEX-RICH) and CERN (Omega-RICH) experience, the major part being for grinding and polishing.

The cost of the CsI MWPCs is scaled from the cost of a small prototype presently under construction in Trieste and has been cross-checked with RD26 experience.

	RICH1	RICH2
radiator - gas system (*)	300	100
radiator - vessel	150	150
mirrors	900	400
MWPC photon detectors	515	260
UV transparent windows (quartz)	240	120
windows mechanics	60	30
MWPC gas system (*)	100	-
MWPC read-out	690	460
total	2955	1520

Table 7.3: Cost estimates for RICH1 and RICH2; units are kCHF. (*) the monitoring system and the MWPC gas system are in common

The electromagnetic calorimeters

The cost estimate for the lead glass electromagnetic calorimeters is based on the current prices of components. For the existing equipment all prices are approximate.

Equipment	description	existing CHF	new CHF
GAMS-4000 cell	lead glass	350	
	PMT FEU-84	180	
	HV base	40	
	cable and connector	85	
	ADC electronics		240
	total (per channel)	655	240
	total (4096 channels)	2700k	980k
GAMS-4000 general	monitoring system		120k
	mechanics	600k	
	total GAMS-4000	3300k	1100k
OLGA cell	lead glass	500	
	PMT	350	
	HV base	40	
	cable and connector	85	
	ADC electronics		240
	total (per channel)	975	240
	total (330 channels)	310k	80k
OLGA general	monitoring system		30k
	mechanics		200k
	total OLGA	310k	310k
ECAL1 TOTAL		3610k	1410k

Table 7.4: Cost of the first electromagnetic calorimeter ECAL1.

Equipment	description	existing CHF	new CHF
GAMS cell	lead glass	350	
	PMT FEU-84	180	
	HV base	40	
	cable and connector	85	
	ADC electronics		240
	total (per channel)	655	240
	total (2000 channels)	1310k	480k
PWO cell	crystal		500
	PMT Hamamatsu		350
	HV base		60
	cable and connector		80
	ADC electronics		240
	total (per channel)		1230
	total (1000 channels)		1230k
75x75 cell	lead glass	400	
	PMT	300	
	HV base	30	
	cable and connector	70	
	ADC electronics		240
	total (per channel)	800	240
	total (700 channels)	560k	170k
general	monitoring system		120k
	mechanics		500k
ECAL2 TOTAL		1870k	2500k

Table 7.5: Cost of the second electromagnetic calorimeter ECAL2.

The hadron calorimeters

Equipment	description	existing CHF	new CHF
MHC-200 cell	Fe+Sc	2000	
	PMT FEU-84	180	
	HV base	40	
	cable and connector	80	
	ADC electronics		240
	total (per channel)	2300	240
	total (200 channels)	460k	48k
Dubna cell	Fe+Sc	1500	
	PMT FEU-84	180	
	HV base	40	
	cable and connector	80	
	ADC electronics		240
	total (per channel)	1800	240
	total (400 channels)	720k	96k
HCAL1 general	monitoring system		20k
	mechanics		200k
HCAL1 total		1180k	364k

Table 7.6: Cost of the first hadron calorimeter HCAL1.

Equipment	description	existing CHF	new CHF
HCAL2 cell	Pb	400	
	Scintillator	190	
	WLS	30	
	PMT FEU-84	180	
	HV base	25	
	cable and connector	80	
	monitoring light source	20	
	machining and assembly		300
	ADC electronics		240
	total (per channel)	925	540
	total (800 channels)	740k	430k
HCAL2 general	mechanics		60k
HCAL2 total		740k	490k

Table 7.7: Cost of the second hadron calorimeter HCAL2.

The muon filters

The muon filters are made up with Fe absorbers and μ trackers, as described in section 5.1.8. Number of channels of the trackers and cost break-up are given in Table 7.8.

Equipment	Description	# Channels	Cost (kCHF)
μ tracker	Plastic Iarocci Tubes	1200	125
First μ-wall	Frontend electronics		
	(ampl. and comparator)	9600	144
	Readout	10600	150
	Low voltage		10
	Cabling		25
Total			454
μ tracker	Drift tubes	3000	105
First μ-wall	Frontend electronics		30
	Readout		50
	Low voltage		20
	Cabling		15
Total			220

Table 7.8: Cost of the Muon Filters (kCHF).

The muon hodoscopes

There are five planes of hodoscopes for triggering on muons. The cost estimate for scintillator, photomultipliers and trigger electronics is summarised in table 7.9.

Description	# Channels	Cost (kCHF)
Hodoscope plane 1	180	180
Hodoscope plane 2	180	180
Hodoscope plane 3	148	148
Hodoscope plane 4	192	192
Hodoscope plane 5	192	192
Trigger electronics		450
Total		1342

Table 7.9: Cost of the muon hodoscopes and trigger electronics.

The DAQ

The costs of the readout system are separated into frontends and the data acquisition system. This includes double buffering memory modules, VME masters for VME readout and data compactification, the high speed interfaces, the multiprocessor DAQ computer and the tape stations. The figures shown in table 7.10 correspond to currently available equipment, however one can expect further improvements of the performance at constant prices.

Description	# items	Cost
VME-Masters with memory	90	1350kCHF
High speed interfaces	90	180kCHF
AlphaServer 8400/350 with 12 processors and I/O interfaces	1	1500kCHF
DLT7000 tape drives	10	100kCHF
Total		3130 kCHF

Table 7.10: Price estimate for the DAQ system.

The scintillating fibre detectors

The number of scintillating fibre channels was evaluated in Sect. 5.2.2. For the Beam Momentum Station and the beam detector upstream and downstream of the target a total of 4100 channels is needed. Table 7.11 summarises the cost of the system assuming 260 16-pad photomultipliers.

Element	Price
Si-Fi detector	310
Analog electronics	800
Frontend electronics	915
Trigger electronics	175
DAQ Read-out	50
High voltage system	120
Monitoring system	25
total	2395

Table 7.11: Cost of the Scintillating Fibre detectors (kCHF).

The first spectrometer magnet SM1m

A rough estimate of the price for the large angle spectrometer magnet SM1m (Fig. 5.21) for the muon beam experiments was performed with the help of W. Flegel (CERN/PPE). The dimensions are given in Table 7.12 and an inclination of ±180 mrad of the pole shoes was assumed. The aperture is given for the (larger) downstream side. The price was calculated from the masses of the materials, using for copper 40 CHF/kg and for iron 3.5 CHF/kg. These prices include machining of the materials and are estimated to be correct within 20 %. For the copper coils a filling factor of 0.7 was assumed. In Table 7.12

the weights and prices separately for copper and iron are summarised. The price of the magnet is about 2 MCHF.

	depth m	width m	height m
aperture	1.00	2.00	1.60
frame	2.00	5.50	4.50
	iron	copper	total
weight [t]	220	33	253
price [kCHF]	770	1300	2070

Table 7.12: Dimensions, weight, and price of the M1m magnet

The Polarised Target

Description	Cost (kCHF)
Superconducting solenoid	1500
Cryostat modification	150
Target material (^{6}LiD)	200
Overhaul of pumps	100
Microwave system (replacement and overhaul)	200
Irradiation: cryostat for material	70
Irradiation: cost	50
Material forming/fabrication ...	30
Target control system (upgrade)	30
Total	2430

Table 7.13: Cost estimate of the polarised target system

Silicon Microstrips and MSGC

The costs for the silicon microstrips and the MSGC to be used in the hadron beam program have been estimated on the base of the experience of WA89 according to the design specifications outlined in sections 5.3.3 and 5.3.4. They are summarised in tables 7.14 and 7.15.

Description	# Channels	Cost
R&D		200
beam silicon		18
target silicon		70
M1-silicon		9
vertex detectors		18
Cooling + slow control		100
readout	40000	350
Total		850

Table 7.14: Costs of silicon microstrip detectors.

Description	# items	Cost
R&D		200
Production	220 plates	330
Masks		60
readout	150000	650
High Voltage		80
Low Voltage + slow control		90
Total		1410

Table 7.15: Costs of MSGC.

7.2 Total Cost of COMPASS

In table 7.16 we summarise the cost of all equipments. We do not take existing equipment into account in the total cost of the COMPASS apparatus.

Honeycomb chambers	2900
MWPC	2520
RICH1	2955
RICH2	1520
ECAL1	1410
ECAL2	2500
HCAL1	364
HCAL2	490
μ-Filters	674
DAQ	3130
Scintillating fibre detectors	2395
Polarised target	2430
Magnet SM1m	2070
μ-Hodoscopes and trigger	1342
Silicon microstrips	850
MSGC	1410
Trigger	400
Grand total	26860

Table 7.16: Summary of the cost estimates for COMPASS in kCHF.

7.3 Responsibilities

The present share of responsibilities amongst the institutes of the COMPASS collaboration for design, construction and operation of the various equipments is given in table 7.17. It has to be understood that in most cases the contributions are subject to approval from the respective funding agencies. Furthermore it has to be understood that for some items the listed groups cannot take the full responsibility of the financial load. The share of the cost of the experiment among the participating institutes will be better defined during the course of the approval of the experiment.

Detector	Description	Institute
Tracking :		
Honeycomb	construction and operation	München, Freiburg
MWPC	construction and operation	Freiburg
Scintillating fibres	beam	Bonn,Erlangen
	spectrometer	Bonn, Torino
Silicon strips	construction and operation	Heidelberg MPI
MSGC	construction and operation	Heidelberg MPI, Torino
Pixel	development	Zürich
Calorimetry :		
ECAL1/2	set up and electronics	IHEP (Protvino) + KEK
HCAL1/2	construction and electronics	Dubna, Moscow, IHEP
ECAL/HCAL	monitoring system	Tel Aviv
μ-detection :		
μ-wall 1	tracking detectors	Dubna
μ-wall 2	tracking detectors	IHEP (Protvino)
μ-wall 1/2	trigger counters	Bonn, Mainz
polarised target :		
Magnet	construction	Nagoya
Target	construction + operation	Bielefeld, Bochum, Helsinki
Recoil proton counter:		
Scintillator barrel	modification and operation	IHEP + KEK
Magnets :		
SM1m	construction	joint German project
Particle identification		
RICH1/2	chambers + electronics	Trieste
RICH1/2	mirrors, mechanics and gas system	Dubna
Electronics :		
DAQ	data buffer, eventbuilding and tapewriting	Osaka, Torino
Trigger :		
Hadron	charm multiplicity jump	Heidelberg MPI
Hadron	charm μ	Bristol
Hadron	charm ET	Rutgers
Hadron	glueballs	IHEP
Hadron	diffraction + Primakoff	Tel Aviv, IHEP
Muon	all	Bonn, Mainz

Table 7.17: Distribution of responsibilities, continued.

8 TIME SCALE AND RUNNING STRATEGIES

In view of the diverse physics program using different beams and experimental set ups the question of running time is uttermost important. Considering a first data taking period of about five years we have foreseen a sharing on equal beam time basis between the hadron and the muon beam program. The scheduling takes into account the different experimental needs for the different parts of the program. It also ensures that each physics issue can be covered with enough statistical accuracy to give a good physics output and allows an evaluation of further physics potentials. The nominal starting date has been set to 1999, but it is more realistic to assume that fully efficient data taking will start only in the year 2000.

Table 1 : Suggested time sharing

year	beam	set-up	physics	detector requirements
1999	hadrons, μ	M1h	test runs	
1999	hadrons ($\pi^- K^-$)	M1h-heavy target	Primakoff, diffract. production	beam detectors, ECAL, tracking
1999	hadrons	M1h-LH$_2$-target	central production	tracking, ECAL
2000	muons	M1m-pol. target	$\Delta G/G$ Δq	tracking, RICH, μ-wall
2000	hadrons	M1h-charm target	c-production s.l. decays	μ-vertex, tracking, RICH μ-wall, calorimetry
2001	muons	M1m-pol. target	$\Delta G/G$ Δq	full apparatus
2002	hadrons	M1h-LH$_2$-target	central production	tracking, ECAL, RICH
	hadrons	M1h-charm target	full charm program	full apparatus
2003	muons	M1m-pol-target	$\Delta G/G$ Δq	full apparatus
	hadrons	M1h-charm target		
2004	muons	M1m-pol-target	$\Delta G/G$ Δq	full apparatus
	hadrons	M1h-charm target		

After a period of about 1/2 year which will be used to start up the apparatus and tune the various detector components a short run will be taken using a tagged hadron beam (π^-,K^-) for the study of polarisabilities of mesons. This program needs minimal tracking equipment, no particle identification with any of the detector-RICHs but good electromagnetic calorimetry, fast DAQ and moderate vertex detectors. As mentioned above the investigation of diffractive production on heavy nuclei can be studied simultaneously.

Following this run we will modify the target area to install a liquid hydrogen target and the necessary detectors to perform a study of central production in pp collisions at 300 GeV/c.

The winter shutdown will then be used to install the polarised target and the necessary detectors to perform a pilot run for the muonic charm production. It is foreseen to swap back to the hadron beam set up to allow a 1/2 year test run for the charm program. Both charm-measurements heavily rely on the particle identification and thus require the RICHs to be operational. These first pilot runs will be used to understand trigger performance, background conditions, event reconstruction and estimate event yields. Although detailed know how exists on the reconstruction of charmed particles we estimate that data production and analysis will need about 1 yr before further data taking shall be considered.

The 2nd year will be devoted solely to the muon beam program and the 3rd year to the hadron beam program, shared between meson spectroscopy and charm physics. The 4th and 5th year will be again shared between hadron and muon physics.

As was mentioned in the section 5.3.1 the modification of the beam line to run 450 GeV/c protons to the hall are substantial and should only be performed within a winter shutdown. We thus consider no 450 GeV/c run within the first five years. However, as the yield in reconstructible short living c-baryons increases with beam energy, we will put strong emphasis on such a running in the time afterwards.

9 REQUEST TO CERN

Time scale and experimental area

We request to use the experimental hall EHN2. For 1997 we foresee detector tests in the order of 2 months with the muon beam.

We request that part of the material of the NA47 experiment, in particular the polarised target system and the spectrometer magnet MEP45, are available for the the experiment and remain in their present location in EHN2 until the start of the new experiment. A revision of the electrical installations and of the air conditioning in the experimental barracks is necessary in order to guarantee a safe operation of the experiment and of hadron beams, if the latter can be made available.

For 1998 we request the hall EHN2 to be available for the installation of the detectors. We request that the iron for the muon walls is provided by CERN. The large muon wall from NA47 can be used for the second muon wall of the new experiment.

At the end of the period covered by this proposal first results will be obtained, but the experimental programme envisaged in the two Letters of Intent, I202 and I204, will not be finished. We therefore keep the option open to submit an addendum to this proposal, which could cover about four more years of data taking.

Beam line

The M2 beam line should be modified in order to be able to transport a secondary proton beam of up to 300 GeV. The installation of a CERN CEDAR system for the identification of beam particles for the hadron programme is requested. For the muon programme we request a stronger focusing of the muon beam at the location of the polarised target. These modification will require additional quadrupoles and stronger power supplies.

Spectrometer magnets

The collaboration will purchase the additional new spectrometer magnet M1m for the muon set-up. For its design we request help from the PPE division. For the hadron set-up we request the magnet MEP48 including a modification of the present gap size. We request from CERN the installation of both magnets including the power supplies. We also request to use the EMC magnet MEP45, presently in EHN2, and the maintenance of all three magnets by CERN.

Beam intensities

Until the termination of the programme covered by the proposal we request to be main user of the M2 beam line for the full time of the SPS proton operation, which we assume to be in the order of 150 days per year. We request for the 100 GeV muon programme a proton intensity of about 7×10^{12} primary protons per spill. For a possible 200 GeV running, which could become necessary to probe the gluon polarisation at smaller x_g a proton intensity of up to 12×10^{12} would be needed. However, such a programme would be considered only when results from the 100 GeV running are available. This will not be before the year 2001. For the hadron programme lower proton intensities are needed.

Test beams

For tests of detectors and the calibration of calorimeters we request beam time in one of the test beam areas in the order of 3–4 weeks per year in the years 1997–1999.

Polarised target

For the polarised target system we request that CERN maintains the infrastructure and provides the logistics for the polarised target including the operation of the helium liquefier in EHN2, liquid nitrogen supply, air conditioning and cooling water as well as the electrical installations. Due to the larger target solenoid the consumption of liquid ^{4}He will somewhat increase. We request to use the existing pumping and instrumentation systems. We also need to store the target materials in a liquid He dewar at CERN, as was done for the NH_3 material of the SMC.

Assembly hall

We request to have the detector and cryostat repair and assembly hall of SMC in building 867 (R-A04), or similar, at our disposal.

Liquid hydrogen target

We request to use the existing liquid hydrogen target, which was used in experiment NA12/2. This request includes its installation and operation by CERN.

RICH

We request that the RICH equipment from the Omega experiment WA89 is available for the new experiment.

Technical support

Presently CERN provides a data aide (PPE) and a technician for maintenance of the SMC spectrometer. This has been invaluable for the execution of the NA47 experiment. We therefore request to support the new experiment to the same extent.

Developments

For the adaption of the GASSIPLEX read-out chip developed at CERN to the needs of our experiment, we request an equivalent of 1/2 man year for chip design.

Computing

The collaboration will set up a computer cluster for the event reconstruction. Nevertheless, some computing resources from CERN will be needed in particular in systems like SP2, SHIFT and CSF.

Infrastructure

We request that CERN provides the moving mechanisms needed for the two spectrometer magnets and for some detectors when changing from the muon to the hadron set-up.

CERN Electronics Contribution

We request to have a CEC granted similar to that of the SMC which amounts to 2.9 MCHF.

Appendix A Longitudinal spin asymmetries in hadron production

Using the parton model and neglecting the intrinsic quark momentum, one can derive the following expressions for the hadron asymmetries

$$A_p^h = \frac{1}{P_B P_T f D} \cdot \frac{N^{\uparrow\downarrow} - N^{\uparrow\uparrow}}{N^{\uparrow\downarrow} + N^{\uparrow\uparrow}} \tag{A.1}$$

on a proton target, for $h = \pi^+, \pi^-, \mathsf{K}^+$ and K^-.

$$\begin{aligned}
A_{\mathsf{p}}^{\pi^+} &= \frac{4D_1\Delta u_v + D_2\Delta d_v + 4(D_1+D_2)\Delta\bar{u} + (D_1+D_2)\Delta\bar{d} + 2D_2\Delta\bar{s}}{4D_1 u_v + D_2 d_v + 4(D_1+D_2)\bar{u} + (D_1+D_2)\bar{d} + 2D_2\bar{s}}, \\
A_{\mathsf{p}}^{\pi^-} &= \frac{4D_2\Delta u_v + D_1\Delta d_v + 4(D_1+D_2)\Delta\bar{u} + (D_1+D_2)\Delta\bar{d} + 2D_2\Delta\bar{s}}{4D_2 u_v + D_1 d_v + 4(D_1+D_2)\bar{u} + (D_1+D_2)\bar{d} + 2D_2\bar{s}}, \\
A_{\mathsf{p}}^{\mathsf{K}^+} &= \frac{4D_3\Delta u_v + D_4\Delta d_v + 4(D_3+D_4)\Delta\bar{u} + 2D_4\Delta\bar{d} + (D_1+D_4)\Delta\bar{s}}{4D_3 u_v + D_4 d_v + 4(D_3+D_4)\bar{u} + 2D_4\bar{d} + (D_1+D_4)\bar{s}}, \\
A_{\mathsf{p}}^{\mathsf{K}^-} &= \frac{4D_4\Delta u_v + D_4\Delta d_v + 4(D_3+D_4)\Delta\bar{u} + 2D_4\Delta\bar{d} + (D_1+D_4)\Delta\bar{s}}{4D_4 u_v + D_4 d_v + 4(D_3+D_4)\bar{u} + 2D_4\bar{d} + (D_1+D_4)\bar{s}},
\end{aligned} \tag{A.2}$$

where u_v and d_v denote the valence quark distributions, $q_v = q - \bar{q}$.

The corresponding formulae for the deuteron are

$$\begin{aligned}
A_{\mathsf{d}}^{\pi^+} &= \frac{(4D_1+D_2)(\Delta u_v + \Delta d_v) + 5(D_1+D_2)(\Delta\bar{u} + \Delta\bar{d}) + 4D_2\Delta\bar{s}}{(4D_1+D_2)(u_v + d_v) + 5(D_1+D_2)(\bar{u} + \bar{d}) + 4D_2\bar{s}}, \\
A_{\mathsf{d}}^{\pi^-} &= \frac{(D_1+4D_2)(\Delta u_v + \Delta d_v) + 5(D_1+D_2)(\Delta\bar{u} + \Delta\bar{d}) + 4D_2\Delta\bar{s}}{(D_1+4D_2)(u_v + d_v) + 5(D_1+D_2)(\bar{u} + \bar{d}) + 4D_2\bar{s}}, \\
A_{\mathsf{d}}^{\mathsf{K}^+} &= \frac{(4D_3+D_4)(\Delta u_v + \Delta d_v) + 2(2D_3+3D_4)(\Delta\bar{u} + \Delta\bar{d}) + 2(D_1+D_4)\Delta\bar{s}}{(4D_3+D_4)(u_v + d_v) + 2(2D_3+3D_4)(\bar{u} + \bar{d}) + 2(D_1+D_4)\bar{s}}, \\
A_{\mathsf{d}}^{\mathsf{K}^-} &= \frac{5D_4(\Delta u_v + \Delta d_v) + 2(2D_3+3D_4)(\Delta\bar{u} + \Delta\bar{d}) + 2(D_1+D_4)\Delta\bar{s}}{5D_4(u_v + d_v) + 2(2D_3+3D_4)(\bar{u} + \bar{d}) + 2(D_1+D_4)\bar{s}},
\end{aligned} \tag{A.3}$$

The asymmetries for the differences of cross sections for positive and negative hadrons do not depend on the fragmentation functions and are given by

$$\begin{aligned}
A_{\mathrm{p}}^{\pi^+-\pi^-} &= \frac{4\Delta u_v - \Delta d_v}{4u_v - d_v}, \\
A_{\mathrm{p}}^{\mathrm{K}^+-\mathrm{K}^-} &= \frac{\Delta u_v}{u_v}, \\
A_{\mathrm{d}}^{\pi^+-\pi^-} &= \frac{\Delta u_v + \Delta d_v}{u_v + d_v}, \\
A_{\mathrm{d}}^{\mathrm{K}^+-\mathrm{K}^-} &= A_{\mathrm{d}}^{\pi^+-\pi^-}.
\end{aligned} \tag{A.4}$$

The symbols $D_{1,2,3,4}$ stand for the fragmentation functions $D_u^{\pi^+,\pi^-,\mathrm{K}^+,\mathrm{K}^-}$. The assumptions made in Eqs. A.2–A.4 about charge conjugation and isospin symmetries were similar to those made by the EMC [288]. Further reduction of the number of independent fragmentation functions required additional assumptions for unfavoured (e.g. $D_d^{[K^-=\bar{u}s]} = D_{\bar{d}}^{[K^-=\bar{u}s]}$) and favoured (e.g. $D_s^{[K^-=\bar{u}s]} = D_d^{[\pi^-=\bar{u}d]}$) fragmentation.

The neutral kaons can be identified by measuring their decays before the magnet and calculating the invariant mass. Therefore only the K_S component of the $\mathrm{K}^0 - \bar{\mathrm{K}}^0$ system can be detected in our experiment. The asymmetries for the K_S on the proton and on the deuteron targets are equal to

$$\begin{aligned}
A_{\mathrm{p}}^{\mathrm{K}_S} &= \frac{4D_c\Delta u_v + D_b\Delta d_v + 8D_c\Delta\bar{u} + 2D_b\Delta\bar{d} + 2D_a\Delta\bar{s}}{4D_c u_v + D_b d_v + 8D_c\bar{u} + 2D_b\bar{d} + 2D_a\bar{s}}, \\
A_{\mathrm{d}}^{\mathrm{K}_S} &= \frac{(D_b + 4D_c)(\Delta u_v + \Delta d_v) + 2(D_b + 4D_c)(\Delta\bar{u} + \Delta\bar{d}) + 4D_a\Delta\bar{s}}{(D_b + 4D_c)(u_v + d_v) + 2(D_b + 4D_c)(\bar{u} + \bar{d}) + 4D_a\bar{s}},
\end{aligned} \tag{A.5}$$

where the definition of symbols and the assumptions about fragmentation functions in Eq. A.5 are the following:

$$\begin{aligned}
D_a &= D_s^{\mathrm{K}_S} = D_{\bar{s}}^{\mathrm{K}_S}, \\
D_b &= D_d^{\mathrm{K}_S} = D_{\bar{d}}^{\mathrm{K}_S}, \\
D_c &= D_u^{\mathrm{K}_S} = D_{\bar{u}}^{\mathrm{K}_S}.
\end{aligned} \tag{A.6}$$

Appendix B Transverse spin asymmetries in hadron production

In this appendix we give explicit expressions for some of the flavour combinations of the $\Delta_T q$ distribution functions which can be measured from the number of events with a leading π in DIS on transversely polarised proton and deuterium targets.

From eq. 3.23, one obtains that the number of events with a leading hadron h in a given kinematical bin is

$$N^{h\pm} = const \cdot \Sigma_q e_q^2 \cdot [D_q^h \cdot q(x) \pm f \cdot P_T \cdot D_{nn} \cdot \Delta_T q(x) \cdot \Delta D_q^h \cdot \sin\phi_c]$$

i.e. there is an azimuthal dependence on the Collins angle ϕ_c with an asymmetry

$$\epsilon = f \cdot P_T \cdot D_{nn} \cdot \frac{\Sigma_q e_q^2 \Delta_T q(x) \cdot \Delta D_q^h}{\Sigma_q e_q^2 \cdot q(x) \cdot D_q^h}$$

which can be estimated from the event ratio

$$\frac{N^{h+} - N^{h-}}{N^{h+} + N^{h-}}.$$

In these formulae P_T is the absolute value of nucleon target polarisation, f is the target polarisation dilution factor, and $D_{nn} = (1-y)/(1-y+y^2/2)$ is the quark transverse-spin transfer coefficient in the hard scattering. D_q^h and ΔD_q^h are the spin-independent and spin-dependent parts of the quark fragmentation functions. The $+$ and $-$ refer to the up and down orientations of the nucleon spin. The Collins angle ϕ_c is computed always for the up target spin configuration.

Combining events with leading π^+ and π^-, produced on proton and/or deuteron targets, the asymmetries are given by simpler formulas. For instance, with the standard assumptions on the fragmentation functions ($D_1 = D_u^{\pi^+} = D_d^{\pi^-} = D_{\bar{u}}^{\pi^-} = D_{\bar{d}}^{\pi^+}$ and $D_2 = D_u^{\pi^-} = D_d^{\pi^+} = D_{\bar{u}}^{\pi^+} = D_{\bar{d}}^{\pi^-}$) and neglecting the contributions of s and $\bar{s}$ quarks:

A. Asymmetries with a proton target:

$$1 \quad . \quad f_p \cdot P_T^p \cdot D_{nn} \cdot \frac{4\Delta_T u + \Delta_T \bar{d} + 4\Delta_T \bar{u} + \Delta_T d}{4u + \bar{d} + 4\bar{u} + d} \cdot \frac{\Delta D_1 + \Delta D_2}{D_1 + D_2}$$

which can be obtained from

$$\frac{(N_p^{\pi^+ +} + N_p^{\pi^- +}) - (N_p^{\pi^+ -} + N_p^{\pi^- -})}{(N_p^{\pi^+ +} + N_p^{\pi^- +}) + (N_p^{\pi^+ -} + N_p^{\pi^- -})};$$

$$2 \quad . \quad f_p \cdot P_T D_{nn} \cdot \frac{4\Delta_T u_v - \Delta_T d_v}{4u + \bar{d} + 4\bar{u} + d} \cdot \frac{\Delta D_1 - \Delta D_2}{D_1 + D_2}$$

where $\Delta_T q_v = \Delta_T q - \Delta_T \bar{q}$, which can be obtained from

$$\frac{(N_p^{\pi^+ +} + N_p^{\pi^- -}) - (N_p^{\pi^+ -} + N_p^{\pi^- +})}{(N_p^{\pi^+ +} + N_p^{\pi^- -}) + (N_p^{\pi^+ -} + N_p^{\pi^- +})}.$$

B. Asymmetries with a deuterium target:

$$1 \quad . \quad f_d \cdot P_T^d \cdot D_{nn} \cdot \frac{\Delta_T u + \Delta_T \bar{d} + \Delta_T \bar{u} + \Delta_T d}{u + \bar{d} + \bar{u} + d} \cdot \frac{\Delta D_1 + \Delta D_2}{D_1 + D_2}$$

which can be obtained from

$$\frac{(N_d^{\pi^+ +} + N_d^{\pi^- +}) - (N_d^{\pi^+ -} + N_d^{\pi^- -})}{(N_d^{\pi^+ +} + N_d^{\pi^- +}) + (N_d^{\pi^+ -} + N_d^{\pi^- -})};$$

$$2 \quad . \quad f_d \cdot P_T^d \cdot D_{nn} \cdot \frac{3(\Delta_T u_v - \Delta_T d_v)}{5(u + \bar{d} + \bar{u} + d)} \cdot \frac{\Delta D_1 - \Delta D_2}{D_1 + D_2}$$

which can be obtained from

$$\frac{(N_d^{\pi^+ +} + N_d^{\pi^- -}) - (N_d^{\pi^+ -} + N_d^{\pi^- +})}{(N_d^{\pi^+ +} + N_d^{\pi^- -}) + (N_d^{\pi^+ -} + N_d^{\pi^- +})}.$$

C. Asymmetry with proton and deuterium targets

$$\frac{f_d \cdot P_T^d}{f_p \cdot P_T^p} \cdot \frac{3(\Delta_T u_v + \Delta_T d_v)}{4\Delta_T u_v - \Delta_T d_v}$$

which can be obtained from

$$\frac{(N_d^{\pi^+ +} + N_d^{\pi^- -}) - (N_d^{\pi^+ -} + N_d^{\pi^- +})}{(N_p^{\pi^+ +} + N_p^{\pi^- -}) - (N_p^{\pi^+ -} + N_p^{\pi^- +})}$$

This asymmetry has an expression very similar to the one obtained in semi-inclusive DIS with longitudinally polarised targets and beam [289], and has the important feature of being independent from the value of the analysing power of the fragmentation process.

Appendix C Doubly Charmed Baryons

This appendix contains parts of: a recent review paper [290] by M. A. Moinester on the subject of double charm baryons and tetraquarks; and S. Paul et al., The CHEOPS Project [291], contribution to Strasbourg Sept. 1995 workshop. We give here a detailed description of systems with double charm, including their spectroscopy, production and decays.

Introduction

The quantum chromodynamics hadron spectrum includes doubly charmed baryons: Ξ^{+}_{cc} (ccd), $\Xi^{++}_{cc}(ccu)$, and Ω^{+}_{cc} (ccs), as well as ccc and ccb, and also the corresponding antiparticles. Properties of ccq baryons were discussed by Bjorken [105], Richard [107], Fleck and Richard and Martin [108], Savage and Wise and Springer [126,292], Kiselev et al. [293,294], Falk et al. [295], Bander and Subbaraman [216], Stong [296], Roncaglia et al. [106], and Bagan et al. [109]. Singly charmed baryons are an active area of current research [25,110,124,297–300], but there are no experimental data on the doubly charmed variety. A double charm state-of-the-art experiment is feasible to observe and to investigate such baryons. The required detectors and data acquisition system would need very high rate capabilities, and therefore would also serve as a testing ground for LHC detectors. Double charm physics is in the mainstream and part of the natural development of QCD research.

The ccq baryons should be described in terms of a combination of perturbative and non-perturbative QCD. For these baryons, the light q orbits a tightly bound cc pair. The study of such configurations and their weak decays can help to set constraints on phenomenological models of quark-quark forces [108, 301–303]. Hadron structures with size scales much less than $1/\Lambda_{qcd}$ should be well described by perturbative QCD. This is so, since the small size assures that α_s is small, and therefore the leading term in the perturbative expansion is adequate. The tightly bound $(\mathrm{cc})_{\bar{3}}$ diquark in ccq may satisfy this condition. For ccq, on the other hand, the radius is dominated by the low mass q, and is therefore large. The relative (cc)-(q) structure may be described similar to mesons $\bar{Q}q$, where the (cc) pair plays the role of the heavy antiquark. Savage and Wise [292] discussed the ccq excitation spectrum for the q degree of freedom (with the cc in its ground state) via the analogy to the spectrum of $\bar{Q}q$ mesons. Fleck and Richard [108] calculated excitation spectra (spin, orbital, radial excitations) and other properties of ccq baryons with a variety of potential and bag models, which successfully describe known hadrons. They show that the lowest radial and orbital excitations of ccq and ccs are associated with cc excitations. And these ccq states are broad since pionic transitions to the ground state are allowed.

The ground state in their calculation consists of a localized (cc) diquark surrounded by a light quark, with the average distance $< r(cc) >$ much smaller than $< r(cq) >$. They find that $< r(cc) >$ increases for the radial and orbital excitations, and that the quark-diquark structure disappears. Stong [296] emphasized how the QQq excitation spectra can be used to phenomenologically determine the QQ potential, to complement the approach taken for $Q\bar{Q}$ quarkonium interactions. The ccq calculations contrast with ccc or ccb or b-quark physics, which are closer to the perturbative regime. As pointed out by Bjorken [105], one should strive to study the Ω_{ccc}^{++} ccc baryon. Its decay properties should be simple, since only spectator diagrams contribute to its decay. Its excitation spectrum, including several narrow levels above the ground state, should be closer to the perturbative regime. The ccq studies are a valuable prelude to such ccc efforts.

An interesting question is whether the binding of the cc pair leads to an increase of the ccq lifetime. The weak decay rate of a spectator c-quark has an m_c^5 mass dependence from phase space, where m_c is the charm quark mass. In quark models, the mass dependence is $(m_c - \mu)^5$ if the effective phase space is reduced by μ MeV. Assuming that $m_c \approx 1.5$ GeV, a binding near $\mu = 125$ MeV would then reduce the the decay rate by 35%. Such effects would be reminiscent of the changes in the decay rates for neutrons bound in nuclei or for bound muons. Bigi [123, 304] and Eichten and Quigg [305] discussed such an increase of lifetime for the B_c^+ meson due to the strong $\bar{b}c$ binding. On the other hand, Bigi and Uraltsev [122, 304, 306] claim that in the self-consistent $1/M_Q$ expansion [307, 308], binding energy does not influence heavy quark lifetimes. Their result was discussed in the context of $\bar{b}$ and c decays [123] in B_c, and may or may not also be relevant for baryons. One may also ask [308] whether or not the c-quark mass is large enough to justify a $1/M_Q$ expansion. The experimentalist approach is that data for ccq and B_c lifetimes and masses are needed to test $1/M_Q$ and phenomenological models. Increased lifetimes would of course make the experiment easier to carry out.

The ccq baryon is also interesting because it helps to probe QCD dynamics in a different way. One should learn new information on the basic production processes in hadron physics. The ccq studies can also help in our understanding of the structure of qqq and cqq baryons, and therefore of QCD in general. D meson structures are successfully described [309] in terms of a central heavy c quark orbited by a light quark. But the descriptions of qqq and cqq structures are less successful. We need to better understand how protons and other baryons are built from quarks. The investigation of the ccq system may be very helpful, since this has a simpler quark structure than a proton. The ccq data should help put constraints on hadron models, improving thereby the description of cqq and qqq systems.

Production cross section of ccq baryons

One can consider production of doubly charmed hadrons of momenta P_c by proton and Sigma and pion beams of momenta P_b. We discuss production at different Feynman X_f-values, $X_f \sim P_c/P_b$, evaluated with laboratory momenta. The cross sections may also depend on the projectile. For example, pion beams may be more effective than Σ^- beams in producing high-X_f D^- mesons. And baryon beams may be more effective than pion beams in producing ccq and cqq baryons at high X_f.

Consider a hadronic interaction in which two $c\bar{c}$ pairs are produced. The two c's combine and then form a ccq baryon. Calculations for ccq production via such interactions have been recently carried out. Some ingredients to the calculations can be stated. For ccq production, one must produce two c quarks (and associated antiquarks), and they must join to form a tightly bound, small size anti-triplet pair. The two c-quarks may arise from two parton showers in the same hadron-hadron collision, or from a single parton shower, or they may be present as an intrinsic charm component of the incident hadron, or otherwise. The two c-quarks may be produced (initial state) with a range of separations and relative momenta (up to say tens of GeV/c). In the final state, if they are tightly bound in a small size cc pair, they should have relative momentum lower than roughly 1 GeV/c. The overlap integral between initial and final state diquarks determines the probability for the cc fusion process. The diquark should then easily combine with a q to form ccq. A ccq production calculation based on two parton showers in the same hadron-hadron collision was discussed by Levin [310]. Halzen et al. [311] gives evidence for multiple parton interactions in a single hadron collision, from data on the production of two lepton pairs in Drell-Yan experiments.

As an aid in comparing different possible calculations, one may parameterize the yield as:

$$\sigma(ccq)/\sigma(c\bar{c}) \approx k[\sigma(c\bar{c})/\sigma(in.)] \approx kR. \tag{C.1}$$

Here, $\sigma(c\bar{c})$ is the charm production cross section, roughly 25 μb; $\sigma(in.)$ is the inelastic scattering cross section, roughly 25 mb; and R is their ratio, roughly 10^{-3} [312]. Here, k is the assumed "suppression" factor for joining two c's together with a third light quark to produce ccq. Eq. 1 does not represent a calculation, and has no compelling theoretical basis. It implicitly factorizes ccq production into a factor (R) that accounts for the production of a second c-quark, and a factor (k) describing a subsequent ccq baryon formation probability. Considering the overlap integral described in the preceding paragraph, one may expect k values less than unity for simple mechanisms of ccq formation. The factor R describing the production of a second charm pair may have a value greater than that given above, as discussed later in the discussion of ccq production via the intrinsic charm mechanism. With the value of R chosen, this situation would be described by a factor k>1. Theoretical cross section calculations are needed, including the X_f-dependence of ccq production. We will explore the experimental consequences of a ccq search for the range k=0.04-1.0, corresponding to $\sigma(ccq)/\sigma(c\bar{c}) \approx 10^{-3} - 4. \times 10^{-5}$. Assuming $\sigma(c\bar{c})$ charm production cross sections of 25 microbarns, this range corresponds to ccq cross sections of 1 - 25 nb/N.

Aoki et al. [313] reported a 2-event, large uncertainty measurement with a π^- beam and emulsion nuclei at $\sqrt{s}$ =26 GeV for the double to single open charm pair production ratio. The $D\bar{D}D\bar{D}$ to $D\bar{D}$ ratio was given as 10^{-2}. A better measurement is certainly needed. The NA3 [314] experiments measured $\sigma(\Psi\Psi)/\sigma(\Psi)$ with 400 GeV/c protons and 150-280 GeV/c π^- interacting with nuclei. NA3 reported a value of $\approx 3 \times 10^{-4}$ for this ratio, with comparable results for the pion and proton experiments. The proton experiment had 15 ± 4 $\Psi\Psi$ events with a production cross section $\sigma(\Psi\Psi) = 27 \pm 10\ pb$. We assume that the $\Psi\Psi$ result is relevant, even though Ψ production is only a small part ($\approx 0.4\%$) of the charm production cross section, with most of the cross section leading to open charm. These two results for double charm production establish a range of values close to the value 10^{-3} for R estimated above in the discussion of Eq. 1.

We can also refer to an empirical formula which reasonably describes the production cross section of a mass M hadron in central collisions. The transverse momentum distribution at not too large p_t follows a form given as [315]:

$$d\sigma/dp_t^2 \sim exp(-C\sqrt{M^2+p_t^2}), \tag{C.2}$$

where C is roughly a universal constant $\sim$ 5 - 6 $(\text{GeV})^{-1}$. The exponential (Boltzmann) dependence on the transverse energy $E_t = \sqrt{M^2+p_t^2}$ has inspired speculation that particle production is thermal, at a temperature $C^{-1} \sim 160$ MeV [315]. We assume that this equation is applicable to ccq production. To illustrate the universality of C, we evaluate it for a few cases. For Λ_c and Ξ^0, empirical fits to data give exp($-bp_t^2$), with b=1.1 $\text{GeV}^{-2}$and b=2.0 GeV^{-2}, respectively [128,316]. With C $\approx$ 2Mb based on Eq. 2, this corresponds to C $\sim$ 5.0 GeV^{-1} for Λ_c, and C $\sim$ 5.3 GeV^{-1} for Ξ^0. For inclusive pion production, experiment gives exp($-bp_t$) with b $\sim$ 6 GeV^{-1} [317]; and C $\sim$ b, since the pion mass is small. Therefore, C= 5-6 GeV^{-1} is valid for Λ_c, Ξ^0 hyperon, and pion production. We integrate over p_t^2, and take M(ccq) and M(c) to be 3.7 and 2.0 GeV respectively. Here M(c) represents the average mass of the charmed mesons and baryons produced with charm cross section $\sigma(c\bar{c})$ ($\sim 25\mu b$). We estimate the ratio as:

$$\sigma(ccq)/\sigma(c\bar{c}) \sim exp[-5[M(ccq)-M(c)]] \sim 4\times10^{-4}. \tag{C.3}$$

This result corresponds to k=0.4 in the parameterization of Eq. 1. In applying Eq. 3 to ccq production, we assume that the suppression of cross section for the heavy ccq production (for q = u,d,s) as compared to the single charm production is due only to the increased mass of ccq. Other effects which may influence the yields (spin factors, details on wave functions, possible threshold suppression factors, etc.) are not considered here. With these caveats, and allowing for consequent large uncertainties, one may apply Eq. 3 with appropriate masses to estimate yield ratios of other particles. For the T, we assume the same production cross section as for the ccq, based on the mass dependence of Eq. 3. To account for large uncertainties related to eq. 3, we will take $\sigma(ccq)/\sigma(c\bar{c}) \sim 10^{-3}-4\times10^{-5}$.

Brodsky and Vogt [318,319] suggested that there may be significant intrinsic charm (IC) $c\bar{c}$ components in hadron wave functions, and therefore also intrinsic double charm (ICC) $cc\bar{c}\bar{c}$ components. The IC probability was obtained from the measurements of charm production in deep inelastic scattering. The Hoffmann and Moore analysis [320] of EMC data, including next-to-leading order (NLO) corrections to the IC component, but not to the extrinsic charm component, yields a 0.3% IC probability in the proton. A recent reanalysis of the EMC charm production data was carried out by Harris, Smith, and Vogt [321]. Their analysis includes the intrinsic and extrinsic charm contributions, both calculated at NLO. They found that an IC component is still needed to fit the EMC data, with a value indicated for the proton of (1.0 ± 0.6)%. Theoretical calculations of the IC component have also been reported [322]. The double intrinsic charm component can lead to ccq production, as the cc pair pre-exists in the incident hadron. One may expect that aside from the IC mechanism, ccq production will be predominantly central. Intrinsic charm ccq production, with its expected high X_f distribution, would therefore be especially attractive.

Brodsky and Vogt [318] discussed double $\Psi\Psi$ production [314] in the framework of IC. The data occur mainly at large X_f, while processes induced by gluon fusion tend to be more central. They claim that the data (transverse momentum, X_f distribution, etc.) suggest that $\Psi\Psi$ production is highly correlated, as expected in the intrinsic charm picture. A recent experiment of Kodama et al. [203] searched for soft diffractive production of open charm in $D\bar{D}$ pairs with a 800 GeV proton beam and a Silicon target. The experiment set a 90% confidence level upper limit of 26 microbarns per Silicon nucleus for diffractive charm production. Kodama et al. estimated that the total diffractive cross section per Silicon nucleus, above the charm threshold, is 12.2 mb. The ratio of these values gives an upper limit of 0.2% for the probability that above the charm threshold, a diffractive event contains a charm pair. Kodama et al. interpreted this as the upper limit on the IC component of the proton. Brodsky et al. [323] discuss the probability for the intrinsic charm in an incident high energy hadron to be freed in a soft diffractive interaction in a high energy hadronic collision. In their formalism, the IC probability is multiplied by a resolution factor μ^2/m_c^2, where μ^2 is an appropriate soft mass scale [323]. If we take the soft scale to be of order Λ_{qcd}=0.2 GeV or the ρ mass, one obtains a significant resolution factor suppression for charm production in a soft process. Thus, the charm fraction that should be observed in a soft hadronic or diffractive cross section should be considerably smaller than the intrinsic charm probability. If the suppression factor is for example 10, that would change the upper limit of the Kodama et al. experiment from 0.2% to 2%. The data would not therefore place a useful limit on the IC component. In the case of hard reactions, such as the deep inelastic lepton scattering of the EMC experiment, the suppression factor is not present. Despite the small IC probability and the suppression factor, Brodsky and Vogt [318, 319] claim that the large X_f J/ψ hadroproduction (NA3) data, including the A-dependence, are consistent with the IC picture. Robinett [324] calculated $\Psi\Psi$ production in terms of multiple parton interactions.

The most probable IC state occurs when the constituents are minimally off-shell; i.e., have the smallest invariant mass. In the rest system, this happens when the constituents are relatively at rest. In a boosted frame, this configuration corresponds to all constituents having the same velocity and rapidity [323, 325]. Most of the momentum, on the other hand, is carried by the heavy quark constituents of these Fock states. Within gauge theory (QCD, QED), particles (quarks, gluons, protons, electrons) may coalesce into bound states primarily when they are at low relative velocity. It is well known that in QED, the coalescence probability depends on the factor α_f/V, where V is the relative velocity. This factor may be large, even if the fine structure constant α_f is small. Coalescence probabilities in some QED processes were calculated by Brodsky et al. [326, 327]. The coalescence via IC in the leading particle effect occurs after the π^- fluctuates into a $|\bar{u}dc\bar{c}\rangle$ Fock state. It happens automatically when the IC Fock state is freed, if the charm and valence quarks move at approximately the same velocity and rapidity [319]. When an intrinsic double charm ICC state is freed in a soft collision, the two charm quarks should also have approximately the same velocity, so that coalescence into a cc state is likely. The two freed c's may scatter and the consequent coalescence probability should depend analogously on $\alpha_s(\mu^2)/V$. The scale μ depends on the exchanged momentum. When it is a soft scale, the effective coupling can be quite large [328]. The cc diquark may subsequently coalesce with a valence quark, which also has the same velocity, to produce ccq.

A detailed ICC ccq production cross section calculation would be of great interest. For production with pion or baryon beams, one may be able to estimate the ccq coalescence rate, using appropriate leading D data as a normalization. One characteristic of IC is an $A^{0.7}$ surface dominated A-dependence, which gives an extra nuclear suppression relative to leading twist fusion processes. One should therefore measure the A-dependence of ccq production at large X_f. Comparison of the data with ICC predictions may give new perspectives on heavy and light quark wavefunctions, and also on coalescence mechanisms for producing leading particle effects.

We can describe some ingredients for a calculation of the ICC contribution to ccq production. The inelastic cross section is roughly 25 mb. Taking 0.3% for the IC component of an incident proton or pion, the naive estimate for the $cc\bar{c}\bar{c}$ probability is $(3. \times 10^{-3})^2 = 9. \times 10^{-6}$. Here, the probability for ICC is taken as the square of IC, which is probably a lower limit. Once one has one pair, the projectile Fock state is already far off-shell, and the amplitude to produce an additional heavy quark pair may only involve an extra power of $\alpha_s(m_c^2)$ [329]. Since most of the cross section at $\sqrt{s} =$ 30 GeV is at low p_t, there may also be a factor of roughly 10 loss for the resolution factor [323]. The cc pair has 3x3=9 colour components, 3 colour antitriplet, and 6 colour sextet. If cc are unpolarized in colour space in the double-intrinsic-charm Fock state (a plausible assumption), there is 1/3 probability for the antitriplet possibility. We denote the ccq coalescence probability by P. One then expects a ccq production cross section: $\sigma = 25 \times 10^6 \times 9 \times 10^{-6} \times 10^{-1} \times P \times 1/3 \sim 10P\ nb/N$. For example, probabilities P of 50%-100% would lead to 5-10 nb/N cross sections. But a calculation for this probability is not yet available.

The energy dependence of ccq and cqq production cross sections is also of interest. Consider data for Λ_c and and Ξ_c from WA89 [128] (330 GeV Σ^-) and WA62 [330] (110 GeV Σ^-). The WA62 data were taken for $X_f > 0.6$, and an estimated large extrapolated cross section of $\sigma B = (5.3 \pm 2.0)$ μb/Be nucleus was reported. WA62 gives a cross section dependence of $d\sigma/dX_f \sim (1 - X_f)^{1.7\pm0.7}$, while WA89 [128] finds roughly $d\sigma/dX_f \sim (1 - X_f)^{4.7\pm1.6\pm0.6}$. It is possible therefore that some or most of the cross section in WA62 is via diffractive rather than central production. With the X_f dependence of WA89, less than 2% of the cross section should be observed at $X_f > 0.6$. If the WA62 data are correct, they have much more cross section than WA89 for the same high X_f range. It leads to the surprising result that cqq (central or diffractive) production is favoured at energies closer to threshold, perhaps due to some unknown production mechanism. Cross sections at high X_f comparable to those of WA62 were also reported by the neutron beam experiment BIS-2 at Serpukhov [331], with beam energies up to 70 GeV. A more recent low energy neutron beam experiment at Serpukhov, EXCHARM [332], also reported clean Λ_c signals at $X_f > 0.5$. However, Bunyatov and Nefedov [333] recently determined cross sections for the production of charmed particles in proton-nucleon interactions at 70 GeV from proton beam dump experiments with the IHEP-JINR neutrino detector. For the region $X_f > 0.5$, they reported total cross sections more than two orders of magnitude lower than the values obtained by BIS-2 [331]. If these new results are correct, then charm production cross sections near threshold are consistent with expectations, and are not anomalously large. Still, it is important that an energy scan be carried out with different beam particles, to better understand the dependence of the cqq cross section on beam energy. If the charm production cross sections near threshold are low as expected, then fixed target experiments should look for ccq production at the highest possible energies.

It will be of interest to compare ccq production in hadron versus electron- positron collisions, even if CHEOPS deals with hadron interactions. Following production of a single heavy quark from the decay of a Z or W boson produced in an electron-positron collision, Savage and Wise [292] discussed the expected suppression for the the production of a second heavy quark by string breaking effects or via a hard gluon. Kiselev et al. [293] calculated low cross sections for double charm production at an electron-positron collider B factory, for $\sqrt{s}$= 10.6 GeV. They find $\sigma(ccq)/\sigma(c\bar{c}) = 7. \times 10^{-5}$. This result is inapplicable to hadronic interactions as in CHEOPS. But it demonstrates the wide interest in this subject.

A number of works [180, 294, 334–342] consider the production and decay of doubly heavy hadrons (bcq, $\bar{b}c$, bbq, ccq, etc.) via gluonic fusion and quark-antiquark annihilation in hadronic production for collider experiments at the FNAL Tevatron or CERN LHC. A CHEOPS fixed target study for ccq (possibly including some B_c mesons) can be a valuable prelude to future collider studies of doubly heavy hadrons. For short lifetime ccq detection, if the cross sections are adequate, it is easier to work in a fixed-target apparatus. More recently, gluonic fusion calculations were carried out by Berezhnoi, Kiselev, Likhoded (BKL) [334] for cc diquark production in hadron collider experiments at large transverse momenta, calculated with a complete set of 36 diagrams to the fourth order of α_s. Such calculations may be more precise [334] than those based on the fragmentation mechanism [295]. Gluonic and quark-antiquark collisions are included, such as $gg \to b\bar{b}$ and $q\bar{q} \to b\bar{b}$. These processes may be followed by gluon bremsstrahlung and splitting and annihilation $\bar{b} \to \bar{b}g \to \bar{b}gg \to \bar{b}c\bar{c}$, resulting finally in $b\bar{b}c\bar{c}$. Such calculations can also give the yield of B_c ($\bar{b}c$) mesons [126,200,295,343–349]. Similarly, one may calculate $cc\bar{c}\bar{c}$ production. The gluonic component is expected to give much more contribution than quark-antiquark at 1.8 TeV, and also at lower energies. The dependence of the cross section on the projectile is then less important.

Considering all estimates and uncertainties described above, we will give yields in CHEOPS using estimated lower and upper limits of 1 nb/N and 25 nb/N for the ccq production cross section.

Signal and background considerations

High energies are needed for studies of baryons with high mass and short lifetime, in order to obtain the Lorentz boost necessary for the separation of secondary and primary vertices. The Lorentz factor for a particle produced at rest in the c.m. frame, with beam of momentum p_b, is $\gamma = \sqrt{p_b/(2M_N)}$, as we show below. For a CERN experiment with $p_b \approx 400$ GeV/c, this corresponds to $\gamma \approx 15$ and a momentum of 55 GeV/c for the ccq. The mean decay length then would be 450 μm for a lifetime of 100 fs.

We give an estimate here for the lifetime boost γ in the laboratory frame for a ccq baryon that is produced at the centre of rapidity via a high energy hadron beam of momentum $p_{b,L}$ and energy $E_{b,L}$. One expects that doubly charmed hadrons should be predominantly produced near threshold in the centre of mass of the colliding hadrons. They would then have sufficient energy in the laboratory frame to be conveniently observed. We give an estimate here for the lifetime boost γ in the laboratory frame for a ccq baryon that is produced at the centre of rapidity via a high energy hadron beam of momentum $p_{b,L}$ and energy $E_{b,L}$ interacting with a target nucleon of mass M_N. We have $\gamma = E_{c,L}/M_c$, where $E_{c,L}$ is the laboratory energy of the produced mass M_c charm baryon. We can estimate a value for $E_{c,L}$ using the invariance (with respect to a Lorentz boost in the z direction) of the light cone momentum fraction $\alpha = (E_c + p_{cz})/(E_b + p_{bz})$ that describes the ratio of the charm baryon momentum to the beam hadron momentum. We equate $\alpha(CM) = \alpha(LAB)$, with $\alpha(CM) \approx M_c/2E_{b,cm}$ and $\alpha(LAB) \approx 2E_{c,L}/2E_{b,L}$. We can express the α in terms of the invariant energy $\sqrt{s}$, using the relationships $s \approx 2E_{b,L}M_N$ and $s \approx 4E_{b,cm}^2$. We have $\alpha(CM) \approx M_c/\sqrt{s}$ and $\alpha(LAB) \approx 2E_{c,L}M_N/s$. Finally, we obtain $\gamma \approx E_{c,L}/M_c \approx \sqrt{s}/2M_N \approx \sqrt{E_{b,L}/2M_N}$.

The backgrounds are not only events from the primary vertex, but also from the decays of the hadrons associated with the two associated $\bar{c}$ quarks produced together with the two c quarks. One may expect that the requirement to see two related, sequential secondary vertices, or to see a doubly charged particle, may provide a significant reduction in background levels.

High energies are needed for studies of high mass, and short lifetime baryons. Thereby, one may produce high energy doubly charmed baryons. The resulting large lifetime boost improves separation of secondary and primary vertices, and improves track and event reconstruction. CHEOPS with 300-450 GeV protons and pions [291] should be sufficiently high. Although beam line constraints may limit initial CHEOPS studies to 300 GeV or lower, the higher energies will be eventually required for a complete ccq experiment.

Depending on the backgrounds, one may require separation distances of secondary from primary vertices of approximately 1-4 σ, where σ is the longitudinal tracking resolution. The requirement for two charm vertices in ccq decays may reduce backgrounds somewhat, so that this separation distance cut may be less stringent than in the case of cqq studies. For a lifetime of $100\ fs$, with a laboratory lifetime boost of 15, the distance from the production point to the decay point is around 450 microns. CHEOPS aims to achieve 150 micron resolution for $X_f > 0.1$, about 50% of the charm events.

The target design is very important. To achieve a high interaction rate and still have acceptable multiple scattering effects, the total target thickness should be less than 2% interaction length, corresponding to about 3 mm of Copper. Low A targets would minimize multiple scattering, but Copper is advantageous due to an $\mathrm{A}^{1/3}$ charm production enhancement. The optimum target design and thickness for double charm is being studied via Monte Carlo simulation, and is discussed below also in connection with trigger requirements.

Some bqq production and decay, with two secondary vertices, may be observed in CHEOPS. Such events are themselves of great interest, and must also be considered as background to ccq production. The bqq and ccq events may be distinguished by the larger bqq lifetime, and the higher transverse energy released in the b decay. It is not the primary aim of CHEOPS to study bqq baryons. Fixed target experiments at CERN have only a very small number of candidate bqq baryon events at a centre of mass energy around 30 GeV [350].

One can identify charm candidates by requiring that one or more decay particles from a short lived parent have a sufficiently large impact parameter or transverse miss distance S relative to the primary interaction point. This transverse miss distance (S) is obtained via extrapolation of tracks that are measured with a high resolution detector close to the target. This quantity is a quasi-Lorentz invariant. Consider a relativistic unpolarized parent baryon or a spin zero meson that decays into a daughter that is relativistic in the parent's centre of mass frame. Cooper [282] has shown that the average transverse miss distance is $S \approx \pi c\tau/2$. For example, Λ_c with $c\tau \approx 60$ microns should have $\mathrm{S} \approx 90$ microns, and Ω_c with $c\tau \approx 18$ microns ($\tau \approx 60$ fs) [128, 351] should have $\mathrm{S} \approx 30$ microns. A filter cut can be made on the sum of the charged decay products of the doubly charmed baryon and the singly charmed baryon daughter's decay products. Events from the primary vertex may be rejected by the cut on S. The S-trigger miss distance condition is satisfied on average for particles with $c\tau > 18$ microns ($\tau > 60$ fs). For particles with shorter lifetimes, the trigger efficiency decreases. CHEOPS DAQ will allow a 25 MHz beam rate, and data will be read out into memory using pipelined front end electronics with built in sparsification. This should allow the use of a computational miss-distance filter prior to the decision to write data to tape or disk.

CHEOPS plans to replace the computational miss-distance trigger with other first stage triggers. One possibility follows the approach of the open charm experiment E791, based on the fact that charm events show a larger total transverse energy E_t than background events. For single charm, E791 showed [284] that requiring a minimum E_t of 7-8 GeV reduces backgrounds by a factor 3-4 with an efficiency of about 75% for charmed hadrons. This approach needs to be explored for doubly charmed hadrons, which should be characterized by yet larger transverse energies. Requiring a minimum E_t of 10 GeV may for example selectively enrich the double charm sample, reducing backgrounds [284] by a factor of 10.

A second tagging possibility uses a multiplicity jump trigger [283] downstream of the interaction target. This is intended to be sensitive to an increase in the number of charged tracks (within a fiducial decay volume closed at two ends by thin quartz Cherenkov detectors) following one or more charm decays. The associated target design is problematic due to the short lifetimes expected for double charm. CHEOPS uses Copper targets interleaved with Silicon detectors, all stacked tightly together. The silicon detectors are used to identify the target segment of the primary interaction. The design is best for long lived charmed hadrons that exit the target, and decay downstream in a fiducial volume between the Cherenkov detectors of the multiplicity jump trigger. In CHEOPS, the tracking detectors are placed after the first multiplicity jump Cherenkov detector, starting about 3 mm downstream of the Copper targets, where the decay volume between the Cherenkov detectors is filled with about fifteen 150 micron silicon planes. The thin silicon tracking detectors, spaced 1 mm apart, allow one to identify secondary vertices. With this target design, for very short lived ccq and subsequent singly charged hadrons, the primary and first of the secondary vertices may both be positioned inside the Copper target. However, a multiplicity jump charm trigger may may still be implemented associated with a secondary vertex further downstream from a longer lived singly charmed hadron from ccq decay, or associated with hadrons arising from one of the two $\bar{c}$ quarks.

For ccq, the silicon tracking detectors may also be used as the active interaction targets. In this application, the multiplicity jump trigger can not be used, and one may rely instead on the transverse energy trigger. One may require that only one track, the beam track, enter the fiducial "target" volume after the first Cherenkov detector, as determined by the pulse height in this detector. Since the silicon target/detectors are spaced 1 mm apart, the secondary vertices may be observed between silicon segments. The complete experimental trigger may include the multiplicity jump trigger (associated with the Copper targets) and the transverse energy trigger (associated with either the Silicon and Copper targets). The total target thickness than includes the Copper and Silicon.

We should also consider trigger and filter options that further enhance the yield of doubly charmed hadrons. One may build a trigger that requires several particles with high transverse momentum, since this may be more likely for doubly charmed hadrons. For Ξ_{cc}^{++}, Bjorken [105] suggested using a detector which triggers (or filters) on a doubly charged (four times minimum ionizing) particle. Bjorken [105] also describes triggers for observing semi-leptonic decay, based on tri-muon detection for Ω_{ccc}^{++} and di-muon detection for ccq. With E_t at 7 GeV, one may also require coincidence with a single muon. These specialized triggers require further study. The yield estimates given below are based on non-leptonic charm triggers designed for singly charmed baryons.

Projected Yields

For CHEOPS with proton and pion beams, one may rely on previous measurements done with similar beams. The open charm production cross section at SPS energies is roughly 25 μb. Taking a suppression factor of k= 0.04-1.0, we have $\sigma(\mathrm{ccq}) \approx 1 - 25$ nb/N. We assume a measured branching ratio B= 10% for the sum of all ccq decays; this being 50% of all the decays leading to only charged particles. We also assume a measured B = 20% for the sum of all cqq decays, this being roughly the value achieved in previous experiments. With these branching ratios, we estimate $\sigma \cdot BB = 1. - 25. \times 0.2 \times 0.1 = 0.02 - 0.5\ nb/N$. If k > 1.0, the expected cross sections would be yet higher.

For CHEOPS, we now evaluate the rate of reconstructed ccq events. The yields expected to observe two uncorrelated charmed hadrons may be about 10 times higher, and will also be of interest. The expectations are based on a beam of 5. $\times 10^7$ per spill, assuming 240 spills per hour of effective beam, or 1.2 $\times 10^{10}$/hour. For a 4000 hour run (2 years), and a 2% interaction target, one achieves roughly 10^{12} interactions per target nucleon. We assume that $\sigma(\mathrm{charm}) = 25$ μb and $\sigma(\mathrm{in}) = 25$ mb for a proton target, and take a charm production enhancement per nucleon of $\mathrm{A}^{1/3}$ (with mass A $\approx$ 64 for CHEOPS). One then obtains a high sensitivity of 1.5 $\times 10^5$ charm events for each nb per nucleon of effective cross section (for nucleons in A $\approx$ 64 nuclei), where $\sigma_{eff} = \sigma BB\varepsilon$. Here ε is the overall efficiency for the experiment.

We consider also the expected CHEOPS efficiency for ccq events, by comparison to E781 estimated [133] cqq efficiencies. Our rough efficiency estimates must eventually be superseded by detailed Monte Carlo simulations of the efficiencies, but that effort goes beyond the objectives of the present review. The E781 efficiencies for cqq decays include a tracking efficiency of 96% per track, a trigger efficiency averaged over X_f (for accepted X_f > 0.1) of roughly 18%, and a signal reconstruction efficiency of roughly 50%. These E781 Monte Carlo simulations [133] gave an average global efficiency of $\sim$ 8%, by considering relatively strong signals from the $\sim$ 200 fs lifetime decay $\Lambda_c^+ \to pK^-\pi^+$, and the $\sim$ 350 fs lifetime decay $\Xi_c^+ \to \Xi^-\pi^+\pi^-$. The charm baryons were assumed [133] to be produced with a cross section of the form $d\sigma/dX_f = (1 - X_f)^{4.2}$, an assumption which is built into the estimation of the trigger efficiency. For heavy ccq production, it is likely that this distribution would shift to lower X_f (corresponding to an exponent greater than 4.2). This is so since the event has two charmed and two anticharmed quarks, and they all must share the available momentum. As a consequence, both the trigger and reconstruction efficiencies would be lower.

The signal reconstruction efficiency depends strongly on the ability of the track finding algorithm [352] to efficiently and unambiguously identify tracks in a given event from the hit data in the vertex detectors. Events with higher charged particle multiplicities (as for ccq) may have overlapping hits in some vertex detector planes, and are more difficult to deal with. Reconstruction efficiencies are also low for low X_f events. High X_f events suffer less multiple scattering, and have improved efficiencies, since the resulting tracks are more nearly straight line, which leads to less ambiguities in the track finding. We therefore consider CHEOPS events only with $\mathrm{X}_f > 0.1$, corresponding also to the E781 lower limit of acceptance. The reconstruction efficiency should in any case be lower for double charm events. Including the tracks associated with the anti-charmed particles, and assuming an average of three charged tracks per charmed particle decay, ccq events may have a very high multiplicity of charged tracks. Such events are much more complex, not just twice as complex as single charm events. Some losses in reconstruction efficiency are due to extra ambiguities in track finding due to the secondary reactions that may occur in the vertex detectors, since these reactions increase the charged particle multiplicity of an event. Since doubly charmed events have a higher charged particle multiplicity in any case, they also should have a higher probability for such secondary reactions. And they also have lower efficiencies due to the tracking efficiency of 96% per track.

One may expect the vertex to be tagged more often (roughly a factor of two) for double charm compared to single charm. This would lead to a higher trigger efficiency. It is encouraging that using the CHEOPS proposed type of vertex detector, multi-vertex events from beauty production were successfully reconstructed [350]. For lifetimes smaller than 60 fs, which is possible for ccq, the trigger efficiency would be reduced. Also, for a weak ccq signal, tighter analysis cuts with resulting lower efficiencies may be required in order to achieve the optimum signal to noise ratio.

Considering all the effects discussed, we make a conservative estimate here that the E781 trigger efficiencies for ccq and cqq events are roughly the same. But we anticipate a loss in (reconstruction · tracking) efficiency for double compared to single charm, and further losses due to the short lifetime of double charm. We make an optimistic guess that the overall average ccq efficiency may be as high as $\varepsilon \simeq 2\%$, 25% of the expected E781 value for cqq detection. Given the larger uncertainties in the expected cross section and backgrounds, this level of precision may be adequate for the purposes of initial rough estimations. Considering all the unknown variables, the actual experimental global efficiency may however be significantly lower than the 2% estimate.

The expected sensitivity for CHEOPS was given above as 150 charm events/(pb/N) of effective cross section. For σBB $\sim$ 20-500 pb/N, one has $\sigma_{eff} < 0.4 - 10.\ pb/N$, and therefore an upper limit of N(ccq) $\approx$ 60-1500 events for CHEOPS. This is the maximum total expected yield for ccu,ccd,ccs production for ground and excited states.

References

[1] A.V. Efremov and O.V. Teryaev, Preprint E2–88–287 (Dubna, 1988).

[2] G. Altarelli and G.G. Ross, Phys. Lett. B **212** (1988) 391.

[3] R.D. Carlitz, J.C. Collins, and A.H. Mueller, Phys. Lett. B **214** (1988) 229.

[4] T. Gehrmann and W.J. Stirling, Z. Phys. C **65** (1994) 461.

[5] T. Gehrmann and W.J. Stirling, Preprint DTP/95/82 (Durham, UK, 1995).

[6] R.D. Ball, S. Forte, and G. Ridolfi, Preprint CERN/TH 95–266 (Geneva, 1995).

[7] M. Glück, E. Reya, M. Stratmann, and W. Vogelsang, Preprint DO-TH 95/13 (Dortmund, Germany, 1995).

[8] M. Glück and E. Reya, Z. Phys. C **39** (1988) 569.

[9] G. Altarelli and W.J. Stirling, Particle World **1** (1989) 40.

[10] M. Glück, E. Reya, and W. Vogelsang, Nucl. Phys. B **351** (1991) 579.

[11] A.D. Watson, Z. Phys. C **12** (1982) 123.

[12] W. Vogelsang, in: W. Buchmüller and G. Ingelman, eds., Proceedings *Physics at HERA*, Hamburg, Oct. 29–30, 1991, (DESY, Hamburg, Germany, 1991).

[13] The EM Collaboration, J.J Aubert *et al.*, Phys. Lett. **167B** (1986) 127.

[14] P.L. Frabetti, Phys. Lett. B **263** (1991) 584; M. Derrick *et al.*, Phys. Lett. B **349** (1995) 225.

[15] The NA14 Collaboration, M.P. Alvarez *et al.*, Z. Phys. C **60** (1993) 53.

[16] H. Abramowicz, E.M. Levin, A. Levy, and U. Maor, Phys. Lett. B **269** (1991) 465.

[17] G. Ingelman, J. Rathsman, and G.A. Schuler, AROMA v. 2.1 Manual, DESY Preprint.

[18] G. Ingelman, J. Rathsman, and A. Edin, LEPTO v. 6.3 Manual, DESY Preprint.

[19] T. Sjöstrand, Comp. Phys. Comm. **82** (1994) 74.

[20] J.C. Anjos *et al.*, Phys. Rev. Lett. **62** (1989) 513.

[21] G. Bellini, in: M. Greco, ed., Proceedings *8th Rencontres de Physique de la Vallee d'Aoste: Results and Perspectives in Particle Physics*, La Thuile, Italy, Mar. 1994, (Editions Frontiières, Gif-sur-Yvette, France, 1994).

[22] S. Frixione, M.L. Mangano, P. Nason, and G. Ridolfi, Phys. Lett. B **308** (1993) 137.

[23] A.P. Contagouris, S. Papadopoulos, and B. Kamal, Phys. Lett. B **246** (1990) 523; M. Karliner and R.W. Robinett, Phys. Lett. B **324** (1994) 209.

[24] M. Glück, E. Reya, and A. Vogt, Z. Phys. C **67** (1995) 433.

[25] The Particle Data Group, L. Montanet *et al.*, Phys. Rev. D **50** (1994) 1173.

[26] The SM Collaboration, B. Adams *et al.*, Phys. Lett. B **329** (1994) 399, erratum Phys. Lett. B **339** (1994) 332.

[27] The SM Collaboration, , B. Adams *et al.*, Phys. Lett. B **357** (1995) 248.

[28] The E-143 Collaboration, K. Abe *et al.*, Phys. Rev. Lett. **74** (1995) 346.

[29] The E-143 Collaboration, K. Abe *et al.*, Phys. Rev. Lett. **75** (1995) 25.

[30] D.L. Adams *et al.*, Phys. Lett. B **336** (1994) 269.

[31] G. Bunce *et al.*, Particle World **3** (1992) 1.

[32] M. Düren and K. Zapfe, Preprint DESY 94–239 (Hamburg, Germany, Dec. 1994).

[33] T. Sloan, *The Feasibility of Polarized Structure Function Measurements at HERA*, talk at Workshop on Future Physics at HERA, Sep. 1995, DESY, Hamburg, Sep. 1995–May, 1996.

[34] J. Blümlein, in: J. Blümlein and W.-D. Nowak, eds., Proceedings *Workshop on the Prospects of Spin Physics at HERA*, Zeuthen, Germany, Aug. 1995, DESY 95-200 (Hamburg, Germany, 1995) 179; R. Ball *et al.*, *ibid.* 350.

[35] W. Bartel, *HERA Upgrades and Impact on Experiments*, talk at Workshop on Future Physics at HERA, Feb. 1996, DESY, Hamburg, Sep. 1995–May, 1996.

[36] The EM Collaboration, J. Ashman *et al.*, Nucl. Phys. B **328** (1989) 1.

[37] V. Papavassiliou, Ph.D. Thesis (Yale U., New Haven, CN, 1988).

[38] The SM Collaboration, B. Adeva *et al.*, submitted to Phys. Lett. B, Preprint CERN/PPE 95–187 (Geneva, Dec. 1995).

[39] E. Rondio *et al.*, Private Communication, March 1995.

[40] The HERMES Collaboration, Technical Design Report DESY-PRC 93/06 (Hamburg, Germany, 1993).

[41] L. Trentadue and G. Veneziano, Phys. Lett. B **323** (1994) 201.

[42] S.J. Brodsky, J. Ellis, and M. Karliner, Phys. Lett. B **206** (1988) 309.

[43] J. Ellis, D. Kharzeev, and A. Kotzinian, Z. Phys. C **69** (1996) 467.

[44] S. Willocq *et al.*, Z. Phys. C **53** (1992) 207.

[45] J.T. Jones *et al.*, Z. Phys. C **28** (1987) 23.

[46] D. Allasia *et al.*, Nucl. Phys. B **224** (1983) 1.

[47] V. Ammosov *et al.*, Nucl. Phys. B **162** (1980) 208.

[48] J. Ellis, M. Karliner, D.E. Kharzeev, and M.G. Sapozhnikov, Phys. Lett. B **353** (1995) 319; M. Alberg, J. Ellis, and D.E. Kharzeev, Phys. Lett. B **356** (1995) 113.

[49] W. Melnitchouk and A.W. Thomas, Z. Phys. A **353** (1995) 331.

[50] M. Burkardt and R.L. Jaffe, Phys. Rev. Lett. **70** (1993) 2537.

[51] A. Anselm, M. Anselmino, F. Murgia, and M.G. Ryskin, Sov. Phys. JETP Lett. **60** (1994) 496.

[52] K. Chen, G.R. Goldstein, R.L. Jaffe, and X. Ji, Nucl. Phys. B **445** (1995) 380.

[53] G. Gustafson and J. Häkkinen, Phys. Lett. B **303** (1993) 350.

[54] The ALEPH Collaboration, D. Buskulic *et al.*, submitted to Phys. Lett. B, Preprint CERN/PPE 96–004 (Geneva, Jan. 1996).

[55] P.J. Mulders and R.D. Tangerman, Preprint NIKHEF 95–053 (Amsterdam, 1995), hep–ph/9510301.

[56] I.I.Y. Bigi, Nuovo Cim. **41A** (1977) 43; *ibid.* 581.

[57] G. Ingelman, in: W. Buchmüller and G. Ingelman, eds., Proceedings *Physics at HERA*, Hamburg, Oct. 29–30, 1991, (DESY, Hamburg, Germany, 1991).

[58] R.L. Jaffe and X. Ji, Phys. Rev. Lett. **67** (1991) 552.

[59] R.L. Jaffe and X. Ji, Nucl. Phys. B **375** (1992) 527.

[60] The HELP Collaboration, Proposal CERN/LEPC 93–14, LEPC/P7 and CERN/LEPC 94–1, LEPC/P7 Add. 1. (Geneva, 1993)

[61] The RHIC Spin Collaboration, RHIC Spin Physics Proposal, (BNL, Upton, NY, Aug. 1992, Update Sept. 1993).

[62] X. Artru, in: J. Collins, S.F. Heppelman, and R.W. Robinett, eds., Proceeding *Polarized Collider Workshop*, University Park, PA, Nov. 15–17, 1990, (AIP Conf. Proc. 223, 1991) 176.

[63] X. Artru and M. Mekhfi, Z. Phys. C **45** (1990) 669.

[64] X. Artru and M. Mekhfi, Nucl. Phys. A **532** (1991) 351c.

[65] B.L. Ioffe and A. Khodjamirian, Phys. Rev. D **51** (1995) 3373

[66] H. He and X. Ji, Phys. Rev. D **52** (1995) 2960.

[67] H. Kim, M. Polyakov, and K. Goeke, Preprint RUB-TPII-26/95 (Ruhr-U. Bochum, Germany, 1995), hep–ph/9509283.

[68] R.L. Jaffe and X.J. Ji, Phys. Rev. Lett. **71** (1993) 2547; X.J. Ji, Phys. Rev. D **49** (1994) 114.

[69] F. Baldracchini *et al.*, Fortschritte der Phys. **30** (1982) 505.

[70] J. Collins, S.F. Heppelmann, and G.A. Ladinsky, Nucl. Phys. B **420** (1994) 565.

[71] J. Collins, Nucl. Phys. B **396** (1993) 161.

[72] The DELPHI Collaboration, W. Bonivento, *et al.*, Contribution eps-0549 to Int. Europhysics Conf. on High Energy Physics, Brussels, Belgium, July 1995, Preprint DELPHI 95-81 PHYS 516 (Geneva, June 1995).

[73] D.L. Adams *et al.*, Phys. Lett. B **264** (1991) 462.

[74] X. Artru, J. Czyzewski, and H. Yabuky, Preprint TPJU 13/95 (Aug. 1995), hep-ep/9508239.

[75] X. Artru, J. Czyzewski, and H. Yabuki, prepLYCEN/9423Lyon, France, 1994, TPJU 12/94; X. Artru, Private Communication.

[76] J. Collins and G.A. Ladinski, Preprint PSU/TH/114 (Penn State U., Dec. 1994).

[77] A. Kotzinian, Nucl. Phys. B **441** (1995) 234.

[78] R.D. Tangerman and P.J. Mulders, Phys. Lett. B **352** (1995) 129.

[79] A.M. Kotzinian and P.J. Mulders, Preprint NIKHEF 95–059 (Amsterdam, 1995), YERPHI 1455(25)-95 (Yerevan, Armenia, 1995), hep–ph/9511420.

[80] E.L. Berger, Preprint ANL-HEP-PR–87–45 (Argonne, IL, 1987).

[81] G. Ross and R. Roberts, Preprint Ral–90–062 (Didcot, U.K., Aug. 1990).

[82] The E-143 Collaboration, K. Abe *et al.*, submitted to Phys. Rev. Lett., Preprint SLAC–PUB–95–6982 (Stanford, CA, August 1995), hep–ex/9511013.

[83] The SM Collaboration, D. Adams *et al.*, Phys. Lett. B **336** (1994) 125.

[84] D.M. Kaplan and S. Kwan, eds., Proceedings *Workshop on the Future of High Sensitivity Charm Experiments: CHARM2000*, Batavia, IL, June 1994, (FERMILAB-CONF-94/190, 1994).

[85] The WA89 Collaboration, H.W. Siebert, Contribution to *Workshop on Heavy Flavour Physics, Lafex Int. School on High Energy Physics (LISHEP95)*, Rio de Janeiro, Brazil, Feb. 1995.

[86] N. Isgur and M.B. Wise, Phys. Rev. D **42** (1990) 2388.

[87] The CLEO Collaboration, T. Bergfeld *et al.*, Phys. Lett. B **323** (1994) 219.

[88] J.G. Körner and P. Kroll, Z. Phys. C **57** (1993) 383; Phys. Lett. B **293** (1992) 201; J.G. Körner and M. Krämer, Phys. Lett. B **275** (1992) 495; P. Kroll, in: K. Goeke, W.Y. Pauchy Hwang, and J. Speth, Proceedings *2nd German-Chinese Symposium on Medium Energy Physics*, Bochum, Germany, Sep. 1992, Contemporary Topics in Medium Energy Physics (Plenum Press, New York, 1992) 163.

[89] The CLEO Collaboration, G. Crawford *et al.*, Phys. Rev. Lett. **75** (1995) 624.

[90] B. Stech, Univ. of Heidelberg, Private Communication, February 1995.

[91] The CLEO Collaboration, P. Avery *et al.*, Preprints CLNS 95/1352, CLEO 95–14.

[92] I. Bigi, in: D.M. Kaplan and S. Kwan, eds., Proceedings *Workshop on the Future of High Sensitivity Charm Experiments: CHARM2000*, Batavia, IL, June 1994, (FERMILAB-CONF-94/190, 1994) and Preprint CERN/TH 94–7370 (Geneva, 1994).

[93] G.S. Abrams *et al.*, Phys. Rev. Lett. **44** (1980) 10.

[94] The ARGUS Collaboration, Phys. Lett. B **210** (1988) 263; The CLEO Collaboration, Phys. Rev. D **43** (1991) 3599.

[95] S. Frixione, M.L. Mangano, P. Nason, and G. Ridolfi, Phys. Lett. B **308** (1993) 137; Nucl. Phys. B **431** (1994) 453.

[96] M. Aguilar-Benitez *et al.*, Phys. Lett. B **161** (1985) 400; Z. Phys. C **40** (1988) 321.

[97] R. Ammar *et al.*, Phys. Rev. Lett. **61** (1988) 2185.

[98] S. Barlag *et al.*, Z. Phys. C **39** (1988) 451; Z. Phys. C **49** (1991) 555.

[99] K. Kodama *et al.*, Phys. Lett. B **263** (1991) 573; Phys. Lett. B **284** (1992) 461.

[100] H. Cobaert *et al.*, Z. Phys. C **36** (1987) 577.

[101] R. Bailey *et al.*, Nucl. Phys. B **239** (1984) 15;
R. Barloutaud *et al.*, Nucl. Phys. B **172** (1980) 25.

[102] S.F. Biagi *et al.*, Phys. Lett. **76B** (1978) 243.

[103] A.N. Aleev *et al.*, Z. Phys. **23B** (1984) 333; Z. Phys. C **37** (1988) 243.

[104] G.A. Alves *et al.*, Phys. Rev. Lett. **72** (1994) 812;
M. Adamovich *et al.*, Phys. Lett. B **305** (1993) 402.

[105] J.D. Bjorken, in: S. Oneda, ed., Proceedings *Int. Conf. on Hadron Spectroscopy*, College Park, MD, Apr. 1985, (AIP Conf. Proc. 132, 1985); Unpublished Draft, *Estimates of Decay Branching Ratios for Hadrons Containing Charm and Bottom Quarks*, July 22, 1986; Unpublished Draft, *Masses of Charm and Strange Baryons*, Aug. 13, 1986.

[106] R. Roncaglia, *et al.*, Phys. Rev. D **51** (1995) 1248; Phys. Rev. D **52** (1995) 1722; Phys. Lett. B **358** (1995) 106; Phys. Rev. D **47** (1993) 4166.

[107] J.M. Richard, in: D.M. Kaplan and S. Kwan, eds., Proceedings *Workshop on the Future of High Sensitivity Charm Experiments: CHARM2000*, Batavia, IL, June 1994, (FERMILAB-CONF-94/190, 1994) and hep–ph/9407224;
J.M. Richard, Nucl. Phys. B **21** (Proc. Suppl.) (1991) 254;
E. Bagan *et al.*, Z. Phys. C **64** (1994) 57;
S. Zouzou and J.M. Richard, Few Body Systems **16** (1994) 1;
J.P. Ader, J.M. Richard, and P. Taxil, Phys. Rev. D **25** (1982) 2370.

[108] S. Fleck and J.M. Richard, Prog. Theo. Phys. **82** (1989) 760; Particle World **1** (1990) 67; A. Martin and J.M. Richard, Phys. Lett. B **355** (1995) 345.

[109] E. Bagan, M. Chabab, and S. Narison, Phys. Lett. B **306** (1993) 350.

[110] J.A. Appel, Ann. Rev. Nucl. Part. Sci. **42** (1992) 367.

[111] G. Bellini, Invited talk at *Int. Workshop Heavy Quarks at Fixed Target*, Charlottesville, VA, USA, Oct. 1994.

[112] M.B. Voloshin and M.A. Shifman, Sov. Phys. JETP **64** (1986) 698.

[113] R. Forty, in: S. Keller and H. Wahl, eds., Proceedings *XIV Int. Conf. on Physics in Collision*, Tallahassee, FL, June 1994, (Edition Frontières, Gif-sur-Yvette, France, 1995) and Preprint CERN/PPE 94–144 (Geneva, 1994).

[114] H. Cheng, Phys. Lett. B **289** (1992) 455.

[115] V. Gupta and K.V.L. Sharma, Int. J. Mod. Phys. A **5** (1990) 879.

[116] The E687 Collaboration, H.W.K. Cheung *et al.*, in: S. Seidel, ed., Proceedings *APS Meeting, DPF 94*, Albuquerque, NM, Aug. 1994, (World Scientific, River Edge, NJ, 1995) 51.

[117] N. Bilic, B. Guberina and J. Trampetic, Nucl. Phys. B **248** (1984) 261

[118] B. Guberina, R. Ruckl and J. Trampetic, Z. Phys. C **33** (1986) 297

[119] B. Blok and M. Shifman, Nucl. Phys. B **399** (1993) 441; *ibid.* 459.

[120] I. Bigi and N.G. Uraltsev, Z. Phys. C **62** (1994) 623.

[121] B. Blok and M. Shifman, in: R. and J. Kirkby, eds., Proceedings *Third Workshop on the Physics at a Tau-Charm Factory*, Marbella, Spain, June 1993, (Editions Frontières, Gif-sur-Yvette, France, 1994).

[122] I.I. Bigi, Preprint UND–HEP–95–BIG02, –BIG06, –BIG01 (Notre Dame U., IN, 1995), hep–ph/9508408, hep–ph/9507364, hep–ph/9501418; Acta Physica Polonica **26** (1995) 641.

[123] I.I. Bigi, Preprint UND-HEP-95-BIG09 (Notre Dame U., IN, Oct. 1995), hep–ph/9510325.

[124] S.R. Klein, Int. J. Modern Phys. A **5** (1990) 1457.

[125] M.A. Sanchis-Lozano, Phys. Lett. B **321** (1994) 407.

[126] M.J. Savage and R.P. Springer, Int. J. Modern Phys. A **6** (1991) 1701.

[127] L. Chau and H. Cheng, Phys. Rev. D **36** (1987) 137; Phys. Lett. B **222** (1989) 285; A. Kamal and R. Verma, Phys. Rev. D **35** (1987) 3515, erratum *ibid.* **36** (1987) 3527.

[128] The WA89 Collaboration, E. Chudakov, Contribution to *Int. Workshop Heavy Quarks at Fixed Target*, Charlottesville, VA, USA, Oct. 1994; The WA89 Collaboration, R. Werding *et al.*, 27th Int. Conf. on High Energy Physics (ICHEP), Glasgow, Scotland, July 1994.

[129] J. Dey *et al.*, Phys. Lett. B **337** (1994) 185.

[130] The CLEO Collaboration, D. Acosta *et al.*, Phys. Rev. D **49** (1994) 5690.

[131] S. Aoki *et al.*, Prog. Theo. Phys. **89** (1993) 131.

[132] M. Adamovich *et al.*, Phys. Lett. B **348** (1995) 256.

[133] J. Russ, in: D.M. Kaplan and S. Kwan, eds., Proceedings *Workshop on the Future of High Sensitivity Charm Experiments: CHARM2000*, Batavia, IL, June 1994, (FERMILAB-CONF-94/190, 1994).

[134] The WA92 Collaboration, D. Barberis *et al.*, in: D.M. Kaplan and S. Kwan, eds., Proceedings *Workshop on the Future of High Sensitivity Charm Experiments: CHARM2000*, Batavia, IL, June 1994, (FERMILAB-CONF-94/190, 1994).

[135] The BaBar Collaboration, Letter of Intent SLAC-443 (Stanford, CA, 1994).

[136] H. Fritzsch and U. Gell–Mann, in: Proceedings *XVI Int. Conf. on High Energy Physics*, Chicago, 1972, 135.

[137] M. Zielinsky *et al.*, Z. Phys. C **31** (1986) 545.

[138] G.Godfrey and N.Isgur, Phys. Rev. D **32** (1985) 189

[139] S.S. Gershtein *et al.*, Z. Phys. C **24** (1984) 305;
R.Akhoury and J.M.Frere, Phys. Lett. B **220** (1989) 258;
The Mark III Collaboration, D. Coffman *et al.*, Phys. Rev. D **41** (1990) 1410.

[140] The GAMS Collaboration, F. Binon *et al.*, Nuovo Cim. **78** (1983) 313; *ibid.* **80** (1984) 363.

[141] The Crystal Barrel Collaboration, C. Amsler *et al.*, Phys. Lett. B **342** (1995) 433.

[142] The Crystal Barrel Collaboration, C. Amsler *et al.*, Phys. Lett. B **353** (1995) 571.

[143] The Crystal Barrel Collaboration, C. Amsler *et al.*, Phys. Lett. B **340** (1994) 259.

[144] The Crystal Barrel Collaboration, C. Amsler *et al.*, in preparation; see also S. Resag, in: Proceedings *6th Int. Conf. on Hadron Spectroscopy (Hadron 95)*, Manchester, U.K., 10–14 July, 1995.

[145] The Crystal Barrel Collaboration, C. Amsler *et al.*, in preparation; see also S. Dombrowsky,in: Proceedings *6th Int. Conf. on Hadron Spectroscopy (Hadron 95)*, Manchester, U.K., 10–14 July, 1995.

[146] S. Abatzis *et al.*, Phys. Lett. B **324** (1994) 509.

[147] F. Antinori *et al.*, Phys. Lett. B **353** (1995) 589.

[148] C. Amsler and F.E. Close, Phys. Lett. B **353** (1995) 385.

[149] E. Klempt, B.C. Metsch, C.R. Münz, and H.R. Petry, Phys. Lett. B **361** (1995) 160.

[150] C. Ritter, B.C. Metsch, C.R. Münz, and H.R. Petry, in preparation.

[151] M. Gaspero, Nucl. Phys. **A562** (1993) 407.

[152] The OBELIX Collaboration, A. Adamo *et al.*, Nucl. Phys. **A558** (1993) 13c.

[153] The Crystal Barrel Collaboration, C. Amsler *et al.*, Phys. Lett. B **322** (1994) 431.

[154] G. Schierholz, Preprint DESY 88-172 (Hamburg, Germany, 1988).

[155] The GAMS Collaboration, A. Singovski *et al.*, Nuovo Cim. **107A** (1994) 1911.

[156] The Mark III Collaboration, L. Chen *et al.*, in: S. Oneda and D.C. Peaslee, eds., Proceedings *Int. Conf. on Hadron Spectroscopy (Hadron 91)*, College Park, MD, 12–16 Aug. 1991, (World Scientific, River Edge, NJ, 1992) 111.

[157] T.A. Armstrong *et al.*, Phys. Lett. B **307** (1993) 394.

[158] P. Baillon *et al.*, Nuovo Cim. **50A** (1967) 393.

[159] D.L. Scharre *et al.*, Phys. Lett. B **97** (1980) 329.

[160] The Crystal Barrel Collaboration, C. Amsler *et al.*, Phys. Lett. B **358** (1995) 389.

[161] R.S. Longacre, Phys. Rev. D **42** (1990) 874.

[162] S.N.Ganguli and P.D.Roy, Phys. Rep. **67** (1980) 203.

[163] The VES Collaboration, D.Amelin *et al.*, Phys. Lett. B **356** (1995) 595.

[164] D. Amelin *et al.*, Preprint IHEP–95–112 (Protvino, Russia, 1995).

[165] B.R. Holstein, Comments Nucl. Part. Phys. **19** (1990) 239.

[166] J. Gasser and H. Leutwyler, Ann. Phys. **158** (1984) 142; Nucl. Phys. B **250** (1985) 465; J.F. Donoghue and B.R. Holstein, Phys. Rev. D **40** (1989) 2378.

[167] J. Wess and B. Zumino, Phys. Lett. B **37** (1971) 95; E. Witten, Nucl. Phys. B **223** (1983) 422; R. Akhoury and A. Alfakih, Ann. Phys. **210** (1991) 81; B. Zumino *et al.*, Nucl. Phys. B **239** (1984) 477; W.A. Bardeen, Phys. Rev. **184** (1969) 1848; J.F. Donoghue and D. Wyler, Nucl. Phys. B **316** (1989) 289; C. Kuang-Chao *et al.*, Phys. Lett. B **134** (1984) 67; J.L. Manes, Nucl. Phys. B **250** (1985) 369.

[168] M.A. Moinester, in: H. Machner and K. Sistemich, eds., Proceedings *Conference on Physics with GeV-Particle Beams*, Jülich, Germany, Aug. 1994, (World Scientific, 1994); R.A. Miskimen *et al.*, in: A. Bernstein and B. Holstein, eds., Proceedings *Chiral Dynamics: Theory and Experiment*, M.I.T., July 1994, (Springer-Verlag, 1995).

[169] M.A. Moinester, in: A. Bernstein and B. Holstein, eds., Proceedings *Chiral Dynamics: Theory and Experiment*, M.I.T., July 1994, (Springer-Verlag, 1995).

[170] J.Bijnens *et al.*, Phys. Lett. B **237** (1990) 488; Z. Phys. C **46** (1990) 599

[171] J. Bijnens, Int. J. Modern Phys. A **8** (1993) 3045; J. Bijnens *et al.*, Phys. Lett. B **237** (1990) 488; Z. Phys. C **46** (1990) 599.

[172] H.J. Lipkin and M.A. Moinester, Phys. Lett. B **287** (1992) 179.

[173] V. Bernard *et al.*, Phys. Rev. D **46** (1992) 2756; Phys. Lett. B **319** (1993) 269.

[174] S. Capstick and B.D. Keister, Phys. Rev. D **47** (1993) 860; Phys. Rev. D **46** (1992) 84, erratum *ibid.* 4102.

[175] D. Babusci *et al.*, Phys. Lett. B **277** (1992) 158.

[176] Yu.M. Antipov *et al.*, Phys. Lett. B **121** (1983) 445; Z. Phys. C **26** (1985) 495.

[177] R. Baldini and S. Bellucci, in: A. Bernstein and B. Holstein, eds., Proceedings *Chiral Dynamics: Theory and Experiment*, M.I.T., July 1994, (Springer-Verlag, 1995).

[178] A.M. Nathan, in: A. Bernstein and B. Holstein, eds., Proceedings *Chiral Dynamics: Theory and Experiment*, M.I.T., Cambridge, MA, July 1994, (Springer-Verlag, 1995); B.R. Holstein and A.M. Nathan, Phys. Rev. D **49** (1994) 6101.

[179] M.N. Butler and A.M. Nathan, in: A. Bernstein and B. Holstein, eds., Proceedings *Chiral Dynamics: Theory and Experiment*, M.I.T., July 1994, (Springer-Verlag, 1995).

[180] A.M. Bernstein and B.R. Holstein, Conference Summary, in: A. Bernstein and B. Holstein, eds., Proceedings *Chiral Dynamics: Theory and Experiment*, M.I.T., July 1994, (Springer-Verlag, 1995).

[181] G. Backenstoss *et al.*, Phys. Lett. B **43** (1973) 431.

[182] T. Jensen *et al.*, Phys. Rev. D **27** (1983) 26.

[183] J. Huston *et al.*, Phys. Rev. **33** (1986) 3199.

[184] L. Capraro *et al.*, Nucl. Phys. B **288** (1987) 659.

[185] M. Zielinski *et al.*, Phys. Rev. Lett. **52** (1984) 1195.

[186] S. Cihangir *et al.*, Phys. Lett. **117B** (1982) 119; *ibid.* 123; Phys. Rev. Lett. **51** (1983) 1.

[187] D. Berg *et al.*, Phys. Lett. B **98** (1981) 119.

[188] L. Xiong, E. Shuryak, and G. Brown, Phys. Rev. D **46** (1992) 3798.

[189] Y.M. Antipov *et al.*, Phys. Rev. D **36** (1987) 21.

[190] R.A. Miskimen, K. Wang, and A. Yegneswaran, Spokesmen, *Study of the Axial Anomaly using the* $\gamma\pi^+ \to \pi^+\pi^0$ *Reaction Near Threshold*, CEBAF Proposal PR-94-015, (Newport News, VA, 1994).

[191] G. D'Ambrosio and G. Isidori, Z. Phys. C **65** (1995) 649.

[192] B.E. MacGibbon *et al.*, Phys. Rev. C **52** (1995) 2097.

[193] L. Frankfurt, G.A. Miller, and M. Strikman, Phys. Rev. Lett. **71** (1993) 2859.

[194] B. Blattel *et al.*, Phys. Rev. D **47** (1993) 2761.

[195] B. Blattel *et al.*, Phys. Rev. Lett. **70** (1993) 898.

[196] L. Frankfurt and M. Strikman, Phys. Rev. Lett. **66** (1991) 2289.

[197] L. Frankfurt, G.A. Miller, and M. Strikman, Ann. Rev. Nucl. Part. Sci. **44** (1994) 501.

[198] G. Baym, L. Frankfurt, and M. Strikman, Nucl. Phys. A **566** (1994) 149c.

[199] M. Zielinski *et al.*, Z. Phys. C **16** (1983) 197.

[200] M. Masetti and F. Sartogo, Phys. Lett. B **357** (1995) 659.

[201] M. Strikmani and V. Guzey, Phys. Rev. C **52** (1995) 1118.

[202] G. Bellini *et al.*, Nucl. Instrum. Methods **107** (1973) 85.

[203] K. Kodma *et al.*, Phys. Lett. B **316** (1993) 188.

[204] M.A. Moinester, D. Ashery, L.G. Landsberg, and H.J. Lipkin, submitted to Z. Phys. A, hep–ph/9510356; Preprint TAUP 22256–95 (Tel Aviv, Israel, 1995); L.G. Landsberg, M.A. Moinester, and M.A. Kubantsev, Preprint IFVE–94–19 (Protvino, Russia, Dec. 1993).

[205] H.J. Lipkin, Phys. Lett. B **45** (1973) 267.

[206] C. Gignoux, B. Silvestre-Brac, and J.M. Richard, Phys. Lett. B **193** (1987) 323.

[207] S. Takeuchi, S. Nussinov, and K. Kubodera, Phys. Lett. B **318** (1993) 1.

[208] S. Zouzou and J.-M. Richard, Few Body Systems **16** (1994) 1.

[209] D.O. Riska and N.N. Scoccola, Phys. Lett. B **299** (1993) 338.

[210] Chi-Keyyung Chow, Phys. Rev. D **51** (1995) 6327.

[211] Y. Oh, B.Y. Park, and D.P. Min, Phys. Lett. B **331** (1994) 362.

[212] M. Shmatikov, Phys. Lett. B **349** (1995) 411; hep–ph/9511369.

[213] D. Ashery, in: B.A. Campbel, A.N. Kamal, P. Kitching, and F.C. Khanna, eds., Prococeedings *6th Lake Louise Winter Institute*, Lake Louise, Canada, Feb. 1991, Particle Physics – The Factory Era (World Scientific, River Edge, NJ, 1991) 280; in: W. Chao and P. Shen, eds., Proceedings *Int. Symposium on Medium Energy Physics*, Beijing, China, Aug. 1994, (World Scientific, Singapore, 1994) 62.

[214] J. Lichtenstadt, Nucl. Phys. B **21** (1991) 264c

[215] The E791 Collaboration, S. May-Tal Beck, in: S. Seidel, ed., Proceedings *APS Meeting, DPF 94*, Albuquerque, NM, Aug. 1994, (World Scientific, River Edge, NJ, 1995) 1177; D. Ashery, in: Proceedings *International Symposium on Exotic Atoms and Nuclei*, Hakone, Japan, Jun. 1995, to be published in in Hyperfine Interactions.

[216] M. Bander and A. Subbaraman, Phys. Rev. D **50** (1994) 5478; Preprint UC-I-TR–95–9 (U. California, Irvine, 1995), hep–ph/9503341.

[217] N.A. Tornqvist, Z. Phys. C **61** (1994) 525; Phys. Rev. Lett. **67** (1991) 556; Nuovo Cim. **A107** (1994) 2471.

[218] T.E.O. Ericson and G. Karl, Phys. Lett. B **309** (1993) 426.

[219] S. Nussinov, U. Tel Aviv, Israel, Private Communication, 1995.

[220] A.V. Manohar and M.B. Wise, Nucl. Phys. B **399** (1993) 17.

[221] J. Weinstein and N. Isgur, Phys. Rev. D **41** (1990) 2236.

[222] J. Carlson, L. Heller, and J.A. Tjon, Phys. Rev. D **37** (1988) 744;
L. Heller and J.A. Tjon, Phys. Rev. D **35** (1987) 969.

[223] R.L. Jaffe, Phys. Rev. D **15** (1967) 267; *ibid.* 281.

[224] M.W. Beiner, B.C. Metsch, and H.R. Petry, submitted to Z. Phys. A (1995), hep–ph/9505215.

[225] M. Shmatikov, Nucl. Phys. A **596** (1996) 423.

[226] P. Grafstrom, Private Communication, February 1996.

[227] H. van der Graaf *et al.*, Nucl. Instrum. Methods A **307** (1991) 220.

[228] F. Bakker *et al.*, Nucl. Instrum. Methods A **330** (1993) 44.

[229] The RD5 Collaboration, C. Albajar *et al.*, Nucl. Instrum. Methods A **364** (1995) 473.

[230] H. Dekker *et al.*, Contribution to *The third international workshop on accelerator alignment*, Annecy, France, Sep. 1993.

[231] The RD26 Collaboration, Preprint CERN/DRDC 94-49 (Geneva, Dec. 1994).

[232] G. Lenzen *et al.*, Nucl. Instrum. Methods A **343** (1994) 268.

[233] The HERA-B Collaboration, Proposal DESY-PRC 94/02 (Hamburg, Germany, May 1994).

[234] R. Mc Carty *et al.*, Nucl. Instrum. Methods A **248** (1986) 69.

[235] W. Adam *et al.*, Nucl. Instrum. Methods A **343** (1994) 68.

[236] U. Müller, Ph.D. Thesis, (Univ. Mainz, Germany, 1994).

[237] R. Abjean *et al.*, Nucl. Instrum. Methods A **354** (1995) 417.

[238] The HADES Collaboration, GSI Proposal for a High-Acceptance Di-Electron Spectrometer, (Darmstadt, Germany).

[239] R.J. Apsimon *et al.*, Nucl. Instrum. Methods A **241** (1985) 339.

[240] R.J. Baur *et al.*, Nucl. Instrum. Methods A **343** (1994) 87.

[241] The RD26 Collaboration, RD–26 Proposal CERN/DRDC 92-3, (Geneva, 13 Jan. 1992).

[242] J. Almeida *et al.*, Nucl. Instrum. Methods A **367** (1995) 332.

[243] J. Seguinot *et al.*, Nucl. Instrum. Methods A **297** (1990) 133.

[244] F. Piuz, in: Proceedings *International Workshop on RICH Detectors*, June 1995, Uppsala, Sweden, to be published in in Nucl. Instrum. Methods.

[245] A. Breskin *et al.*, Preprint WIS-93.31.July-PH (Weizmann Institute, Israel) and in: Proceedings *International Workshop on RICH Detectors*, June 1995, Uppsala, Sweden, to be published in in Nucl. Instrum. Methods.

[246] A. Braem *et al.*, Nucl. Instrum. Methods A **343** (1994) 163.

[247] F. Piuz *et al.*, Nucl. Instrum. Methods A **333** (1993) 404.

[248] J.C. Santiard *et al.*, Preprint CERN-ECP/94-17 (Geneva, Oct. 1994).

[249] W. Beusch *et al.*, Nucl. Instrum. Methods A **323** (1992) 373.

[250] F. Binon *et al.*, Preprint SPSC/84-45/p214 (CERN, Geneva, 1985).

[251] O.Buyanov *et al.*, Nucl. Instrum. Methods A **349** (1994) 62.

[252] G. Alexeev *et al.*, Nucl. Instrum. Methods A **364** (1995) 307.

[253] F. Binon *et al.*, Nucl. Instrum. Methods A **256** (1987) 444.

[254] A.N. Aleev *et al.*, Instrum. Exp. Tech. **33** (1990) 1032.

[255] G. Alexeev *et al.*, Preprint IHEP 90–157 (Protvino, Russia, 1990)

[256] E. Iarocci, Nucl. Instrum. Methods **217** (1983) 30.

[257] Y. Bonushkin *et al.*, Nucl. Instrum. Methods A **300** (1991) 268.

[258] P. Abzeu *et al.*, CERN–PPE 95–194 (CERN, Geneva).

[259] Yu. M. Antipov *et al.*, Nucl. Instrum. Methods A **297** (1990) 121.

[260] G.K. Mallot, SMC Internal Note SMC–95–011 (CERN, Geneva, March 1995).

[261] S. Peraire, CERN/SL-BT, Private Communication, 1995.

[262] The SM Collaboration, B. Adeva *et al.*, Nucl. Instrum. Methods A **343** (1994) 363

[263] N. Doble, L. Gatignon, G. von Holtey, and F. Novoskoltsev, Nucl. Instrum. Methods A **343** (1994) 351.

[264] T.J. Ketel *et al.*, Internal Notes SMC–95–036, HMC–95–002 (CERN, Geneva, Oct. 1995).

[265] The RD17 Collaboration, V. Agoritsas *et al.*, CERN/DRDC 91–8, DRDC/P25; CERN/DRDC 93–47.

[266] J. Kyynäräinen, in: H. Dutz and W. Meyer, eds., Proceedings *7th Workshop on Polarized Target Materials and Techniques*, Bad Honnef, Germany, 3–6 June 1994, Nucl. Instrum. Methods A **356** (1995) 47.

[267] A. Abragam and M. Goldman, Rep. Prog. Phys. **41** (1978) 395.

[268] A. Daël *et al.*, IEEE Trans. on Magnetics **28** (1992) 560.

[269] H. Dutz *et al.*, to be published in (1996).

[270] N.W. Schellingerhout *et al.*, Phys. Rev. C **48** (1993) 2714.

[271] B. van der Brandt *et al.*, in: K.H. Althoff, W. Meyer, E. Steffens, and W. Thiel, eds., Proceedings *9th International Symposium on High Energy Spin Physics*, Bonn, Germany, Sep. 1990, (Springer-Verlag, Berlin, 1991) 320; see also J. Ball *et al.*, (AIP Conf. Proc. 343, 1995) 550.

[272] S. Goertz *et al.*, in: H. Dutz and W. Meyer, eds., Proceedings *7th Workshop on Polarized Target Materials and Techniques*, Bad Honnef, Germany, 3–6 June 1994, Nucl. Instrum. Methods A **356** (1995) 20.

[273] W. Flegel, CERN/PPE-EC, Private Communication, 1995.

[274] M. Adinolfi *et al.*, Nucl. Instrum. Methods A **329** (1993) 117.

[275] The RD19 Collaboration, E. Heijne *et al.*, Preprint CERN/ECP 94–1 (Geneva, 1994);
work in this field is also reported by M. Wright *et al.*, Preprint LBL–32912 (Berkeley, CA, 1992).

[276] E. Heijne, CERN/ECP, Private Communication, February 1996.

[277] D. Alde *et al.*, Nucl. Instrum. Methods A **342** (1994) 389.

[278] R. Bouclier *et al.*, Preprint CERN/PPE 95–95 (Geneva, July 1995)

[279] S. Brons *et al.*, Talk presented at the *II. Workshop on MSGC*, Sept. 1994, Padua, Italy.

[280] F. Angelini *et al.*, Preprint INFN PI/AE 93/10 (Pisa, Italy, 1993)

[281] The RD6 Collaboration, V. Commishau *et al.*, Preprint CERN/DRDC 93–46 (Geneva, 1993).

[282] P. Cooper, Private Communication. 1981.

[283] A.M. Halling and S. Kwan, Nucl. Instrum. Methods A **333** (1993) 324.

[284] D. Christian, in: D.M. Kaplan and S. Kwan, eds., Proceedings *Workshop on the Future of High Sensitivity Charm Experiments: CHARM2000*, Batavia, IL, June 1994, (FERMILAB-CONF-94/190, 1994).

[285] S. Paul, Preprint CERN/PPE 92–199 (Geneva, 1992).

[286] The RD–20 Collaboration, Preprint CERN/DRDC 94–39 (Geneva, 1994).

[287] Y. Arai *et al.*, IEEE J. of solid state circuits **27** (1992) Nr. 3.

[288] The EM Collaboration, M. Arneodo *et al.*, Nucl. Phys. B **321** (1989) 541.

[289] L.L. Frankfurt *et al.*, Phys. Lett. B **230** (1989) 141.

[290] M.A. Moinester, submitted to Z. Phys. C, Preprint TAUP 2255–95 (Tel Aviv, Israel, 1995), hep–ph/9506405.

[291] S. Paul, Contribution to *"Production and Decay of Hyperons, Charm and Beauty Hadrons*, Strasbourg, France, Sept. 1995.

[292] M.J. Savage and M.B. Wise, Phys. Lett. B **248** (1990) 177.

[293] V.V. Kiselev *et al.*, Phys. Lett. **332** (1994) 411; Yad. Fiz. **57** (1994) 733;
V.V. Kiselev, Int. J. Mod. Phys. A **10** (1995) 465; S.S. Gershtein *et al.*,
Usp. Fiz. Nauk. **165** (1995) 1; Phys. Rev. D **51** (1995) 3613.

[294] V.V. Kiselev *et al.*, Sov. J. Nucl. Phys. **46** (1987) 535.

[295] A.F. Falk, M. Luke, M.J. Savage, and M.B. Wise, Phys. Rev. D **49** (1994) 555.

[296] M.L. Stong, Preprint TTP 95–02 (U. Karlsruhe, Germany, 1995), hep–ph/9505217.

[297] S.P.K. Tavernier, Rep. Prog. Phys. **50** (1987) 1439.

[298] H.W. Siebert, Nucl. Phys. B **21** (Proc. Suppl.) (1991) 223.

[299] J.G. Körner and H.W. Siebert, Ann. Rev. Nucl. Part. Sci. **41** (1992) 511.

[300] D.M. Kaplan and S. Kwan, eds., Proceedings *Workshop on the Future of High Sensitivity Charm Experiments: CHARM2000*, Batavia, IL, June 1994, (FERMILAB-CONF-94/190, 1994).

[301] J.L. Rosner, Comm. Nucl. Part. Phys. **21** (1995) 369.

[302] S.N. Mukherjee *et al.*, Phys. Rep. **231** (1993) 201.

[303] W. Lucha, F.F. Schoberl, and D. Gromes, Phys. Rep. **200** (1991) 127.

[304] I.I. Bigi and N.G. Uraltsev, Phys. Lett. B **280** (1992) 271.

[305] E.J. Eichten and C. Quigg, Phys. Rev. D **49** (1994) 5845

[306] I.I. Bigi, N.G. Uraltsev, and A.I. Vainshtein, Phys. Lett. B **293** (1992) 430 erratum *ibid.* **297** (1993) 477.

[307] M. Shifman, Preprint TPI-MINN-95/31-T, UMN-TH-1413-95 (Oct. 1995), hep–ph/9510377.

[308] T. Mannel, J. Phys. G **21** (1995) 1007.

[309] M. Bauer, B. Stech, and M. Wirbel, Z. Phys. C **34** (1987) 103.

[310] E. Levin, Private Communication, 1995.

[311] F. Halzen, P. Hoyer, and W.Y. Stirling, Phys. Lett. B **188** (1987) 375.

[312] B. D'Almagne, in: E. Bloom and A. Fridman, eds., Proceedings *Int. Symposium on the Production and Decay of Heavy Flavors*, Stanford, CA., Sep. 1987, (New York Acad. Sci., New York, 1988); The E653 Collaboration, K. Kodama *et al.*, Phys. Lett. B **263** (1991) 579; M.L. Mangano, P. Nason, and G. Ridolfi, Nucl. Phys. B **405** (1993) 507.

[313] The WA75 Collaboration, S. Aoki *et al.*, Phys. Lett. B **187** (1987) 185.

[314] The NA3 Collaboration, J. Badier *et al.*, Phys. Lett. B **158** (1985) 85; Phys. Lett. B **114** (1982) 457; Phys. Lett. B **124** (1983) 535.

[315] R. Hagedorn, Preprint CERN/TH 94–7190 (Geneva, March 1994);
R. Hagedorn, in: K. Kajantie, ed., Proceedings *Quark Matter 84*, Lecture Notes in Physics Vol. 221 (Springer-Verlag, New York, 1985);
H. Grote, R. Hagedorn, and J. Ranft, *Atlas of Particle Production Spectra*, CERN Report, 1970.

[316] F.S. Rotondo, Phys. Rev. D **47** (1993) 3871.

[317] S.D. Ellis and R. Stroynowski, Rev. Mod. Phys. **49** (1977) 753.

[318] R. Vogt and S.J. Brodsky, Phys. Lett. B **349** (1995) 569; Nucl. Phys. B **438** (1995) 261; R.V. Gavai *et al.*, Int. J. Modern Phys. A **10** (1995) 2999; R. Vogt, Nucl. Phys. A **553** (1993) 791c; R. Vogt, S.J. Brodsky, and P. Hoyer, Nucl. Phys. B **383** (1992) 643; Nucl. Phys. B **360** (1991) 67; R. Vogt, Nucl. Phys. B **466** (1995) 159.

[319] R. Vogt and S.J. Brodsky, Nucl. Phys. B **438** (1995) 261.

[320] E. Hoffmann and R. Moore, Z. Phys. C **20** (1983) 71.

[321] B.W. Harris, J. Smith, and R. Vogt, Preprint LBL–37266 (Berkeley, CA, Aug. 1995), hep–ph/9508403.

[322] F.S. Navarra, M. Nielsen, C.A.A. Nunes, and M. Teixeira, hep–ph/9504388;
J.F. Donoghue and E. Golowich, Phys. Rev. D **15** (1977) 3421.

[323] S.J. Brodsky, P. Hoyer, A.H. Mueller, and W.K. Tang, Nucl. Phys. B **369** (1992) 519; and S.J. Brodsky, Private Communication.

[324] R.W. Robinett, Phys. Lett. B **230** (1989) 153.

[325] S.J. Brodsky, P. Hoyer, C. Peterson, and N. Sakai, Phys. Lett. B **93** (1980) 451; S.J. Brodsky, C. Peterson, and N. Sakai, Phys. Rev. D **23** (1981) 2745.

[326] S.J. Brodsky, J.F. Gunion, and D.E. Soper, Phys. Rev. D **36** (1987) 2710; S.J. Brodsky, Private Communication.

[327] C.T. Munger, S.J. Brodsky, and I. Schmidt, Phys. Rev. D **49** (1994) 3228.

[328] S.J. Brodsky, A.H. Hoang, J.H. Kuhn, and T. Teubner, Phys. Lett. B **359** (1995) 355.

[329] S.J. Brodsky, Private Communication.

[330] The WA62 Collaboration, S.F. Bigi *et al.*, Z. Phys. C **28** (1985) 175.

[331] A.N. Aleev *et al.*, Z. Phys. C **23** (1984) 333.

[332] The EXCHARM Collaboration, V.D. Kekelidze *et al.*, Contribution to *Int. Workshop Heavy Quarks at Fixed Target*, Charlottesville, VA, USA, Oct. 1994; G. Tatishvili, Private Communication.

[333] S. A. Bunyatov, Yu. A. Nefedov, Preprint, JINR, Dubna, 1995; J. Blumlein et al., Phys. Lett. B279 (1992) 405; L. S. Barabash, Sov. J. Phys. of Atomic Nuclei 57 (1994) 1974.

[334] A.V. Berezhnoi, V.V. Kiselev, and A.K. Likhoded, Preprint IHEP 95–87 (Protvino, Russia, 1995), hep–ph/9507242; and Private Communication, July 1995.

[335] M.A. Doncheski, J. Steegborn, and M.L. Stong, Preprint OCIP/C-95-8, TTP95-24 (Carleton U., Ottawa, Canada, July 1995), hep–ph/9507220.

[336] ATLAS Internal Notes, Phys–NO–041, Phys–NO–058 (Geneva, 1994); P. Eerola *et al.*, Nucl. Instrum. Methods A **351** (1994) 84.

[337] A. Fridman and B. Margolis, Preprint CERN/TH 93–6878 (Geneva, 1993).

[338] P. Lebrun and R.J. Oakes, Preprint FERMILAB-Conf-93/303 (Batavia, IL, 1993).

[339] M.J. White and M.J. Savage, Phys. Lett. B **271** (1991) 410.

[340] M.A. Sanchis-Lozano, Phys. Lett. B **321** (1994) 407; F. Albiol *et al.*, Preprint IFIC-95-24 (June 1995), hep–ph/9506306.

[341] K. Kolodziej, A. Leike, and R. Rueckl, Phys. Lett. B **355** (1995) 337.

[342] A.V. Berezhnoi A.K. Likhoded, and O.P. Yushchenko, Preprint IHEP 95–59 (Protvino, Russia, 1995), hep–ph/9504302.

[343] P. Nason *et al.*, in: G. Bellini and L. Brogiato, eds., Proceedings *Advanced Study Conf. on Heavy Flavors*, Pavia, Italy, Sept. 1993, (Edition Frontières, Gif-sur-Yvette, France, 1994), Preprint CERN/TH 94–7134 (Geneva, 1994).

[344] E. Braaten, K. Cheung, and T.C. Yuan, Phys. Rev. D **48** (1993) 5049.

[345] C.H. Chang and Y.Q. Chen, Phys. Rev. D **48** (1993) 4086.

[346] M. Lusignoli, M. Masetti, and S. Petrarca, Phys. Lett. B **266** (1991) 142.

[347] S.S. Gershtein, A.K. Likhoded, and S.R. Slabospitsky, Int. J. Modern Phys. A **13** (1991) 2309.

[348] M.A. Sanchis-Lozano, Nucl. Phys. B **440** (1995) 251.

[349] K. Cheung, in: J.F. Gunion, T. Han, and J. Ohnemus, eds., Procedings *4th Int. Conf. on Physics Beyond the Standard Model*, Lake Tahoe, CA, Dec. 1994, (World Scientific, River Edge, NJ, 1995), hep–ph/9503286.

[350] The BEATRICE Collaboration, D. Barberis, in: D.M. Kaplan and S. Kwan, eds., Proceedings *Workshop on the Future of High Sensitivity Charm Experiments: CHARM2000*, Batavia, IL, June 1994, (FERMILAB-CONF-94/190, 1994).

[351] The E687 Collaboration, P.L. Frabetti *et al.*, Phys. Lett. B **357** (1995) 678.

[352] N.M. Nikityuk, Phys. Part. Nucl. **26** (1995) 302.